ACCRETION GROWTH AND SLAG-METAL REACTIONS IN INJECTION METALLURGY

A thesis

presented for the degree of

Doctor of Philosophy

of the

University of London

and for the Diploma of Imperial College

by

SHIGERU OHGUCHI

Department of Metallurgy
and Materials Science,
Imperial College of Science
and Technology,
London, SW7 2BP

March 1983

ABSTRACT

The present work is focussed on heat transfer and mass transfer phenomena in gas and gas-powder injection into liquid metals.

1. Accretion formation.

Accretions are formed because the cooling effect of the gases causes metal to solidify around the tuyere tip. A mathematical model has been developed to calculate the heat transfer around a tuyere and in the molten metal for both pipe-like and porous accretions, which are the two extreme cases of actual accretions. The effects of gas injection conditions, metal superheat and heat transfer properties were discussed.

2. Desulphurization and dephosphorization of hot metal.

Experiments were carried out on desulphurization using submerged injection of $CaO-CaF_2-Al_2O_3$ powder, and on simultaneous desulphurization and dephosphorization using surface injection of $CaO-CaF_2-CaCl_2-Fe_2O_3$ powder with gas stirring. The results were discussed from the kinetic point of view. The effect of the silicon content in the hot metal on the simultaneous reaction was investigated.

3. A kinetic model for refining using submerged injection.

In submerged injection processes, the reactions occur during the rise of the powder particles dispersed in the melt (transitory reaction) and between the bulk slag and the bulk metal (permanent contact reaction). Given sufficient data on the rate constants for permanent contact reaction alone and permanent contact plus transitory reaction (submerged injection), the model allows the calculation of the separate contributions of the reactions.

A simple bulk mixing model was also proposed to enable the application of the kinetic model to cases where mixing was inadequate to maintain a uniform concentration in the bulk.

This model was applied to the laboratory-scale desulphurization experiments and it was shown that the relative contributions of the two types of reaction mechanism were roughly equal.

TABLE OF CONTENTS

LIST OF FIGURES AND PLATES

FIGURE

LIST OF TABLES

Table

Chapter 1: GENERAL INTRODUCTION

There has been a remarkably rapid growth in the application of injection techniques to the steel industry in recent years. A large number of reactors making use of injection processes, such as Q-BOP, AOD, combined top/bottom blowing converter, powder injection refining and intense gas stirring in ladle treatment, have been installed despite the stagnation in steel production since the oil crisis in 1973. There has been a concomitant and growing interest in the study of refining using injection processes [1-5] since the powder injection processes in ladles and torpedo-cars were established, and combined top/bottom blowing converters were born.

In the operation of Q-BOP, AOD and combined top/bottom blowing converters, it is well known that accretions (so called "knurdles" or "mushrooms") are formed around the tuyere tip because the cooling effect of the gases causes metal to solidify, and that the controlled accretion formation minimises erosion and corrosion of the tuyere by molten metal. In spite of the importance of accretion formation, no mathematical model was available to predict the conditions under which accretions would form. In Chapter 2 and 3 the finite difference method is used to calculate the heat transfer around a tuyere and in the molten metal for both pipe-like and porous accretions, which are the two extreme cases of the actual accretions.

A small powder injection apparatus, suitable for laboratory-scale experiments, was developed in the present work. The experimental apparatus and procedure are described in Chapter 4.

In submerged injection processes, the reactions occur during the rise of the powder particles dispersed in the melt (transitory reaction) and between the bulk slag and the bulk metal (permanent contact reaction). A number of investigations have been made to clarify whether the transitory reaction or permanent contact reaction dominate powder injection refining, but consistent agreement has not been achieved so far. This is due to lack of a suitable reaction model taking account of the contributions of the two reactions. In Chapter 5 a model has been developed which shows clearly the important factors affecting the kinetics of refining using submerged injection. The model allows the calculation of the separate contributions of the transitory and permanent contact reactions.

When considering the kinetics of slag/metal reactions, one often neglects the bulk mixing transport by assuming a uniform bulk concentration (as in Chapter 5). However, in some industrial processes for metal refining, such as desulphurization in torpedo-cars, the bulk mixing is inadequate to maintain the bulk concentration uniform, and it is very important to evaluate the effect of bulk mixing on the solute dispersion. In Chapter 6 a simple bulk mixing model has been developed which enables the application of the kinetic model during powder injection (Chapter 5) to the cases where bulk mixing is inadequate.

Currently a large effort, specially in industry in Japan, is being made on the study of the simultaneous dephosphorization and desulphurization[6] of molten pig iron to enable "slagless" blowing in the converter . In most of the trials, submerged powder injec-

tion or surface powder feeding with intense gas stirring has been utilized to achieve efficient and rapid removal of phosphorus and sulphur. It is reported that initial silicon contents in pig iron must be low (less than 0.2% typically) to perform sufficient phosphorus removal. However the effect of the silicon contents on the kinetics of the simultaneous dephosphorization and desulphurization has not been made clear. Simultaneous reaction experiments using surface powder injection with gas stirring were carried out to clarify the effect of silicon from the kinetic point of view, and these are described in Chapter 7.

In this thesis each chapter has been written as a self-contained unit to meet the requirements of readers with specific interests.

Chapter 2: HEAT TRANSFER CALCULATIONS FOR PIPE-LIKE ACCRETION FORMATION AROUND A SUBMERGED GAS INJECTION TUYERE.

Abstract

A mathematical model has been developed for heat transfer and accretion formation around a gas injection tuyere. In this model a method was developed to calculate convective heat transfer from the bulk liquid metal to the moving liquid/solid accretion interface. The mathematical equations for steady- and unsteady-states were solved by the finite difference method. In the steady state calculation the effects of the superheat, gas flow rate, thermal conductivity of refractory and heat transfer coefficients at gas/accretion and gas/refractory interfaces were examined. From the unsteady-state calculation the characteristics of the growth of pipe-like accretions were clarified.

Chapter 2: HEAT TRANSFER CALCULATIONS FOR PIPE-LIKE ACCRETION FORMATION AROUND A SUBMERGED GAS INJECTION TUYERE.

2.1. Introduction

In recent years, accretion formation around gas injection tuyeres has become of increasing interest, with the widespread application of submerged gas injection in the steel industry, in processes such as Q-BOP, combined top and bottom blowing converters, AOD, argon gas stirring of metal baths and powder-injection into molten cast iron or steel. The formation of so called "knurdles" or "mushrooms", which are metallic outgrowths, is well known in AOD[7] and Q-BOP[8] operations. It is reported that controlled accretion formation minimises erosion and corrosion of tuyeres by molten metal[9].

Accretions fall broadly between two extreme categories. These are (a) pipe-like accretions[7] with gas flow channels predominantly up the centre and (b) porous and fully capped mushroom-like accretions with gas flow channels spreading radially outwards from the tuyere exit[8]. Sections of steel accretions are shown in Plate 1 by courtesy of Okohira and Nippon Steel Corporation[10]. These accretions were experimentally obtained by argon gas injection into a ladle from the bottom. Plates 1(a) and (b) respectively show pipe-like and fully capped mushroom-like accretions.

The earlier work on heat transfer calculations around a tuyere was limited to the calculation of the temperature distribution in the refractory and/or the tuyere. Using simple boundary

conditions and the relaxation method, Krivsky and Schuhmann[11a] calculated the temperature distribution in a refractory wall surrounding the tuyere pipe in a copper converter. They suggested that the pronounced cooling effect of the gas flow in the tuyere was the cause of accretions. However they did not study accretion formation as such and also did not consider the rise in gas temperature in the tuyere. Guther and Opel[11b] also carried out heat transfer calculations around a tuyere without any accretions. Denier, Grosjean and Zanetta[12], in their pilot and industrial trials for oxygen injection in bottom-blown LWS converters, measured the temperature in the tuyere tube (inner tube of copper and outer of steel), in the bricks surrounding the tuyere and in the oxygen reaction zone. They also developed a mathematical model to describe heat flow within the tuyere.

Until the author and Robertson[13] and Boxall et al[14] published their work in April 1982, no mathematical model was available to predict accretion shapes. These two mathematical models correpond to pipe-like accretions. The model presented by Boxall et al[14] is essentially a one-dimensional steady-state calculation. They neglected the heat flux in the vertical direction (gas injection direction), and assuming that the heat flux from the metal bath is horizontal, they calculated the accretion radius from the heat balance equations between the bath and the gas. In the present work, two-dimensional steady- and unsteady-state calculations have been carried out to estimate the conditions under which pipe-like accretions occur and the shape of the accretions by considering heat transfer both in the refrac-

tory around the tuyere and in the molten metal. This chapter is based on the work described in reference 13.

2.2. Modelling of Heat Transfer Around a Tuyere

A section of the cylindrical heat transfer zone is shown in Figure 2.1, incorporating the cylindrical tuyere, the assumed path of injection gas in the liquid metal and the refractory around the tuyere. As is evident from Figure 2.1, it is assumed that the jet of gas penetrating into the liquid metal has the same effective diameter as that of the tuyere. Calculations have been carried out only for a simple cylindrical tuyere. The actual paths of the gas in an accretion are of complicated shapes consisting of numerous narrow conduits[7]. To account for this the value of the heat transfer coefficient for gas/metal was chosen higher than for gas/refractory. This aspect will be discussed in detail later.

The idea of a fictitious thermal diffusion zone has been introduced to account for heat transfer from liquid steel to solidified steel and for the moving boundary nature of the problem. Beyond this thermal diffusion zone it is assumed that the bulk liquid metal temperature is homogeneous due to strong agitation by injected gas. Thus, the temperature gradient in the liquid metal exists only in the fictitious thermal diffusion zone.

The mean heat flux density (q_d) across the thermal diffusion zone is expressed by

$$q_d = k_d \cdot T_s/R_d \qquad (2.1)$$

where T_s is the temperature difference between solidification temperature and bulk temperature (superheat), and k_d and R_d are

respectively the thermal conductivity and thickness of diffusion zone.

It is important to note that, since the thermal diffusion zone shown in Figure 2.1 has a curvature, the heat flux density q_d in Equation 2.1 is an average value across the thermal diffusion zone. The heat flux density in a region with curvature varies along the heat flow direction (Figure 2.2). The magnitude of this effect can be easily analyzed for a cylindrical or a spherical shape. For a cylindrical body, the relevant analysis is as follows. The temperature distribution in the cylinder is generally expressed as

$$T = C_1 \ln r + C_2 \quad (C_1, C_2; \text{constants})$$

Therefore the solid surface temperature, which is equal to the melting point T_m, and the bulk liquid temperature T_b are

$$T_m = C_1 \ln r_c + C_2$$

$$T_b = C_1 \ln (r_c + R_d) + C_2$$

where r_c is the radius of the curvature of the cylindrical solid body. The heat flux on the solid surface (q_s) and the average value across the thermal diffusion zone (q_d) can be written as

$$q_s = k \left(\frac{dT}{dr}\right)_{r_c} = k\, C_1/r_c$$

$$q_d = k\, (T_b - T_m)/R_d$$

$$= k\, C_1\, (\ln (r_c + R_d) - \ln r_c)/R_d$$

Therefore the magnitude of the flux density concentration (q_s/q_d) is

$$q_s/q_d = R_d/r_c \ln (1 + R_d/r_c)$$

A similar analysis can be carried out for a spherical surface, and the ultimate result is

$$q_s/q_d = 1 + R_d/r_c$$

The magnitudes of the heat flux density concentration for the cylindrical and spherical cases are indicated in Figure 2.3.

Practically, it is very difficult to estimate the actual value of R_d, because it is locally altered with the shape of the accretion and the properties of the fluid flow. In the present work a constant value of R_d was chosen, and the value of k_d was adjusted to obtain a particular value of q_d for given T_s. A particular ratio of k_d/R_d is equivalent to assuming a particular value of heat transfer coefficient on a plane surface i.e.,

$$q_d = (k_d/R_d) \cdot T_s = h_1 \cdot T_s \qquad (2.2)$$

The assumption of constant R_d leads to higher fluxes at the surface when the accretion is strongly curved. Since this is probably the case in practice it is not a bad assumption to use.

2.3. Formulation

1) Governing equation.

The section of the cylindrical region in which heat transfer calculations are done is shown in Figure 2.4. By assuming axial symmetry, the governing heat transfer equation for liquid steel, solid steel and refractory in cylindrical co-ordinates becomes

$$\frac{1}{\alpha}\frac{\partial T}{\partial t} = \frac{\partial^2 T}{\partial Z^2} + \frac{1}{r}\frac{\partial T}{\partial r} + \frac{\partial^2 T}{\partial r^2} \qquad (2.3)$$

2) Gas temperature.

The heat balance for the gas rising through the bore in the refractory region can be described by

$$C_p\,(T_g - T_{go}) = \int_{Z_o}^{Z} (2h_{gR}\,(T_W - T_g)/\rho.r_o.u)dZ \qquad (2.4)$$

By converting Equation 2.4 to differential form, one can get the heat balance equation in the refractory

$$\rho C_p\,\frac{dT_g}{dZ} = \frac{2h_{gR}}{r_o.u}\,(T_W - T_g) \qquad (2.5)$$

A similar equation can be obtained for the heat transfer from accretion to gas. The only difference from Equation 2.5 is the value of the heat transfer coefficient, which is the effective heat transfer coefficient (h_{gs}) in the accretion. The equation is

$$\rho Cp\,\frac{dTg}{dZ} = \frac{2h_{gs}}{r_o.u}\,(T_W - T_g) \qquad (2.6)$$

3) Boundary conditions.

The boundary conditions for different regions are as follows

(a) Outside of refractory (boundary (1) in Figure 2.4).

$$T = \text{constant (outside temperature of refractory)} \qquad (2.7)$$

(b) Interface between refractory and solid steel (boundary (2) in Figure 2.4).

$$\begin{aligned} (k_S.\partial T/\partial Z)_S &= (k_R.\partial T/\partial Z)_R \\ (T)_S &= (T)_R \end{aligned} \qquad (2.8)$$

(c) Interface between refractory and liquid steel (boundary (3) in Figure 2.4).

$$(k_d \cdot \partial T/\partial Z)_1 = (k_R \cdot \partial T/\partial Z)_R$$
$$(T)_1 = (T)_R \qquad (2.9)$$

(d) Interface between liquid and solid steel (boundary (4) in Figure 2.4)

$$(k_d \cdot \partial T/\partial n)_1 = (k_s \cdot \partial T/\partial n)_s$$
$$(T)_1 = (T)_s = T_m(\text{melting point}) \qquad (2.10)$$

(e) Subinterface between bulk liquid and fictitious thermal diffusion zone (boundary (5) in Figure 2.4)

$$T = T_b \text{ constant (bulk liquid temperature)} \qquad (2.11)$$

(f) Heat transfer boundary between accretion and gas (boundary (6) in Figure 2.4)

$$h_{gs} (T_w - T_g) = k_s (\partial T/\partial r)_{r_o} \qquad (2.12)$$

(g) Heat transfer boundary between refractory and gas (boundary (7) in Figure 2.4)

$$h_{gR} (T_w - T_g) = k_R (\partial T/\partial r)_{r_o} \qquad (2.13)$$

(h) Side surface of cylindrical region to be calculated (boundary (8) in Figure 2.4)

This boundary is assumed to be thermally insulated

$$\partial T/\partial r = 0 \qquad (2.14)$$

(i) Inlet gas temperature (boundary (9) in Figure 2.4)

$$T_g = T_{go} \text{ constant (inlet gas temperature)} \qquad (2.15)$$

2.4. Calculation and Data. Steady-State

To reduce the computational labour, Equation 2.3 was modified to the following form. Replacing r by X = ln r, Equation 2.3 for the steady state is

$$\frac{\partial^2 T}{\partial Z^2} + e^{-2X} \frac{\partial^2 T}{\partial X^2} = 0 \qquad (2.16)$$

Equation 2.16 was solved with the gas temperature equations and boundary conditions by the successive over relaxation method [15a]. After each iteration the fictitious thermal diffusion zone was reset, so that the bulk liquid region could remain equidistant from the solidified region. The procedure for setting the thermal diffusion zone of constant thickness is described in Figure 2.5. Consider the circle of radius R_d, the centres of which are located at the mesh points immediately inside the solid/liquid interface. The mesh points of liquid steel falling in the circles are taken as those of the thermal diffusion zone. Then, liquid steel mesh points of the rest of the area are regarded as those of the bulk liquid and are kept at constant temperature.

For the presentation of the fixed interface boundaries a general finite difference expression was used. As an example mesh points and temperatures at solid steel/refractory interface, where thermal conductivity and mesh point interval change, are shown in Figure 2.6. In this figure, i-1, i, i+1, etc are the mesh point subscripts of Z-direction, while those of r-direction are omitted. In Figure 2.6 the right-hand side of the mesh point i is the solid steel region, which has thermal conductivity k_s and

mesh interval ΔZ_s, and the left-hand side is the refractory region, which has thermal conductivity k_R and mesh interval ΔZ_R. T_i is the temperature of the mesh point at the interface. To calculate T_i, one can introduce two fictitious pivotal temperature (T^*_{i-1}, T^*_{i+1}). T^*_{i-1} is the fictitious steel temperature extended in the refractory region, and T^*_{i+1} is the fictitious refractory temperature extended in the steel zone. Using these fictitious temperatures the boundary condition Equation 2.8 is expressed by the following central-difference equation.

$$k_s \cdot \frac{T_{i+1} - T^*_{i-1}}{2.\Delta Z_s} = k_R \cdot \frac{T^*_{i+1} - T_{i-1}}{2.\Delta Z_R} \qquad (2.17)$$

At mesh point i, two more different equations derived from Equation 2.16 can be formed. One is the governing equation for solid steel temperatures T^*_{i-1}, T_i, T_{i+1}, and the other is for refractory temperatures T_{i-1}, T_i, T^*_{i+1}. Using these three different equations the three unknown temperatures T^*_{i-1}, T_i, T^*_{i+1} can be calculated.

The following mathematical modification was employed in the calculation of the thermal diffusion zone to facilitate computation of the moving boundary of the solidified region. Temperature and thermal conductivity of the diffusion zone, i.e., T and k_d are replaced by modified temperature Θ and thermal conductivity k_s, which is chosen as equal to the value of solid steel. This modification is expressed as

$$(T, k_d) \rightarrow (\Theta, k_s) \text{ in liquid region}$$

where Θ is defined by

$$\Theta = T_m + (T - T_m) \cdot k_d/k_s \qquad (2.18)$$

This modification does not affect the governing equation and the boundary conditions. For example, the left hand side of Equation 2.9 or Equation 2.10 is

$$(k_d \cdot \partial T/\partial Z)_l = (k_d \cdot \frac{\partial T}{\partial \Theta} \cdot \frac{\partial \Theta}{\partial Z})_l = (k_s \cdot \partial \Theta/\partial Z)_l$$

$$(T)_l = T_m = (\Theta)_l$$

The advantage of this modification is that we can avoid the moving boundary problem (solid/liquid interface), because there is no discontinuity of gradient between solid steel temperature and modified liquid temperature, and the solid/liquid boundary condition (Equation 2.10) is automatically satisfied. Actual computation was performed using the above mentioned modified temperature and thermal conductivity, and after convergence of the relaxation calculation the original temperature was recalculated.

Material properties and typical gas injection conditions for computation are presented in Table 2.1 and in Table 2.2 repsectively. The thermal conductivity of the refractory is that of typical steelmaking brick (siliceous fireclay or medium alumina fireclay). Generally the values in Table 2.1 and Table 2.2 were used, unless specifically mentioned.

The heat transfer coefficient between argon gas and refractory was estimated by using Colburn's equation, which is

$$Nu = 0.023 \cdot Re^{0.8} \cdot Pr^{1/3} \qquad (2.19)$$

As the path of gas in the accretion actually consists of many narrow conduits, the effective heat transfer coefficient in metal is chosen higher than that in the refractory zone. The relation between the effective heat transfer coefficient and number of

hypothetical gas conduits in the accretion is indicated in Figure 2.7. If the effective heat transfer coefficient in the accretion is higher than the three-fold value of that in the refractory region, the size of the accretion does not change much, as is shown later in the results.

Constant material properties of argon gas were assumed for computation, though gas temperature was changing extensively along the tuyere length. The error caused by this assumption is small. The temperature dependent coefficient in Equation 2.5 or Equation 2.6 is eventually only the heat transfer coefficient, because the change of gas temperature does not affect mass flow rate per unit area ($\rho.u$) at all, and the specific heat of argon gas is almost independent of temperature. The temperature dependence of heat transfer coefficient can be estimated by Equation 2.19. Density of argon gas is inversely proportional to the absolute temperature. Viscosity and thermal conductivity are proportional to the absolute temperature raised to the power of 0.7[16]. Thus, the heat transfer coefficient of argon gas is proportional to the absolute temperature raised to the power of 0.14, which means that the heat transfer coefficient does not depend on temperature very strongly. In addition, the value of heat transfer coefficient at an average temperature of $727^{o}C$ was adopted, so that the error in the overall heat transfer does not affect the shape of the accretion very much.

The actual computation was done on the CDC Cyber 174 computer at Imperial College. Total number of meshpoints for the finite difference representation was 1530~2760 , and a typical run consumed about 300 sec of computer time. The computer program

REL6 is given in Appendix A.2.

2.5. Results. Steady-State

As an example, calculated results for accretion formation under steady state conditions are shown in Figure 2.8, which indicates the shape of accretion, isotherms in the refractory and gas temperature. The calculated accretion shape shows a good agreement with the ice accretion experimentally obtained by cold nitrogen/water model[14]. However, the calculated shape is slender compared with that observed for some actual accretions [7]. The reason is that the path of the gas is assumed to be a bundle of tubes located at the centre of the accretion, while actual accretions often have numerous divergent paths.

The increment of gas temperature is small in the refractory zone, but it is significant in the accretion, owing to the high heat transfer coefficient and the high conductivity of the steel accretion.

Figures 2.9 and 2.10 indicate the effect of superheat on the shape of the accretion and on the height and the bottom radius of the accretion. The accretion size is considerably altered by superheat, becoming very large at low superheat.

The variations of accretion shape and gas temperature with gas flow rate are shown in Figures 2.11 and 2.12, where heat transfer coefficient between refractory wall and gas were estimated by Equation 2.19, and heat transfer coefficients in steel accretion zone were also varied so as to keep the ratio h_{gs}/h_{gR} constant. This was done since high gas flow rates will increase h_{gs} by roughly

the same amount as they increase h_{gR}.

Figure 2.13 shows the variation of the accretion shape with thermal conductivity of the refractory. The bottom radius of the accretion increases with increase of thermal conductivity of the refractory due to the effect of heat removal through the refractory zone. On the other hand, the height of the accretion does not substantially change with change in the thermal conductivity of the refractory.

The effect of variation of the heat transfer coefficient between accretion and gas on the size and shape of the accretion is indicated in Figure 2.14. Accretion height has a maximum at a particular value of the heat transfer coefficient, while the bottom radius of accretion monotonously increases. It is seen that the maximum point of accretion height is located about the point with an h_{gs} value of 0.01 cal/sec cm^2 ^oC. The gradient of the accretion height and bottom radius change very gradually for h_{gs} values above 0.01. Therefore, as long as the effective heat transfer coefficient in the accretion (h_{gs}) is higher than 0.01 cal/sec cm^2 ^oC, variation of h_{gs} does not give a very significant change in the height of the accretion.

For the superheat of 7.5^oC, variation of heat transfer coefficients between refractory and gas does not make any noticeable difference in the shape of accretion. It slightly affects gas temperature, especially near the boundary between accretion and refractory, but the difference decreases with ascent of gas in the accretion as is shown in Figure 2.15. Under conditions of high superheat, i.e. small accretion size, the effect of the heat transfer coefficient can be seen, and Figure 2.16 shows the

variation of the accretion shape with different heat transfer coefficients between refractory and gas for the superheat of $20^{o}C$. In this case, the bottom radius of the accretion increases with increase of the heat transfer coefficient.

2.6. Calculation. Unsteady-State

The unsteady state calculations were carried out for a constant superheat of $10^{o}C$ in the liquid metal, with an initial linear temperature gradient in the refractory from 1000 to $200^{o}C$ (Figure 2.17).

Replacing r by $X = \ln r$, the governing equation (Equation 2.3) for the unsteady state is

$$\frac{1}{\alpha}\frac{\partial T}{\partial t} = \frac{\partial^2 T}{\partial Z^2} + e^{-2X}\frac{\partial^2 T}{\partial x^2} \qquad (2.20)$$

Throughout the unsteady state calculation, solidification and remelting occur during the process of accretion formation. Therefore the latent heat of fusion must be taken into account. On the assumption that melting or solidification occur over a temperature range, namely the mushy zone (solid and liquid mixture), the latent heat of fusion was converted into a high effective specific heat of the mushy zone. The thermal conductivity of the mushy zone was assumed to be of the same value as that of the solid in order to facilitate the computation.

Argon gas injection into molten steel through a refractory tuyere was again chosen as a basis for the calculations.

The boundary conditions are identical with those of the steady state calculation, being shown in Figure 2.4. For the boundary

between the solid steel and the mushy zone in the present calculation, no special boundary condition is necessary since the thermal conductivities of both phases are equal. On the other hand, the boundary between the mushy zone and the liquid steel is accompanied by a discontinuity in the thermal conductivity. To facilitate the calculation of the mushy zone/liquid steel boundary, the same modified temperature was applied to the diffusion zone, (Equation 2.18).

Making use of the above modification, the governing equation in the fictitious thermal diffusion zone become

$$\frac{\partial \Theta}{\partial t} = \frac{k_d}{\rho C_p} \left(\frac{\partial^2 \Theta}{\partial r^2} + \frac{1}{r} \cdot \frac{\partial \Theta}{\partial r} + \frac{\partial^2 \Theta}{\partial Z^2} \right)$$

One can see that the thermal diffusivity ($k_d/\rho C_p$) is not changed by the modification of temperature. However the thermal conductivity and the specific heat do change by this modification of temperature. That is;

$$(T,\ k_d,\ C_p) \rightarrow (\Theta,\ k_s,\ C_p \cdot k_s/k_d)$$

Consequently the boundary condition for the mushy-zone/liquid-steel boundary become

$$\partial T/\partial n = \partial \Theta/\partial n$$

$$T = \Theta$$

The governing equation was solved with the gas temperature equation by the alternating implicit method (Peaceman and Rachford's Method)[15b]. Material properties and gas injection conditions used are presented in Tables 2.1 and 2.2 respectively. The finite-difference mesh employed is shown in Figure 2.18. The total number

of the mesh points was 660. The mesh intervals of radius direction in the vicinity of the gas conduit, where temperature gradients are steep, and also where solidification occurs, were very fine owing to the logarithmic modification of radius. Small mesh intervals were also chosen close to the steel/refractory interface where solidification and remelting occur, as is seen from the figure.

The mathematical expression for a temperature field of this problem is strongly non-linear because of the nature of the moving boundary problem, including the setting up of the thermal diffusion zone, and the change of effective specific heat due to solidification. Therefore, the time interval Δt should be small enough to obtain a stable and accurate solution by the finite-difference method. In this work the computations were tried using several different sets of time intervals so as to obtain an adequate set. The three sets of time intervals used are presented in Table 2.3. and the results are shown in Figure 2.19. The time intervals of these three sets were fine in the early stages of the calculation, when the temperature change was rapid, becoming coarse later to save computing time. The coarsest set of time intervals (c) gave more rapid growth of the accretion than the others, showing slight instability after 3 min , though it did not diverge completely. The results obtained by sets a and b were stable and gave good agreement for the change of the accretion radius at 7cm height, but they showed a little discrepancy for the accretion height in the early stages. However, this discrepancy was not very large and both results agreed after 1 min. Hence set (a) was chosen for further calculations, because finer time intervals such as set (b) required enormous computing time. Using set (a), the calculation of the accretion growth was carried out up to 12 min.

The CPU time required was nearly 2000 sec on the CDC Cyber 174 computer at Imperial College. The computer program FDM18 is given in Appendix A.2.

2.7. Results and Discussion. Unsteady-State

The accretion shape and isotherms in the refractory after 2 sec, 12 sec, 60 sec and 720 sec are shown in Figure 2.20. Change of the accretion shape with time is shown in Figure 2.21. In these figures, the accretion shape is represented by the liquidus line. The accretion first grows in the direction of the height and becomes a very slender shape. Then the accretion gradually increases in width. This prediction has been qualitatively confirmed using a cold nitrogen/water model at BSC Corporate Laboratories, Teesside[14]. As mentioned earlier, the height of the accretion in the early stage may be slightly overestimated. As seen in the figures, a solid steel shell is formed on the refractory surface in the early stage, remelting later on. This is due to the effect of the initial condition, where the temperatures in the refractory away from the nozzle were set lower than the steady state values.

In Figure 2.20 high thermal stress regions in the refractory are also shown. The high thermal stress regions are defined arbitrarily as those where the difference of the temperature gradient from the initial condition is more than $60^{o}C/cm$. The actual thermal-induced stress has not been calculated, but the area with a large increase in the temperature gradient can be regarded as a high thermal stress region. The high thermal stress region lies around the gas conduit and in the vicinity

of the steel/refractory interface, and the location with the highest thermal stress is the vicinity of the intersection of the steel/refractory interface and the gas conduit wall. According to Kawasaki Steel, the tuyere wearing on Q-BOP is mainly due to cracking and peeling off caused by the thermal-spalling of the refractory[9]. They prolonged the bottom life of Q-BOP significantly by use of the refractory with high thermal-spalling resistance and by improvement on the furnace operation and the brick layout[17]. The results of the present calculation offers more background to the above facts.

2.8. Conclusion

A mathematical model for heat transfer and accretion formation around a gas injection tuyere has been developed. In this model the temperature gradient in liquid metal exists only in the thermal diffusion zone, and it is assumed that the bulk liquid metal beyond the thermal diffusion zone has a homogeneous temperature. The equations for the steady state have been solved numerically by the successive over relaxation method. The results are summarized as follows,

1) Decrease of superheat or increase of gas flow rate increases the size of the accretion.
2) The value of the thermal conductivity of refractory affects the bottom radius of accretion, but it does not greatly affect the height of accretion.
3) Accretion height has a maximum at a particular value of the effective heat transfer coefficient between accretion and gas. The bottom radius of accretion monotonously

increases with increasing heat transfer coefficient between accretion and gas.

4) The value of the heat transfer coefficient between refractory and gas affects the bottom radius only in the case of high superheat.

For the unsteady-state growth of the accretion the results show that

1) The accretion grows just as a narrow tube increasing in height and rapidly reaches its maximum height.
2) The accretion then increases in radius, slowly reaching its steady-state shape.
3) During the accretion growth the temperature distribution in the refractory changes significantly due to the cooling caused by the gas flow. This must lead to considerable thermal stress in the refractory. The location with the largest change of temperature gradient from the the initial condition is at the intersection of the inner refractory surface and the gas conduit wall.

List of Symbols. Chapter 2

C_p specific heat

h_{gR} heat transfer coefficient between refractory and gas

h_{gs} heat transfer coefficient between steel accretion and gas

h_l heat transfer coefficient between accretion and liquid steel

k thermal conductivity

k_d thermal conductivity of fictitious thermal diffusion zone

k_R thermal conductivity of refractory

k_s thermal conductivity of solid steel

n normal ordinate

Nu Nusselt number of gas

Pr Prandtl number of gas

q_d mean heat flux across thermal diffusion zone

q_s heat flux on the solid surface

r radius, cylindrical co-ordinate

r_c radius of curvature

R_d thickness of fictitious thermal diffusion zone

Re Reynolds number of gas

r_o radius of nozzle bore

T temperature

T_b bulk liquid temperature

T_g gas temperature

T_{go} inlet gas temperature

T_i temperature of mesh point i in finite difference representation

T_i^* temperature of fictitious mesh point i in finite difference representation

T_m melting point

T_s superheat ($T_b - T_m$)

T_w wall temperature of gas conduit

Δt time intervals for finite difference calculation

u gas velocity

X ln r

Z height, cylindrical co-ordinate

ΔZ_R mesh interval in refractory region

ΔZ_s mesh interval in steel region

α thermal diffusivity

Θ modified temperature in liquid region

ρ density of gas

TABLE 2.1

Material Properties. Steady-State Calculations

			in SI unit
Steel	k_s	0.07 cal/sec cm^{o}C	29 W/mK
	T_m	1540^{o}C	
Refractory	k_R	0.003 cal/sec cm^{o}C	1.3 W/mK
Argon gas at 727^{o}C	ρ	4.87 x 10^{-4} g/cm^3	
	C_p	0.124 cal/g ^{o}C	0.519 J/gK
Thermal conductivity of argon		1.02 x 10^{-4} cal/sec cm^{o}C	0.0427 W/mK
Viscosity of argon		5.42 x 10^{-4} g/cm sec	

Material Properties. Unsteady-State Calculations

Steel			in SI unit
up to 1530^{o}C	ρ	7.8 g/cm^3	
(solid)	C_p	0.15 cal/g^{o}C	0.63 J/gK
	k_s	0.07 cal/s cm^{o}C	29 W/mK
	α	0.06 cm^2/s	
1530~1540^{o}C	ρ	7.4 g/cm^3	
(mushy zone)	C_p	6.5 cal/g^{o}C	27.2 J/gK
	k_s	0.07 cal/s cm^{o}C	29 W/mK
	α	0.0015 cm^2/s	
above 1540^{o}C	ρ	7 g/cm^3	
(liquid)	C_p	0.15 cal/g^{o}C	0.63 J/gK
diffusion	(k_d	0.7 cal/s cm^{o}C	293 W/mK)*
zone.	(α	0.7 cm^2/s)	
Refractory			
	ρ	2.0 g/cm^3	
	C_p	0.25 cal/g^{o}C	1.05 J/gK
	k_R	0.003 cal/s cm^{o}C	1.2 W/mK
	α	0.006 cm^2/s	
Argon Gas			
	ρ	4.87 x 10^{-4} g/cm^3	
	C_p	0.124 cal/g^{o}C	0.519 J/gK
	k	1.02 x 10^{-4} cal/s cm^{o}C	0.0427 W/mK
vicosity		5.42 x 10^{-4} g/s cm	

* k_d is not a genuine material property, because it is fixed by heat transfer condition in the thermal diffusion zone.

TABLE 2.2

Gas Injection Conditions

Radius of nozzle bore (r_o)	0.6 cm
Refractory thickness	24 cm
Outside temperature of refractory	200°C
Superheat of liquid steel (T_s)	10°C
Gas flow rate	12200 cm^3/s at 727°C (200 N l/min)
h_{gR}	0.003 cal/s $cm^{2o}C$ (126 W/m^2K)
h_{gs}	0.010 cal/s $cm^{2o}C$ (418 W/m^2K)
R_d	3.5 cm
k_d	0.7 cal/s cm^oC (293 W/mK)
$h_l (=k_d/R_d)$	0.2 cal/s $cm^{2o}C$

TABLE 2.3

Time Intervals for Finite Difference Calculations

	Time Steps	Time (sec)	Time intervals (Δt) (sec)
(a) Standard	1~50	0~0.5	0.01
	51~120	0.5~4.0	0.05
	121~	4.0~	0.1
(b) fine Δt	1~100	0~0.5	0.005
	101~240	0.5~4.0	0.025
	241~	4.0~	0.05
(c) coarse Δt	1~50	0~1.0	0.02
	51~120	1.0~8.0	0.1
	121~	8.0~	0.2

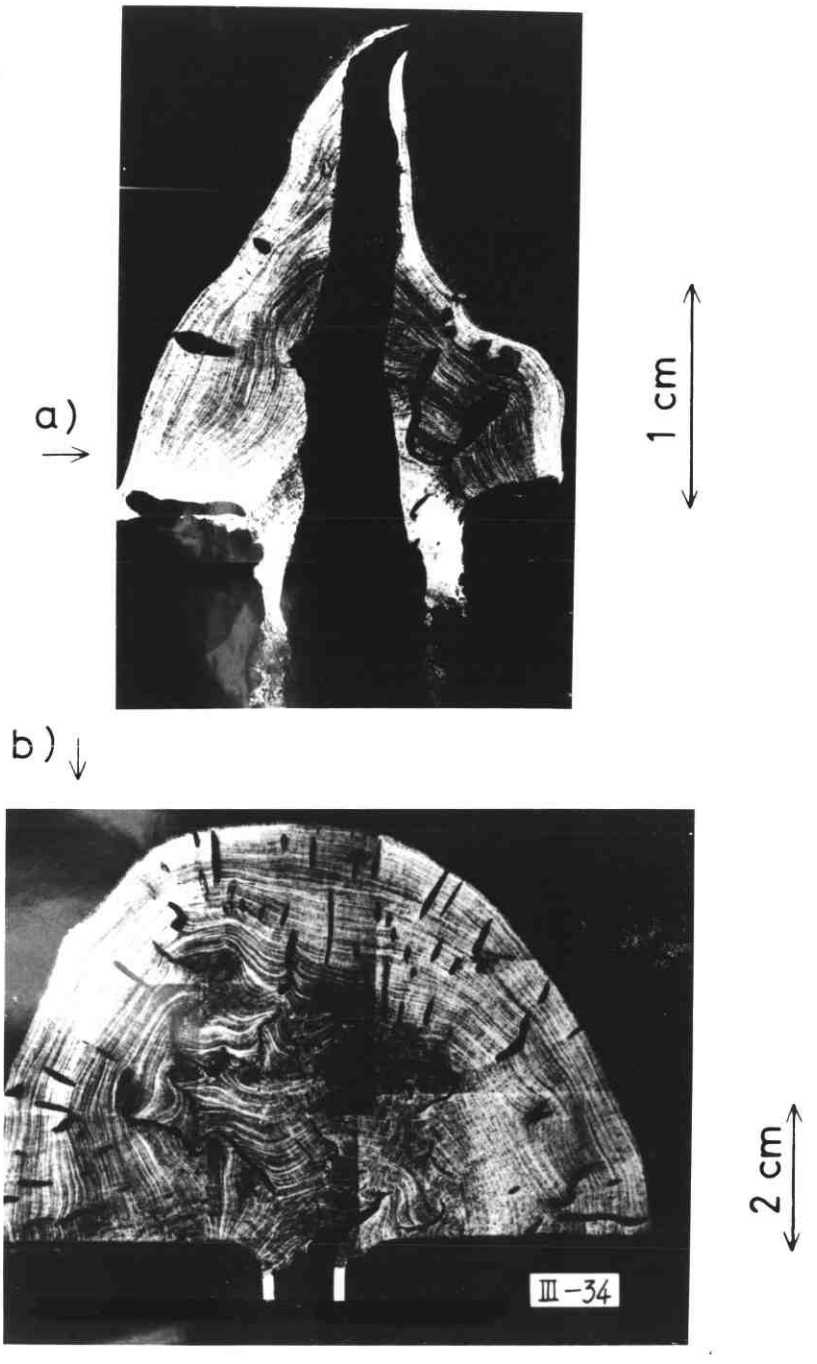

Plate 1. Sections of steel accretions.

a) Pipe-like accretion

b) Fully capped mushroom-like accretion

(Porous accretion)

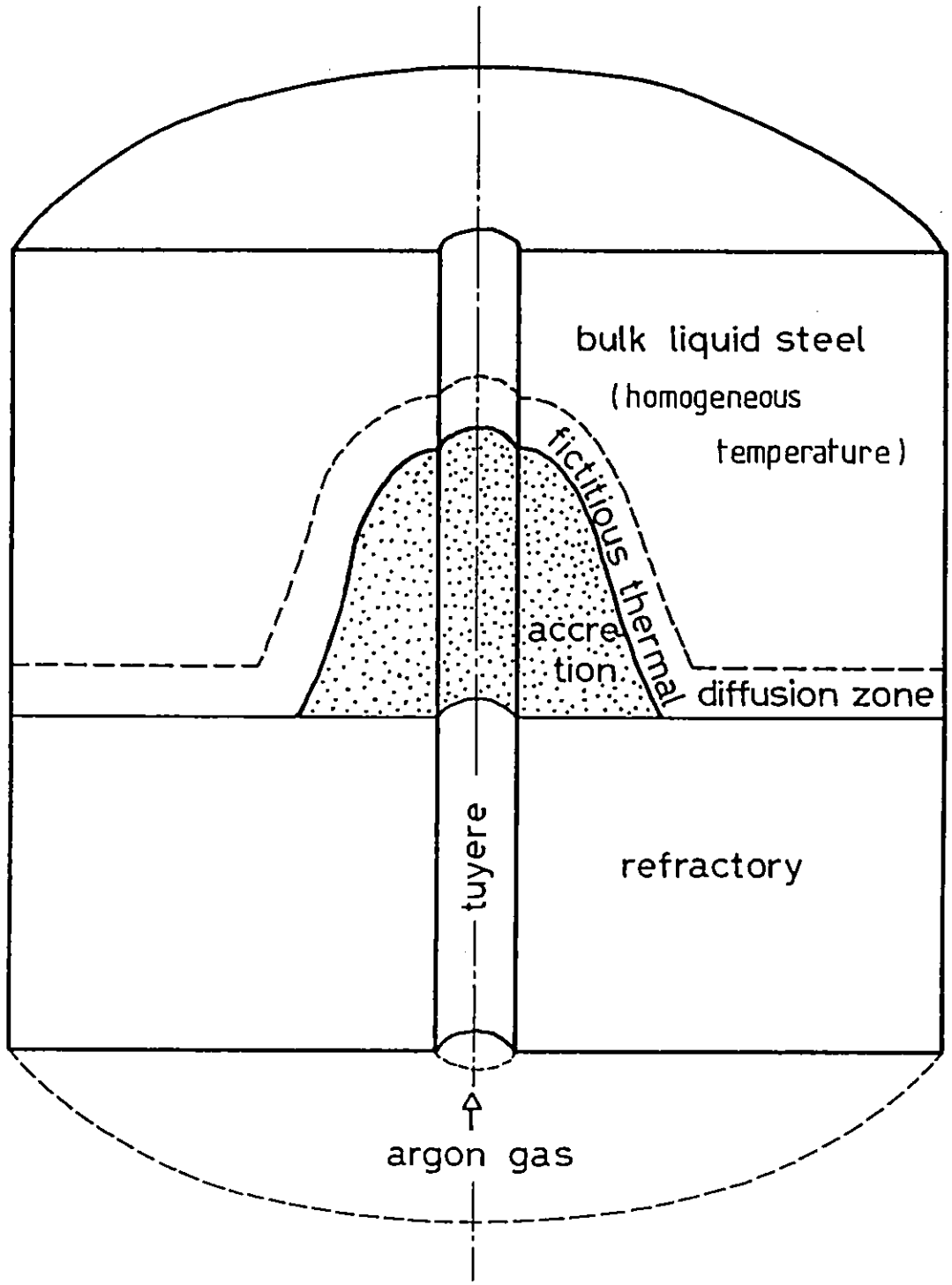

Fig.2.1. Cylindrical region for the modelling of heat transfer around a tuyere.

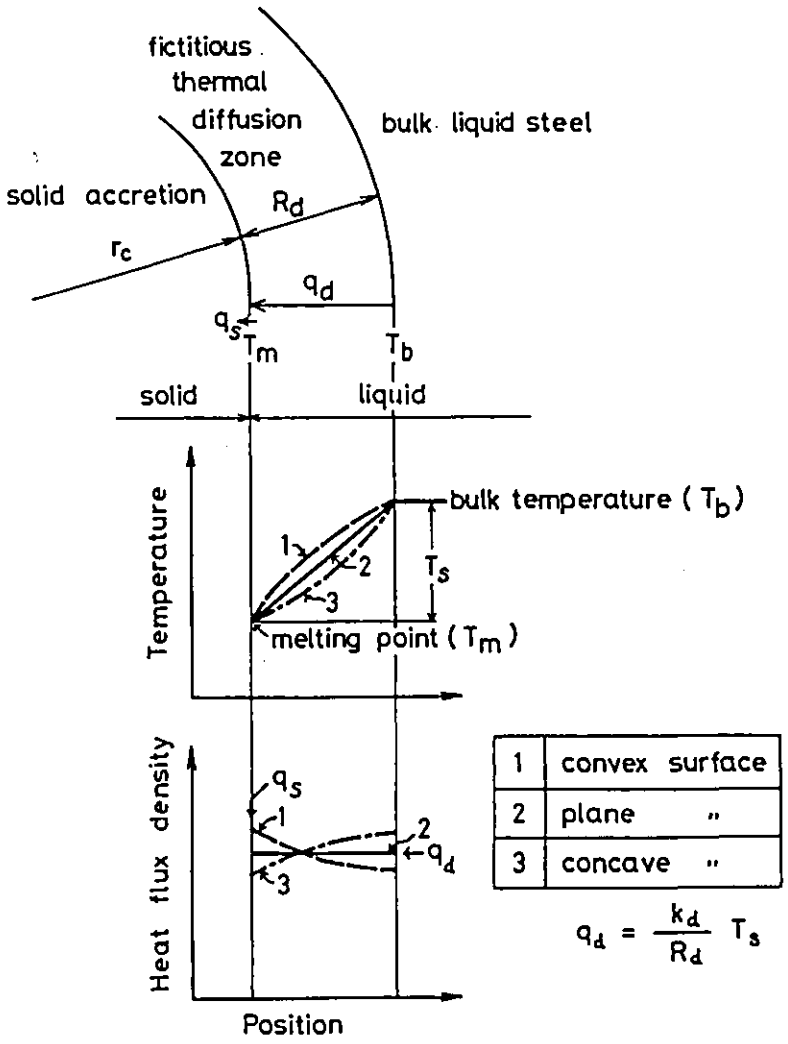

Fig.2.2. Temperature distribution and heat flux density across the fictitious thermal diffusion zone.

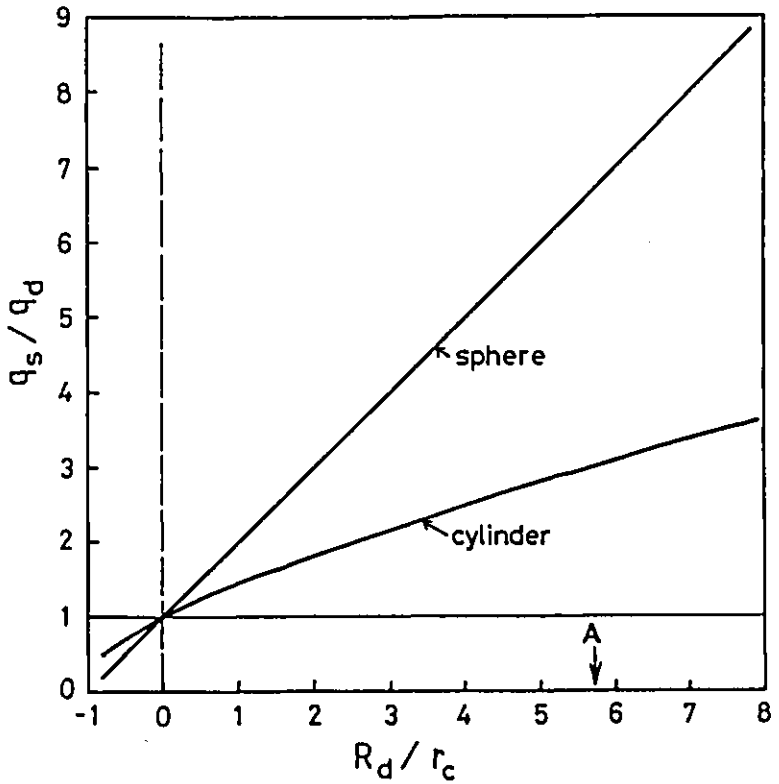

Fig.2.3. Effect of R_d/r_c on the magnitude of heat flux density concentration (q_s/q_d). Arrow A indicates the highest value in this work with $R_d \approx 3.5$cm and r equal to nozzle radius of 0.6cm. In this work shape was effectively cylindrical.

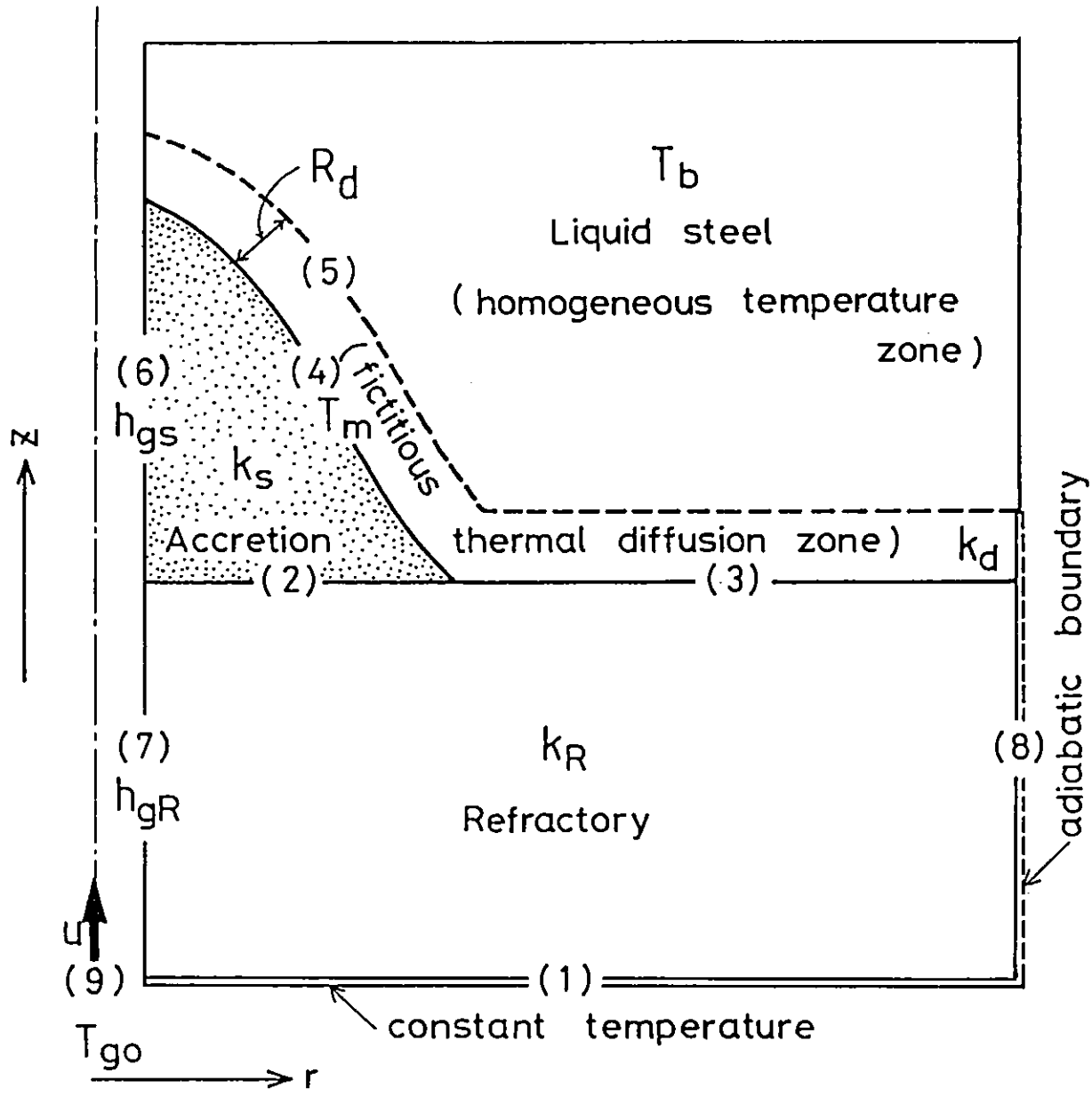

Fig .2.4. Boundary conditions for the calculation of accretion formation.

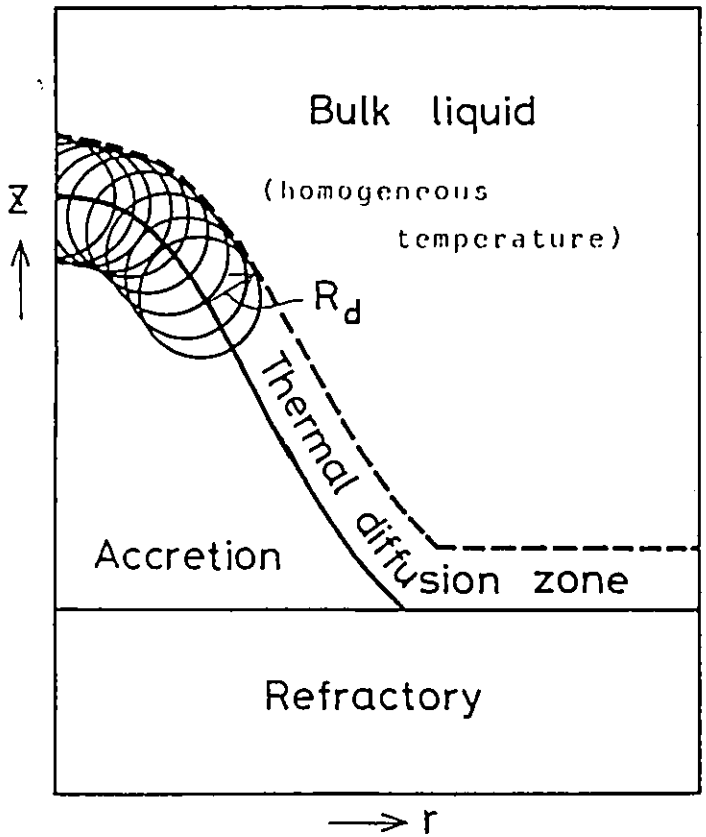

Fig .2.5. Setting of thermal diffusion zone.

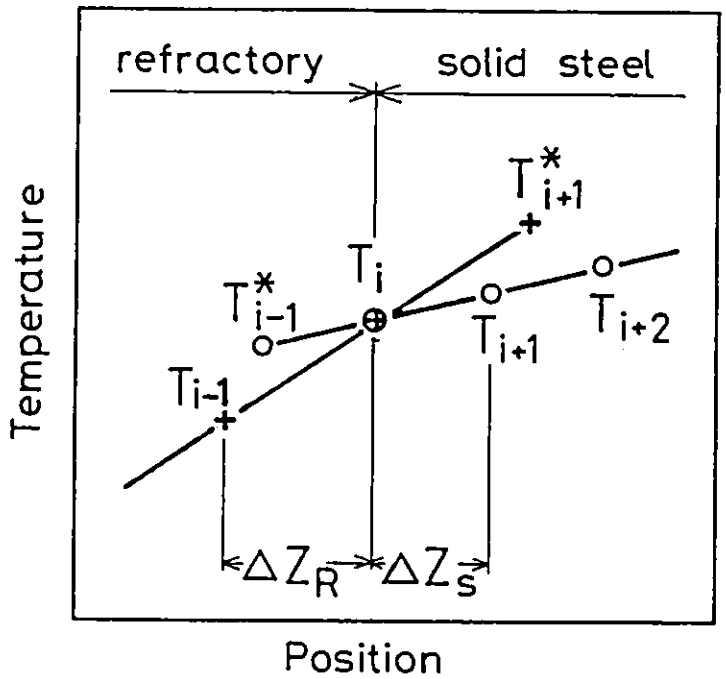

Fig.2.6. Boundary condition of solid state/ refractory interface.

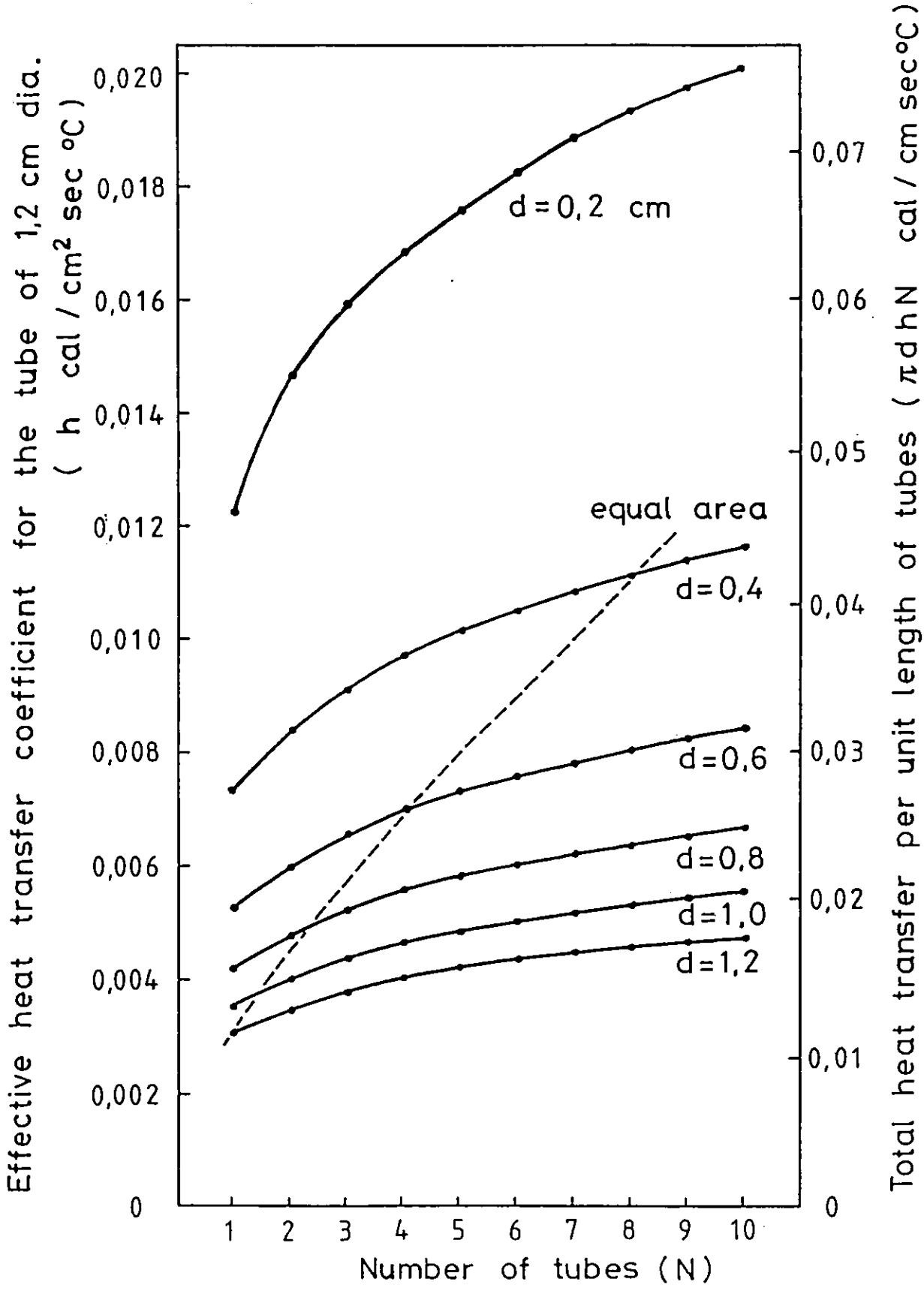

Fig.2.7. Variation of the effective heat transfer coefficient with number of tubes and their diameter. Gas flow rate is 12210 cm^3/sec at 727°C.

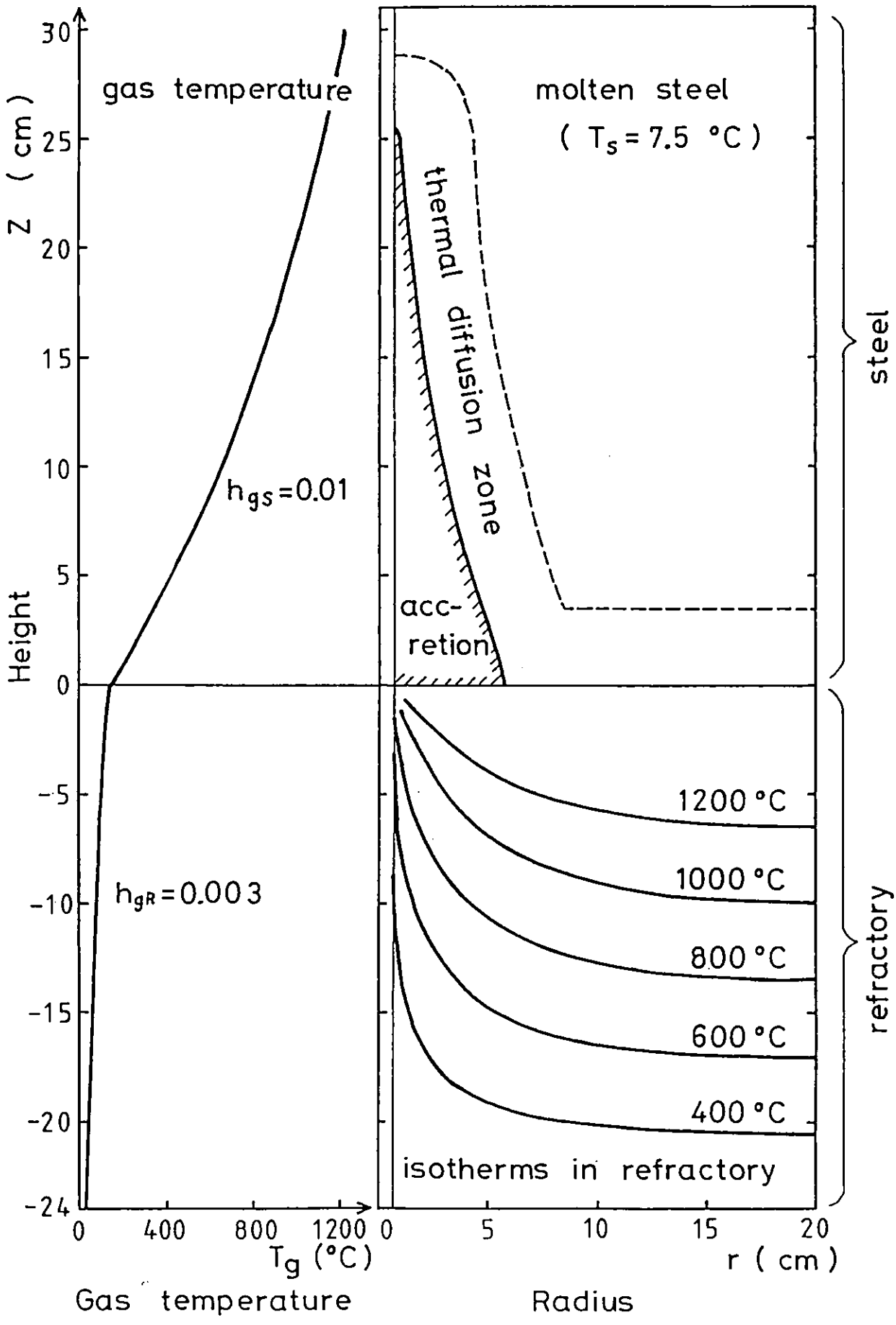

Fig.2.8. An example of calculated results of accretion formation for 7.5°C superheat.

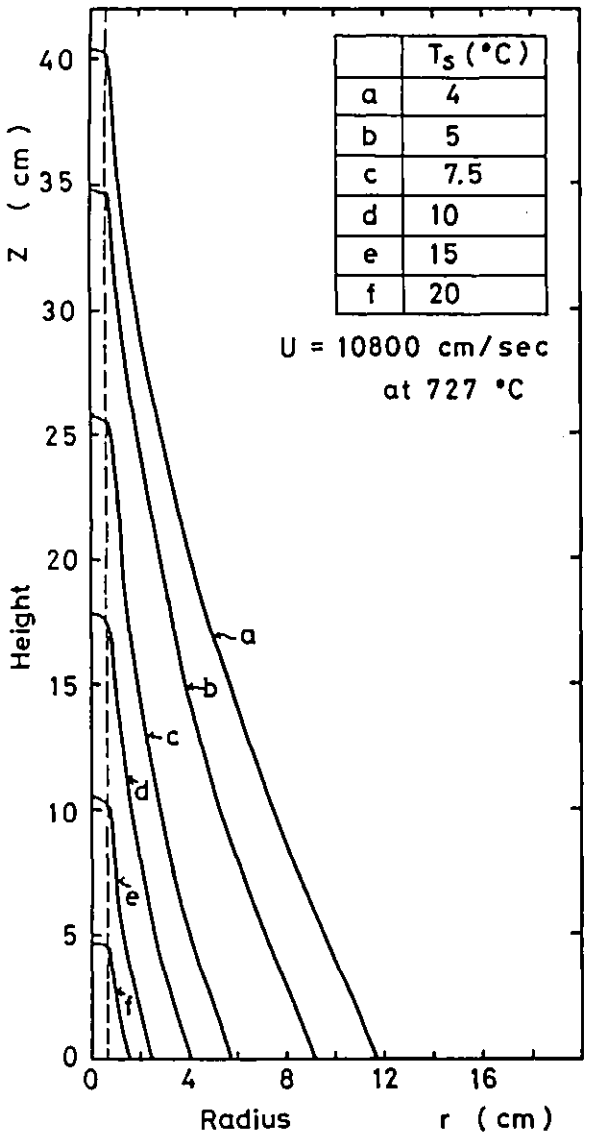

Fig.2.9. Effect of superheat on the shape of accretion.

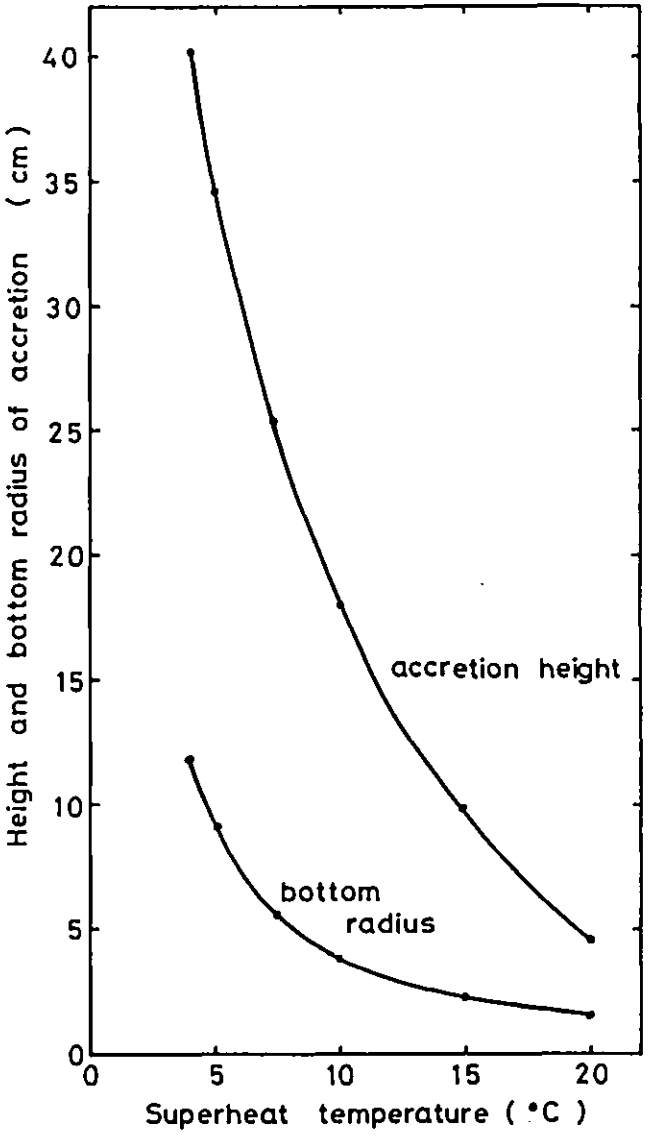

Fig.2.10. Effect of superheat on the height and the bottom radius of accretion.

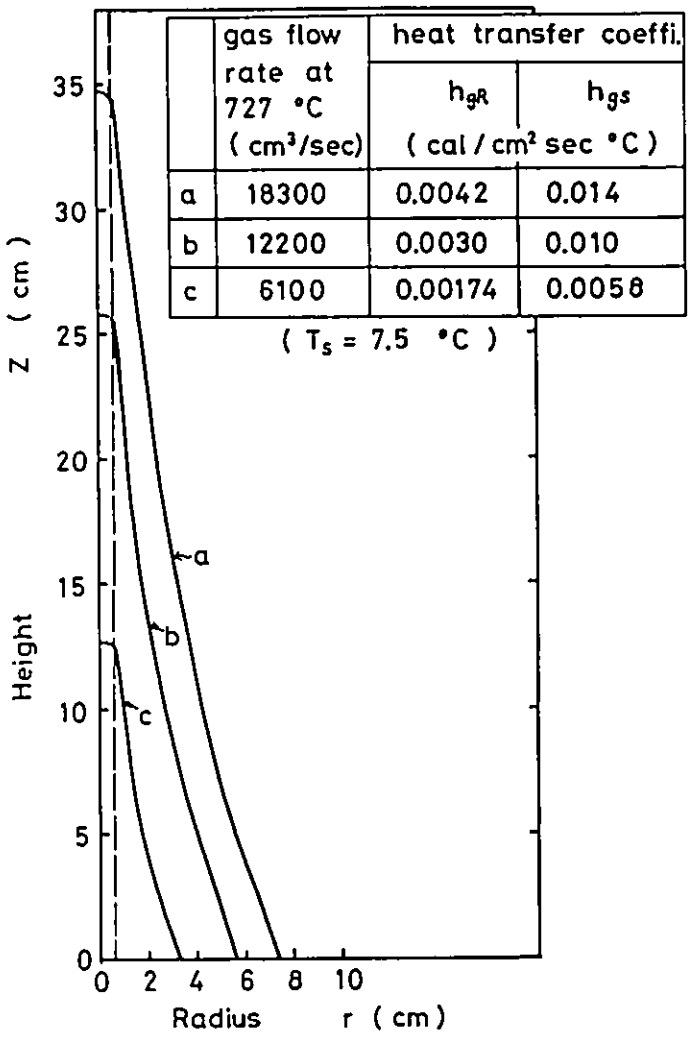

	gas flow rate at 727 °C (cm^3/sec)	heat transfer coeffi. h_{gR} (cal / cm^2 sec °C)	heat transfer coeffi. h_{gs} (cal / cm^2 sec °C)
a	18300	0.0042	0.014
b	12200	0.0030	0.010
c	6100	0.00174	0.0058

(T_s = 7.5 °C)

Fig.2.11. Variation of the accretion shape with gas flow rate.

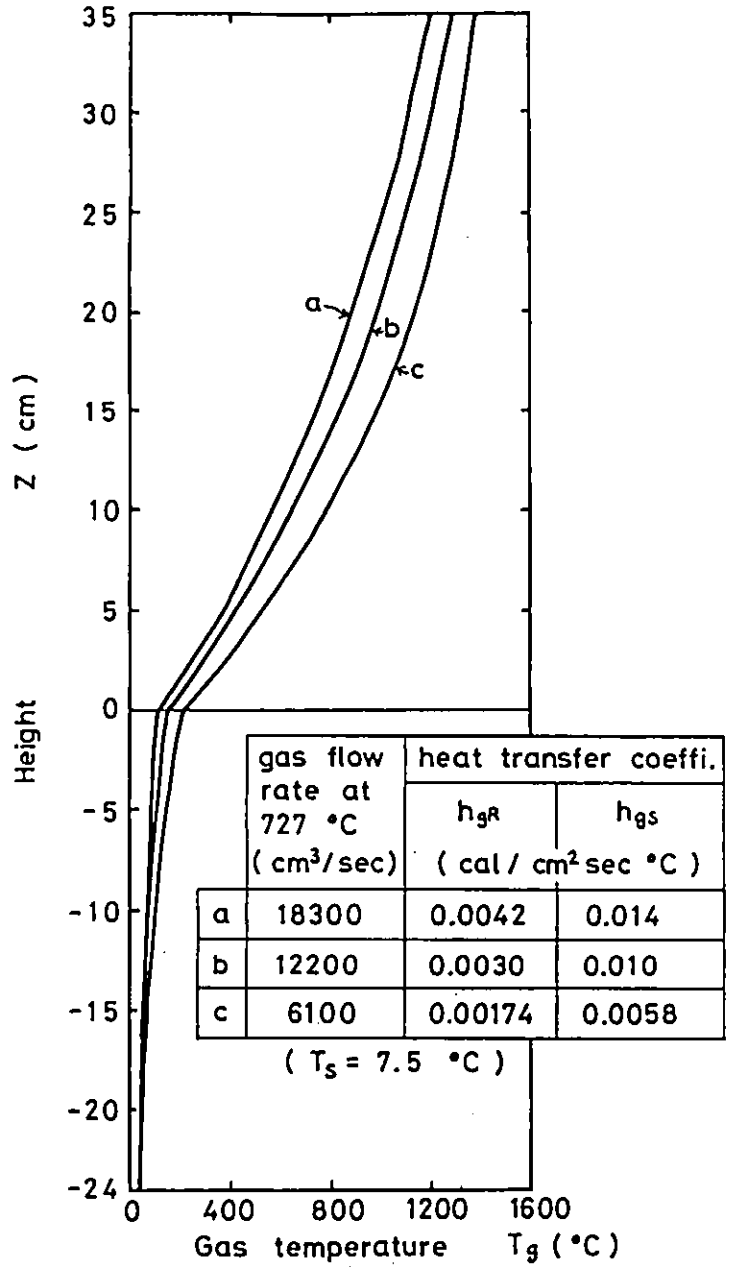

	gas flow rate at 727 °C (cm^3/sec)	heat transfer coeffi. h_{gR} (cal / cm^2 sec °C)	heat transfer coeffi. h_{gs} (cal / cm^2 sec °C)
a	18300	0.0042	0.014
b	12200	0.0030	0.010
c	6100	0.00174	0.0058

(T_s = 7.5 °C)

Fig.2.12. Variation of the gas temperature with gas flow rate.

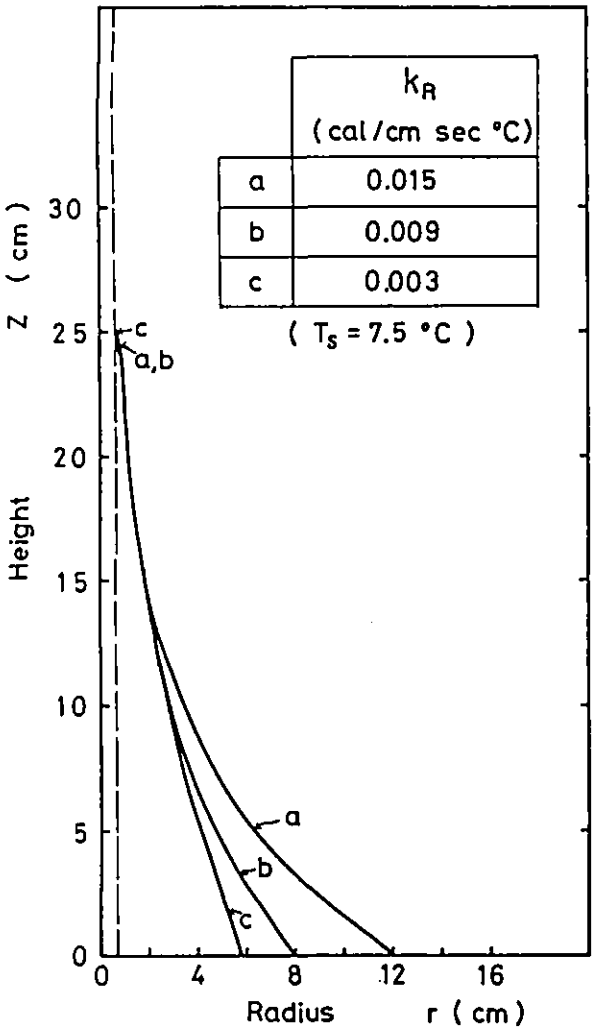

Fig.2.13. Variation of the accretion shape with thermal conductivity of the refractory.

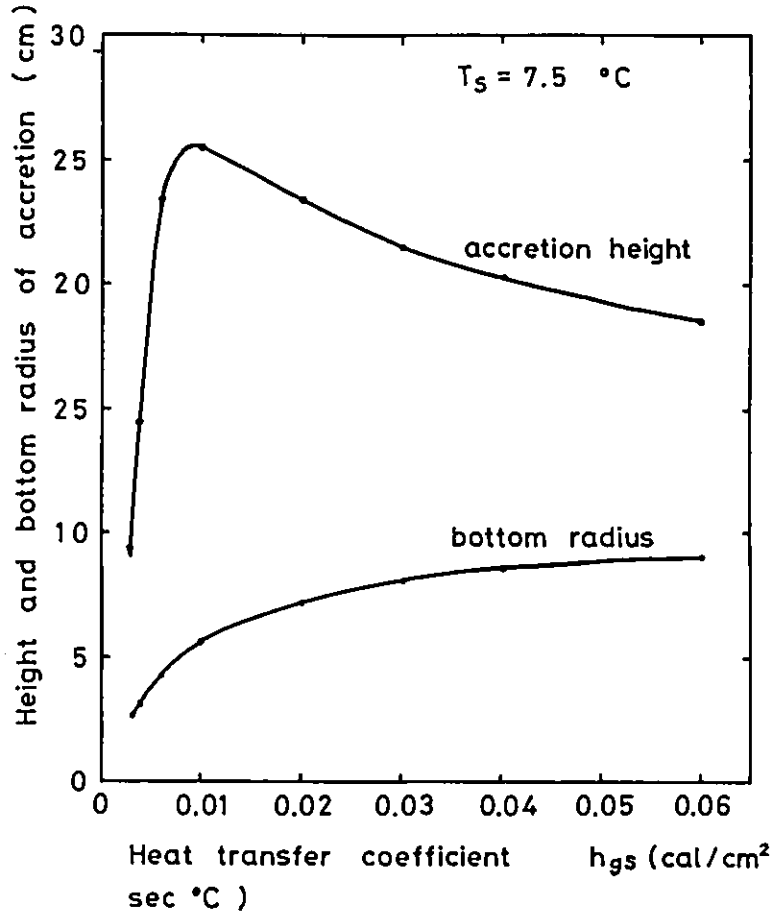

Fig.2.14. Effect of heat transfer coefficient between accretion and gas on the height and the bottom radius of accretion.

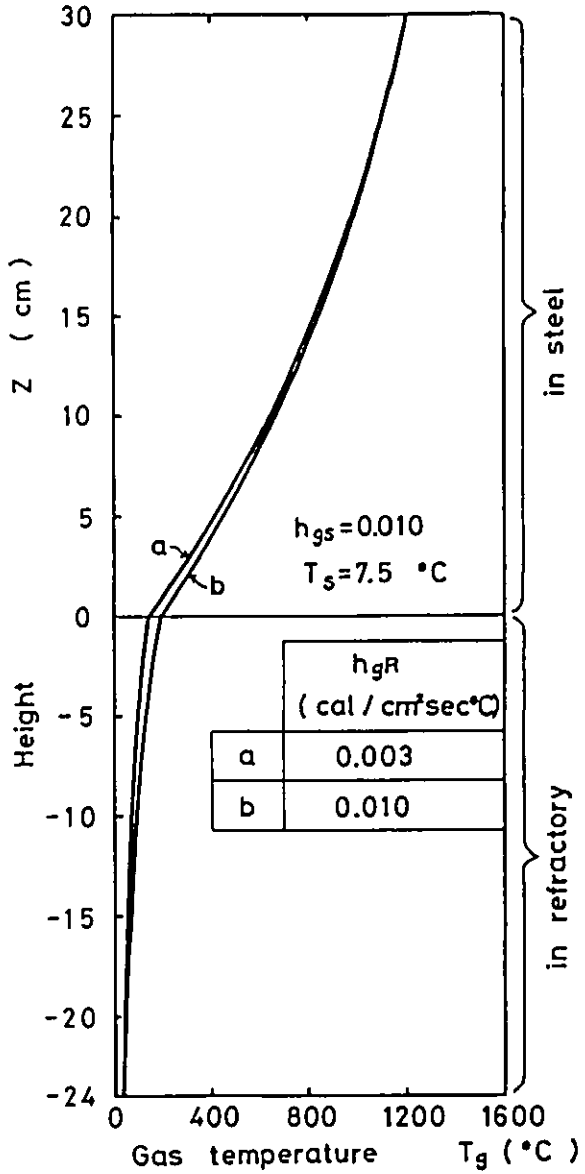

Fig.2.15. Variation of the gas temperature with different heat transfer coefficients between refractory and gas (superheat = 7.5°C).

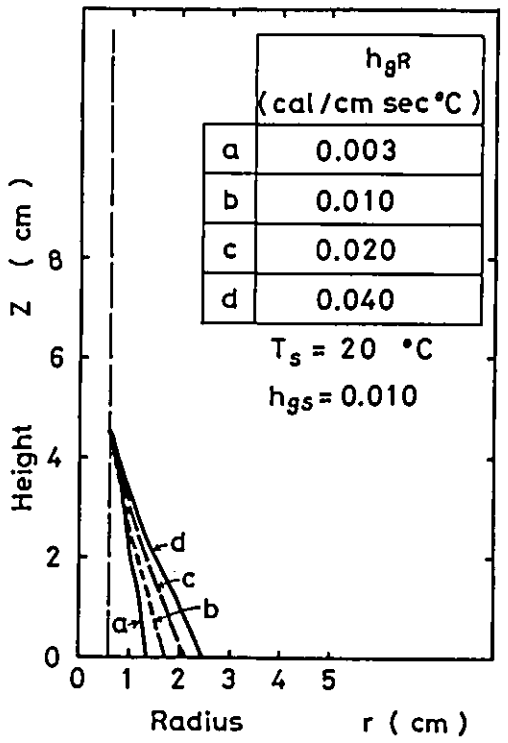

Fig.2.16. Variation of the accretion shape with heat transfer coefficient between refractory and gas (superheat = 20°C).

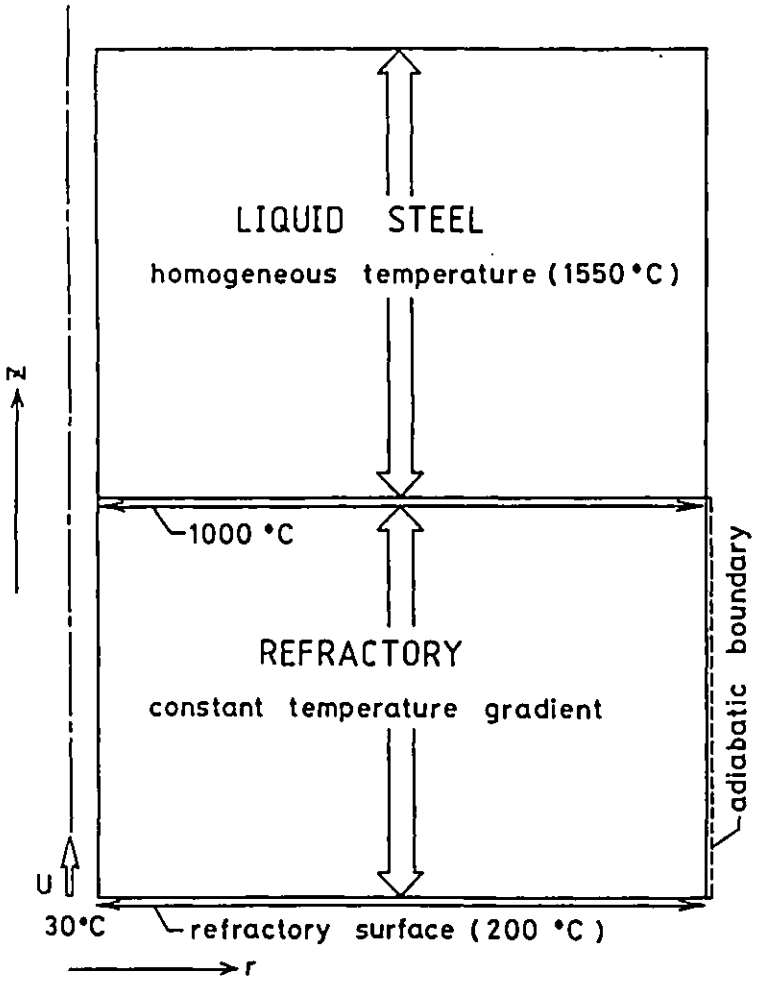

Fig.2.17. Initial condition for unsteady state calculation.

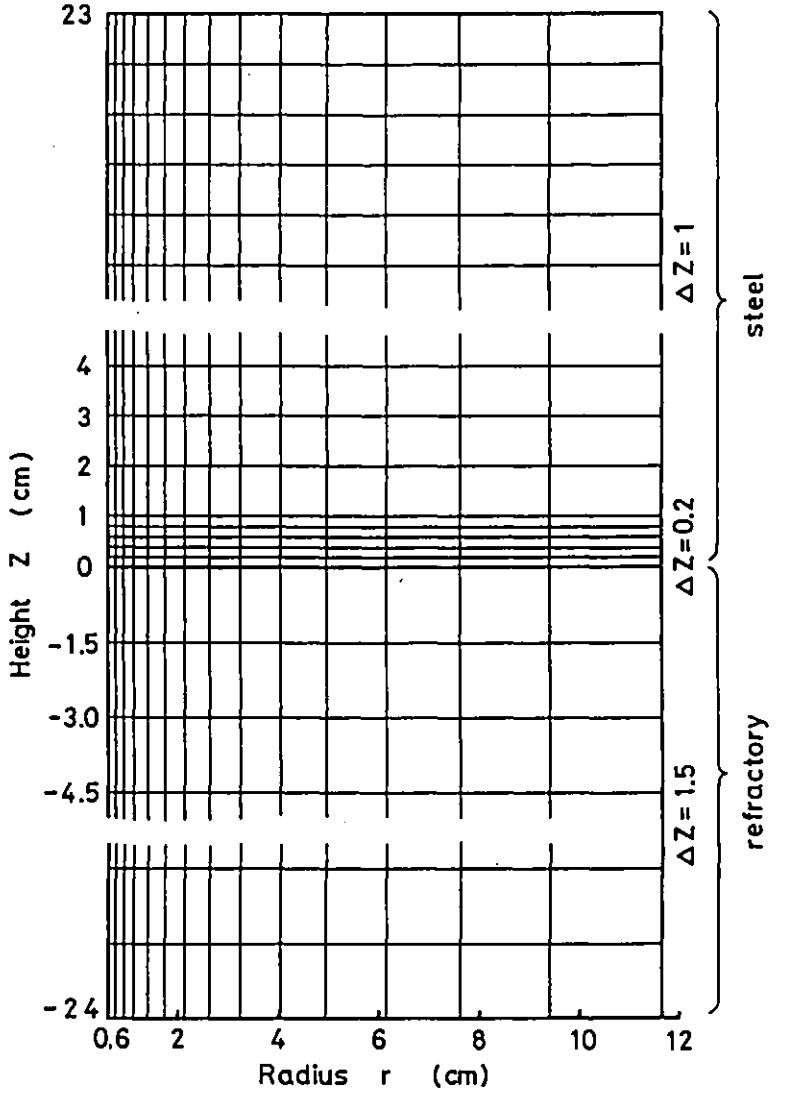

Fig.2.18. Finite difference approximation mesh for unsteady state calculation.

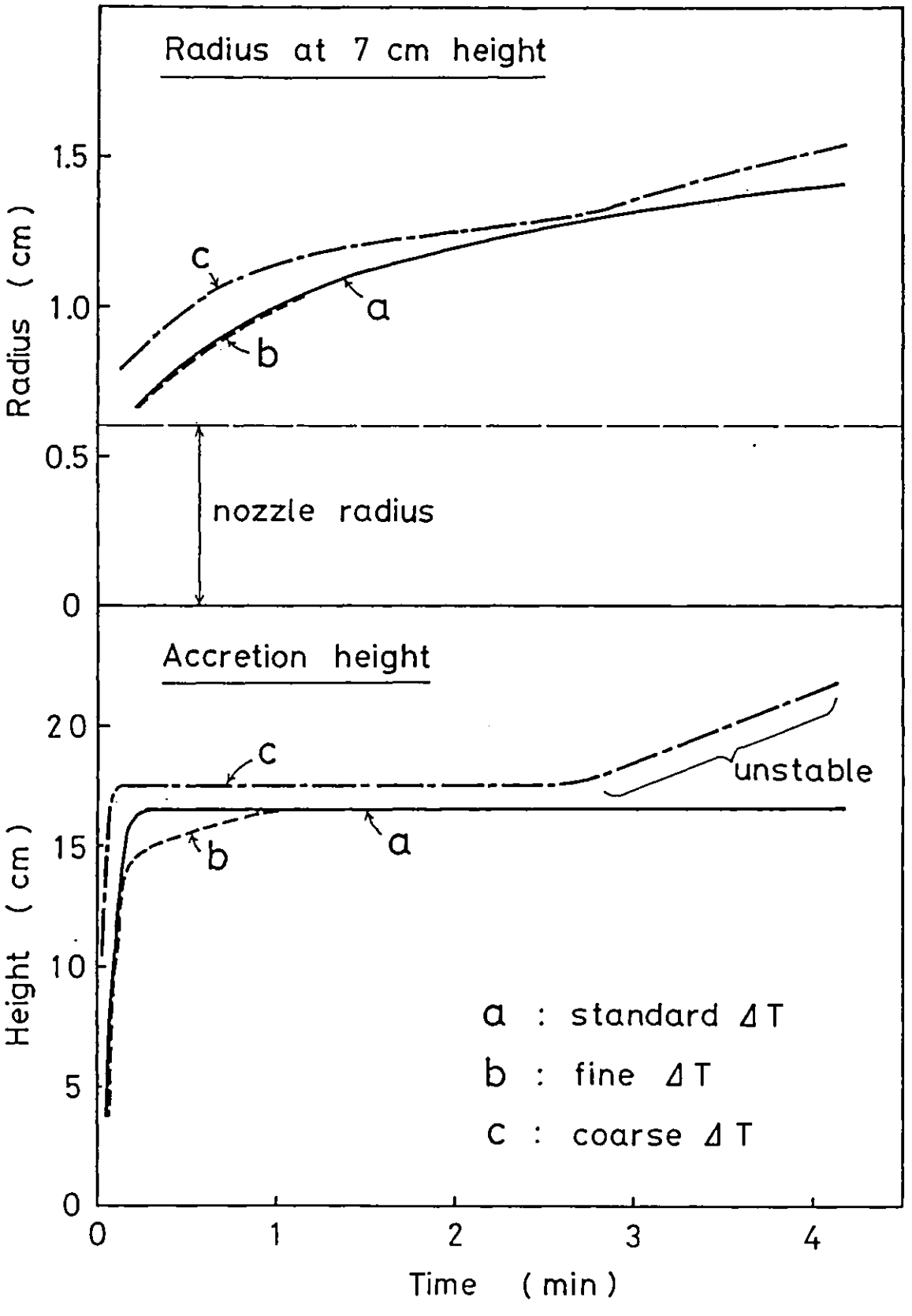

Fig.2.19. Comparison of sets of time intervals on the accretion height and the radius at 7cm height. Sets of time intervals are presented in Table 3.

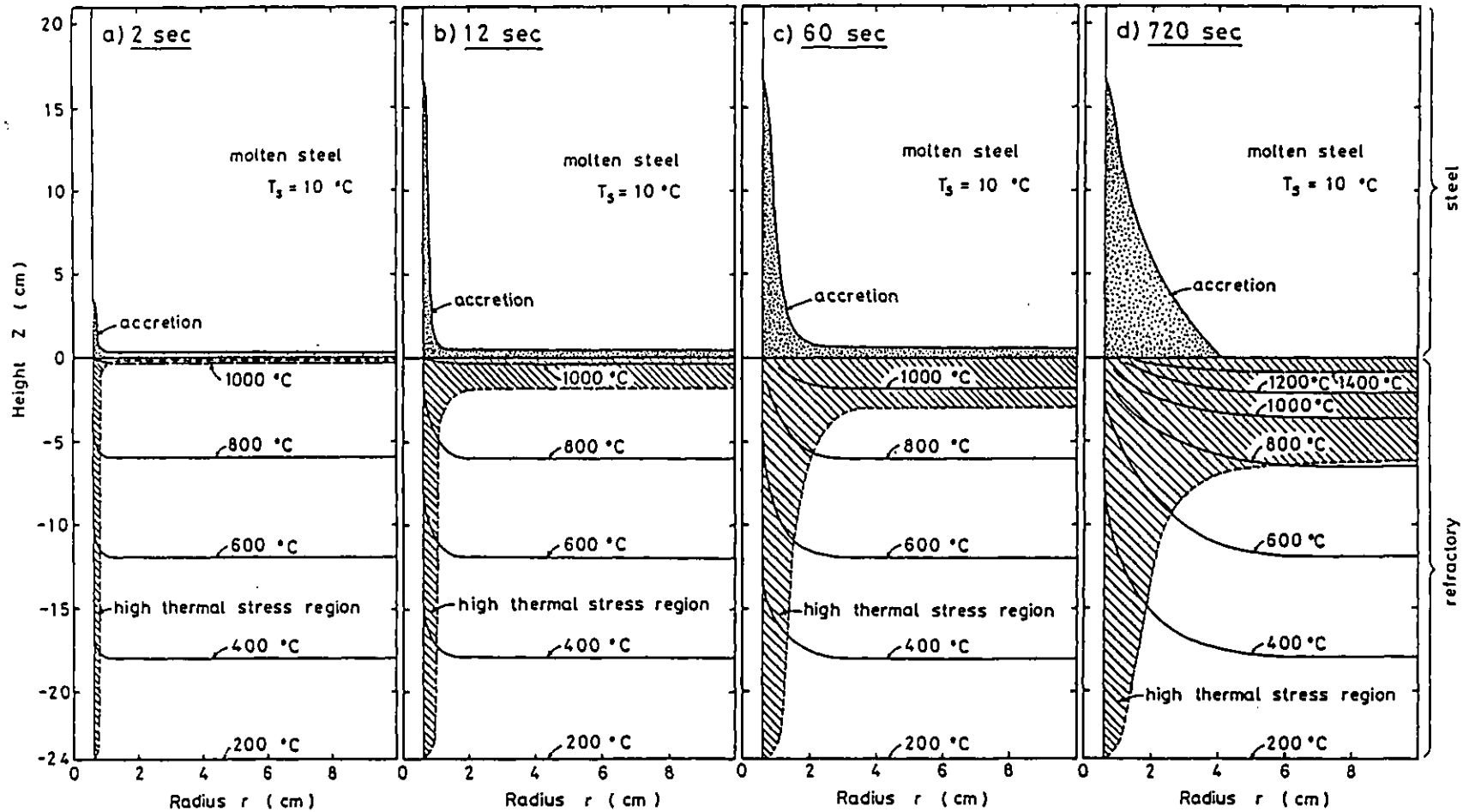

Fig .2.20. Accretion shape and isotherms in refractory with high thermal stress region for 2 sec, 12 sec, 60 sec and 720 sec.

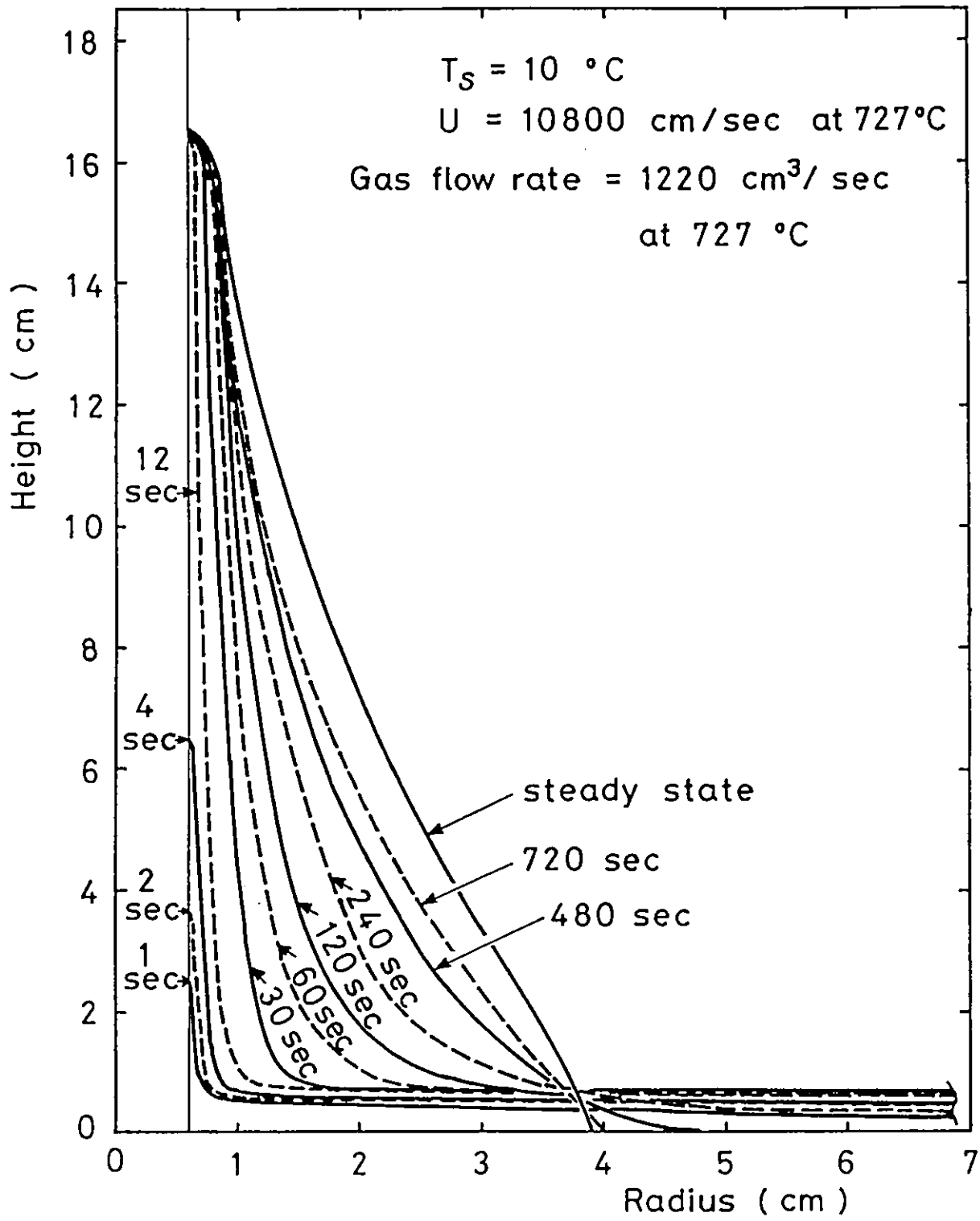

Fig.2.21. Change of accretion shape with time.

Chapter 3: FORMATION OF POROUS ACCRETIONS AROUND A TUYERE DURING GAS INJECTION

Abstract

A porous accretion model for heat transfer and accretion formation around a gas injection tuyere has been developed in order to calculate shapes of fully-capped mushroom-like accretions. In this model the cooling gas flow in the accretion is assumed to follow potential flow. Argon gas injection into molten steel through a refractory tuyere was chosen as a basis for the calculation. A mathematical formulation for the steady state has been solved by the finite difference method , using a relaxation technique. The effects of superheat, gas flow rate, volumetric heat transfer coefficient , thermal conductivity of the accretion and a field with a pressure gradient are discussed. The porous accretion model has also been extended to cases where the structure is intermediate between the two extremes of the porous and pipe-like accretions.

Chapter 3: FORMATION OF POROUS ACCRETIONS AROUND A TUYERE DURING GAS INJECTION

3.1. Introduction

In the previous chapter, it was mentioned that accretions fall broadly between two extreme categories: (a) pipe-like accretions and (b) porous and fully-capped mushroom-like accretions, and a mathematical model was developed for the pipe-like accretions. However, some of the actual accretions in Q-BOP[8] show hemispherical shapes with an enormous number of capillaries. The pipe-like model could not be applied for such accretions.

In this chapter a porous accretion model has been developed to cope with these accretions. Argon gas injection into molten steel through a refractory tuyere was chosen as a basis for the calculation. A mathematical model for the heat transfer and gas flow was solved for steady-state using a relaxation technique.

This chapter is based on a paper[18] to be published in Ironmaking and Steelmaking (accepted for publication by the Metals Society, November 1982).

3.2. Modelling and Formulation

A section of the cylindrical region incorporating the gas injection tuyere is shown in the top of Figure 3.1. Assuming that the accretion is porous, the gas flow in the accretion was approximated by potential flow. The gas flowing in the tuyere and in the accretion respectively removes heat from the refrac-

tory wall and directly from the accretion. The fictitious thermal diffusion zone described in Chapter 2 has been utilised to account for heat transfer from the liquid steel to the solid. Beyond this thermal diffusion zone the bulk liquid steel is assumed to be of a homogeneous temperature owing to the strong bath agitation. Thus, the temperature gradient in the liquid steel exists only in the fictitious thermal diffusion zone. The mean heat flux density ($\dot{q}_d$) across the thermal diffusion zone is expressed by

$$\dot{q}_d = k_d.T_s/R_d = h_1 T_s \qquad (3.1)$$

where T_s is the superheat of the liquid metal, and k_d and R_d are respectively the thermal conductivity and thickness of the diffusion zone.

Material properties and the other coefficients are usually assumed to be constant regardless of the temperature or the local gas flow rate. The flow potential on the surface of the accretion is usually kept constant. Some calculations were carried out with the volumetric heat transfer coefficient varied according to the local gas flow rate. Some other calculations have been made for the accretion in a pressure gradient to estimate the effect of the liquid metal head.

1) Governing equation for heat transfer.

As this problem is axi-symmetric, two dimensional cylindrical co-ordinates were used. The governing heat transfer equation is

$$\frac{\partial^2 T}{\partial Z^2} + \frac{1}{r}\frac{\partial T}{\partial r} + \frac{\partial^2 T}{\partial r^2} + \frac{\dot{q}}{k} = 0 \qquad (3.2)$$

where $\dot{q}$ is a heat generation per unit volume. $\dot{q}$ expresses the effect of gas cooling and acts as a heat sink term in the accretion, being null in the refractory or in the liquid steel. That is;

$$\dot{q} = h_v (T_g - T) \quad \text{in accretion}$$

$$\dot{q} = 0 \quad \text{in refractory or in liquid steel}$$

where h_v is the volumetric heat transfer coefficient and T_g is the gas temperature.

2) Gas temperature in the tuyere

The heat balance for the gas rising through the tuyere in the refractory region is

$$C_p (T_g - T_{go}) = \int_{Z_o}^{Z} (2h_{gR} (T_w - T_g)/\rho . r_o . u) dZ \qquad (3.3)$$

3) Gas temperature in the accretion.

Gas temperature in the accretion was computed by summation of the heat transferred from solid to gas phase along the gas flow. The actual calculation is an integration of the heat sink term $\dot{q}$ on the finite difference mesh. The heat removed from the solid increases the gas temperature. The heat balance gives

$$-\Delta V \dot{q} = h_v \Delta V (T - T_g)$$
$$= C_p F (T_{out} - T_{in}) \qquad (3.4)$$

where ΔV is the volume of the finite difference cell, and T_{out} and T_{in} are respectively the outlet and the inlet gas tempe-

rature for the cell. F is the total mass flow rate of the gas through the cell. For a typical cell, the gas flows in from the south-side and west-side cells, schematically being shown in Figure 3.2.

Defining the gas temperature as

$$T_g = (T_{out} + T_{in})/2 \qquad (3.5)$$

and, making use of Equation 3.4, one can obtain

$$T_{out} = \left(T_{in} + \frac{h_v \Delta V (2T - T_{in})}{2C_p F}\right) / \left(1 + \frac{h_v \Delta V}{2C_p F}\right) \qquad (3.6)$$

where

$$F = f_s S_s + f_w S_w$$

$$T_{in} = (f_s S_s T_{gs\text{-}out} + f_w S_w T_{gw\text{-}out})/F$$

For the nomenclature, please see the list of symbols.
The above expressions of F and T_{in} are for a typical cell, and generally attention must be paid to the gas flow directions through the cell. For instance, the gas flow is only from the south-side cell in the case of the cell on the axis of symmetry. In the calculation of the shape of an accretion in a surrounding flow potential gradient the actual gas flow directions must be determined by comparison with the flow potential in the neighbouring cells, because the flow directions cannot be known beforehand.

4) Boundary conditions for heat transfer.

The boundary conditions Figure 3.1 used for the heat transfer calculations are similar to those in Chapter 2. The exception is axis of symmetry in the accretion (boundary (6) in Figure 3.1)

which is

$$\partial T/\partial r = 0$$

5) Governing equation for gas flow in accretion

It is assumed that the mass flow of the gas obeys a potential flow, except in the porous and pipe-like combined model which is to be discussed later on. The governing equation for gas flow in the accretion is

$$\frac{\partial^2 P}{\partial Z^2} + \frac{1}{r}\frac{\partial P}{\partial r} + \frac{\partial^2 P}{\partial r^2} = 0 \qquad (3.7)$$

where P is the flow potential. The mass flow rate of the gas per unit area is given by

$$f_Z = \lambda . \partial P/\partial Z$$
$$r_r = \lambda . \partial P/\partial r$$

where λ is the coefficient which relates the flow potential to the mass flow rate, being similar to the thermal conductivity in heat transfer. In this work λ was taken as unity. The value of flow potential P varies according to λ, but the flow rate of the gas is not affected by the selection of the λ value, because in this calculation the total flow of injection gas is set as one of the boundary conditions for gas flow.

The actual pressures which correspond to values of the flow potential depend on the resistance which the porous accretion offers to flow. This factor can be experimentally estimated from measurement of the pressure drop in accretions taken from a converter.

6) Boundary conditions for gas flow

(a) Accretion/refractory boundary

No gas gets through this boundary.

$$\partial p/\partial Z = 0$$

(b) Accretion surface

On the accretion surface, the flow potential is kept at zero in most calculations, corresponding to the case where the static pressure difference of the liquid metal between the top and bottom of an accretion is negligible when compared with the pressure loss in the accretion.

The effect of a static pressure gradient in the surrounding liquid metal in the vertical direction can be expressed by setting the flow potential on the accretion surface as

$$\partial P/\partial Z = \text{constant}$$

(c) Axis of symmetry

$$\partial P/\partial r = 0$$

(d) Gas flow in the tuyere

A total mass flow rate of the gas is set in the tuyere, and flows into the accretion from the end of the tuyere.

3.3. Calculations and Data

Using the finite-difference method, the equations have been solved by the Gauss-Seidel point relaxation techniques[15c]. This method was chosen because of its simplicity and stability and because of its convenience in the calculation of the fictitious thermal diffusion zone, the location of which is not known

in advance, is a kind of moving boundary problem. The temperature outside the thermal diffusion zone is forced to be homogeneous. For the two reasons given above a point-by-point relaxation method is particularly suitable for this problem. The derivation of the finite difference equations is given in Appendix A.1.

A computing flow chart for the porous accretion calculation is shown in Figure 3.3. The total number of mesh points employed was between 448 and 1012, and the typical mesh size in the steel region was 1cm by 1cm. The calculation time required was 80-300 sec on the CDC Cyber 174 computer at Imperial College. Typical computer programs are given in Appendix A.2.

Material properties and typical injection conditions used for the computation are presented in Table 3.1. The material properties for argon gas are those at 727^{o}C. The relevant data are essentially the same as those of Chapter 2, and generally the values in Table 3.1 were used, unless specifically mentioned. For the volumetric heat transfer coefficient, 418 kW/m^{3}K (0.1 cal/s cm^{3} ^{o}C) was adopted. This value was estimated from heat transfer coefficients for packed beds[19], or from the structure of an actual accretion with many small holes[8]. The heat transfer coefficient from the bulk liquid metal to the accretion was estimated from general correlations for forced convective heat transfer in liquid metals (low Pr) and from experimental data on the melting of solid steel rods in molten cast iron[20]. For the thermal conductivity of the porous accretion, that of solid steel was applied.

It is generally difficult to estimate accurate values for the volumetric heat transfer coefficient and the effective thermal

conductivity of accretions, but the values chosen for these parameters scarcely affect the dimensions of the accretion. This aspect will be discussed later on.

3.4. Results and Discussion

As an example, calculated results for the porous accretion model are shown in Figures 3.4 and 3.5, which indicate the accretion shape, isotherms of solid and gas and flow potential contours. The calculated accretion shape is almost hemispherical. This is consistent with the hemispherical steel accretion obtained by argon gas injection (Plate 1(b) in Chapter 2) , and also with the actual Q-BOP accretion whose centre is located at the end of the cooling tuyere[8]. The isotherms of the solid and the gas in the accretion and iso-flow-potential contours are almost concentric hemispheres, indicating the radial flow of the heat and gas in the accretion.

1) Effect of superheat and gas flow rate.

Figure 3.6 shows the effect of the superheat on the size of the accretion. The accretion shape does not change much with different superheats, but the size is considerably altered by superheat, becoming very large at low superheat. Figure 3.7 shows the variation of the accretion size with gas flow rate. As a matter of course, the accretion size becomes larger with a high gas flow rate.

2) Effect of volumetric heat transfer coefficient.

Several calculations have been carried out with different volumetric heat transfer coefficients h_v so as to clarify its effect. The accretion shape and size scarcely change, at most within a mesh

point interval, as long as the h_v value is larger than a critical value, which is 105 kW/m^3K in the present case. If the h_v value become smaller than the critical one, the accretion suddenly collapses, because it becomes difficult to provide enough cooling for the maintenance of the accretion. In Figure 3.8 the solid and gas temperatures in the accretion with different volumetric heat transfer coefficient h_v are shown, using results from along the centre axis of the accretion. The temperature difference between the solid and the gas is large near the centre, becoming small towards the surface, and the temperatures are almost equal near the accretion surface. The larger h_v value gives less difference between the two temperatures.

The same kind of diagram is shown in Figure 3.9 in the case of volumetric heat transfer coefficients depending on the local gas flow rate. The expression for the volumetric heat transfer coefficients as a function of gas flow per unit area is obtained by modifying that in reference 19. The results shown in Figure 3.9 are similar to those in Figure 3.8. Therefore, the value of the volumetric heat transfer coefficient h_v hardly affects the accretion shape or size in the range of 109-1300 kW/m^3K in the present condition.

3) Thermal conductivity of the accretion.

In the calculations, the thermal conductivity of solid steel was used for the porous accretion. It may be necessary to take into account the effect of the porosity. Therefore the thermal conductivity of the accretion was varied extensively. However, the dimensions of the accretion hardly changed. Figure 3.10

shows the solid and gas temperature on the centre axis of the accretion with different thermal conductivities. The temperature difference between the solid and the gas is very small in the case of a very low thermal conductivity, being large for a high thermal conductivity especially in the centre area. The thermal conductivity of the accretion hardly affects the present calculations of accretion size and shape.

4) Effect of an external pressure gradient.

The effect of a static pressure gradient of the surrounding liquid metal in the height direction can be examined by setting a flow potential gradient in the liquid metal phase, because the flow potential difference can be regarded as relative difference of the pressure. Figure 3.11 shows the results corresponding to a relatively low pressure gradient, where the surrounding pressure difference over the height of the accretion is about 3% of the pressure drop in the accretion. Outflow of the gas is seen over all the surface of the accretion. The accretion shape does not change much, showing only a slight decrease of the bottom radius. Iso-flow-potential contours, which are equivalent to iso-pressure contours, are still concentric in the central area of the accretion, but they shift from concentric contours near the accretion surface. Gas near the surface tends to flow upwards.

In the next case, shown in Figure 3.12, a steep pressure gradient, i.e. almost a quarter of the pressure drop in the accretion, was employed. The result shows that the gas escapes only from the top part of the accretion surface. In this case, the pressure gradient outside the accretion is so steep that the flow-

potential at the accretion surface is lower inside the accretion than it is outside, except on the top part of the accretion. Thereby, a straightforward calculation of the gas flow under this circumstance causes an unreasonable reverse flow across the accretion surface from the outside to the inside. To avoid this impossibility, the model was altered so that the accretion is not porous across its outer surface in the region where the flow potneital inside the accretion is less than that outside. In other words the pressure difference is supported by a solid skin of steel. This assumption is quite realistic because, if reverse flow occurs, liquid steel will come into the accretion and will solidify instantly. The accretion shape does not change much in this case either, though the gas flow pattern changes considerably in the outer part of the accretion.

The case of actual gas injection in industry is probably that of Figure 3.11. In industrial gas injection such as the AOD process, a high total pressure is used (17 bar) and the surrounding pressure difference in the liquid metal over the height of an accretion is relatively small compared with the pressure loss in the accretion. In fact, spout holes for argon gas can be seen over the whole surface of the steel accretion shown in Plate 1(b) in Chapter 2.

From the above results it is clear that the gas flow in the outer part of the accretion scarcely affects the accretion shape. The heat sink values in hemispherical shells of radius r and unit thickness are shown in Figure 3.13. The substantial heat sink occurs mainly well inside the accretion. Thus it is understandable that the gas flow in the outer area hardly affects the accretion

shape.

5) Simple model for calculation of accretion size.

Accretion shapes obtained by the porous accretion model are fairly simple and symmetrical so that, assuming a hemispherical accretion shape, the radius of the accretion has been estimated from a simple heat balance. The heat which flows into a hemispherical accretion is set equal to the heat removed by the cooling gas in the accretion. That is;

$$2\,\pi r^2 . h_l . T_s = C_p . F_{total} . \Delta T_{gas}$$

where T_s is the superheat of the liquid metal, and ΔT_{gas} is the temperature rise of cooling gas in the accretion. F_{total} is the total mass flow rate of the cooling gas. Hence the accretion radius is

$$r = \left(\frac{C_p \cdot F_{total} \cdot \Delta T_{gas}}{2\pi \cdot h_l \cdot T_s} \right)^{\frac{1}{2}} \qquad (3.8)$$

Relations between r and T_s in the above equation are shown in Figure 3.14 with different gas flow rates. In the same figure, accretion heights and bottom radii from the results of Figures 3.6 and 3.7 are also shown. The accretion size obtained by Equation 3.8 gives good agreement with the results from the finite difference calculations. Equation 3.8 is thought to be sufficient and very useful for a practical purpose, namely to estimate the size of a porous accretion.

Alternatively, it will also be useful for the estimation of the heat transfer coefficients between liquid metal and accretions using the actual dimensions of accretions obtained by experiments. For example, it was derived that h_l = 0.14 cal/s cm^2 ^oC (5.9 kW/m^2K) using the data of the accretion shown in Plate 1(b) in Chapter 2, which are T_s = 130^oC, F_{total} = 21 g/s (700 Nl/min), r = 6cm.

In Figure 3.14, the plots of the accretion height obtained from the finite difference calculations tend to shift towards the smaller side for small accretions. This is because a small accretion has a strong curvature and the heat flow per unit area on the accretion surface is larger than that of a large accretion.

6) Extension to accretions of intermediate structure between porous and pipe-like.

In this chapter, calculations for the porous accretion model have been presented so far. Nevertheless, some actual accretions show intermediate shapes between the porous accretion and the pipe-like accretion, and the present porous accretion model has been extended to cover these. An essential difference between the two extreme models is the way the gas flows in the accretion. In the pipe-like model, the gas in the accretion flows exactly in the same manner as in a tuyere. On the contrary, in the case of porous accretion model, gas flows as a potential flow in the accretion.

In the intermediate structure model, some part of the gas discharged from the tuyere flows only upwards in the central column of the finite difference mesh as if gas flows in a pipe

(pipe-flow-gas), and the rest of the gas follows potential flow. The ratio of the pipe-flow-gas $R_{pipe\text{-}flow}$ in the central column is assumed as an exponential function of height Z, such as

$$R_{pipe\text{-}flow} = a^{Z/Z_o} \quad (a = 0\sim1,\ Z_o = 1\ cm)$$

where "a" is a shape-factor which represents the distribution of the pipe-flow-gas in the central column. Figure 3.15 shows the relation between the pipe-flow-gas fraction and the height with various shape-factors. The gas converted from the pipe flow to the potential flow was treated through the source term in the flow potential calculation. When the shape-factor is zero, all the gas follows potential flow (porous accretion) and when the shape-factor is equal to one, all the gas flows upwards in the central column (pipe-like accretion).

Figure 3.16 shows the change of the accretion shape with shape-factor. In the range of a = 0~0.5, the accretion shape does not change much, showing a hemispherical shape. When the shape-factor becomes larger, the accretion becomes tall and thin. In the case where the shape factor is almost equal to one, the accretion shape is very similar to that obtained by the pipe-like model. In the previous chapter the accretion shown in Plate 1(a) has been described as a typical pipe-like accretion. Strictly speaking, this had an intermediate structure because some small subconduits spreading radially towards the side surface were observed. The accretion shape in Plate 1(a) in Chapter 2 is seen to correspond to the shape of a = 0.90~0.95 in Figure 3.16, though these cannot be directly compared because of the different injection conditions.

Keeping the shape-factor equal to 0.8, the effect of superheat on the accretion dimension is indicated in Figure 3.17.

The accretion becomes slender with high superheat. A comparison of accretion dimensions with different gas flow rates indicated similar results, low gas flow rate giving a more slender shape. From these results, at constant shape-factor, it is seen that as an accretion becomes smaller its shape becomes more slender. The fact that smaller accretions are more slender at constant values of shape factor and Z_o arises because less gas has been transferred from the pipe-like flow to the porous flow.

3.5. Concluding remarks

A porous accretion model of heat transfer and accretion formation around a gas injection tuyere has been developed. In this model, the cooling gas flow in the accretion follows potential flow. A mathematical formulation for the steady state has been solved by the finite difference method. The results are summarized as follows.

1) Accretion shapes obtained are almost hemispherical. Isotherms of solid and gas in the accretion, and iso-flow-potential contours are almost of concentric hemispheres.

2) Decrease of superheat or increase of gas flow rate increases the size of the accretion.

3) Volumetric heat transfer coefficients between cooling gas and solid accretion, and thermal conductivity of the solid accretion hardly affect the accretion dimensions. However, if the h_v value becomes smaller than a critical value (105 kW/m^3K in the present

case), the accretion suddenly collapses.

4) The effect of a small pressure gradient around the accretion is not significant.

5) Substantial heat removal by cooling gas occurs in the central part of the accretion. Gas flow in the outer part of the accretion scarcely affects the accretion shape.

6) A simple model for calculation of the porous accretion size was also presented. This may be useful to estimate the heat transfer coefficient on the accretion surface from experimental data.

The present porous accretion model has been extended to an intermediate structure model.

7) By selection of the shape-factor this model can reproduce accretions from the porous model to the pipe-like model.

8) In the case of a constant shape-factor and Z_0 small accretions tend to be more slender than large ones.

List of Symbols.Chapter 3

a	shape-factor for the pipe-flow-gas distribution
C_p	specific heat of gas
f	mass flow rate of gas per unit area.
F	mass flow rate of gas through the cell
F_{total}	total mass flow rate of gas discharged from tuyere
h_{gR}	heat transfer coefficient between gas and refractory
h_l	heat transfer coefficient between accretion and liquid metal
h_v	volumetric heat transfer coefficient between gas and accretion

k thermal conductivity

n normal ordinate to the boundary

P flow potential

$\dot{q}$ heat generation per unit volume

$\dot{q}_d$ mean heat flux density across thermal diffusion zone

r radius of cylindrical co-ordinate

R_d thickness of fictitious thermal diffusion zone

r_o bore radius of tuyere

$R_{pipe\text{-}flow}$ ratio of pipe-flow-gas

Δr radius interval of finite difference approximation

S surface area of finite difference cell

T temperature

T_s superheat

T_w wall temperature of tuyere bore

ΔT_{gas} temperature rise of gas in accretion

u gas velocity

ΔV volume of finite difference cell

Z height of cylindrical co-ordinate

Z_o reference height (1cm)

ΔZ height interval of finite difference approximation

Greek

Θ modified temperature in liquid region

λ coefficient which relates flow potential to mass flow rate

ρ density of gas

Subscripts

b bulk liquid

d fictitious thermal diffusion zone

g gas

in inflow

l liquid

m melting point

o initial value for integration

out outflow

R refractory

s solid or south cell boundary of finite difference cell

w wall of tuyere bore or west cell boundary of finite difference cell.

TABLE 3.1

Material Properties and Typical Data for Computation

Steel	k_s	0.07cal/s cm ^oC	29 W/mK
	k_d	0.6 cal/s cm ^oC	251 W/mK
	T_m	1540^oC	
Refractory	k_R	0.003cal/s cm ^oC	1.3 W/mK
Argon gas at 727^oC	ρ	4.87 x 10^{-4}g/cm^3	
	C_p	0.124cal/g ^oC	0.52 J/gK
Radius of tuyere bore		0.6cm	
Refractory thickness		24cm	
Outside temperature of refractory.		200^oC	
Gas flow rate		5.95 g/s	(200 Nl/min)
		12200 cm^3/s at 727^oC	
h_v		0.1cal/s cm^3 ^oC	418 kW/m^{3}K
h_{gR}		0.0012cal/s cm^2 ^oC	0.050 kW/m^{2}K
R_d		3.0cm	
($h_l = k_d/R_d$		0.2cal/s cm^2 ^oC	8.37 kW/m^{2}K)

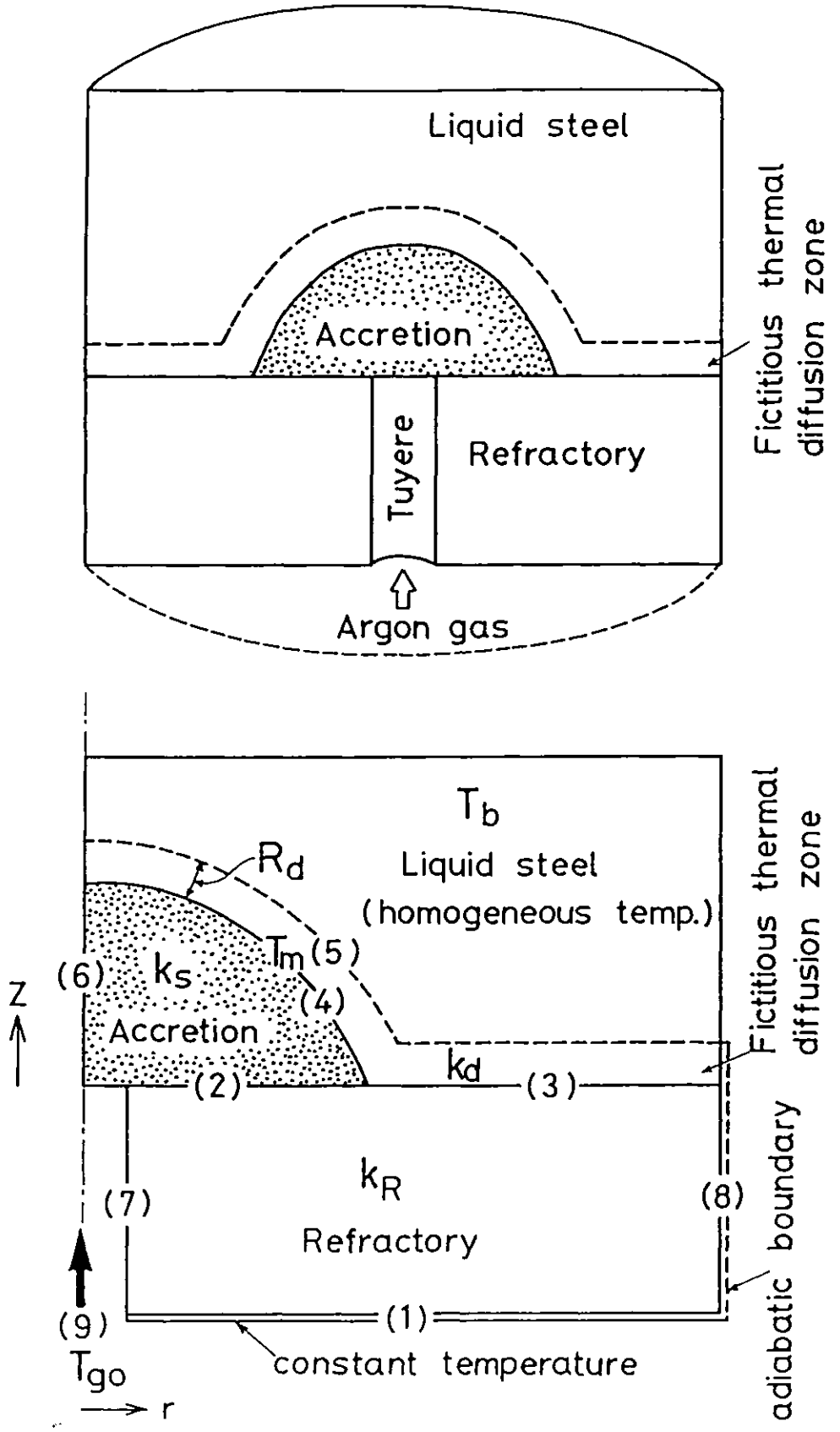

Fig.3.1. Cylindrical region for modelling and the boundary conditions for heat transfer.

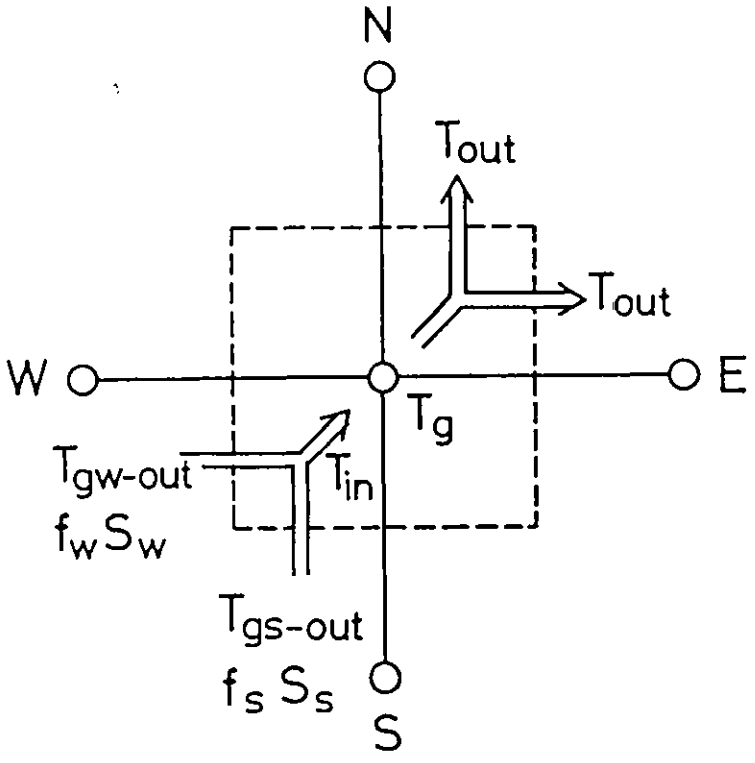

Fig.3.2. Calculation of gas temperature in accretion.

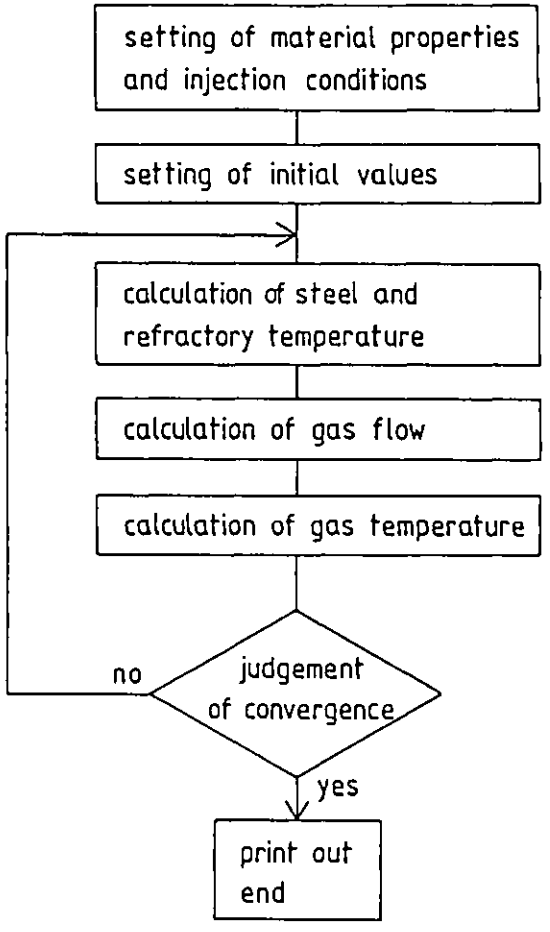

Fig.3.3. Flow chart for the porous accretion calculation.

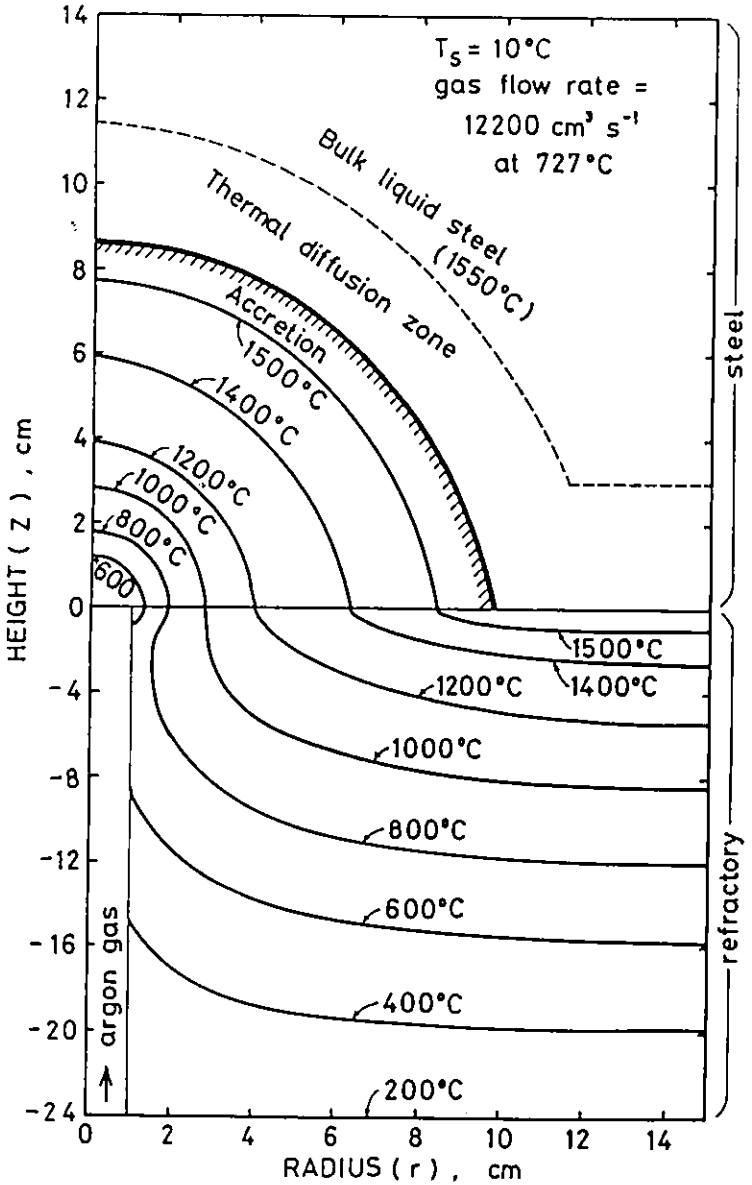

Fig.3.4. Accretion shape and isotherms.

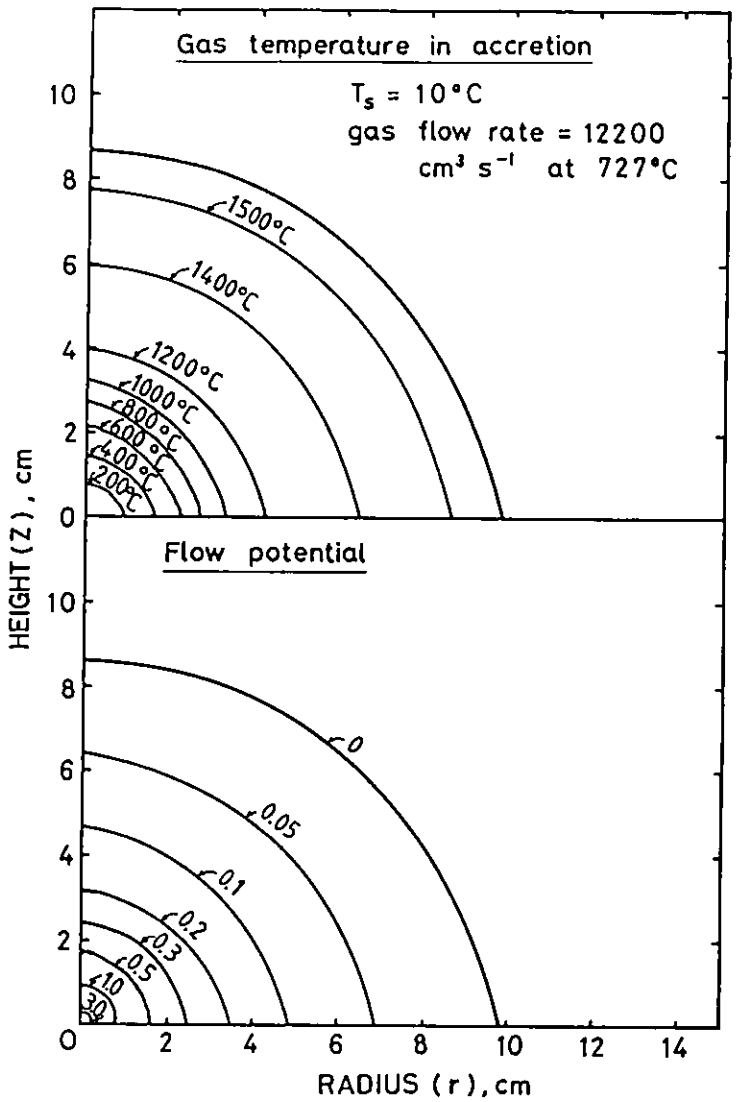

Fig.3.5. Gas temperature and flow potential in accretion.

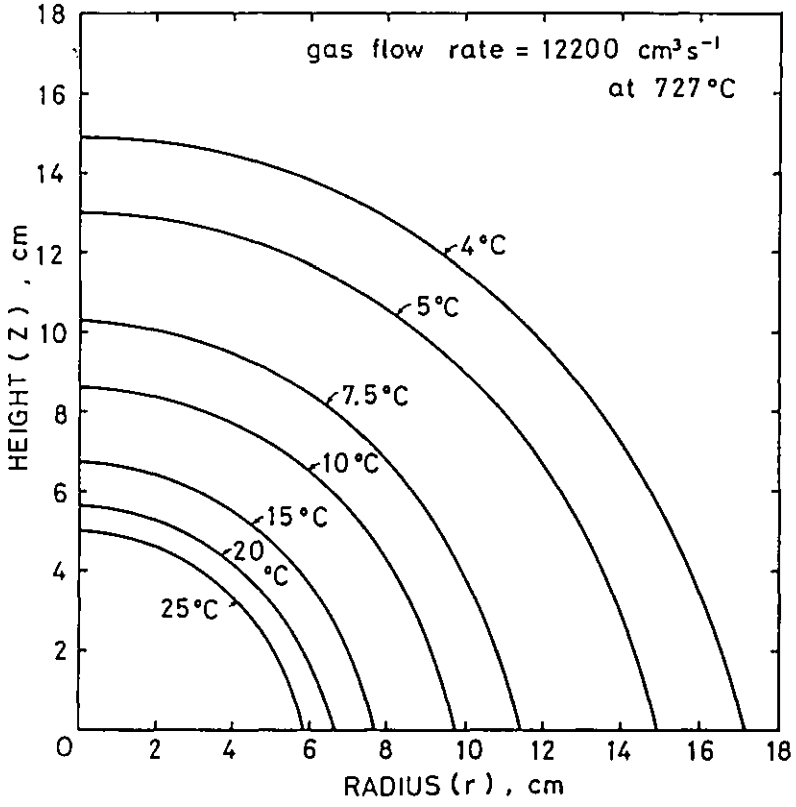

Fig.3.6. Effect of superheat on the size of accretion.

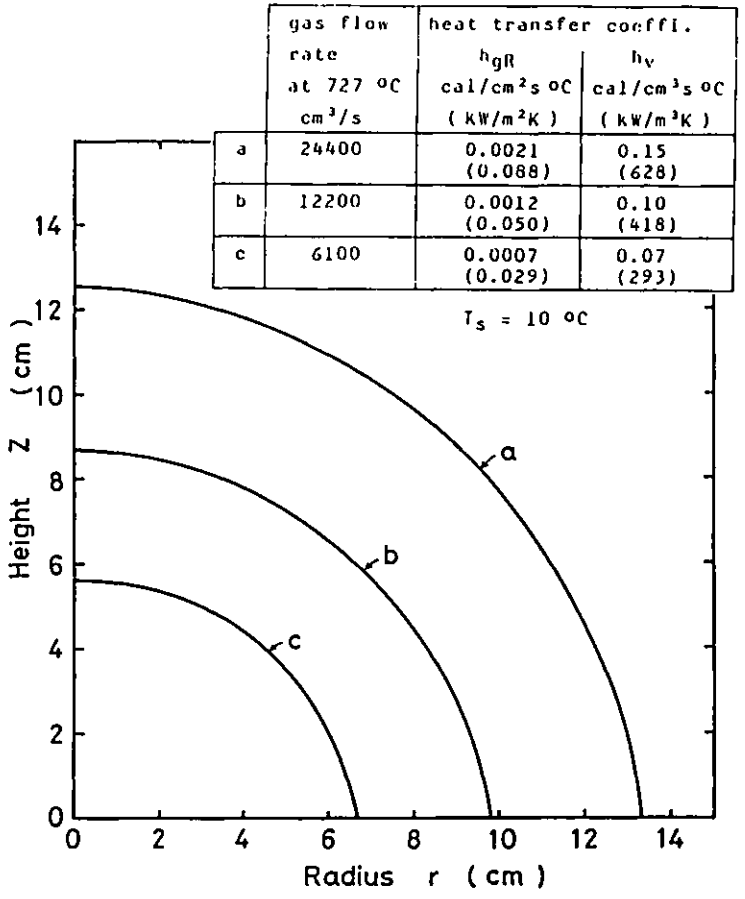

Fig.3.7. Variation of the accretion size with gas flow rate.

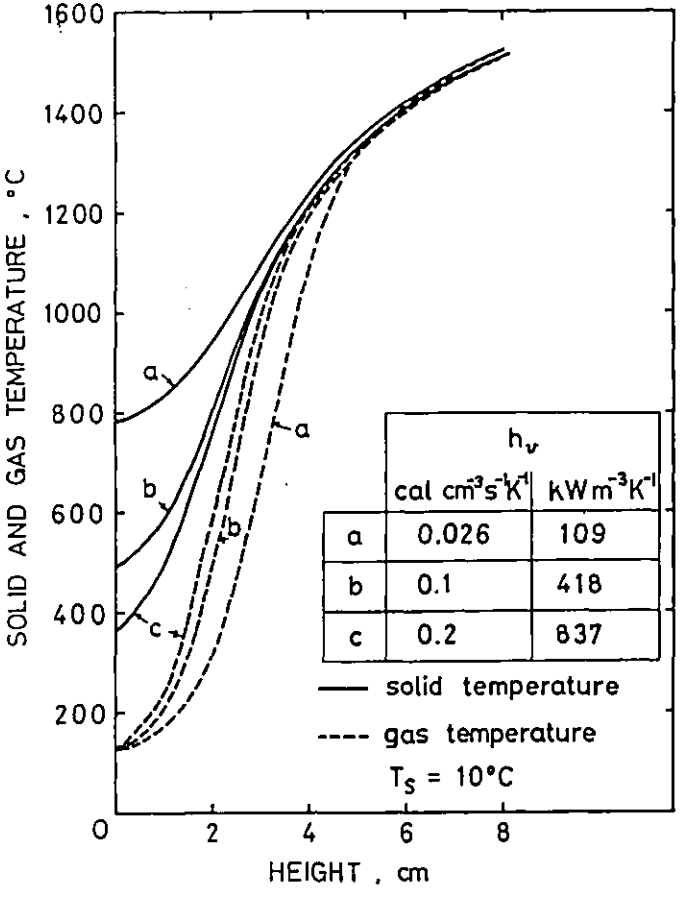

Fig.3.8. Solid and gas temperature on the vertical axis of accretion with different volumetric heat transfer coefficients, h_v.

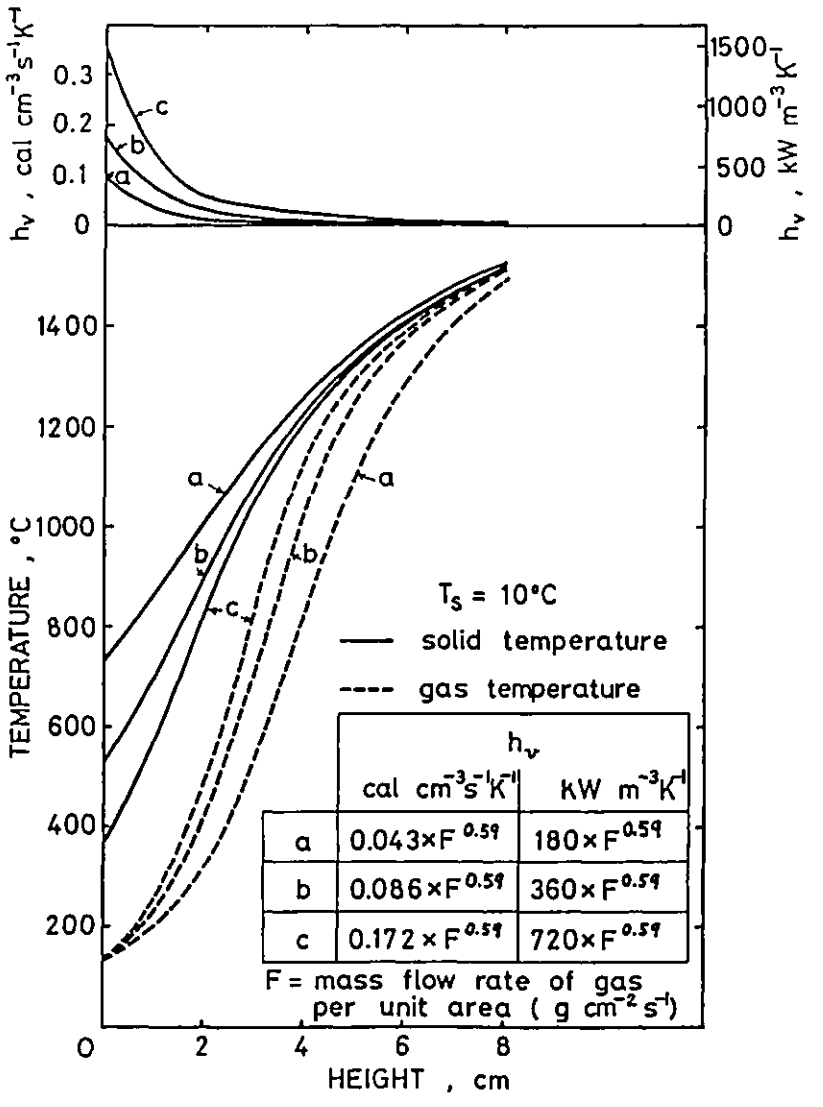

Fig.3.9. Solid and gas temperature on the vertical axis of accretion with volumetric heat transfer coefficient dependent on local gas flow rate.

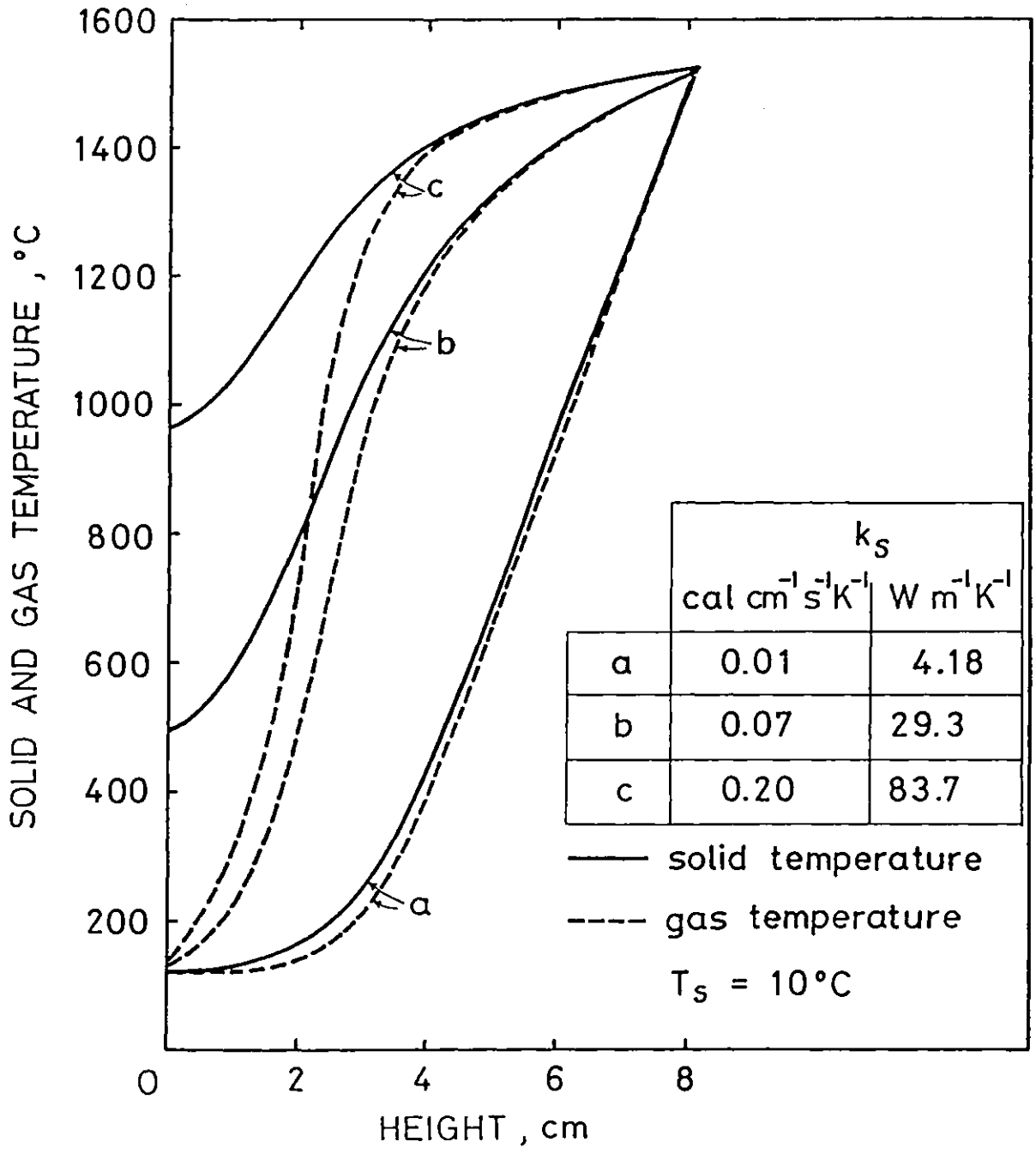

Fig.3.10. Solid and gas temperature on the vertical axis of accretion with different thermal conductivities, k_s.

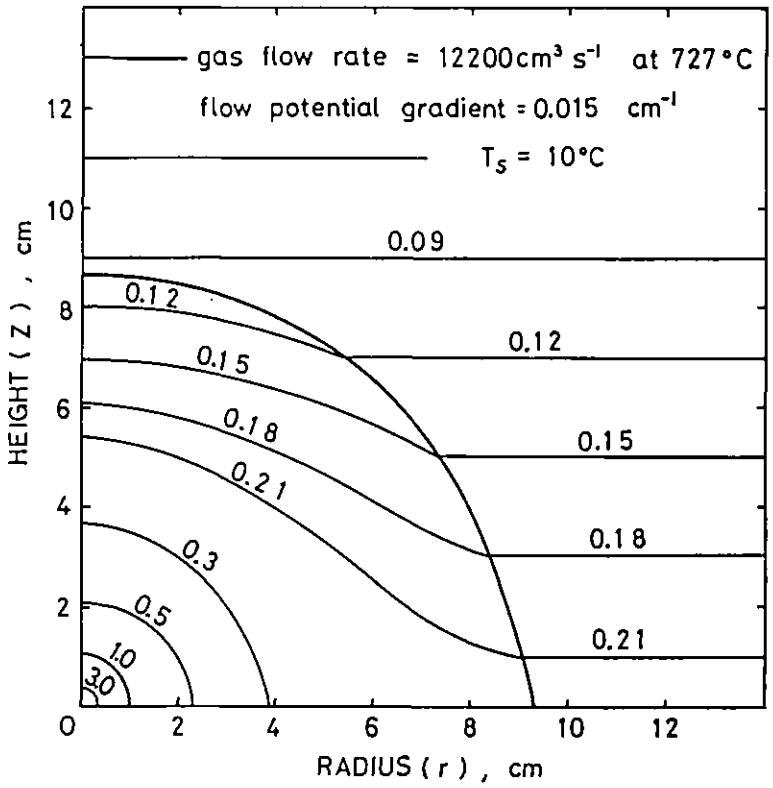

Fig.3.11. Shape and flow potential distribution for an accretion placed in a constant potential gradient field.

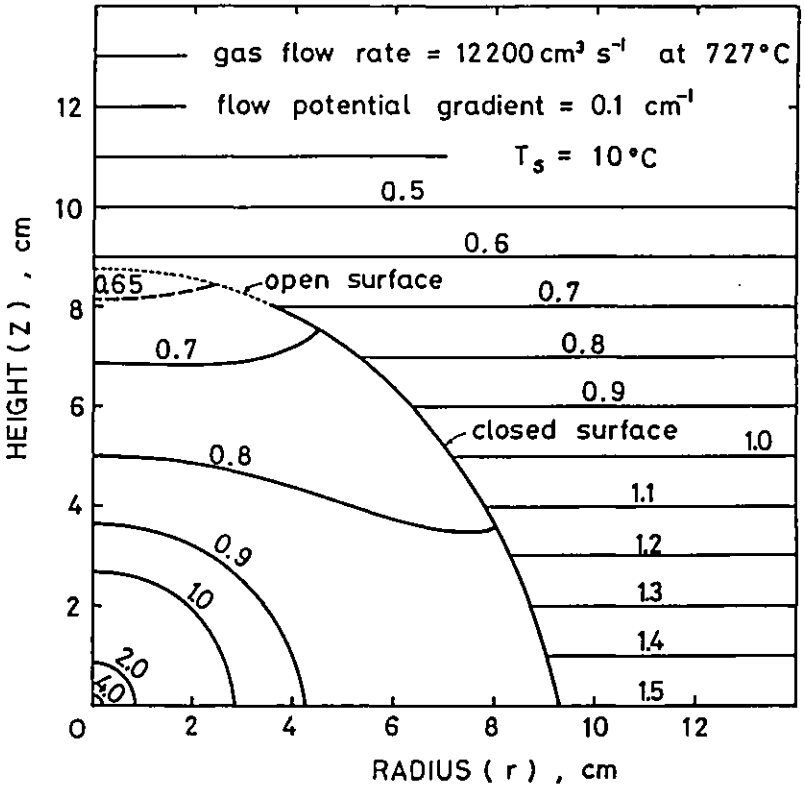

Fig.3.12. Flow potential distribution for an accretion placed in a steep potential gradient field.

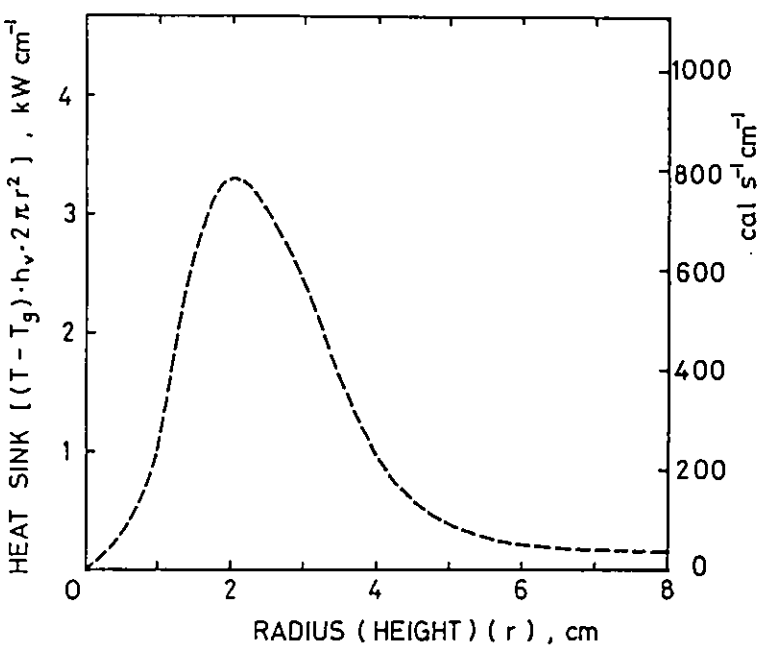

Fig.3.13. Heat sink in hemispherical shells of radius r and unit thickness using results along the vertical axis. Superheat 10°C, gas flow rate 5.95 g/sec.

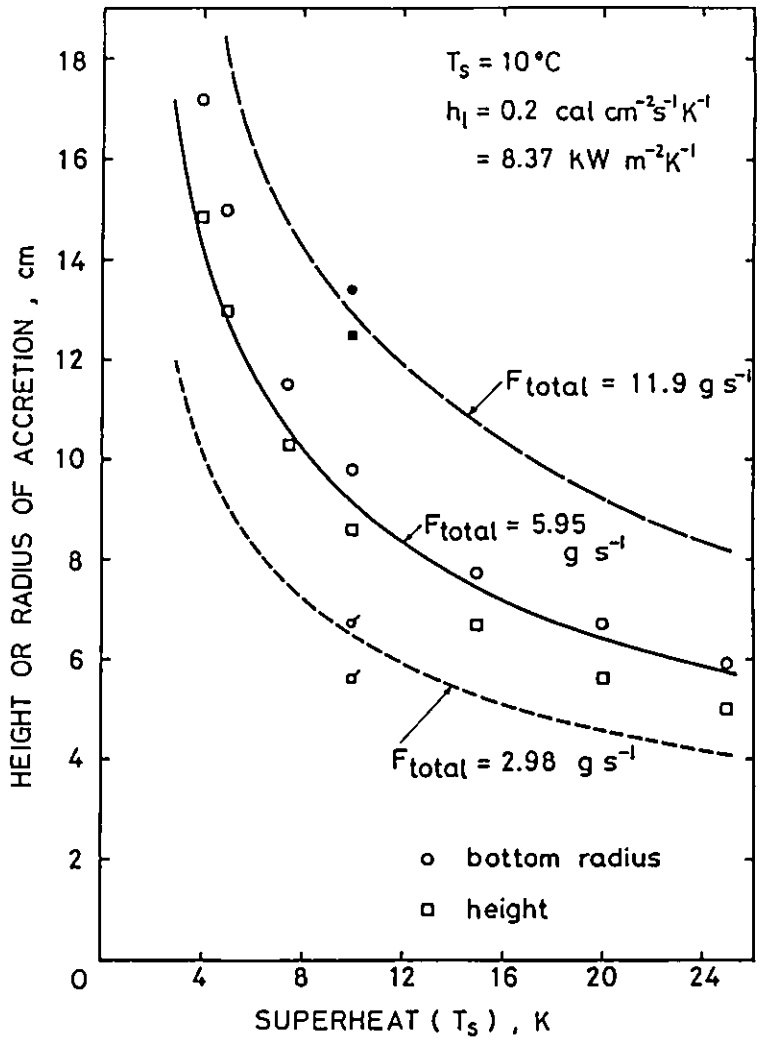

Fig.3.14. Accretion size obtained by simple heat balance model. Accretion heights and bottom radii from the results of finite difference calculation are also shown.

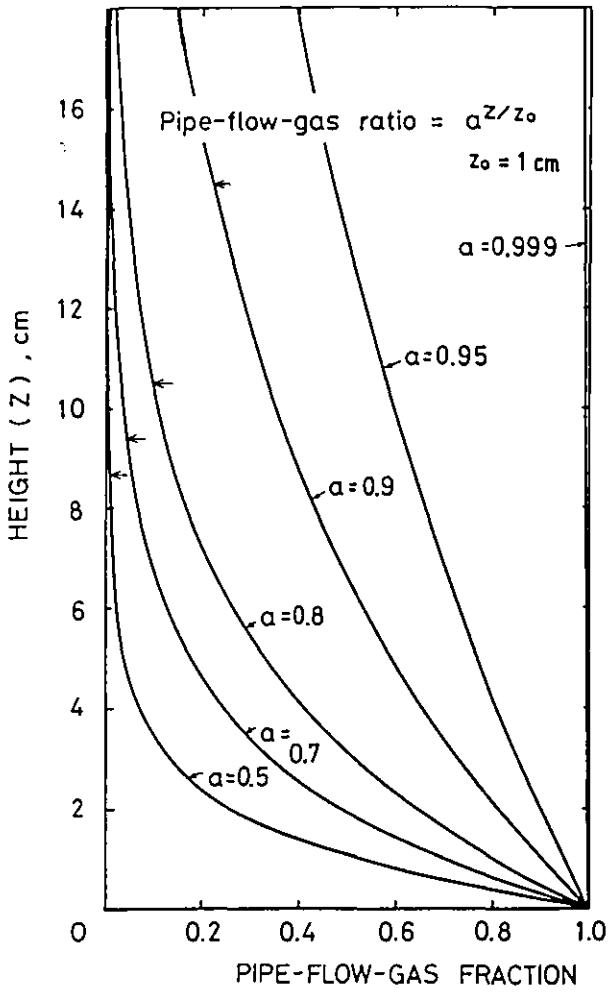

Fig.3.15. Relation between pipe-flow-gas fraction and height with various shape-factor a. Arrow "←" indicates height of accretion at superheat 10°C.

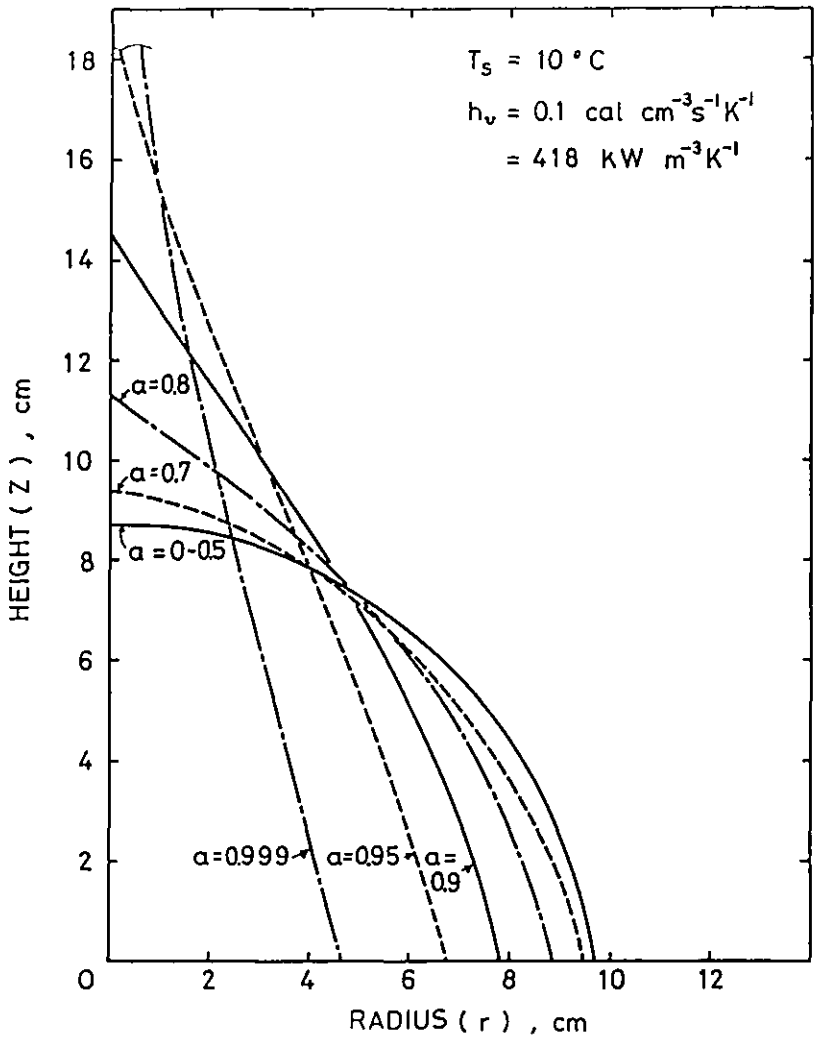

Fig.3.16. Change of accretion shape with shape-factor.

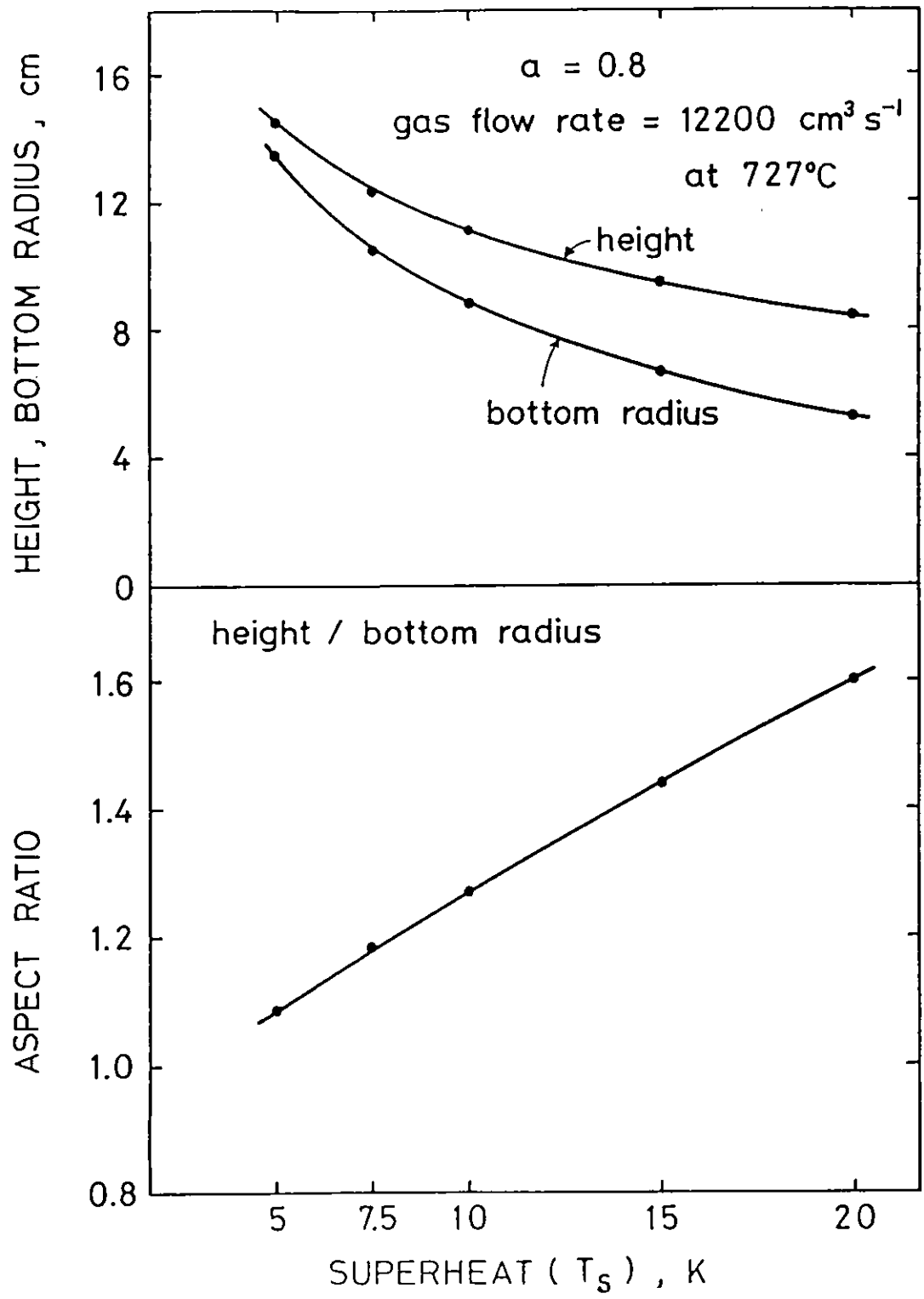

Fig.3.17. Effect of superheat on the accretion height, bottom radius and aspect ratio (height/bottom radius), when shape-factor is 0.8.

Chapter 4: POWDER INJECTION EXPERIMENTS

Chapter 4: POWDER INJECTION EXPERIMENTS

Powder injection experiments were carried out using a small scale powder injection system which was specially developed. Desulphurization of molten pig iron using $CaO-CaF_2-Al_2O_3$ powder was chosen as a basis of the submerged powder injection experiments. Experiments on simultaneous dephosphorization and desulphurization of molten pig iron were also carried out using surface powder injection with gas stirring. In this chapter the experimental apparatus and procedures and water model experiments to select a nozzle diameter are described.

4.1. Powder Injection System

In order to carry out the experiments on a small scale using melts of less than 5kg, it was necessary to fabricate a powder injection system with a stable and low powder feeding rate. Powder feeding rates and carrier gas flow rates should be adjustable independently. A fluidized bed was used as a powder entraining device in another small scale experiment[21] in the laboratory, but it was obvious that it was difficult to obtain stable feeding rates, and to control gas flow rate and powder feeding rate separately with the fluidized bed method. Hara et al[22] fed powder by putting an ampoule, which contained some powder, into the gas flow line, and scraped out the powder into the gas conduit manually. However, this method may result in unsteady powder feeding rates, and a manual scraping operation was considered to be laborious. Engh et al[23] developed their own special powder dispenser (rotary disc feeder), but the details of their

feeder are not clear. The other methods (pusher dispenser, vibratory dispenser) are described by Wikander[24]. Rotary feeders are often applied on an industrial scale.

In the present work, a small powder injection apparatus, suitable for laboratory-scale experiments was developed. A schematic diagram of the system is shown in Figure 4.1. A small screw feeder system (Figure 4.2) was suspended by a load-cell in a transparent "Perspex" pressure vessel. The powder feeding rate was measured from the weight change of the suspended powder feeding system by registering the load-cell output with a pen recorder. Figure 4.3. shows an example of the pen recorder chart registering the weight change of the powder containing column, and the powder feeding rate was very constant. In the figure the relationship between supplied voltage for the driving motor and the powder feeding rate is also shown. A mini-vibrator attached on the powder container prevented sticky powder from bridging in the container. The pressure vessel enclosing the powder feeder system was installed above the furnace, so that the gas and powder mixture travelled only downwards to avoid clogging of the powder in the entraining tube. The inner diameter of the entraining tube and injection lance, except at the nozzle tip, was 3mm.

The injection lance shown in Figure 4.4. was made of a double wall alumina tube. The role of the outer tube was to absorb thermal shock and to protect the inner tube. The internal diameter of the submerged injection nozzle tip was 1mm, which was decided from water model experiments, and which ensured a very high gas velocity (about half the sonic velocity) at the nozzle tip.

A graphite anti-splash tube was put on the crucible to reduce any metal loss caused by splashing.

4.2. Selection of Nozzle Diameter and Powder Particle Size using a Water Model

To determine a suitable nozzle diameter and powder particle size, powder injection experiments using a water model were carried out. During actual gas/powder injection using molten hot metal, nozzle clogging tended to occur because of the solidification of hot metal which had splashed back into the nozzle tip and/or because of the agglomeration of powder at the nozzle tip. The situation in the case of powder injection using a water model may not be exactly analogous to that during injection into hot molten metal. However, nozzle clogging readily occurred in the water model, due to the agglomeration of powder particles at the nozzle tip. Therefore it was expected that the water model could be used to avoid unnecessary nozzle clogging in hot runs.

Silica and alumina powders were injected into water with argon gas using the powder injection system described in the previous section. Figure 4.5 shows the particle size distributions of the powders used. Figures 4.6, 4.7 and 4.8 show the results of the water model experiments with different powders. The powder feeding rate was 7 ~ 10 g/min, and the injection depth was 4 ~ 6 cm. Glass and graphite nozzles with various tip diameters were used, and the points marked G in Figure 4.6 and 4.8 denote the runs in which a graphite nozzle was used. The internal diameter of the glass nozzle reduced smoothly towards the tip, while the graphite nozzle had an inclined step in the nozzle tip as is shown in Figure 4.6.

Figures 4.6 - 4.8 show the effect of particle size and that the coarsest powder (silica 1) gave the best performance. Presumably the larger inertia of the individual coarser powder particles tended to prevent any incipient clogging. In experiments where the two finer powders were injected into air under comparable conditions there were no problems with clogging for the nozzle diameters used, so that the problems with these particles are thought to be due mainly to splashing back of liquid into the nozzle tip.

For the silica powder, which gave a reasonable injection performance, the effect of nozzle diameter and flowrate are shown in Figure 4.6. The nozzle diameter that gave the minimum possible gas flow rate without clogging was about 1mm. In the region where nozzle diameter was less than 0.8mm, nozzle clogging occurred even during powder injection into air. This suggests that the left hand boundary of the operating region occurred simply because the ratio of particle to nozzle diameter (1/4) was so large that the particles interfered with one another and blocked the flow. The right hand boundary in Figure 4.6.occurred only in submerged powder injection. Therefore in this region nozzle clogging was ascribed to water penetration into the nozzle tip.

In hot runs using molten iron a small gas flow rate for powder injection is preferable to avoid an adverse splash during small scale experiments. By reference to the water model experiments the nozzle diameter and the powder size were chosen as 1mm and 100 ~ 200 mesh (0.075 ~ 0.15mm). These were almost the same as those used by Saxena[25].

4.3. Melting Unit

A high frequency vacuum furnace (LEYBOLD-HERAEUS Type IS 1/III and RADYNE TS generator, 3kHz) with an alumina crucible was used to melt cast iron. The crucible assembly is shown in Figure 4.9. Temperature was measured using a thermo-couple (Pt - 6% Rh/ Pt - 30% Rh) lance immersed in the molten metal throughout the experiment.

4.4. Experimental Procedure

The injection powder was prepared as follows. Powder of the desired composition was made into briquettes in a press. The briquette of powder was premelted using a graphite crucible, and was cast into a block. After crushing, powder of the desired particle size was collected by sieving. The powder particle size chosen was 0.075 ~ 0.15mm (100 ~ 200 mesh) for the desulphurization experiments using submerged injection with 1mm bore nozzle tip or 0.075 ~ 0.3mm (52 ~ 200 mesh) for the simultaneous dephosphorization and desulphurization experiments using surface injection with a 2mm bore nozzle. As the powder, especially that containing $CaCl_2$, was hygroscopic, the premelted block of powder was kept in a desiccator, and crushing and sieving of the powder was carried out immediately before a powder injection run.

Powder injection experiments were carried out under an argon atmosphere. Argon was also used as carrier gas (6 ~ 7 Nl/min) for the powder injection. The depth of immersion of the submerged injection lance was 4cm. Sampling was carried out using silica suction tubes. Sulphur analyses for the desulphurization experi-

ments were made by a combustion method[26] or by a "Leco" analyser (by courtesy of Foseco International Ltd). Chemical analyses for the simultaneous dephosphorization and desulphurization experiments were made by Process Research & Development Laboratories, Nippon steel Corporation.

4.5. Some Results of Submerged Powder Injection Experiments

About 20 trials of desulphurization using submerged powder injection using $CaF_2/CaO/Al_2O_3$ powder were made in collaboration with Dr. B. Deo, but successful runs, in which over 50g of powder were injected, were achieved only after several trials. In the other runs nozzle clogging occurred. Even in a successful run, splash of metal was significant due to the high gas injection rate despite the use of the anti-splash tube. Metal loss during 20 ~ 30 min injection was 100 ~ 200 g, including the accretion caused by splashing. It was very difficult to obtain reliable performance during submerged powder injection experiments using the present small scale apparatus. In fact the smallest scale of powder injection experiments known in the literature is with 9 ~ 10 kg melts[22,23]. The present system seems to be slightly too small to achieve reliable submerged powder injection experiments without any nozzle clogging.

Figure 4.10 shows desulphurization curves of some of the successful powder injection runs. The experimental temperature was 1310°C. Gas injection was continued after stopping the powder flow. In runs 18 and 19 metallic aluminium was added to the molten cast iron as indicated in the figure. In run 19 some top slag already existed and some sulphur removal occurred before powder injection. As is

seen from the figure, the sulphur concentration decreased linearly during powder injection or in the early stage of the powder injection.

Discussion on the kinetics of desulphurization using submerged powder injection will be given in Chapter 5. Experimental conditions and the results for simultaneous dephosphorization and desulphurization will be shown in Chapter 7.

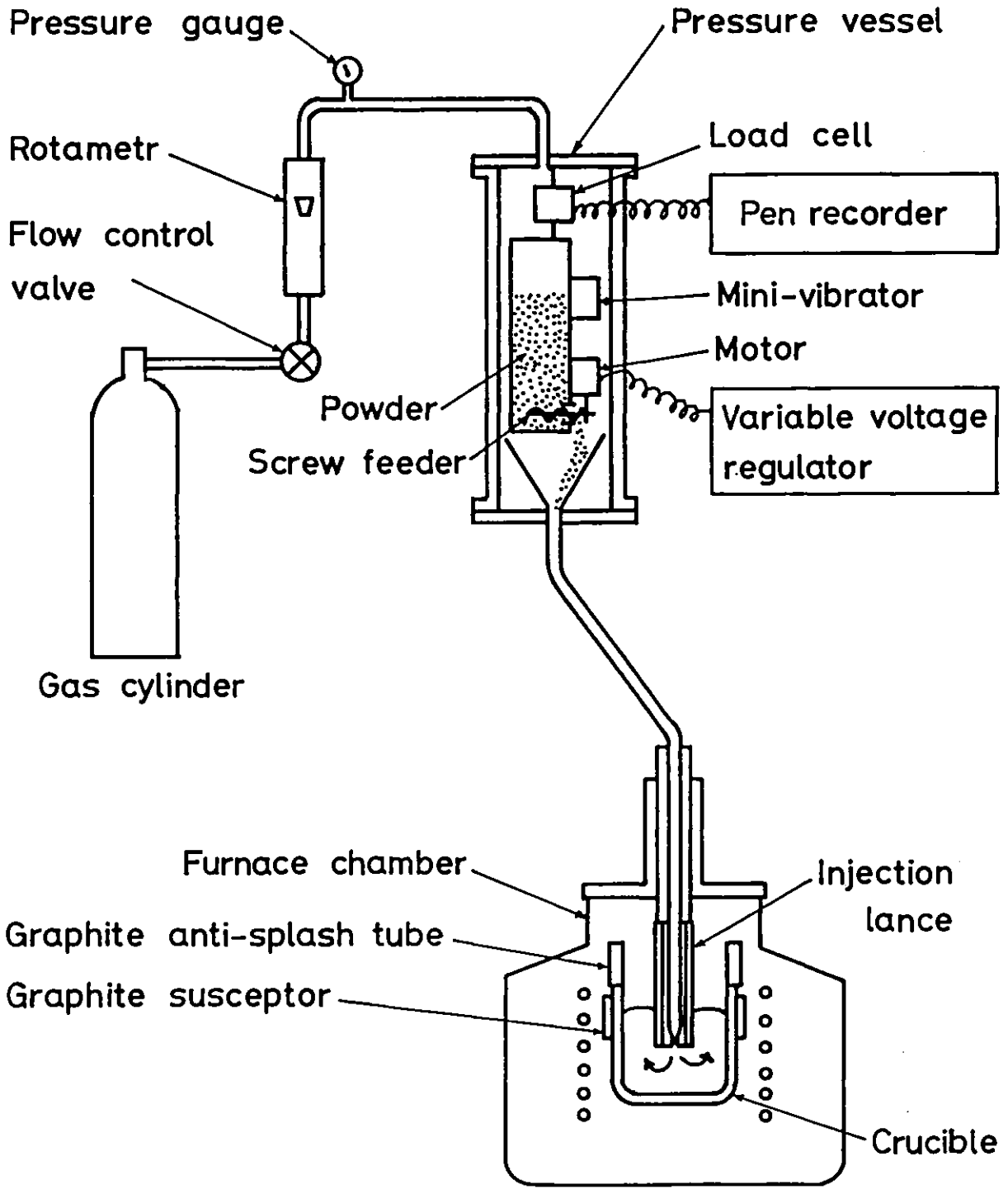

Fig.4.1. Powder injection system.

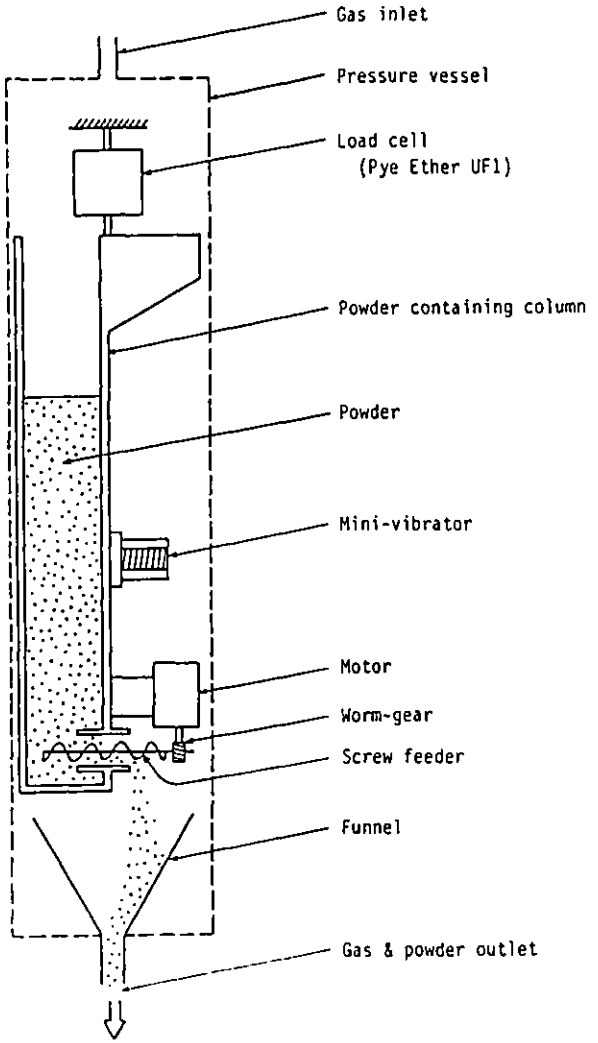

Fig.4.2. Schematic diagram of powder feeder.

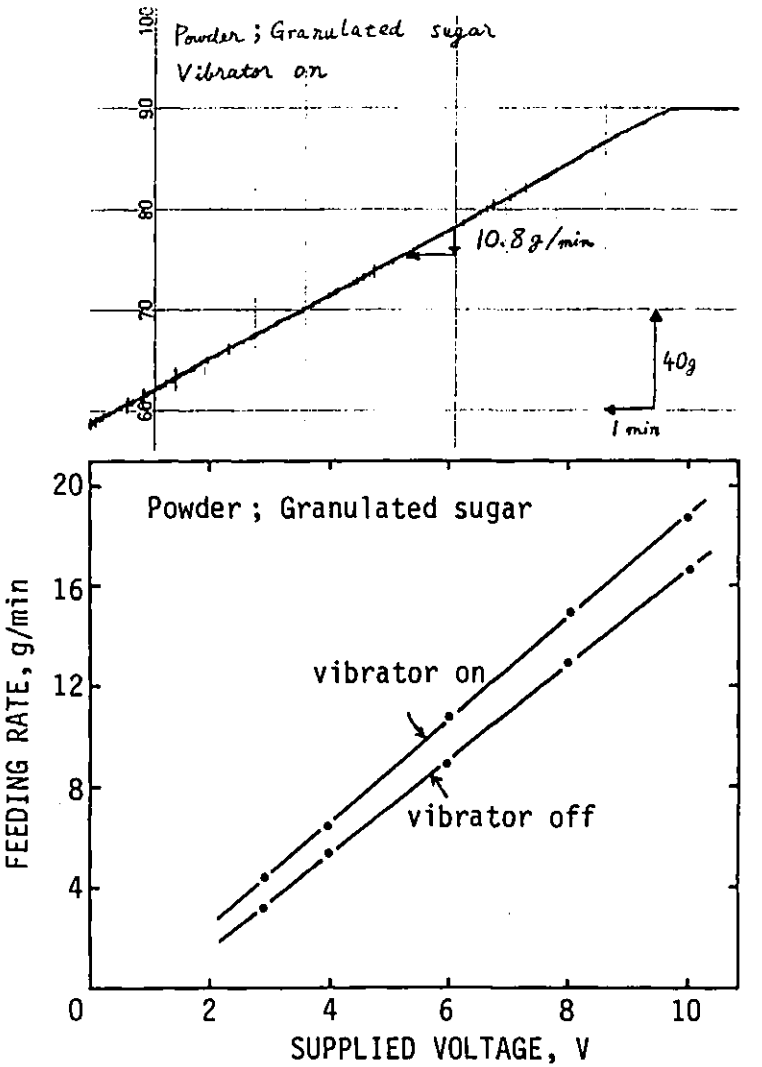

Fig.4.3. An example of pen recorder chart registering weight change of the powder containing column. Relation between supplied voltage for driving motor and powder feeding rate.

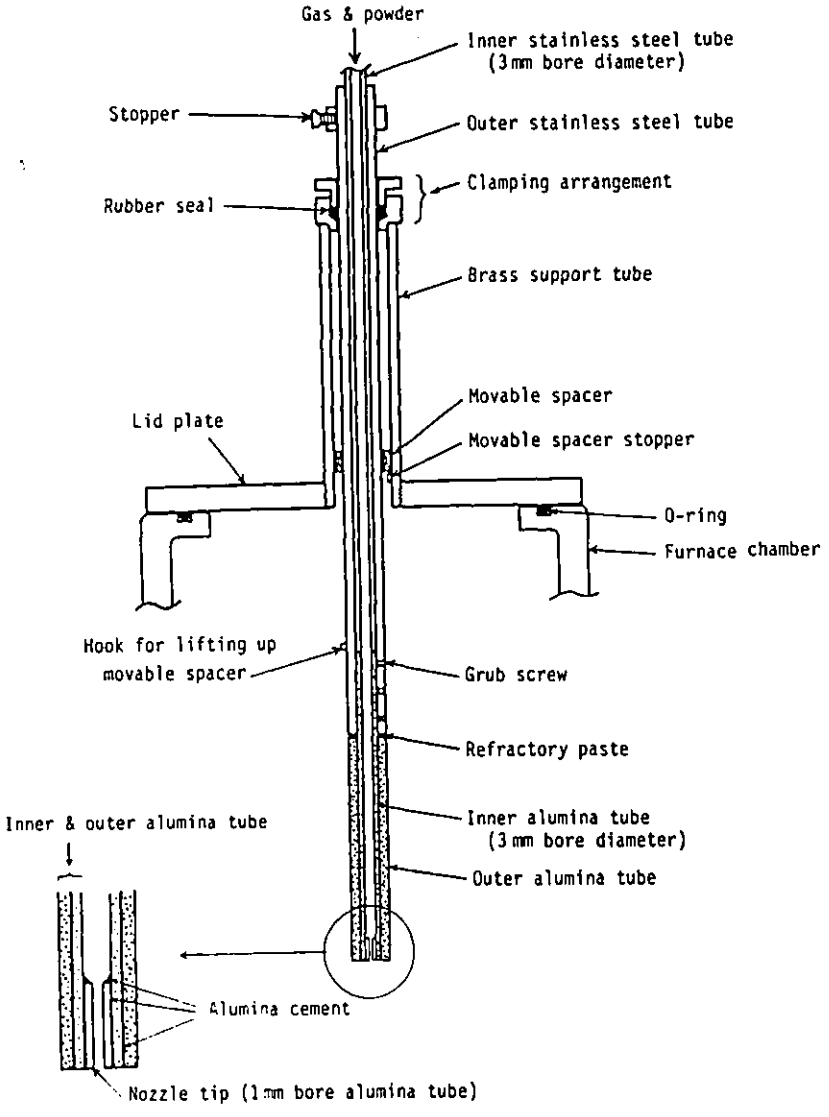

Fig.4.4. Structure of injection lance.

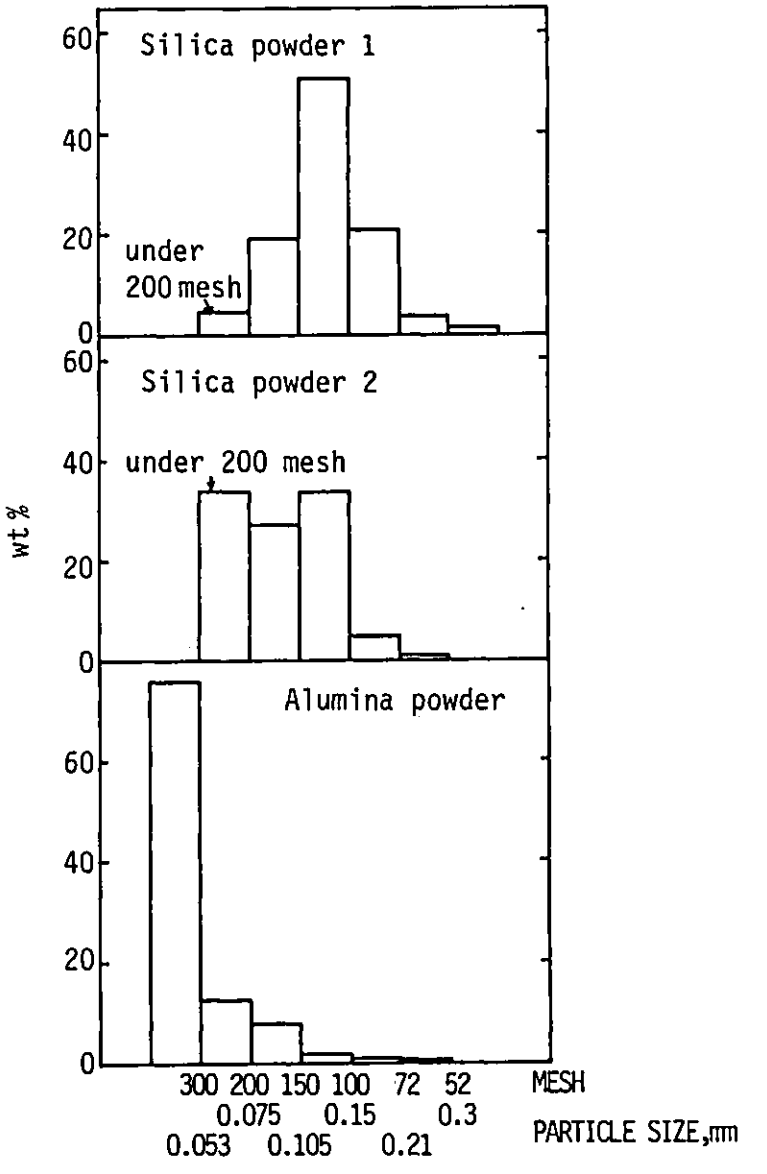

Fig.4.5. Particle size distribution of the powders.

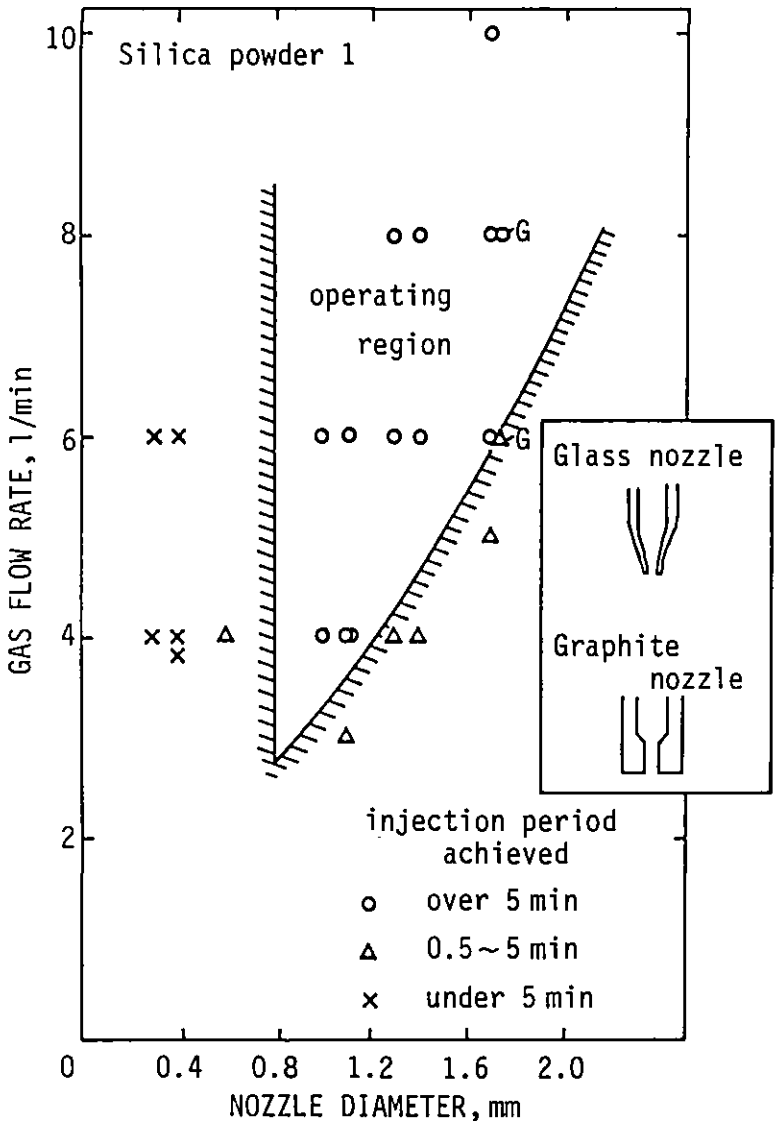

Fig.4.6. Powder injection into water using silica powder 1.

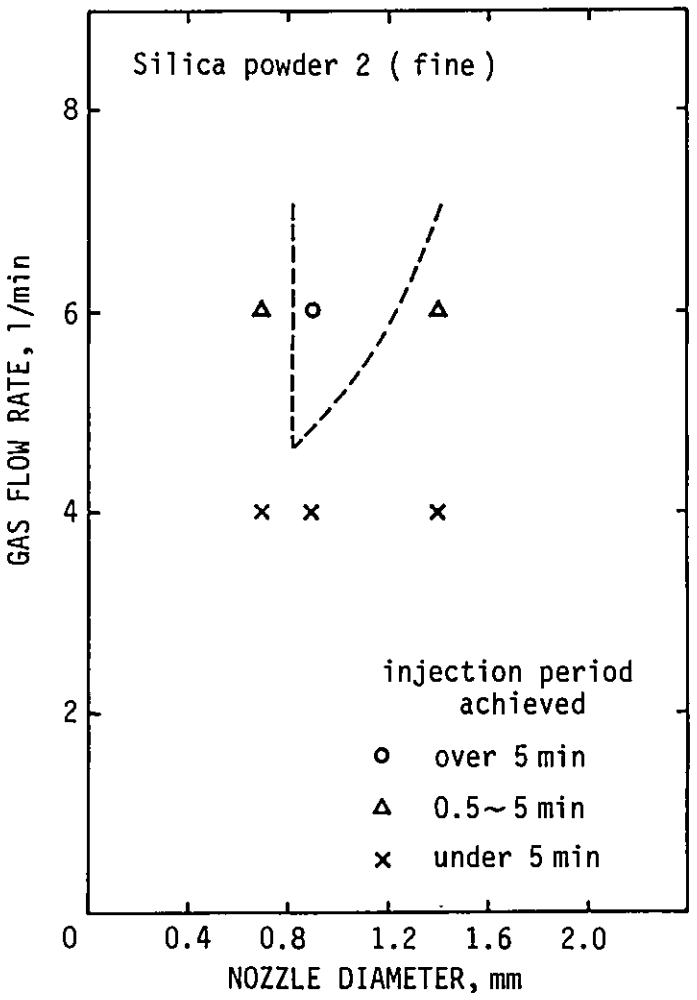

Fig.4.7. Powder injection into water using fine silica powder 2.

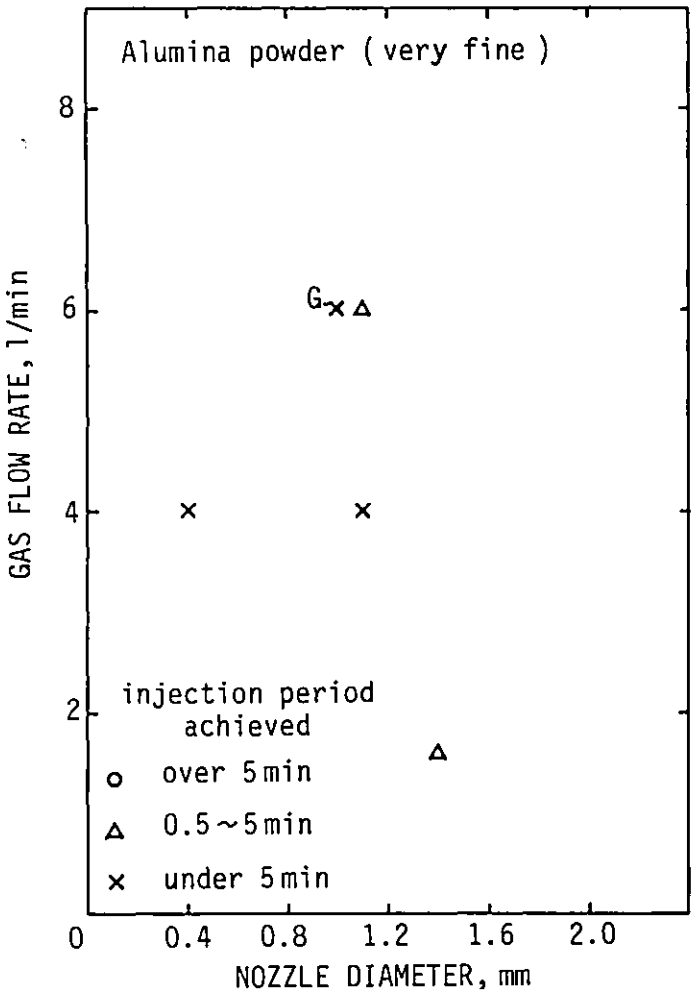

Fig.4.8. Powder injection into water using fine alumia powder.

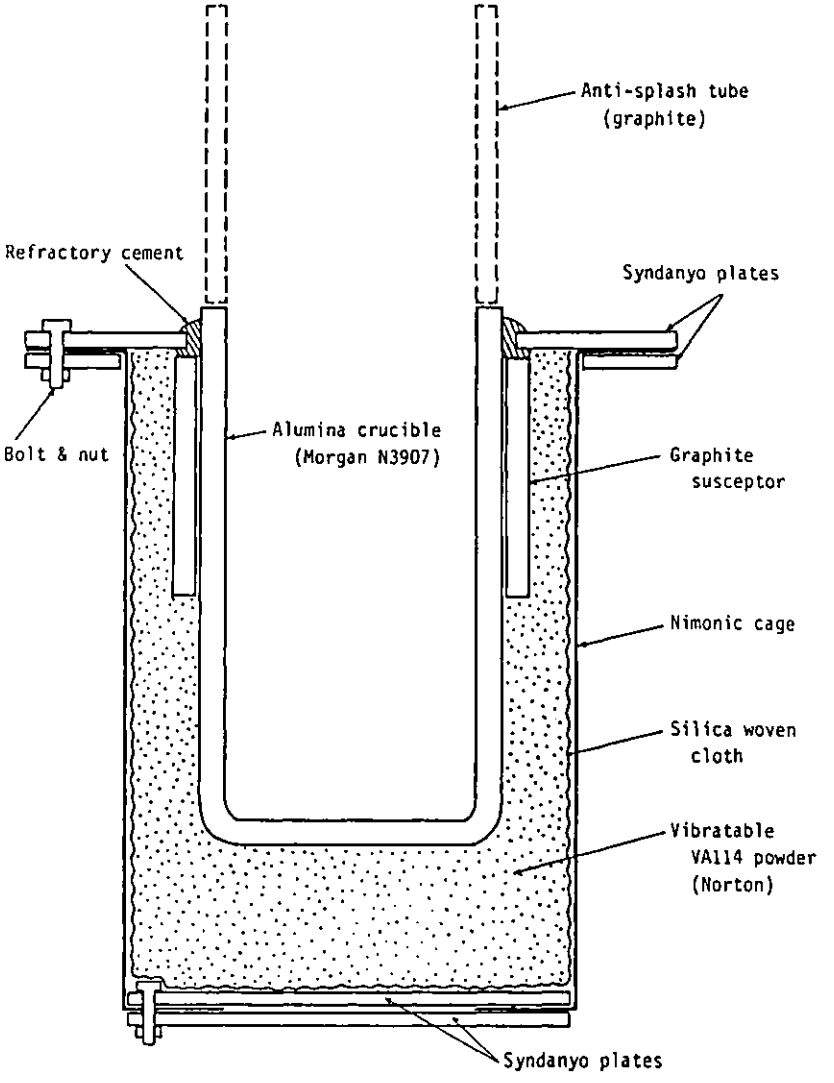

Fig.4.9. Crucible assembly.

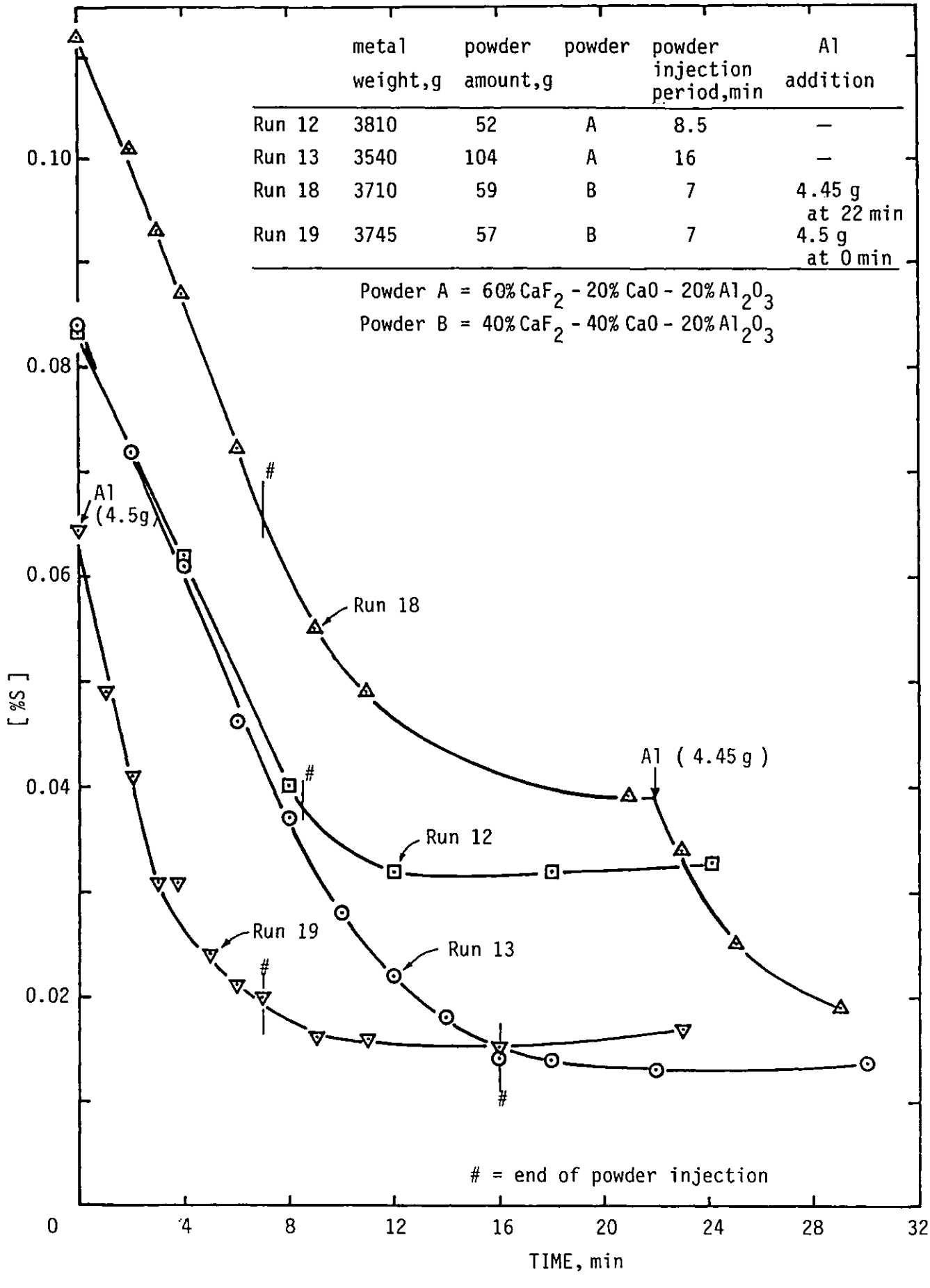

Fig.4.10. Example of submerged powder injection runs.

Chapter 5: A KINETIC MODEL FOR REFINING USING SUBMERGED INJECTION

Abstract

A model has been developed which shows clearly the important factors affecting the kinetics of refining using submerged injection. The model allows the calculation of the separate contributions of the reaction with injected powder during its rise (transitory reaction) and the reaction with top slag (permanent contact reaction), and enables quantitative evaluation of an "excess" desulphurization and a consequent "reversion" of sulphur. Allowance has been made for a decrease in the effective rate constant once the slag is saturated with sulphides. The model was applied to small scale powder injection experiments. The contributions of the two reactions during CaO-based powder injection, and comparison of powder injection and dumping are discussed. The rate constant measured during the rise of bubbles was compared with the value predicted by Engh's theory.

Chapter 5: A KINETIC MODEL FOR REFINING USING SUBMERGED INJECTION

5.1. Introduction

In recent years powder injection refining has made significant progress and analysis and modelling of powder injection processes are becoming of great interest. Schenck et al[27,28] proposed three basic mechanisms for reactions occurring between two immiscible phases, and Lehner[29] applied these ideas to submerged powder injection. The two possible reaction sites (Figure 5.1) are,
(a) during the rise of the powder particles dispersed in the melt (transitory reaction) and (b) between the bulk slag, which is always present on the surface, and the bulk metal (permanent contact reaction). A number of investigations have been made to clarify whether the transitory reaction or the permanent contact reaction dominate powder injection refining, but consistent agreement has not been achieved so far. This is due to lack of a suitable reaction model taking the contributions from both permanent contact and transitory reactions into account. Concerning reaction mechanisms during desulphurization using CaO-based powder injection, some researchers reported that the transitory reaction dominated the process[30-33], but others claimed the permanent contact reaction to be the major factor[34,35]. This aspect will be discussed later.

Currently two models that can evaluate the contributions from both reaction sites are known to us, but these are either unsatisfactory from the kinetic point of view or too specific for general applications. Lehner[29] extended the model of Schneck et al[27,28]

by introducing a parameter which expressed the portion of slag in a recirculated permanent reactor. His model is essentially based on a mass balance, and the kinetics are not considered, being assumed to be rapid.

El-Kaddah and Szekely[36] proposed a detailed model in which the coupled equations of fluid flow, particle motion and distribution, and mass transfer were solved numerically. This approach is undoubtedly the most sophisticated yet attempted and offers extremely useful insights into the process. However the model is specific to particular cases and it is difficult to study the effect of changes in a large number of parameters without incurring excessive costs for computation. In their paper they have not referred in detail to the problem of permanent contact and transitory reactions, although these were separately calculated in the particular cases for which they carried out computations.

In this work, a model has been developed which shows clearly the important factors affecting the kinetics of refining using submerged injection, as in the case of CaO-based powder injection to desulphurize pig iron. The model allows the calculation of the separate contributions of the transitory and permanent contact reactions. It has been applied to powder injection experiments on a laboratory scale.

5.2. Modelling

The flux considered in this model is liquid at steelmaking temperature and neither volatile nor soluble in the molten metal, e.g. $CaO-CaF_2-Al_2O_3$ flux. The total amount of flux existing in a ladle can therefore be calculated from the injection rate and time.

The bulk phases are assumed to be well mixed because of the gas stirring, and the rate determining stage of the sulphur removal is supposed to be the reaction or mass transfer at or near the reaction interfaces.

The kinetics of desulphurization are assumed to be given by the equation

$$J = k\ (C_m - C_s/L)$$

where J is flux density, and L is the effective partition coefficient and k is a rate constant. This equation is based on the finding reported in many classical papers[37-42] that the kinetics of desulphurization using CaO-based slags were approximately first order, based on an overall driving force. From the point of view of this paper it is important only that the above equations represents the desulphurization kinetics reasonably correctly in a mathematical sense. In fact if the reaction rate were mass transfer controlled, k would be equal to the overall mass transfer coefficient (k_{ov}) given by

$$1/k_{ov} = 1/k_m + 1/(k_s\ .\ L)$$

The sulphur removal rate during powder injection is the sum of the permanent contact reaction (reaction with top slag) and transitory reaction (direct reaction with injected powder during flotation).

$$-V_m\ \frac{dC_m}{dt} = Rate_p + Rate_t \qquad (5.1)$$

The desulphurization due to the permanent contact reaction is

$$Rate_p = A_p.k_{p\text{-}ov}\ (C_m - C_s/L) \qquad (5.2)$$

The above equation is the same as the general rate equation, but the slag volume is changing with time during powder injection.

Evaluation of the transitory reaction is carried out as follows. The desulphurization reaction on a powder particle, which is probably liquid phase trapped on a gas bubble during flotation in the metal bath, is expressed as

$$\frac{dC_{pow}}{d\tau} = (A_{pow}/V_{pow})\ k_{t\text{-}ov}\ (C_m - C_{pow}/L) \qquad (5.3)$$

where τ is the time since the powder particle discharged from the nozzle into the melt. The situation is shown in Figure 5.1. As the time required for rising of the powder (τ_e) is short compared with the total powder injection period, the concentration in metal phase C_m in Equation 5.3. can be regarded to be constant during flotation of the particular powder particle. Accordingly, assuming that the fresh powder contains no sulphur, the solution of Equation 5.3 becomes

$$C_{pow} = L.C_m\ (1 - \exp\ (-A_{pow}.k_{t\text{-}ov}.\tau/L.V_{pow})) \qquad (5.4)$$

At the metal/top-slag interface, where the powder particle is about to join the bulk phase of top slag (denoted by subscript e), the sulphur concentration in the powder particle is

$$C_{pow\text{-}e} = L.C_m.E \qquad (5.5)$$

where $E = 1 - \exp\ (-A_{pow}.k_{t\text{-}ov}.\tau_e/L.V_{pow}))$

or $E = 1 - \exp\ (-A_t.k_{t\text{-}ov}/(L.v_{in}))$ (5.6)

The parameter E represents an efficiency of the transitory reaction, namely, how close the transitory reaction can proceed to effective equilibrium with metal phase sulphur contents. As is seen from Equation 5.5, E = 1 means that sulphur equilibrium is achieved during flotation between the powder particle and the surrounding metal phase. As the rate of the transitory sulphur removal is a product of the powder injection rate and the sulphur content in the powder particle at the end of the flotation, it is given by

$$\text{Rate}_t = v_{in} \cdot C_{pow\text{-}e} \qquad (5.7)$$

The total sulphur removal rate due to both the permanent contact and transitory mechanisms is

$$-V_m \frac{dC_m}{dt} = A_p \cdot k_{p\text{-}ov} (C_m - C_s/L) + v_{in} \cdot C_{pow\text{-}e} \qquad (5.8)$$

where the second term of the right-hand side expresses the transitory reaction, and is effective only during powder injection, being null after that.

A sulphur balance between metal and slag gives

$$\left.\begin{aligned} &(C_o - C_m)\, V_m = C_s \cdot t' \cdot v_{in} \\ \text{where} \quad &t' = t \quad (0 \leq t \leq t_{in}) \\ &t' = t_{in} \quad (t_{in} \leq t) \end{aligned}\right\} \qquad (5.9)$$

where t_{in} is the powder injection period.

Provided that the rate constant for the permanent reactions ($A_p \cdot k_{p\text{-}ov}/V_m$) and the parameter for transitory reaction (E) are known under the given conditions, one can calculate the desulphu-

rization curve from Equations 5.5, 5.8 and 5.9 using a simple numerical scheme such as the finite difference method or numerical integration. The separate contribution of the permanent contact and transitory reactions can be evaluated from Equations 5.2 and 5.7.

On application of this mathematical model, the rate constant for the permanent contact reaction should be measured in reference experiments without the transitory reaction, such as powder feeding onto the metal surface with gas stirring, or it may be estimated from theoretical or empirical relations. Then, one can evaluate the parameter E for the transitory contact reaction by comparison of the model simulation with the experimental data obtained on the submerged powder injection operations (permanent contact plus transitory reactions), and the separate contribution of the reactions can be estimated from the model calculations.

5.3. Expressions using Dimensionless Groups

The equations are made dimensionless by using the following variables.

$x = C_s/(L.C_o)$; dimensionless concentration in slag phase

$y = C_m/C_o$; dimensionless concentration in metal phase

$A = \frac{k_{p\text{-}ov}.A_p}{V_m} \cdot \frac{V_m}{L.v_{in}}$; dimensionless rate constant for permanent c. reaction (product of the rate constant and reference time).

$= A_p.k_{p\text{-}ov}/(L.v_{in})$

$B = A_t.k_{t\text{-}ov}/(L.v_{in})$; dimensionless rate constant for transitory reaction.

$$= k_{t\text{-}ov} \cdot (A_{pow} \cdot \tau_e / V_{pow}) / L$$

$t^* = L.t.v_{in} / V_m$; dimensionless time, where

$$t_{ref} = V_m / (L.v_{in})$$

$$= t / t_{ref}$$

The sulphur removal rate (Equation 5.8) becomes

$$- \frac{dy}{dt^*} = A\,(y-x) + x_{pow\text{-}e} \qquad (5.10)$$

where $x_{pow\text{-}e} = E.y$ (during injection) (5.11)

E is given by

$$E = 1 - \exp(-B)$$

The mass balance (Equation 9) becomes

$$1 - y = t^{*\prime}.x \qquad (5.12)$$

where $t^{*\prime} = t^* \ (0 \leq t^* \leq t^*_{in})$

$t^{*\prime} = t^*_{in} \ (t^*_{in} \leq t^*)$

5.4. Sulphide Saturation in Slag Phase

Generally speaking, sulphide solubilities in slags are limited: for example, the CaS solubility in $CaO\text{-}Al_2O_3$ slag is 0.01~ 0.04 mole fraction[43]. Once the slag is saturated with a sulphide, the rate determining stage of the desulphurizazion will change (with for example precipitation of the pure sulphide) and the desulphurization will slow down or eventually stop. This effect plays an important part in the simulation of actual data obtained by experiments. Modifications of the model have been made to cope with the sulphide saturation. When the sulphur concentration exceeds the saturation

level, the rate constants are reduced by a factor of α . Incidentally, in the present work the term "sulphide saturation" is used for the operation of the lower rate constants.

Concerning the permanent contact reaction, the rate constant $k_{p\text{-}ov}$ was simply reduced to $\alpha \cdot k_{p\text{-}ov}$ when the sulphur contents in the top slag exceeded the saturation level:

$$\text{if} \quad C_s \geq C_{sat},\ k_{p\text{-}ov} \rightarrow \alpha \cdot k_{p\text{-}ov} \quad (\alpha = 0 \sim 1)$$

For the transitory reaction, the same manipulation was made:

$$\text{if} \quad C_{pow} \geq C_{sat},\ k_{t\text{-}ov} \rightarrow \alpha \cdot k_{t\text{-}ov}$$

The situation in the case of the transitory reaction is slightly complicated, being shown in Figure 5.2. In the early stage of the rise of a powder particle the rate constant has to be kept at $k_{t\text{-}ov}$, and Equation 5.4. is applied for the sulphur content of the powder particle, until it exceeds the saturation level:

$$0 \leq C_{pow} < C_{sat};\ C_{pow} = L.C_m \left(1 - \exp\left(-A_{pow}.k_{t\text{-}ov}.\tau/(L.V_{pow})\right)\right) \quad (5.4)$$

At the saturation point:

$$C_{pow} = C_{sat} = L.C_m \left(1 - \exp\left(-A_{pow}.k_{t\text{-}ov}.\tau_{sat}/(L.V_{pow})\right)\right.$$

When the sulphur contents exceeds the saturation level, reducing the rate constant to $\alpha.k_{t\text{-}ov}$, we obtain $C_{pow} > C_{sat}$:

$$C_{pow} = L.C_m + (C_{sat} - L.C_m) \times \left\{ \frac{\exp\left(-A_{pow}.k_{t\text{-}ov}.\tau/(L.V_{pow})\right)}{1 - C_{sat}/(L.C_m)} \right\}^{\alpha} \quad (5.13)$$

Hence, when the sulphide saturation occurs, the sulphur concentration of the powder particle at the end of its rise in the metal bath becomes

$$C_{pow\text{-}e} = L.C_m + (C_{sat} - L.C_m) \times \left\{ \frac{1 - E}{1 - C_{sat}/(L.C_m)} \right\}^{\alpha} \qquad (5.14)$$

where E is defined by Equation 5.6. Thus, under conditions where the sulphide saturation in a powder particle occurs, Equation 5.14 should be applied for the calculation of $C_{pow\text{-}e}$ instead of Equation 5.5.

In the dimensionless expressions, the calculations accompanying the sulphide saturation are as follows. If the sulphur content in the top slag exceeds the saturation level, the rate constant for the permanent contact reaction is reduced:

$$\text{if} \quad x \geq x_{sat}, \; A \rightarrow \alpha . \; A$$

When the saturation in a powder particle during its rise in the metal bath occurs, $x_{pow\text{-}e}$ can be expressed by Equation 5.15 instead of Equation 5.11.

$$\text{if } x_{pow} \geq x_{sat};$$

$$x_{pow\text{-}e} = y + (x_{sat} - y) \times \left\{ \frac{1 - E}{1 - x_{sat}/y} \right\}^{\alpha} \qquad (5.15)$$

where $E = 1 - \exp(-B)$

5.5. Calculations

Calculations using the dimensionless variables are carried out to show how the parameters of the transitory and permanent contact reactions affect the performance of a powder injection process and how the performance may be improved by varying the relative contributions of the two reactions.

From Equations 5.11 and 5.12 the desulphurization equation in dimensionless form (Equation 5.10) becomes

$$-\frac{dy}{dt^*} = A\,(y - (1-y) / t^{*\prime}) + E.y$$

Making use of a central-difference approximation between time steps of j and j + 1, the explicit expression for a new value of y is

$$y_{j+1} = ((1-G)\, y_j + A.\ \Delta t^*/t^{*\prime}) / (1+G) \qquad (5.16)$$

where G is defined by

$$G = (A\,(1+1/t^{*\prime}) + E)\ \Delta t^*/2 \qquad (5.17)$$

and where y_{j+1} and y_j are respectively y values at the time steps of j+1 and j, and Δt^* is the time intervals. Thereby, the desulphurization curves can be computed using this very simple numerical scheme. The time intervals used for the calculation were between 0.002 and 0.01 in dimensionless time.

5.6. Results and Discussion form Dimensionless Calculations

An example of the dimensionless calculations is shown in Figure 5.3. under conditions of A = 0.4, E = 0.08, t^*_{in} = 6. Dimensionless sulphur concentrations in the metal and top slag phases are shown there, and the broken line shows an imaginary effective equilibrium curve, from the sulphur balance between the metal and top slag phases, i.e. the concentration curve in the case of an infinite rate constant for the permanent reaction. The separate contributions of the transitory and permanent contact reactions are also indicated in the top part of the figure.

The sulphur removal rate of the two reactions respectively decreases with time. As the desulphurization rate owing to the permanent contact reaction decreases more quickly, the relative contribution of the transitory reactions increases during the powder injection process. This arises because the sulphur concentration in the top slag approaches the equilibrium with time, and the driving force for the permanent contact reaction becomes very small at the last stage of the powder injection. On the other hand the transitory reaction retains a significant sulphur removal driving force even at the last stage, because fresh powder, which contains no sulphur, is continuously fed for the transitory reaction.

Figure 5.4. shows another example of the calculations under similar conditions to those of Figure 5.3, but the rate constant for the transitory reaction was made high (E = 0.4). In this case an excess sulphur removal occurs, due to the transitory reaction, the metal phase concentration becoming lower than that of the imaginary equilibrium curve after 2.7 in dimensionless time. As is seen from the top part of the figure, the permanent contact reaction after the dimensionless time 2.7 acts as a reversion reaction rather than desulphurization, and after the end of the powder injection the reversion of sulphur from the top slag phase to the metal continues. This sort of reversion or excess desulphurization as a result of the significant transitory reactions has been suggested from experimental[31,32] and theoretical[27,28] work, but none of these papers solved the problem quantitatively. Given sufficient data for the kinetics, the present model allows

calculation of the separate contributions of the two reactions, and gives quantitative results for the excess desulphurization during powder injection and the reversion after the end of powder injection.

If, in industrial practice, the powder injection operation is accompanied by a significant excess desulphurization such as shown in Figure 5.4, the permanent contact reaction causes sulphur reversion after the end of the powder injection. In order to minimize this reversion, it would be helpful to stop gas stirring at the same time as powder injection. Deslagging immediately after the end of the powder injection would also be very effective. On the other hand, if there is no excess desulphurization, e.g. Figure 5.3., the permanent reaction helps sulphur removal, so that gas stirring after powder injection is useful to achieve further desulphurization.

When studying the various figures readers should bear in mind that typical values for A and E are 0.5 and 0.2 respectively. The effect of the transitory reaction parameter E with a constant permanent contact reaction rate is shown in Figure 5.5. With increase in E, the performance of the powder injection process is improved. In the cases of large E values the excess desulphurization owing to the transitory reaction is clearly seen, and is followed by a sulphur reversion after the powder injection.

Effects of the rate parameter for permanent contact reaction A are shown in Figures 5.6, 5.7 and 5.8. Figure 5.6 simulates a case of powder feeding onto the surface without transitory reaction. It is seen from the figure that with a value of A = 0.4

the permanent contact reaction itself can perform the desulphurization pretty well even without the aid of the transitory reaction. Figure 5.7 shows the effect of A when the transitory reaction parameter E is 0.1. This is the behaviour to be expected in an actual powder injection process. Figure 5.8A shows the results in the case of a large transitory reaction parameter (E = 0.6). With excess desulphurization the permanent contact reaction causes the reversion of sulphur, so that small values of A give better performance. However, it is noted that even in cases where the excess desulphurization occurs, the permanent contact reaction enhances the sulphur removal during the early stages of the powder injection. Figure 5.8B describes the early stage of the desulphurization curves shown in Figure 5.8A using inclined co-ordinates, and the points where excess desulphurization first occurs (intersection between each curve and the imaginary equilibrium curve) are indicated by arrows in the figure. With the aid of the permanent contact reaction the excess desulphurization begins earlier in the case of a large value of A. The permanent contact reaction then turns to the reversion reaction, reducing the total sulphur removal rate.

Figure 5.9 shows iso-sulphur-removal contours on an A-E map at the end of the powder injection period $t^*_{in} = 6$. The equilibrium value for the sulphur removal efficiency is 85.7%, and a higher efficiency means the occurrence of excess desulphurization. As is seen from the figure, large E values (over 0.16 in case of $t^*_{in} = 6$) are necessary for the occurrence of excess desulphurization. A rapid permanent contact reaction is rather harmful for sulphur removal at large E, while an increase in A improves the sulphur removal for small E, especially in the case of both small A and E. At

large A the boundary between excess desulphurization and no excess occurs at a roughly constant value of E.

Figure 5.10 shows how the powder injection rate (or injection period) affects the performance of the powder injection operation for a constant total amount of powder. In the figure the abscissa is denoted in terms of real time, because the dimensionless time scale changes with the injection rate. The calculation conditions are given in Table 5.1, together with the minimum concentration achieved (y_{min}). It is seen that y_{min} is halved by reducing the powder injection period by eight. This improvement in performance is due to the increase in the relative contribution of the transitory reaction.

5.7. Experimental

Experiments on the desulphurization of molten cast iron were carried out using 60% CaO - 20% CaF_2 - 20% Al_2O_3 premelted powder. The experimental apparatus and procedure used were described in Chapter 4. The depth of immersion of the lance was 4 cm. The experimental temperature was 1310°C.

1) Experimental results

Figure 5.11 shows the desulphurization curve obtained by a powder injection experiment Run 13. In this experiment, 104g of powder was injected in 16 min, and gas stirring was continued after the powder injection. As is seen from the figure, the sulphur content in the metal phase decreased linearly in the early stage of the powder injection, which suggested the occurrence of sulphide saturation in the top slag. Figure 5.12 shows the sulphur concen-

trations in the top slag, which were calculated from the metal phase concentration. In the figure, results from simple powder dumping experiments Runs 10 and 11 are also shown. 50g of powder was dumped onto the surface of the molten cast iron in these runs. It is seen that the sulphide saturation level was about 3.3 weight % in the present case.

2) Rate constant for permanent contact reaction

Kinetic data for the permanent contact reaction are necessary to make use of the present model, and powder dumping experiments with gas stirring only were carried out.

Sufficient powder was added in bulk to avoid any likelihood of sulphide saturation. This type of test allows the value of K_p to be accurately estimated even if it has a high value, since the limiting case of infinite K_p would lead to an immediate drop in the metal sulphur concentration to the steady state value. Any finite value of K_p can be easily distinguished from this extreme condition. In fact the experiments did give a good estimate of the K_p value. This fact will be important later in this paper.

The desulphurization rate constant under the condition of constant slag amount can be evaluated from the following equations;

$$- \frac{d\,[\%S]}{dt} = K_p \left([\%S] - (\%S)/L_{wt} \right)$$

where $$K_p = A_p . k_{p\text{-}wt} / V_m$$

The solution of the above equation is

$$- \frac{1}{1 + W_m/(L_{wt} . W_s)} \ln \left(\frac{[\%S] - [\%S]_\infty}{[\%S]_o - [\%S]_\infty} \right) = K_p . t \qquad (5.18)$$

Figure 5.13 shows the results of the powder dumping Runs 25 and 14. In Run 14 the gas flow rate was low from 300s to 420s because of nozzle clogging, and there was no gas stirring from 420s to 600s while the gas injection nozzle was being changed. Figure 5.14 shows the plot of Equation 5.18, where the data used from Run 14 are only for the first 300s. The solid line in the figure gives a mean rate constant of K_p = 0.0028/s. A close observation of the data suggests a high K_p value in the early stages, decreasing during desulphurization. It is reported that the vigorous desulphurization reaction causes a significant decrease in the interfacial tension[44] and that an abnormal ripple at the slag/metal interface occurs during vigorous desulphurization reaction[45]. These phenomena may increase both A_p and K_p . Taking account of the difference in metal mass between Runs 13 and 25, a constant value of K_p = 0.003/s was adopted for the simulation of the powder injection experiment Run 13. The use of a constant mean value of K_p is not thought to lead to any significant error in the present case. The high initial rate constant in an experiment when fresh powder is added all at once to metal, giving a high driving force, would not be expected to apply to the permanent contact reaction where the driving force for reaction is relatively low.

5.8. Simulation of Experimental Data

For convenience in the application of the present model, the equations were modified using mass-based concentrations such as weight percents.

The sulphur removal rate (Equation 5.8) becomes

$$-\frac{d\,[\%S]}{dt} = K_p\,(\,[\%S] - (\%S)/L_{wt}) + P_{in}\cdot(\%S)_{pow\text{-}e}/W_m \qquad (5.19)$$

where $K_p = A_p \cdot k_{p\text{-}wt}/V_m$

and $1/k_{p\text{-}wt} = 1/k_m + \rho_m/(\rho_s \cdot k_s \cdot L_{wt})$

L_{wt} is the sulphur partition coefficient in mass based concentration at the steady state ($(\%S)_\infty$ / $[\%S]_\infty$), and P_{in} is the powder injection rate in mass/time. Sulphur concentration of a powder particle which is about to join the top slag $(\%S)_{pow\text{-}e}$ is given by

$(\%S)_{pow\text{-}e} < (\%S)_{sat}$ (no saturation):

$$(\%S)_{pow\text{-}e} = E \cdot L_{wt} \cdot [\%S]$$

or $(\%S)_{pow\text{-}e} \geq (\%S)_{sat}$ (sulphide saturation):

$$(\%S)_{pow\text{-}e} = L_{wt} \cdot [\%S] + ((\%S)_{sat} - L_{wt} \cdot [\%S])\ x \left\{ \frac{1 - E}{1 - (\%S)_{sat}/(L_{wt} \cdot [\%S])} \right\}^{\alpha}$$

where $E = 1 - \exp\,(-A_{pow} \cdot k_{t\text{-}wt} \cdot \tau_e/(L_{wt} \cdot V_{pow}))$

or $E = 1 - \exp\,(-A_t \cdot k_{t\text{-}wt}/(L_{wt} \cdot v_{in}))$ (5.20)

and $1/k_{t\text{-}wt} = \rho_s/(\rho_m \cdot k_{t\text{-}m}) + 1/(k_{t\text{-}s} \cdot L_{wt})$

The above expression for E is exactly equivalent to Equation 5.6.

When sulphide saturation occurs in the top slag phase, the rate constant for the permanent contact reaction is reduced to $\alpha.k_{p\text{-}wt}$ in the same manner as described before:

if $(\%S) \geq (\%S)_{sat}$, $k_{p\text{-}wt} \rightarrow \alpha.k_{p\text{-}wt}$

The mass balance equation is

$$(\%S) = ([\%S]_o - [\%S]) W_m/W_s \qquad (5.21)$$

where $W_s = P_{in}.t$ ($0 \leqslant t \leqslant t_{in}$, during powder injection)

$W_s = P_{in}.t_{in}$ ($t_{in} \leqslant t$, after powder injection)

The powder injection experiment (Run 13) was simulated by the present model expressed in terms of weight percent. The rate constant K_p = 0.003/s was adopted for the permanent contact reaction, as mentioned in the previous section. Calculations were made with different values of the transitory reaction parameter E. Figure 5.15 shows the results when ignoring the sulphide saturation in slag, where none of the calculated lines fit the experimental data. The experimental result shows a slower and more linear decrease in sulphur content in the early stage . Therefore the model taking account of sulphide saturation in slag was applied. Figure 5.16 shows the results, giving linear lines in the early stage of the injection as a consequence of sulphide saturation. The value of the rate reduction factor α used is 0.1, which was chosen arbitrarily. However, the selection of the rate reduction factor in the range of 0.0~0.15 did not show any significant change in the results. As is seen in the figure, the experimental data show good agreement with the simulation curve for K_p = 0.003/s and E = 0.14. Therefore the value of the transitory reaction parameter in the present powder injection experiment was deduced to be E = 0.14.

However the model indicates that the results are only sensitive to changes in the value of E towards the end of the reaction. The occurrence of sulphide saturation makes it difficult to determine the relative contributions of the permanent contact and transitory reactions. If the reaction continues forward after powder injection and with continued gas agitation then the value of E must have been low and transitory reaction relatively unimportant. If reversion of sulphur occurs then the value of E must have been high. Of course care must be taken to ensure that any sulphur reversion observed is not a "chemical" reversion. This latter type of reversion is caused by a decrease in the effective partition coefficient, as a result of aluminium "fade" or other increase in the oxygen potential.

In order to minimise the adverse effect of sulphide saturation in any attempt to determine the relative importance of the permanent and transitory contact reactions, it might appear that experiments should be performed with higher values of powder consumption per unit mass of liquid metal. In fact this is not very helpful because sulphide saturation will still occur in the early stages and it will cease to be a factor only at the low sulphur levels occurring towards the end of reaction. A better approach for avoiding sulphide saturation in experimental heats would be to start with low sulphur levels in the metal.

Figure 5.17 shows the detailed results obtained from the simulation of Run 13 using E = 0.14. It is seen from the figure that up to 420s the top slag phase is saturated with sulphide and the sulphur concentration in metal phase decreases linearly. The

separate contributions of the two reactions are shown in the top part of the figure. The desulphurization rate owing to the permanent contact reaction increases with time, while sulphide saturation occurs in the top slag phase, and thereafter shows a relatively rapid decrease with time. On the other hand, the transitory reaction rate decreases monotonously, as the sulphur content in the powder particles does not ever exceed the saturation level in this case. In fact the maximum sulphur concentration in the powder particles was 2.2%.

5.9. Discussion

1) Transitory and permanent contact reactions on CaO-based powder injection.

It is of great interest to clarify whether the transitory reaction or the permanent contact reaction play the major role in powder injection processes, but agreement in the literature has not been achieved so far. Limiting the problem to CaO-based powder injection, opinions are also divided. Turunen[30] showed an effect of injection lance depth on desulphurization using $CaO-CaF_2$ powder, and this suggests a large contribution by the transitory reaction. Ritakallio[31] explained that the apparently very high sulphur distributions of over 3000 obtained by Gruner et al[46] during $CaO-CaF_2$ powder injection were due to the effect of the transitory reaction. Brotzmann and Papamantellos[32] reported that the achievement of lower phosphorous and sulphur contents than those predicted from the supposed equilibrium values on the OBM converter was because of the transitory reaction. Tanaka et al[33] deduced that the transitory reaction was more important than the permanent

contact reaction, from a comparison of the submerged injection and gas stirring experiments with a theoretical model. On the other hand, Wada et al[34] concluded that the permanent contact reaction during flux injection was more important than the transitory reaction, because the desulphurization behaviour was largely influenced by the properties and composition of the top slag, and because the characteristics of the injection powders scarcely affected the results. Tanabe et al[35a-35c] reported that the permanent contact reaction dominated the desulphurization process, and they developed a process on an industrial plant making use of the top slag reaction without submerged powder injection, because the desulphurization performance using only top slag with gas stirring was by no means inferior to the $CaO-CaF_2-Al_2O_3$ powder injection process.

These inconsistencies have arisen because of lack of quantitative evaluations on the separate contributions of the transitory and permanent contact reactions. This work has provided a method to evaluate them clearly. In the case of the present small scale experiment Run 13, the contributions of the two reactions were roughly equal, and have already been shown in detail in Figure 5.17. Under similar conditions of gas stirring, powder addition etc, it is still true that the permanent contact reaction only, without the aid of transitory reaction, can perform the desulphurization pretty well, as is seen from Figure 5.6. An example is given by Run 13 where the A value was 0.53.

In general the contribution of the transitory reaction is probably equal to or greater than that of the permanent contact

reaction, though the effective equilibrium sulphur content is settled by the permanent contact reaction, and though desulphurization using CaO-based fluxes can be sufficiently performed without any transitory reaction in most cases. The sequence of the desulphurization reaction during powder injection is such that, once molten, the injected powder containing no sulphur first removes sulphur from the metal phase by means of the transitory reaction. Secondly the top slag, which already contains some sulphur carried in by the transitory process, can react and finally achieve the effective equilibrium state by the permanent contact reaction. Therefore the permanent contact reaction is considerably suppressed under the existence of a significant transitory reaction. From these considerations, it is understandable that different conclusions were deduced in previous work on powder injection. The present calculation model will be very useful in the evaluation of the separate contributions of the two reactions and in the clarification of the reaction mechanism of the powder injection process.

2) Scale-up

Generally speaking, the contribution of the permanent contact reaction may be larger for small scale practice, because the smaller the scale the larger the specific area. Robertson and Staples[49] carried out model studies on mass transfer across a metal/slag interface stirred by bubbles using amalgam/aqueous and lead/molten salt systems, and derived that the mass transfer coefficient $k_{p\text{-}ov}$ was proportional to $V_g^{0.5}/d$ where d is the ladle diameter. On the industrial gas injection practices Usui et al[50] deduced an

empirical relation $k_{p\text{-}ov} \propto \varepsilon/A_p$ where ε was total input energy for stirring. ($k_{p\text{-}ov}$ value in Usui's relation is calculated using a nominal interfacial area). Robertson and Staples' correlation predicts that the rate constant k_p ($= A_p.k_{p\text{-}ov}/V_m$) decreases with scale-up under geometric similarity and constant gas injection rate per unit volume of metal ($K_p \propto d^{-0.5}$). On the other hand Usui's empirical relation gives an increase in K_p with scale-up under the same conditions ($K_p \propto \varepsilon / V_m$), because the total stirring energy is not only proportional to the gas flow rate, but also depends on the depth of injection. Thus the predictions of Robertson and Usui are inconsistent, and further investigations seem to be necessary to estimate the scale-up effect.

It should be emphasised that the desulphurization processes using top slag ($CaO\text{-}SiO_2\text{-}Al_2O_3$)[35a-35c] or solid desulphurizer (CaC_2)[51] dumped onto the metal bath with intense gas stirring show good performance in industrial practice. Therefore the rate constant for permanent contact reaction in industrial injection practices must be large enough to perform a substantial sulphur removal during the injection period. In fact a large overall mass transfer coefficient $k_{p\text{-}ov}$ = 0.24 ~0.46 cm/s was measured on 250 ton ladle desulphurization process using top slag with intense gas stirring[35b]. This large $k_{p\text{-}ov}$ value, calculated using the nominal area, probably includes an effect of an increase in the effective reaction area by the formation of an emulsion close to the slag/metal interface where gas bubbles agitate it and by the entrainment of slag particles in the metal flow as a consequence of the intense bath stirring. Using the $k_{p\text{-}ov}$ of 0.24 ~0.46 cm/s

on the full scale, the K_p value is estimated to be 0.0007~ 0.0013/s, which is comparable to the value K_p = 0.003/s obtained from the present laboratory experiments, despite the large difference in their scales.

3) Comparison of powder injection and dumping

As mentioned earlier, Tanabe et al[35a-35c] showed that the desulphurization performance using only top slag and gas stirring was by no means inferior to powder injection processes. The present model can easily cope with the simulations on such a powder dumping process by a minor modification of the mass balance equations.

Figure 5.18 shows the desulphurization curves simulated for the powder injection process Run 13, for powder dumping in the beginning and for the case where half the powder is dumped in the beginning and the other half is injected. The calculation conditions were based on those of Run 13, and in all cases the same mixing intensity, namely the same rate constant for the permanent contact reaction, was used.

As is seen from the figure, the cases where all or half of the powder is dumped in the beginning show rapid desulphurization in the early stages. This is because in these cases sufficient slag exists from the beginning so that sulphide saturation in the top slag can be successfully avoided.

The desulphurization rate for the powder injection only is small in the early stages but relatively large in the later stages and therefore the final performance is narrowly better than that for the full powder dumping simulation. The case of half dumping

and half injection shows the best performance, making the most of both the transitory and permanent contact reactions. Though the performances of the three cases are almost the same after 960s, the desulphurization rate in the early stage can be improved by addition of the powdered flux to the top slag in the beginning.

This kind of simulation will be helpful in improving the efficiency of powder injection operations by such means as the reduction of the treatment time. This would be especially useful in any cases where the available powder injection is limited by the need to avoid slopping or a limitation in the equipment installed.

4) Comparison of the rate constant of the transitory reaction with Engh's theory.

Making use of the present model calculations, one can make reliable evaluations of the experimental rate parameter for the transitory reaction, and it is interesting to compare this with a theoretical prediction.

The model proposed by Engh et al[23] is thought to be applicable to the present experimental conditions (fine powdered flux injection). In their model the injected powder was assumed not to penetrate into the melt, but to cover the whole surface of the gas bubbles. Engh gave the total interfacial area available for the transitory reaction as

$$A_t = 3 \cdot V_g \cdot \Omega \cdot H/(r.v_b)$$

where the bubble radius r and its rising velocity v_b were expressed by

$$r = 12. \sigma/(\rho_m \cdot f \cdot v_b^2)$$

$$v_b = (4.\sigma.\ g/(f.\rho_m))^{0.25}$$

Engh estimated the mass transfer coefficient in the metal phase as

$$k_m = (8.\ D.\ v_b/(\pi.r))^{0.5}$$

These equations yield the following results in terms of the independent variables

$$r = 6\ (\sigma/(\rho_m.f.g))^{0.5}$$

$$k_m = 0.77.D^{0.5}\ (f.\rho_m.g^3/\sigma)^{0.125}$$

$$A_t.k_m = 0.27.D^{0.5}\ (f.\rho_m/\sigma)^{7/8}.g^{3/8}.V_g.\Omega.H$$

Assuming that the transfer resistance in the slag film is negligible (because of the high L values)

$$k_{t\text{-}ov} = k_m$$

Engh's model has been applied to the present case. Using $V_g = 660 cm^3/s$ at 1310^oC, H = 4cm, σ= 1400 dyne/cm, $\rho_m = 7 g/cm^3$ and $D = 10^{-5} cm^2/s$ (Diffusivity was estimated from compiled data[47] by extrapolation to 1310^oC), and also applying the values used by Engh, namely Ω = 1.5 and f = 0.5, we obtain

$$A_t = 88 cm^2,\ k_{t\text{-}ov} = 0.015 cm/s \text{ and } A_t.k_{t\text{-}ov} = 1.3 cm^3/s$$

On the other hand, the parameter for the transitory reaction was deduced from experiment as E = 0.14. From Equations 5.6 or 5.20 , we then obtain

$$A_t.k_{t\text{-}ov}/(L.v_{in}) = A_t.k_{t\text{-}wt}/(L_{wt}.v_{in}) = 0.151$$

Using L = 80 (L_{wt} = 186) and $v_{in} = 0.036\ cm^3/s$, the product of the reaction area and the rate constant is given by

$$A_t.k_{t\text{-}ov} = 0.43\ cm^3/s$$

The value estimated from Engh's theory of $1.3cm^3/s$ is three times as large as that deduced from the present experiment. This is not a bad agreement, taking into account the uncertainty of both Engh's theory and the experiment. However, when applying Engh's theory, the injection depth H was taken as 4cm, which is the submerged depth of the injection lance. The effective depth for bubble rising may be slightly larger on account of jet penetration into the melt.

A possible explanation of the large value from Engh's theory is as follows. He assumed that the slag film covered the whole surface of the gas bubbles. However, it is known that bubbles of equivalent diameter greater than 2cm rising through molten metal show spherical-cap shape. Conochie[48], using the open-top bubble technique, found that the slag existed only on the base of a spherical-cap bubble. Because the top surface of the rising bubble is always swept with metal flow, it is unlikely that the slag film remains there. The two possible situations are shown in Figure 5.19. This correction reduces the reaction interfacial area A_t in Engh's model by 1/2 or 1/3, and gives much better agreement with experiment.

Another interesting result from Engh's model relates to the importance of the transitory reaction at larger scales. For equal E values at any scale Equation 5.6 shows that $A_t.k_{t-ov}/(L.v_{in})$ must be constant. Using the $A_t.k_m$ formula predicted by Engh (and omitting all the terms independent of scale) equality in $A_t.k_{t-ov}/L.v_{in}$ is achieved when $V_g.H/v_{in}$ is constant.

5.10. Concluding Remarks

In the present work, a model has been presented which shows clearly the important factors affecting the kinetics of refining using submerged injection as in the case of CaO-based powder injection to desulphurize molten iron. Given adequate experimental data, the model allows the calculation of the separate contributions of the transitory and permanent contact reactions, and enables one to make quantitative evaluations of the excess desulphurization and the reversion of sulphur. Allowance has been made for a decrease in the effective rate constant, once the slag is saturated with sulphides. This allowance plays an important role in the simulation of the experimental data.

The model was applied to simulate the data from small scale powder injection experiments. The contributions of the transitory and permanent contact reactions were roughly equal in the injection experiment discussed. Comments were made on the contributions of the two reactions using CaO-based powder injection and on the comparison of submerged powder injection and dumping. A comparison of the measured rate constant of the transitory reaction with Engh's theory was made, and correction of the reaction area gave good agreement between theory and experiment. The present model will be useful in improving the efficiency of the powder injection process and to elucidate its reaction mechanisms.

List of Symbols. Chapter 5.

A	area or dimensionless rate constant for permanent contact reaction.
A_p	reaction area for permanent contact reaction.
A_{pow}	transitory reaction area for a powder particle.
A_t	total reaction area for transitory contact reaction.
B	dimensionless rate constant for transitory contact reaction.
C	volume-based concentration (mole/volume).
C_{pow}	volume-based concentration in a powder particle.
D	diffusivity of sulphur in molten iron.
d	cell diameter of reaction vessel.
E	parameter for transitory reaction defined by Equations 5.6 or 5.20.
f	friction factor for rise of gas bubble.
G	defined by Equation 5.17.
g	acceleration of gravity.
H	immersion depth of lance.
J	flux density of sulphur.
k	rate constant.
k_{ov}	overall mass transfer rate constant in volume-based concentration.
K_p	$= A_p.k_{p\text{-}wt}/V_m$.
L	partition coefficient in volume-based concentration.
L_{wt}	partition coefficient in mass-based concentration.
P_{in}	powder injection rate in weight/time.
r	equivalent bubble radius.
(%S)	sulphur content in slag phase by weight percent.
[%S]	sulphur content in metal phase by weight percent.

t	time.
t^*	dimensionless time.
$t', t^{*'}$	defined by Equations 5.9 and 5.12 respectively.
t_{in}	powder injection period.
Δt	time interval of finite difference method.
V	volume.
v_b	bubble velocity.
V_g	flow rate of injection gas.
v_{in}	powder injection rate in volume.
V_{pow}	volume of a powder particle.
W	weight.
x	dimensionless concentration in slag phase.
y	dimensionless concentration in metal phase.

Greek

α	reduction factor of rate constant when sulphide saturation occurs.
ε	total energy input for stirring.
ρ	density.
σ	surface tension of metal.
τ	time proceeding for a powder particle discharged from nozzle.
Ω	shape factor of gas bubble (surface area of bubble/surface area of equivalent sphere).

Subscripts

e	end of rise of a powder particle in metal bath.
g	injection gas.
in	powder injection.

j time step of finite difference method.

m metal phase.

min minimum concentration.

ov overall.

p permanent contact reaction.

pow powder.

ref reference time.

s slag phase.

sat sulphide saturation in slag.

t transitory reaction.

wt in terms of mass-based concentration (e.g. wt %).

o initial.

∞ at equilibrium state.

TABLE 5.1

Calculation conditions for Fig 5.10 and minimum sulphur concentration

	v_{in} (cm^3/s)	t_{in} (s)	total powder $v_i \times t_{in}$ (cm^3)	t^*_{in}	A	E	y_{min}
a	1/2	1600	800	6	0.8	0.6	0.098
b	1	800	800	6	0.4	0.6	0.077
c	2	400	800	6	0.2	0.6	0.058
d	4	200	800	6	0.1	0.6	0.045

$$A_p.k_{p\text{-}ov}/L = 0.4\ cm^3/s$$

$$V_m/L = 133.3\ cm^3$$

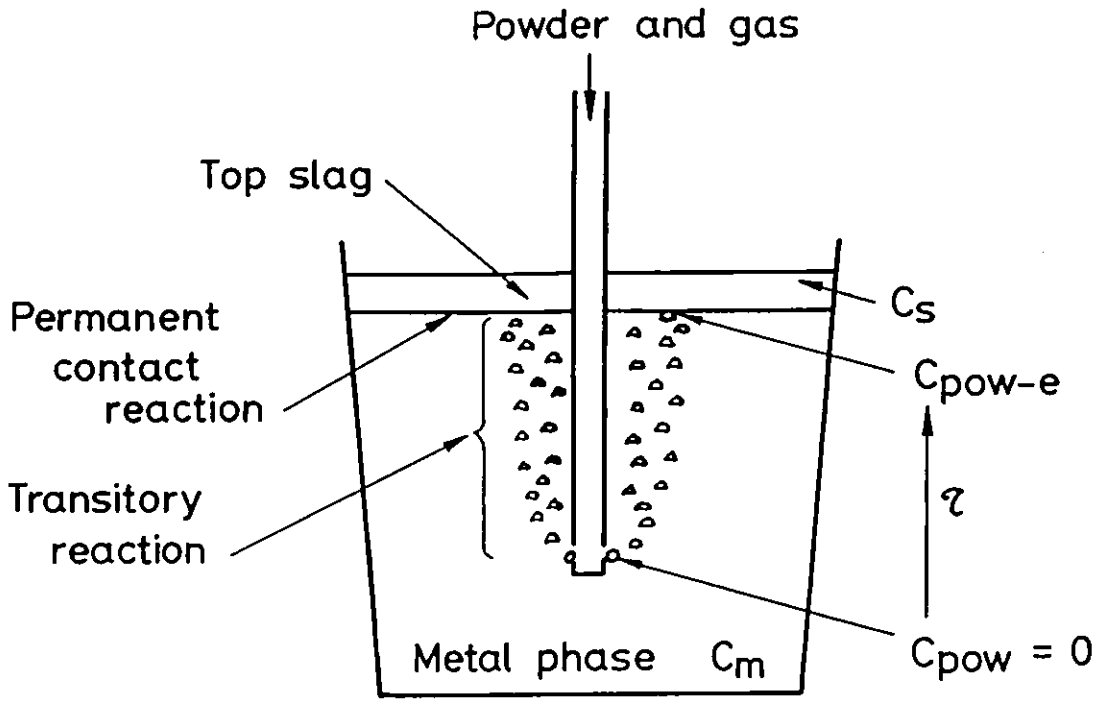

Fig.5.1. Schematic diagram of reaction sites during powder injection refining.

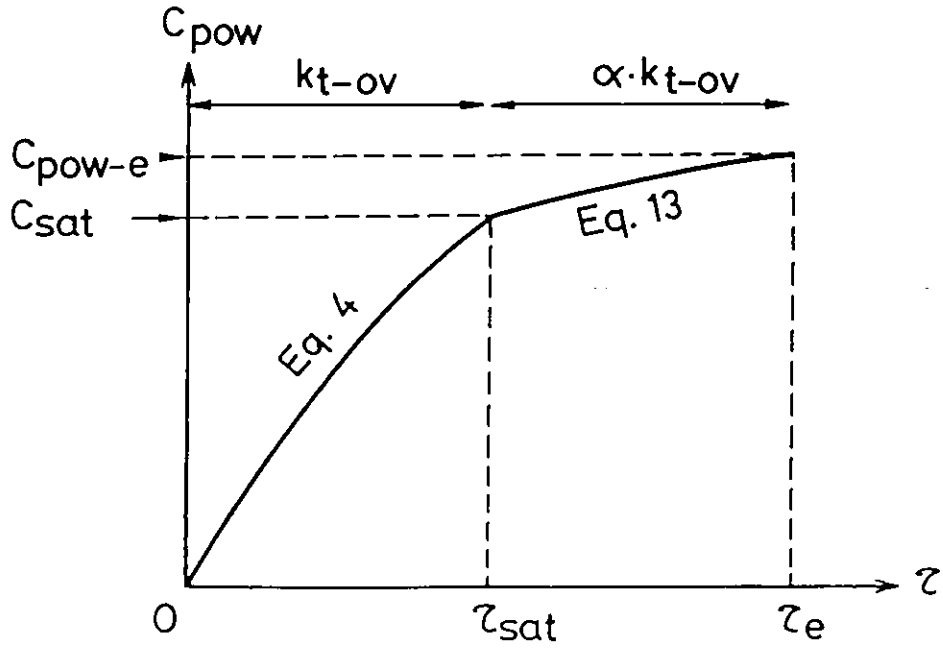

Fig.5.2. Sulphur concentration change of powder particle during rise in metal bath when sulphide saturation occurs.

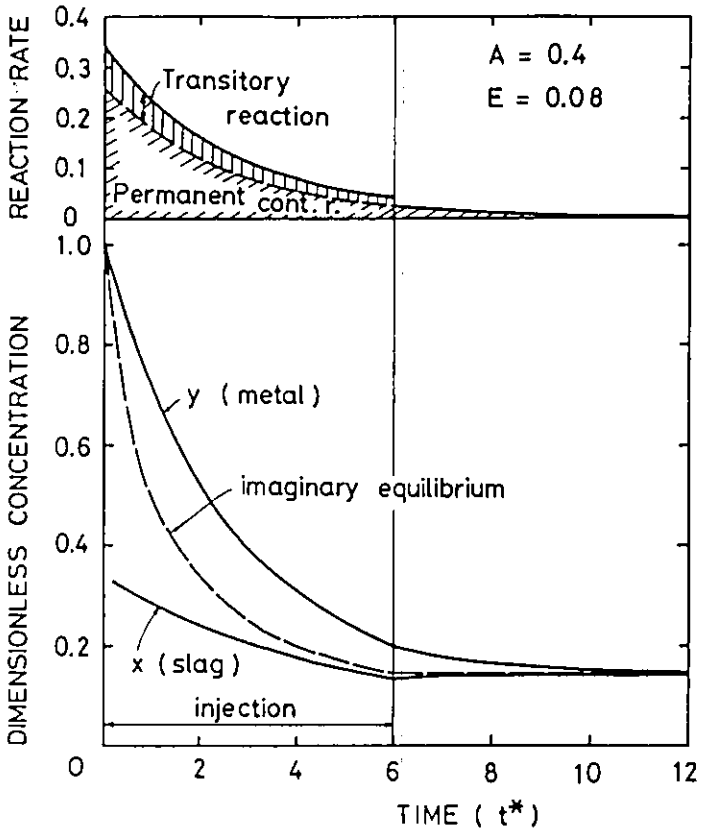

Fig.5.3. An example of dimensionless calculations (A = 0.4, E = 0.08).

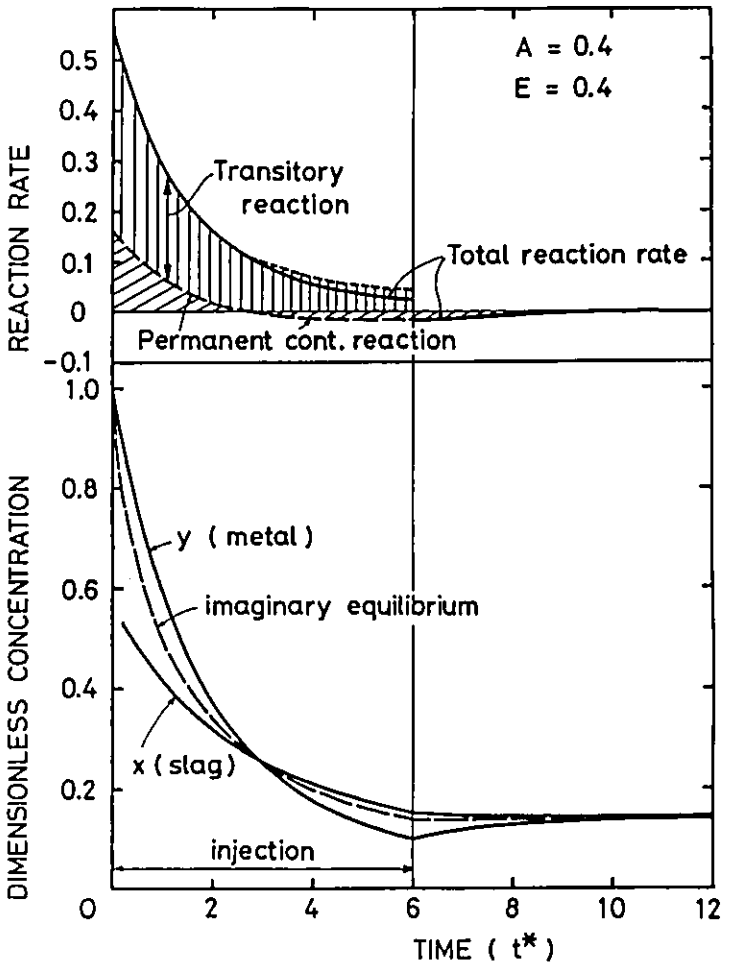

Fig.5.4. An example of dimensionless calculations under the condition where excess reaction occurs (A = 0.4, E = 0.4).

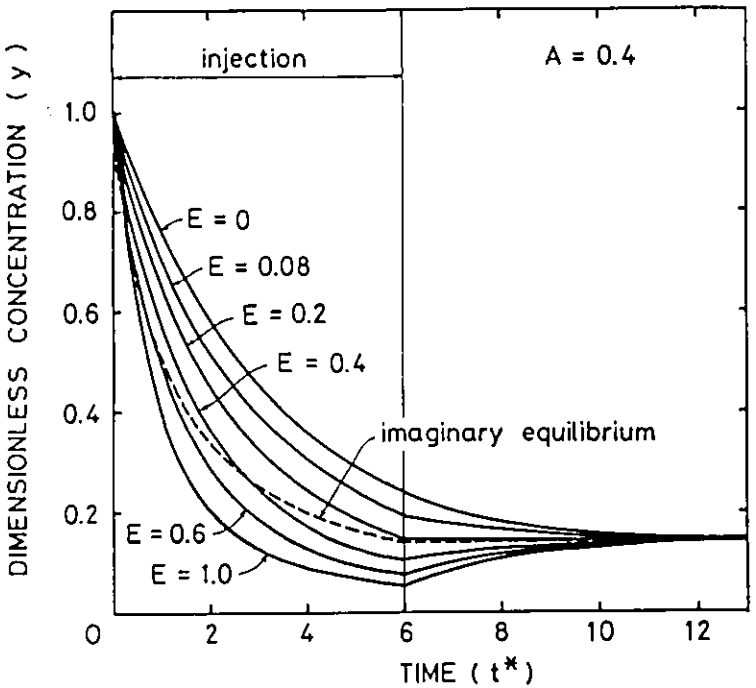

Fig.5.5. Effect of transitory reaction parameter E under a constant permanent contact reaction rate parameter (A = 0.4).

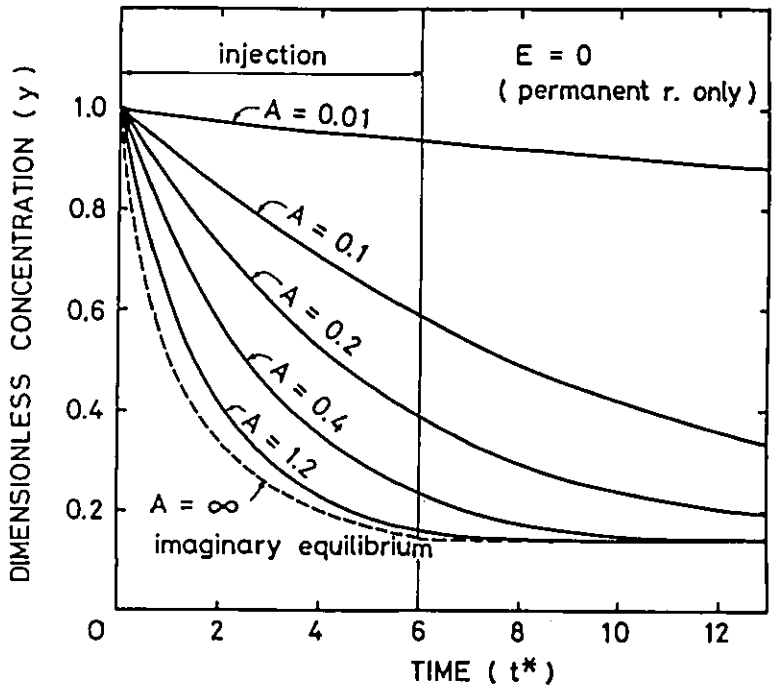

Fig.5.6. Effect of the rate parameter A for permanent contact reaction under the condition where powder is fed constantly without transitory reaction (E = 0).

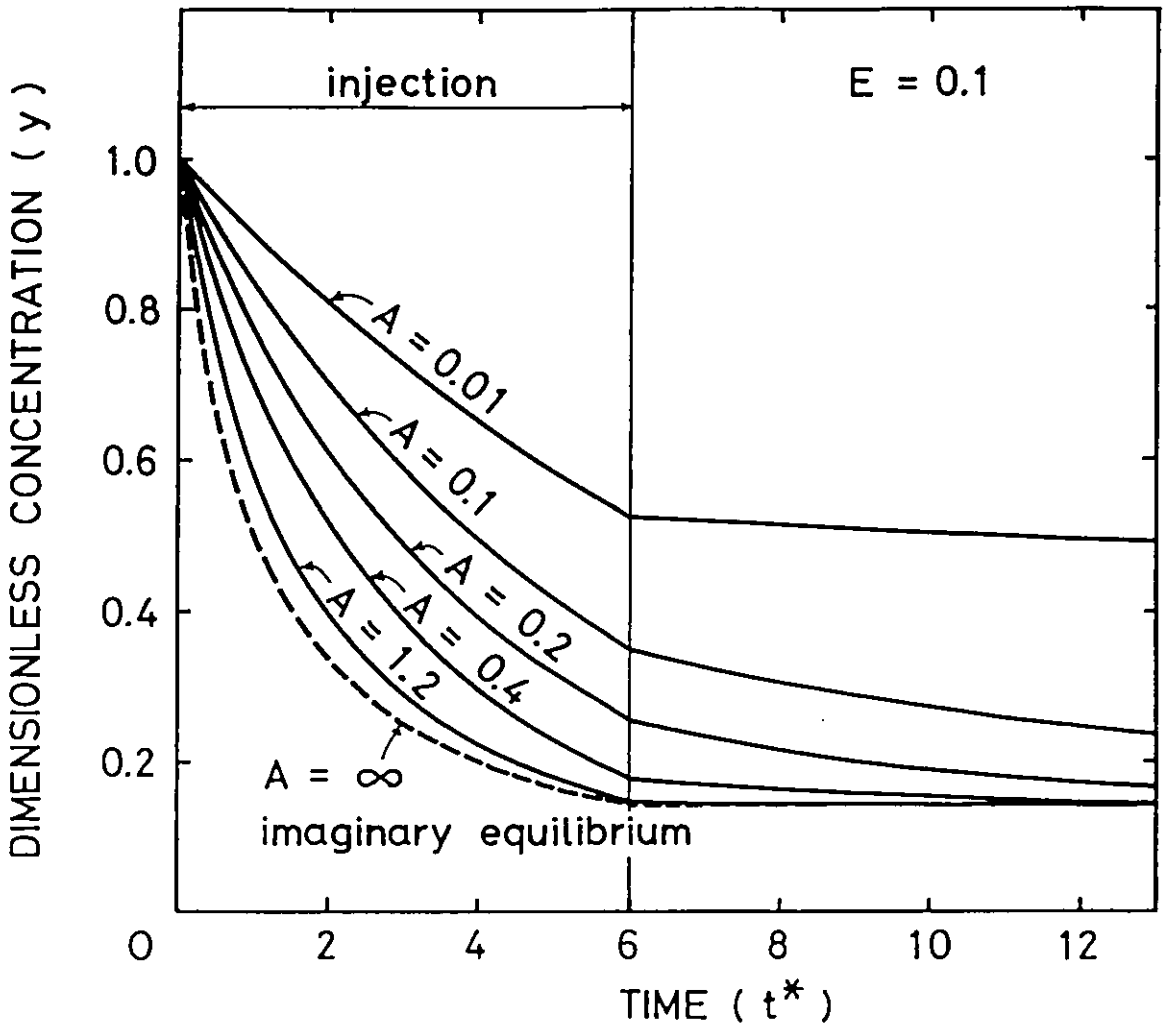

Fig.5.7. Effect of the rate parameter A for permanent contact reaction with transitory reaction (E = 0.1). No excess desulphurization occurs.

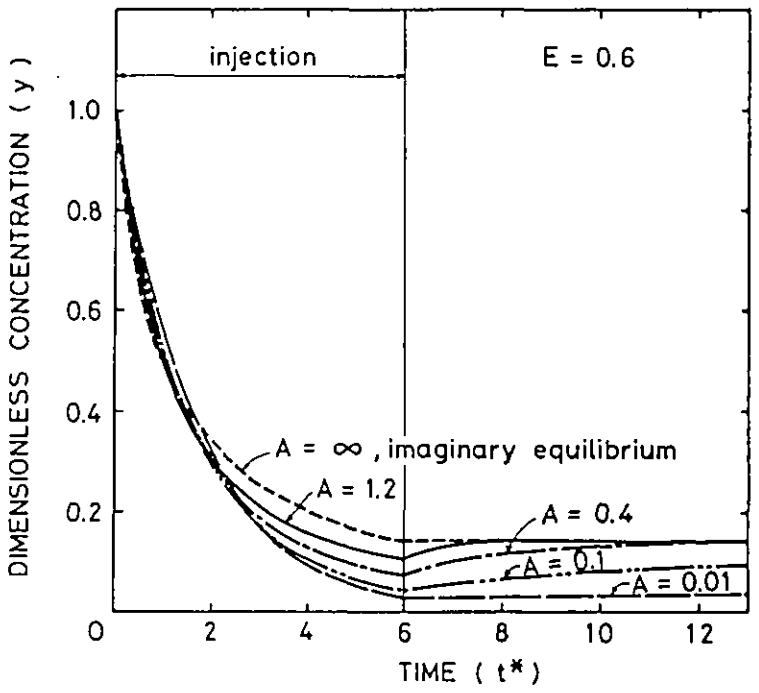

Fig.5.8A. Effect of the rate parameter A for permanent contact reaction under a condition where excess desulphurization occurs (E = 0.6).

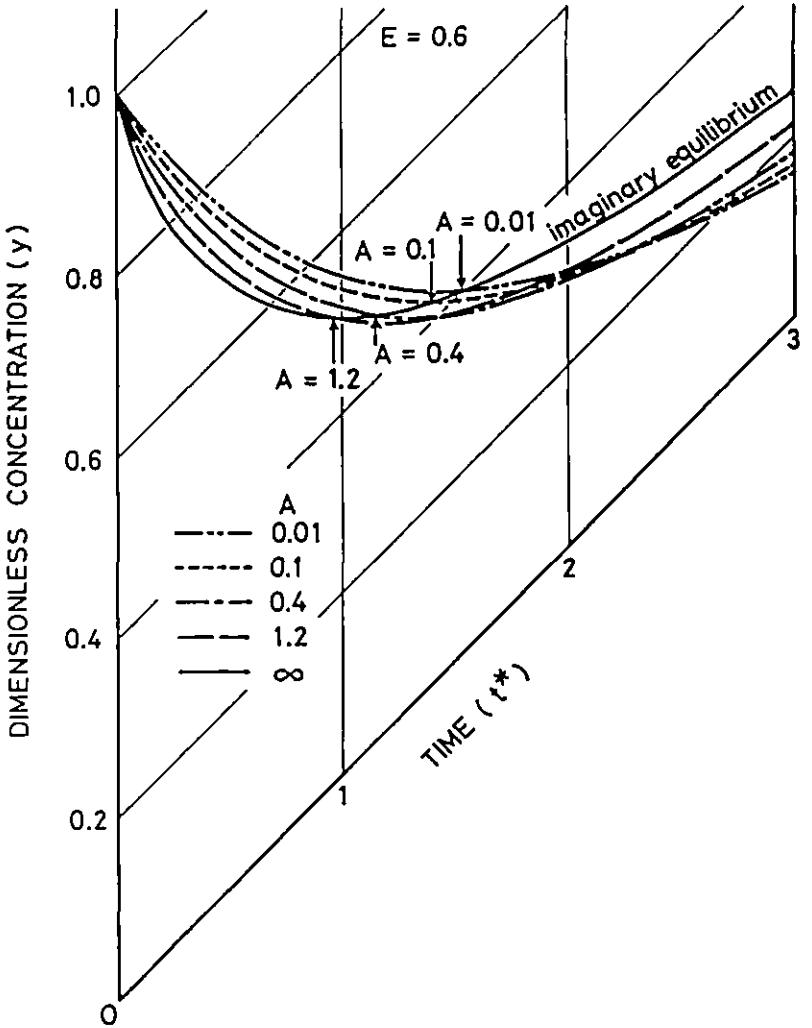

Fig.5.8B. Early stage of the desulphurization curves in Fig.5.8A using inclined co-ordinates. An arrow indicates the intersection between each curve and imaginary equilibrium curve.

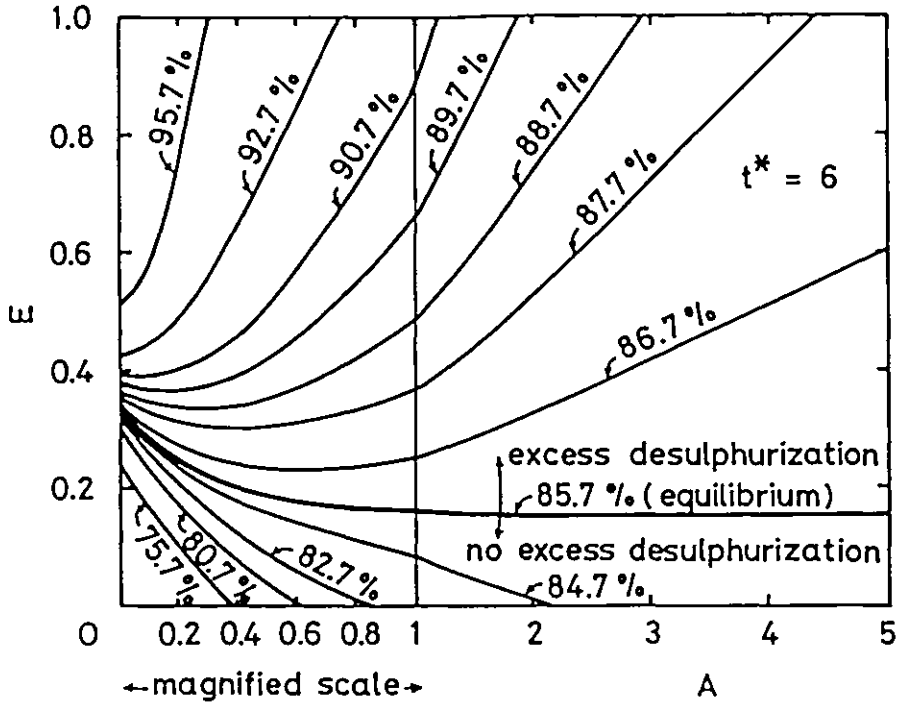

Fig.5.9. Iso-sulphur-removal contours on an A-E map at the end of the powder injection period $t^*_{in} = 6$.

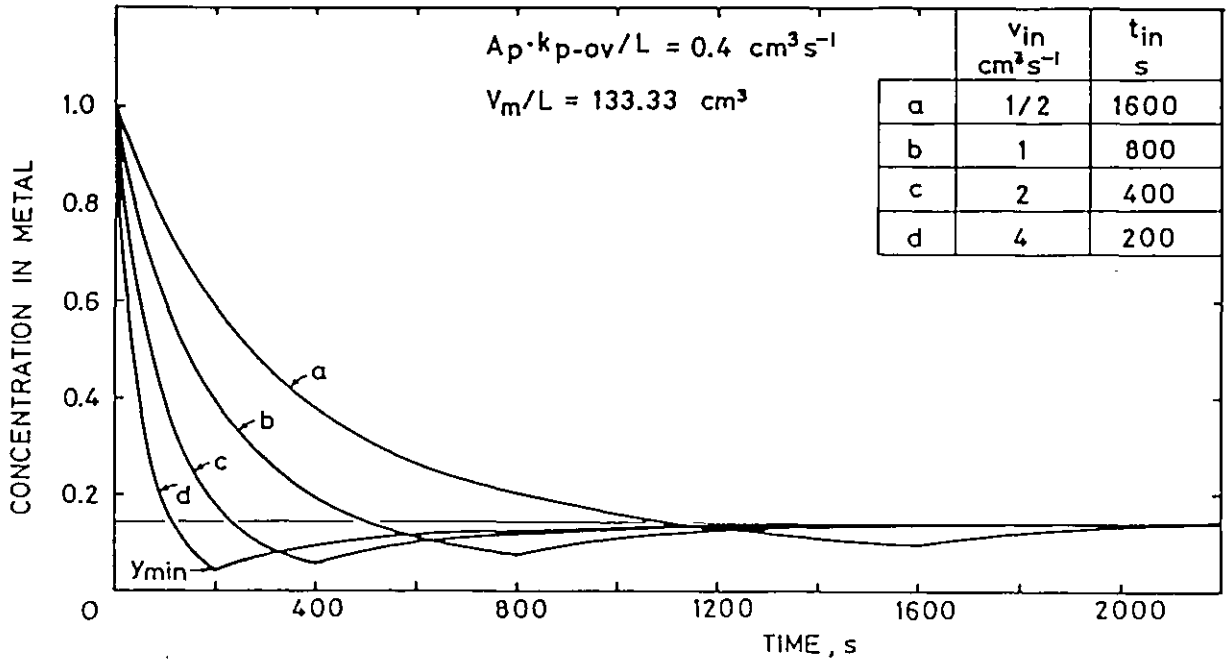

	v_{in} cm³s⁻¹	t_{in} s
a	1/2	1600
b	1	800
c	2	400
d	4	200

Fig.5.10. Effect of powder injection rate (injection period) with constant amount of total powder. Calculation conditions are given in Table 5.1.

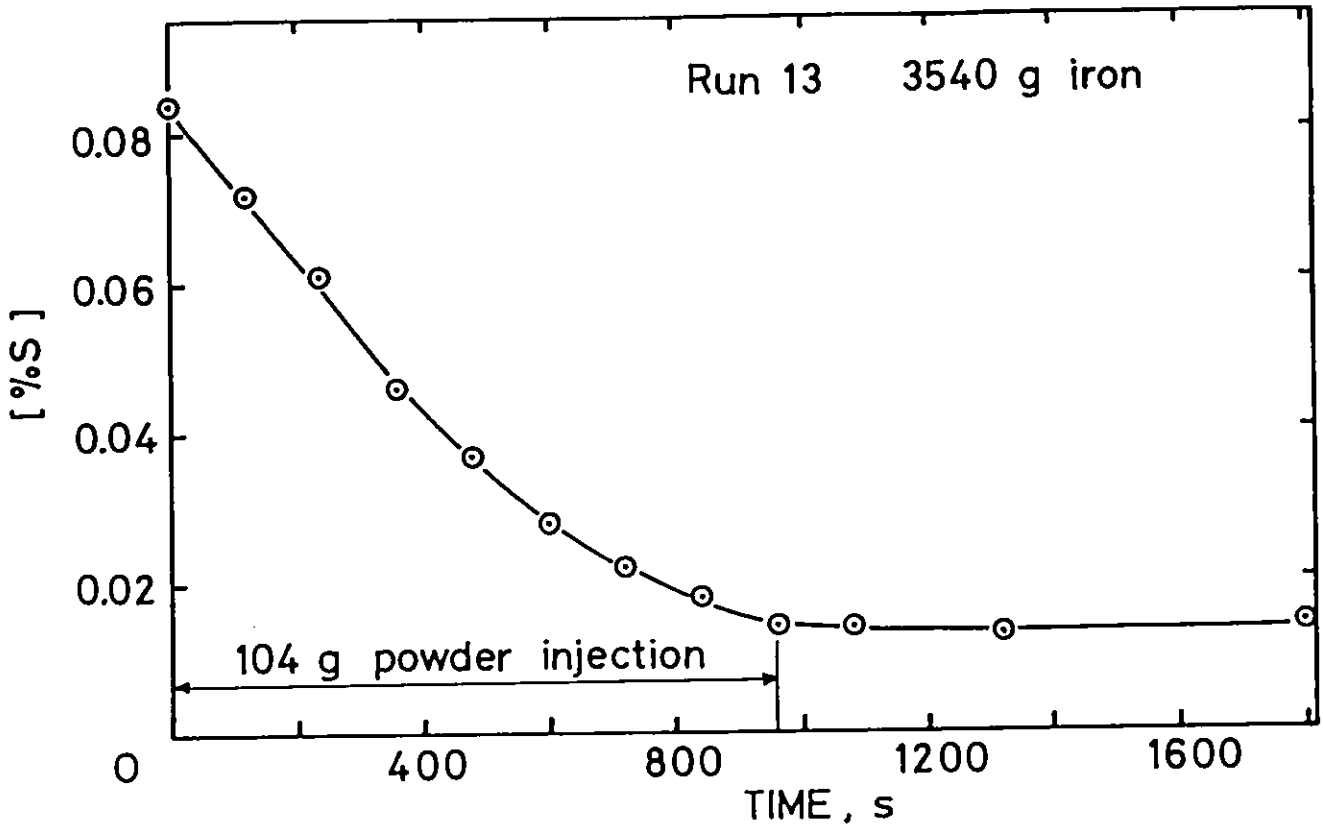

Fig.5.11. Desulphurization curve for powder injection experiment.

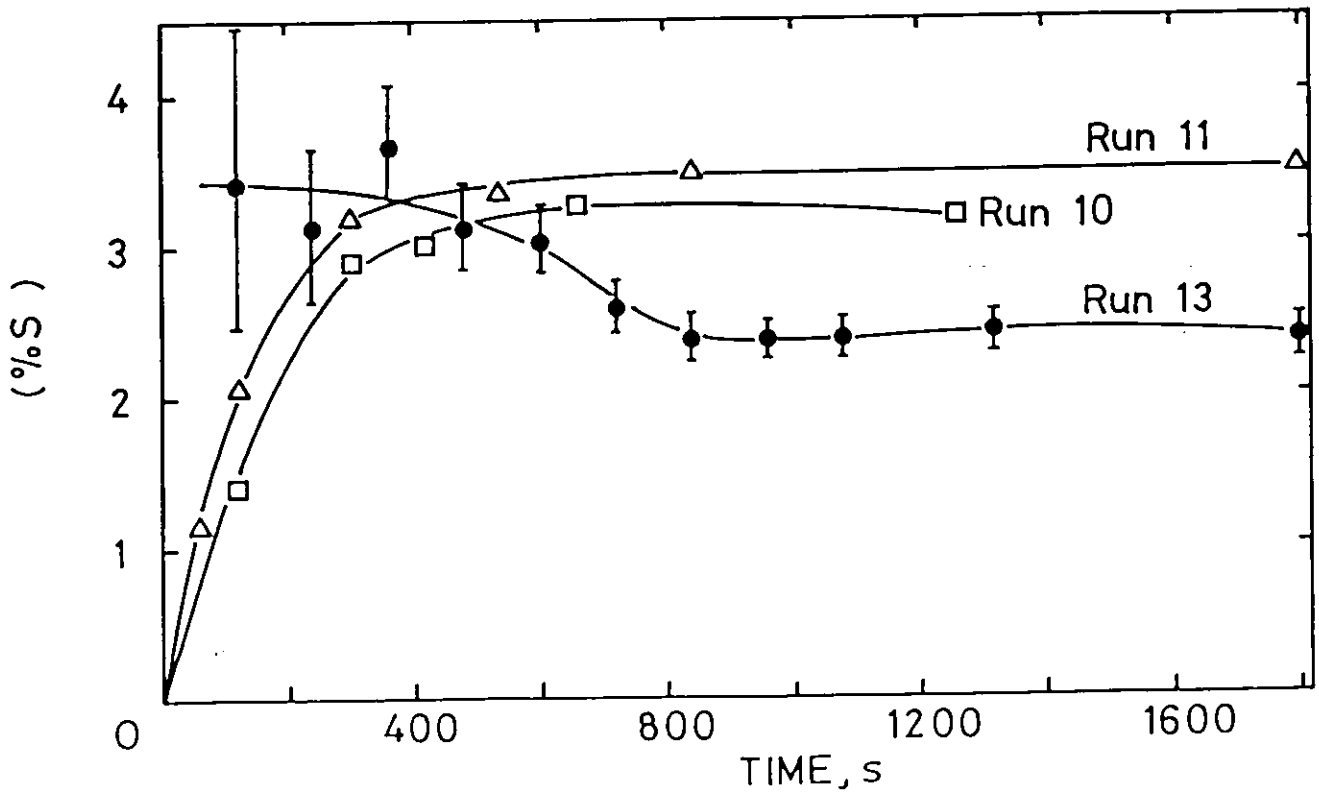

Fig.5.12. Sulphur concentration in slag.

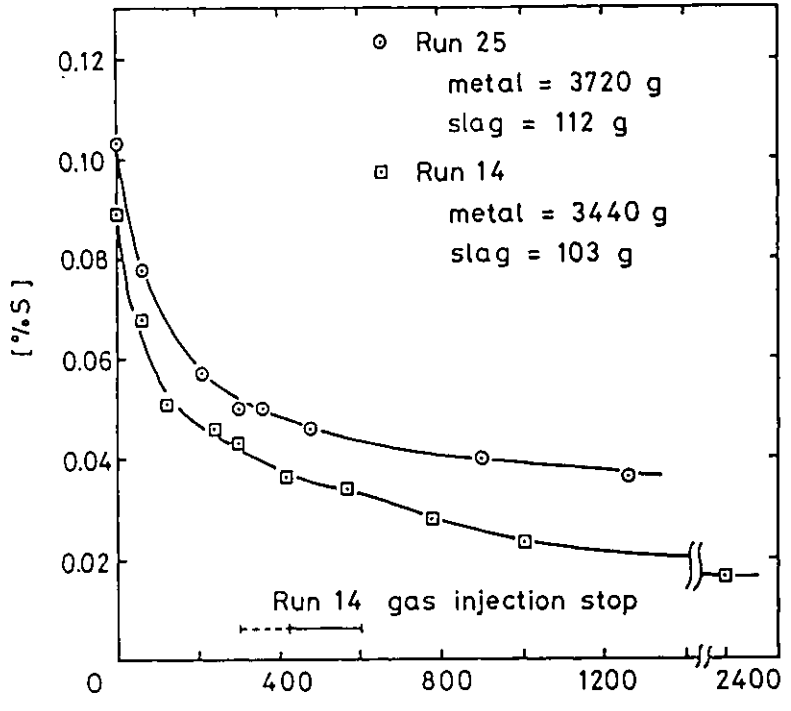

Fig.5.13. Desulphurization curve for powder dumping experiments.

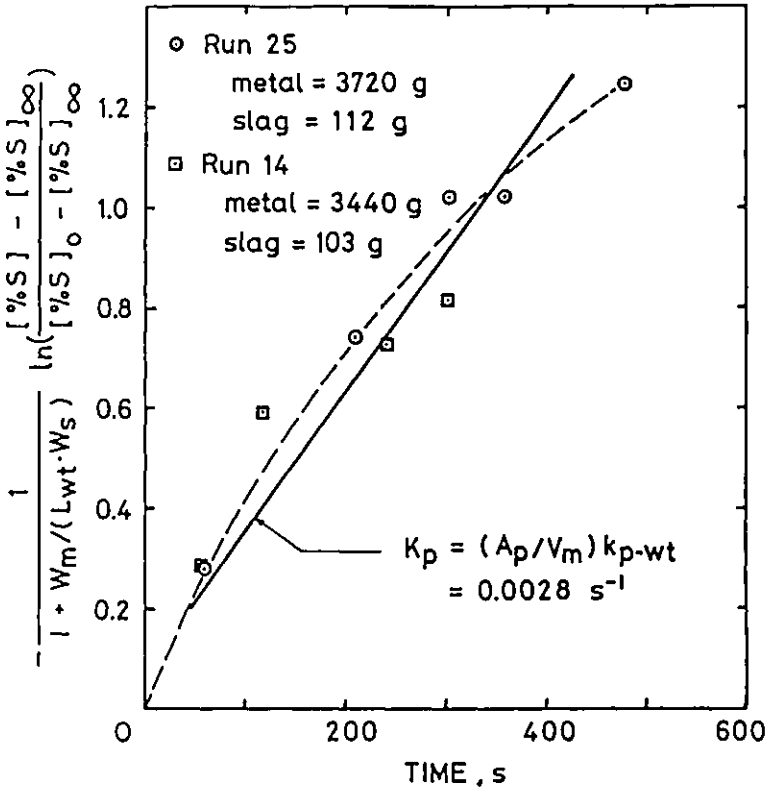

Fig.5.14. Derivation of the rate constant for permanent contact reaction.

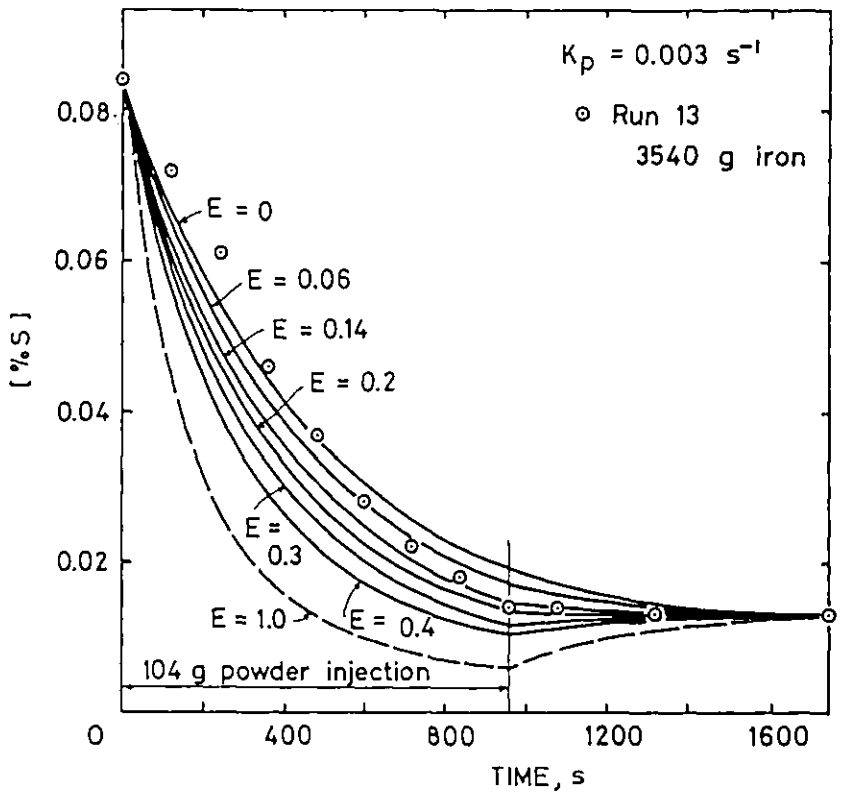

Fig.5.15. Comparison of experimental data with transitory and permanent contact reaction model ignoring sulphide saturation.

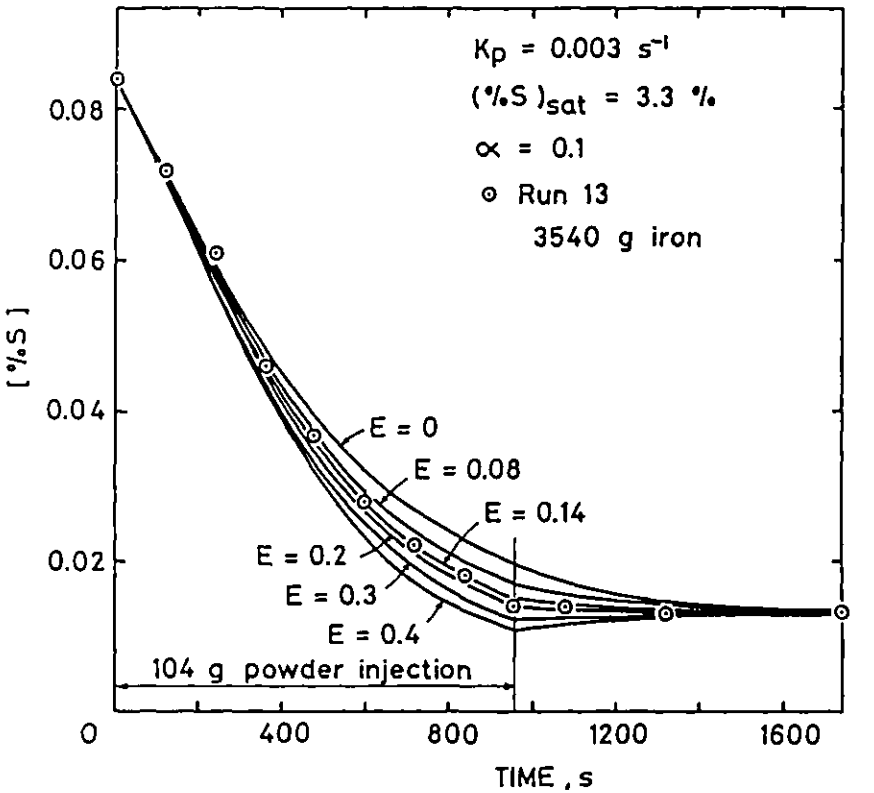

Fig.5.16. Comparison of experimental data with transitoy and permanent contact reaction model taking account of sulphide saturation in slag.

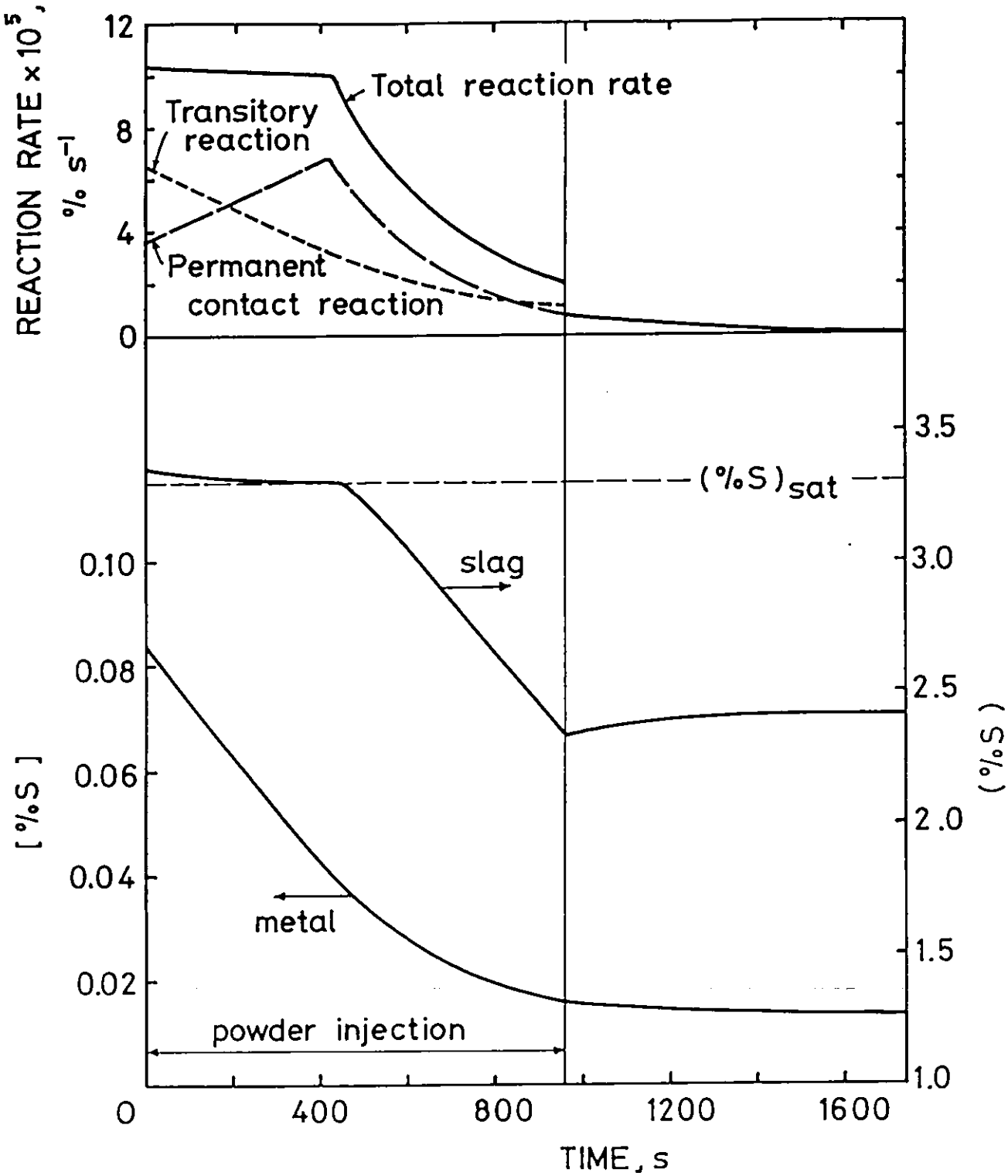

Fig.5.17. Results simulated by transitory and permanent contact reaction model for Run 13.

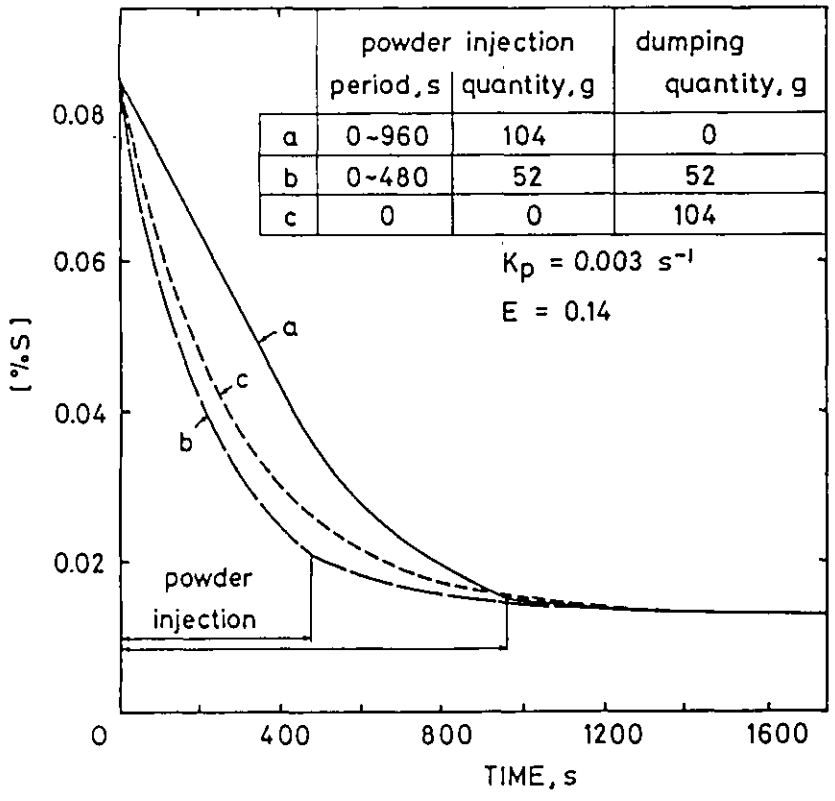

Fig.5.18. Comparison of powder injection and dumping.

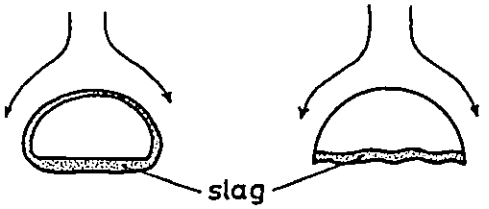

a) Engh's model b) Present proposal

Fig.5.19. a) Bubble whose whole surface is covered with slag (Engh[23]), and b) Spherical-cap bubble where slag exists at bottom (present proposal).

Chapter 6: BULK PHASE MIXING MODEL AND ITS APPLICATION TO KINETICS ON POWDER INJECTION REFINING

Abstract

In some industrial processes for metal refining, such as desulphurization in torpedo cars, the bulk mixing is inadequate to maintain the bulk concentration uniform, and it is very important to evaluate the effect of bulk mixing on the solute dispersion process.

A simple bulk mixing model has been developed which enables clear evaluation of the bulk mixing transport in terms of a mixing time. The model has been applied to the kinetics of powder injection refining. The relative importance of bulk mixing, kinetics at the reaction site and powder injection rate on the overall kinetics are also discussed.

Chapter 6: BULK PHASE MIXING MODEL AND ITS APPLICATION TO KINETICS ON POWDER INJECTION REFINING

6.1. Introduction

In recent years the study of bath agitation, and the resultant mixing of the bulk phases, has become of great practical importance since the widespread utilization of gas stirring processes such as Q-BOP, combined top/bottom blowing converters, powder injection refining and ladle treatment with intense gas stirring. It has been reported that the metallurgical characteristics of a combined top/bottom blowing converter , can be explained in terms of the mixing time of the metal bath[52-54]. The mixing time is undoubtedly a very important parameter necessary to characterise the overall kinetics in a metallurgical reactor, and can be measured experimentally by the addition of a tracer, or estimated from correlation with a mixing intensity[55,56].

On the other hand in most of the classical work on kinetics for slag/metal reactions the rate determining stage has been assumed to be a reaction at the interface or mass transfer in the vicinity of the interface, and the mixing transport in the bulk phases was assumed to be rapid (this is quite a good assumption in small scale experiments). In the kinetic model of powder injection refining (transitory and permanent contact reaction model) described in Chapter 5, it was also assumed that the bulk phases

were well mixed due to intense bath stirring.

However, in a large-scale reactor the problem of the bulk phase mixing becomes important. In an industrial desulphurization practice for molten cast iron, using a powder injection process in a torpedo car, Haida et al[57] reported that non-uniform distribution of sulphur in a torpedo car had an adverse effect to the efficiency of utilization of desulphurizer. Cavaghan et al[58] stated that, when the torpedo car design at the Redcar Works of BSC was revised to obtain a much smaller length/diameter ratio, one of the reasons was to improve mixing of the metal bath. Therefore, when applying the transitory and permanent contact reaction model to a reactor with inadequate mixing, such as torpedo car desulphurization, one has to take the problem of bulk mixing into account.

Haida et al[57] tried to combine the bulk mixing effect with desulphurization kinetics during submerged powder injection in a torpedo car, and explained the efficiency of utilization of desulphurizer from the point of mixing intensity, but only in a specific case. El-Kaddah and Szekely[36] developed a mathematical model for desulphurization kinetics in an argon-stirred ladle, which was a reaction model added to a numerical calculation of the turbulent recirculating flow. Though their model is very ingenious, and enables the evaluation of the rate processes in the reaction zone and the bulk mixing effect, three-dimensional calculation is necessary for application to cases such as the torpedo car. This would require enormous computer memory and costs. In the present work a simple bulk mixing model has been developed which is a rather

practical approach in anticipation of its application to industrial practice. This model has been applied to the case of powder injection refining using the kinetic model described in the previous chapter.

6.2. Modelling

In this model the mixing effect of the bulk phase is evaluated in terms of a single parameter, the mixing time, which is relatively easy to measure and is one of the most important parameters in a batch reactor. It is essential to measure mixing time experimentally or to obtain a reasonable estimate from theories before the application of the model.

1) Governing Equation for Bulk Mixing

To express the dispersion process of a solute concentration due to mixing, the following mathematical expression is used

$$\frac{\partial C}{\partial t} = M \frac{\partial^2 C}{\partial x^{*2}} \qquad (6.1)$$

where M is a parameter for mixing transport with dimensions of $(\text{time})^{-1}$, and x^* is a fictitious dimensionless length ($x^* = 0 \sim 1$). $x^* = 1$ represents the site where reaction occurs, and $x^* = 0$ is the other end of the reaction vessel. It is noted that x^* is used only for the expression of the fact of non-uniform solute distribution, and it is not always necessary to relate it to an actual position in the vessel. This equation is the same type as that of a diffusion process, and can be solved using well known numerical methods, such as the Crank-Nicolson method[15d].

Equation 6.1 can be made dimensionless using the following variables.

$$t^* = t/t_{mix}$$

$$C^* = C/C_{ref}$$

where t_{mix} and C_{ref} are respectively mixing time and arbitrary reference concentration. The dimensionless form is

$$\frac{\partial C^*}{\partial t^*} = (M.t_{mix}) \frac{\partial^2 C^*}{\partial x^{*2}} \qquad (6.2)$$

At any x* value, this equation will give the same C* vs t* curve, since t* is normalized by t_{mix}. Hence we obtain

$$M.t_{mix} = \text{constant}$$

2) Determination of $M.t_{mix}$ Value

It is assumed that the mixing time in the present work is the time required for the concentration non-uniformity to settle within 2% of the ultimate homogeneous state during a simulation of tracer dispersion using Equation 6.1. In the simulation of tracer dispersion, a tracer is added at a position x* = 0 at a time t = 0, and the concentration change at x* = 1 with time is shown in Figure 6.1, where the M values used are 0.004 and 0.01/s. From the simulation the constant value of $M.t_{mix}$ was determined as

$$M.t_{mix} = 0.467$$

Hence, the mixing parameter M is given by

$$M = 0.467/t_{mix} \qquad (6.3)$$

As mentioned earlier, this relation is for the mixing time that gives 98% uniformity of tracer dispersion. A different

definition for the mixing time gives a different constant value. For example the value of $M.t_{mix}$ is 0.373 in the case of 95% uniformity.

As is seen from Figure 6.1, the curve of tracerconcentration versus time at $x^* = 1$ has a sigmoidal shape. This characteristic is very similar to that of the tracer experiment[55] shown in Figure 6.2. This suggests that the present mathematical expression (Equation 6.1) is very realistic. This is presumably because an eddy diffusion process dominates the dispersion of tracer in the actual experiments. (See section 6.2.5)).

3) Combination with Kinetics of Interface Reaction

The present bulk mixing model is combined with a conventional kinetic model at the reaction interface (including mass transfer kinetics in the vicinity of the interface). The concept is shown in Figure 6.3.

In this model, dispersion of the solute in the bulk phase is given by Equation 6.1. The mean bulk concentration C_b is given by

$$C_b = \int_0^1 C \, dx^* \qquad (6.4)$$

At the reaction interface ($x^* = 1$) a conventional kinetic model is applied. For example, when simple first order kinetics are considered at the interface, the total reaction rate J, which is total solute flux across the interface, is expressed by

$$J = V.K \, (C_1 - C_s/L) \qquad (6.5)$$

where C_1 and C_s are respectively concentrations at interface ($x^* = 1$) and in slag phase (bulk slag phase is assumed to be well mixed). L is a partition coefficient.

The reaction kinetics at the interface provide the following boundary conditions for the bulk mixing equation (Equation 6.1).

$$\text{at } x^* = 1 : C = C_1 \qquad (6.6)$$

$$J = -B.M \frac{\partial C}{\partial x^*} \qquad (6.7)$$

B can be evaluated by analogy to the derivation of the diffusion equation. Supposing a diffusion cell with thickness Δx^* and volume ΔV, which is shown in Figure 6.4, the accumulation of solute is expressed from the balance of the influx (J_{in}) and outflux (J_{out}).

$$\Delta V \frac{\partial C}{\partial t} = J_{in} - J_{out}$$

$$= -B.M \left(\frac{\partial C}{\partial x^*} \Big|_{x^*} - \frac{\partial C}{\partial x^*} \Big|_{x^* + \Delta x^*} \right)$$

as ΔV is given by $\Delta x^*.V$ where V is volume of the bath, the above equation becomes

$$\Delta x^*.V \frac{\partial C}{\partial t} = B.M \left(\frac{\partial C}{\partial x^*} \Big|_{x^* + \Delta x^*} - \frac{\partial C}{\partial x^*} \Big|_{x^*} \right)$$

$$\therefore V \frac{\partial C}{\partial t} = B.M \frac{\partial^2 C}{\partial x^{*2}} \qquad (6.8)$$

Comparison of Equation 6.8 with Equation 6.1 gives B = V, namely coefficient B is volume of the bath itself. This relation was also confirmed by a numerical simulation.

Hence, the flux Equation 6.7 is rewritten as

$$J = -V.M \frac{\partial C}{\partial x^*} \qquad (6.9)$$

4) Application of the Mixing Model

First, the actual mixing time in the reaction vessel should be measured by experiments of tracer dispersion, and then the mixing parameter M can be obtained from Equation 6.3.

The solute dispersion process in the bulk phase can be calculated by solving Equation 6.1 numerically with the initial and boundary conditions. The boundary conditions at $x^* = 1$ are given from the kinetics of the interface reaction (Equations 6.5, 6.6 and 6.9), where Equation 6.5 is only one example of the many possible boundary conditions which might be necessary to account for interface reactions. The boundary condition at the other end ($x^* = 0$) is given by

$$\frac{\partial C}{\partial x^*} = 0 \qquad \text{at } x^* = 0 \qquad (6.10)$$

in the case where no reaction occurs there. From the solution of Equ. 6.1 the bulk mean concentration can be calculated using Equ. 6.4.

This procedure provides a clear evaluation of the mixing transport in the bulk phase, which is very important under circumstances such that the rate of transport by mixing cannot be neglected, e.g. torpedo car desulphurization.

5) Possible Relationship with Eddy Diffusion

The dispersion process with stirring can be expressed using the eddy diffusivity as

$$\frac{\partial C}{\partial t} = D_e \frac{\partial^2 C}{\partial x^2}$$

where D_e is an effective mean eddy diffusivity in the agitated bath.

Making this equation dimensionless using a representative length L of the vessel, one obtains

$$\frac{\partial C^*}{\partial t^*} = \frac{t_{mix} \cdot D_e}{L^2} \frac{\partial^2 C^*}{\partial x^{*2}} \qquad (6.11)$$

where $t^* = t/t_{mix}$, $C^* = C/C_{ref}$

and $x^* = x/L$ $(x^* = 0 \sim 1)$

Comparison of Equation 6.11 with Equation 6.2 gives

$$M = D_e/L^2 \qquad (6.12)$$

Therefore, mixing parameter M in the present model corresponds to D_e/L^2. This is also consistent with a consideration for diffusion flux. In the present mixing model the flux due to mixing transport is given by

$$-J = V.M \frac{\partial C}{\partial x^*} \qquad (6.13)$$

In an eddy diffusion process, it is given by

$$-J = A.D_e \frac{\partial C}{\partial x}$$

$$= \frac{A.D_e}{L} \frac{\partial C}{\partial x^*} \qquad (6.14)$$

where A is a diffusion area. As V = A.L, the above relations (Equations 6.13 and 6.14) lead to the same results as Equation 6.12.

6.3. Application to Kinetics during Powder Injection

The bulk mixing model has been applied to the case of powder injection described in the previous chapter.

The flux equation in terms of mass/time at the reaction inter-

face (Equation 6.9) can be written, using weight percent, as

$$J = - \frac{\rho.V.M}{100} \frac{\partial[\%S]}{\partial x^*}$$

From this flux equation and Equation 5.19 in Chapter 5, the boundary condition at the reaction interface is given by

$$-M \frac{\partial[\%S]}{\partial x^*} = K_p ([\%S] - (\%S)/L_{wt}) + P_{in}.(\%S)_{pow-e}/W_m \quad (6.15)$$

Concerning Equation 6.15, please refer to Chapter 5.

The governing equation for mixing transport expressed in weight percent (an equivalent equation to Equation 6.1) was solved by the Crank-Nicolson method[15d] with boundary conditions (Equation 6.15 and an equivalent equation to Equation 6.10). The calculations were carried out based on the conditions of Run 13 (powder injection) in Chapter 5.

The results are shown in Figure 6.5, where the rate parameters during powder injection refining (K_p and E) obtained in Chapter 5 are adopted. As is seen from the figure, desulphurization slows down with increase in the mixing time. The mixing time for Run 13 was estimated to be 50s from an empirical relation with stirring energy by gas injection[55], and it may be even less if stirring energy due to the electromagnetic field of the high frequency furnace is taken into account. It is seen from the figure that the transfer resistance due to mixing transport was negligible for shorter mixing times than 50s in this case.

6.4. Discussion

To understand the effect of bulk mixing on kinetics, some calculations were carried out under similar conditions to Figure 6.5, but no transitory reaction was considered ($E = 0$). The results are shown in Figure 6.6, and it is seen that the effect of bulk mixing is more important for the case of fast interface reaction.

For the comparison of relative contributions of the transport processes, the driving forces for the mixing transport and for the interface reaction were computed under the same conditions as Figure 6.6 (permanent contact reaction only, other data are based on Run 13).

The driving forces for mixing transport $[\%S]_{mix}$ and for the interface reaction $[\%S]_r$ were defined by

$$[\%S]_{mix} = [\%S]_b - [\%S]_1$$

$$[\%S]_r = [\%S]_1 - (\%S)/L_{wt}$$

where subscripts b and 1 denote bulk mean and reaction "interface" concentrations. The driving force obtained at $[\%S]_b = 0.05$, namely at constant sulphur removal, are shown in Figure 6.7.

In the figure the driving force for the interface reaction is plotted on the negative side of the ordinate, while the mixing driving force are plotted on the positive side. The total driving force is, therefore, indicated as the distance between the two corresponding curves. As is seen from the figures, at a fixed value of the rate constant for the interface reaction the mixing driving force

increases with increase in the mixing time, while the driving force for the interface reaction decreases. At constant mixing time, a large reaction rate constant results in a larger driving force for the mixing transport and a smaller one for the interface reaction. The total driving force decreases either with decrease in the mixing time or with increase in the rate constant of the interface reaction, unless one of the rates is extremely slow. This suggests that if both the mixing transport and interface reaction are sufficiently fast during powder injection, the total rate of sulphur removal is determined by the powder feeding rate.

From these results, it is shown that there are three major rate determining processes (powder feeding, reaction at the interface, mixing of bulk phase) during powder injection, as is shown in Figure 6.8. In the figure, these rate determining processes are represented by the following three factors which have dimensions of time.

Powder feeding rate is represented by the time t_f necessary to feed a sufficient amount of powder. It is given by

$$t_f = W_m / (P_{in} \cdot L_{wt}) \qquad (6.16)$$

where P_{in} is the powder injection rate in mass of powder/time, and W_m is the mass of metal.

For the reaction at the interface the reciprocal of the rate constant K was chosen and expressed as time t_r required for sufficient reaction. That is

$$t_r = 1/K = V/(A_r.k) \qquad (6.17)$$

For the mixing process the bulk mixing time t_{mix} was chosen. These factors are useful in a qualitative consideration of the kinetics during powder injection.

The ternary diagram in Figure 6.8 shows the concept of the rate determining processes with the three factors. Vertex 1 ($t_f = \infty$) of the ternary diagram corresponds to the case where powder feeding solely determines the total reaction rate, and Vertices 2 and 3 correspond to the cases where the reaction at interface or the bulk phase mixing solely determine the rate.

According to the ternary diagram, the rate determining processes of Run 13 during powder injection can be explained as follows.

As mentioned earlier, the mixing transport in this case was fast throughout the experiment. In the early stage of powder injection, the efficacy of the partition coefficient L_{wt} was limited due to the occurrence of the sulphide saturation, and the t_f value was large as was expected from Equation 6.16. Therefore, in the early stage the powder feeding dominated the rate determining stage (Vertex 1 on the ternary diagram), and the sulphur contents in metal phase decreased linearly with powder feeding.

In the later stage, the t_f value became small as powder feeding proceeded, and t_r became comparable to t_f after ceasing of the sulphide saturation in the top slag. Then, both powder feeding and reaction at interface layer played a major role in the later stage. On the ternary diagram, this means that Run 13 moved towards Vertex 2 from the early position of Vertex 1.

It is necessary to normalize t_r, t_{mix} and t_f for a quantitative comparison. In the case of a first order kinetic reaction at the interface, the total flux J can be written from Equations 6.5 and 6.17.

$$J = V\ (C_l - C_s/L)/t_r$$
$$= V\ (\text{Driving force})/t_r \qquad (6.18)$$

From numerical simulation, it was confirmed that the mixing transport could be approximated as first order kinetics except for the initial stage. The resultant flux is given by

$$J = V\ (C_b - C_l)/(0.87\ t_{mix})$$
$$= V\ (\text{Driving force})/(0.87\ t_{mix}) \qquad (6.19)$$

It is seen from comparison of Equations 6.18 and 6.19 that 0.87 t_{mix} is equivalent to t_r (in case of a first order reaction), and this normalizing factor allows quantitative comparison.

On the other hand the effect of powder feeding on the total mass flow cannot be made equivalent to first order kinetics. Therefore t_f cannot be normalized. However, the ratio t_f/t_r is in fact the dimensionless parameter A in Chapter 5, and the effect can be seen from Figures 5.6 - 5.9. When A equals 1.2, the reaction kinetics were close to the imaginary equilibrium at all times. This shows that for t_f/t_r greater than 1.2 the powder feeding controls the kinetics.

On the ternary diagram the side 1 - 2 corresponds to a case assumed in Chapter 5, where the bulk mixing process is neglected. In this chapter a bulk mixing model has been proposed, and enables the extension of the kinetic model on powder injection to the whole area of the ternary diagram.

6.5. Concluding Remarks

A simple bulk mixing model has been developed which enables clear evaluation of the bulk mixing transport. In this model the mixing effect is evaluated in terms of mixing time. This model has been applied to kinetics of powder injection refining, and discussion was made about the three rate determining processes during powder injection. This model will be useful in application of a kinetic model considered at interface layer to a reaction vessel with inadequate bulk mixing.

List of Symbols. Chapter 6.

A_r reaction area.

B coefficient in Equation 6.7.

C concentration (volume base).

C* dimensionless concentration.

D_e effective mean eddy diffusivity.

E parameter for transitory reaction.

J total solute flux.

k first order rate constant or mass transfer coefficient (length/time).

K rate constant (= $A_r.k/V$) in $(time)^{-1}$.

K_p rate constant for permanent contact reaction in $(time)^{-1}$.

L partition coefficient or representative length of vessel.

L_{wt} partition coefficient using weight percent.

M mixing parameter in $(time)^{-1}$.

P_{in} powder injection rate in mass/time.

[%S] sulphur concentration in metal in weight percent.

(%S) sulphur concentration in slag in weight percent.

t time

t^* dimensionless time.

t_{mix} mixing time

V volume of metal bath.

ΔV volume of diffusion cell considered.

W_m mass of metal.

x length ordinate.

x^* fictitious dimensionless length.

Δx^* thickness of diffusion cell considered.

ρ density of molten metal.

Subscripts

b bulk mean.

e eddy.

f powder feeding.

in inflow.

m metal.

mix mixing.

out outflow

pow-e powder at end of rise.

r reaction at interface layer

ref reference

s slag.

wt in weight

0 at $x^* = 0$

1 at $x^* = 1$ (reaction site).

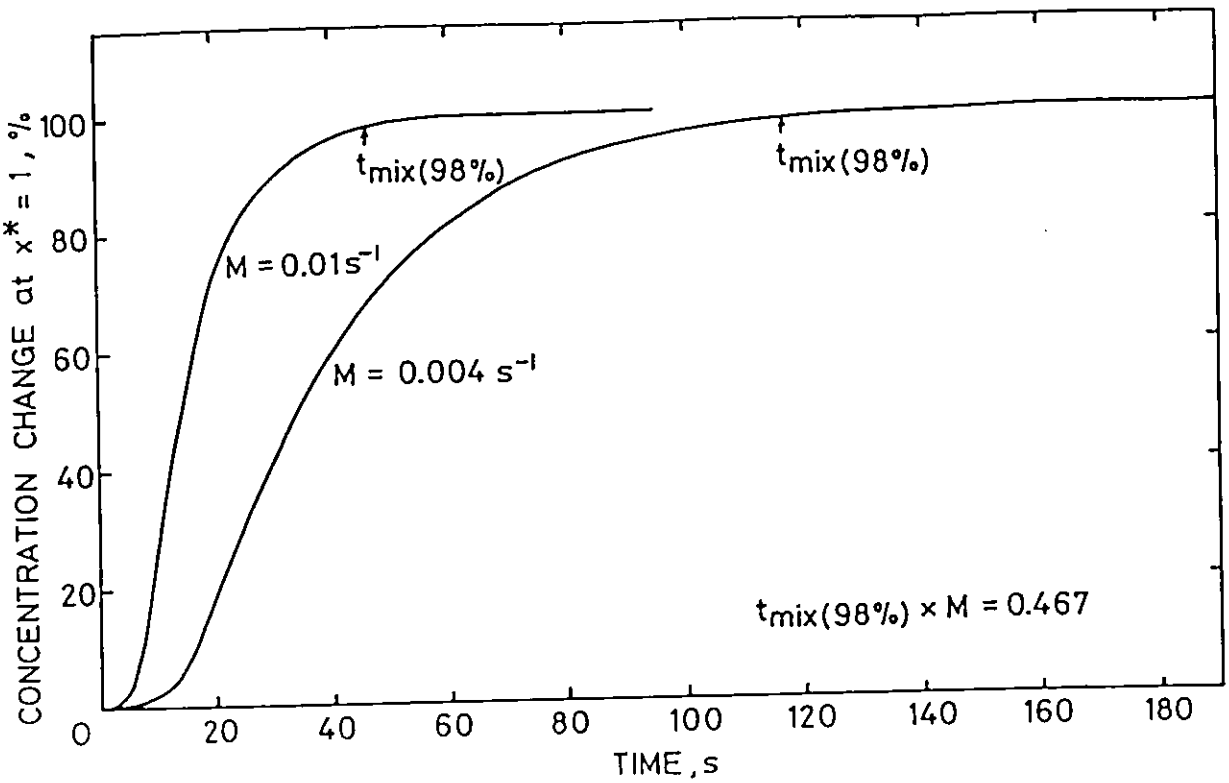

Fig.6.1. Concentration transition curve of simulation for tracer dispersion by bulk mixing model.

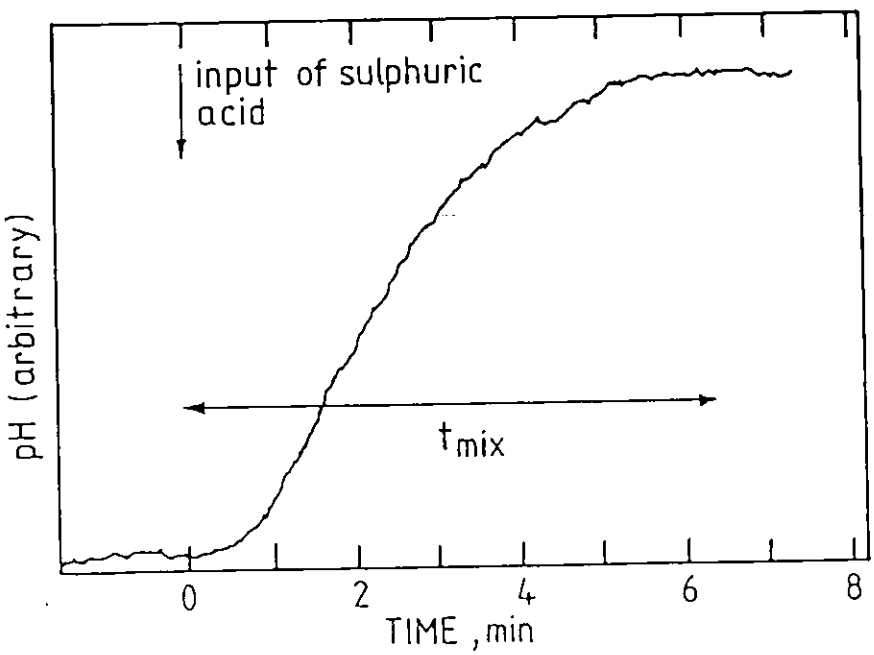

Fig.6.2. Typical example of tracer dispersion vs. time curve in model experiment[55].

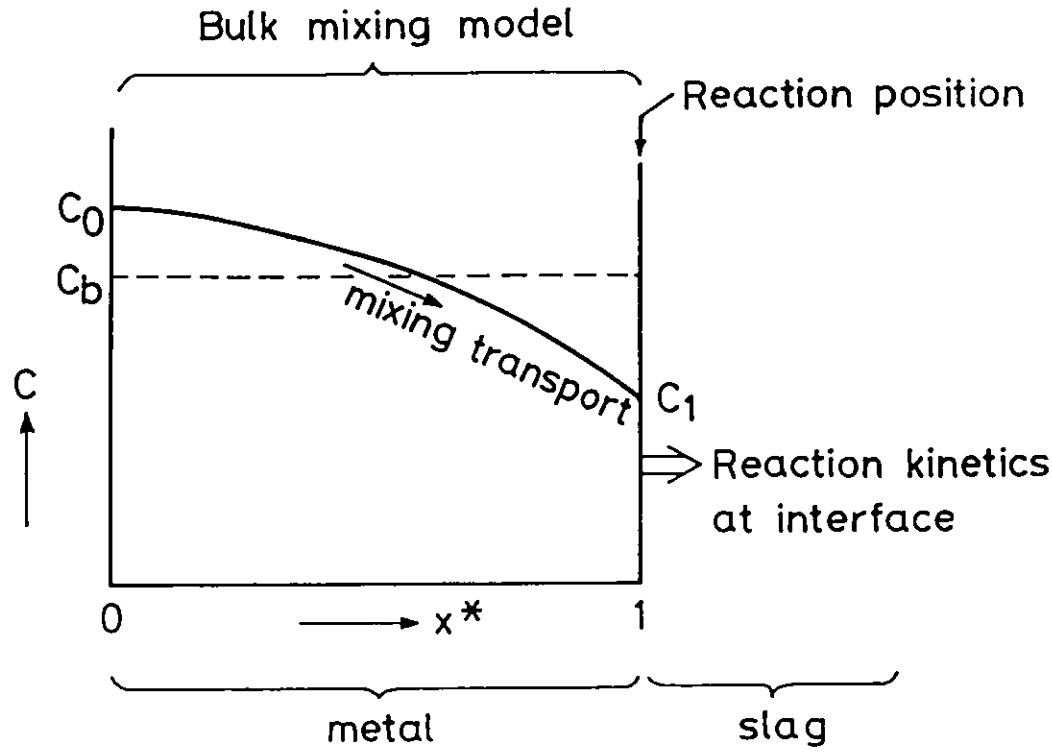

Fig.6.3. Combination of bulk mixing model with kinetics at interface.

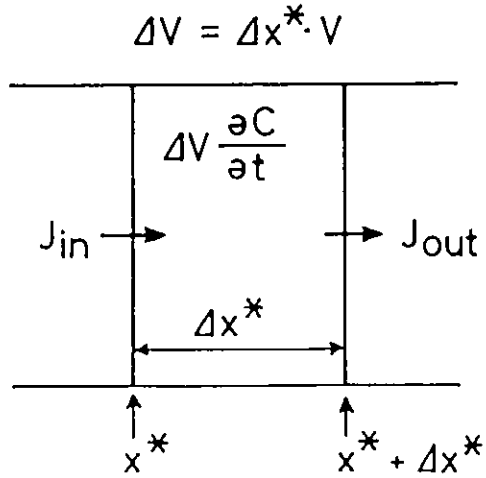

Fig.6.4. Diffusion cell for derivation of B.

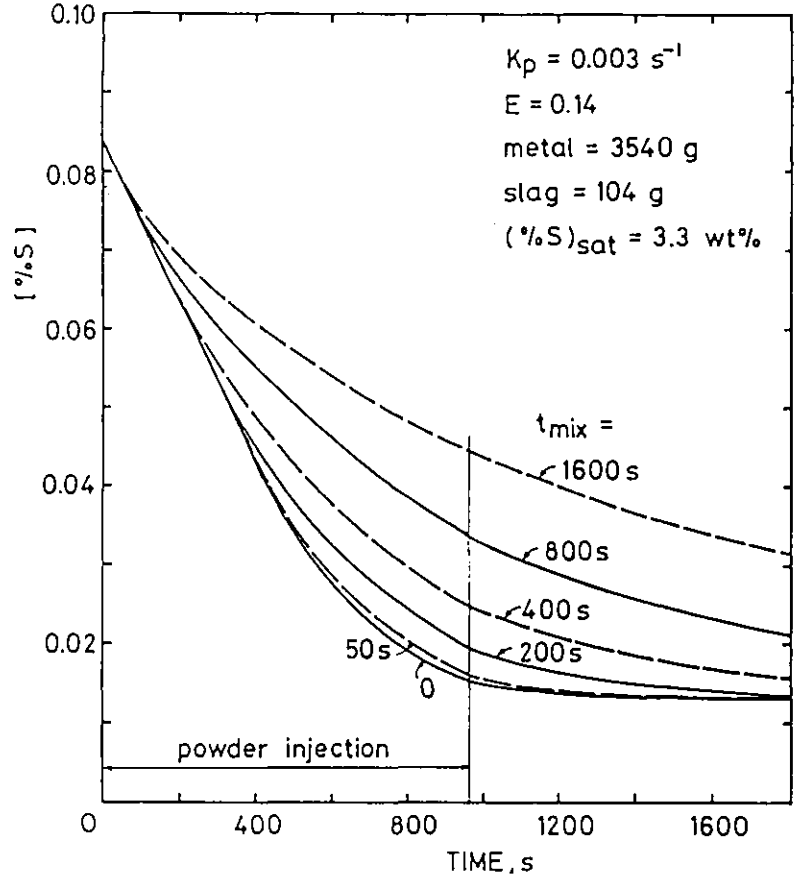

Fig.6.5. Simulation of desulphurization curve for powder injection (Run 13) with different mixing time.

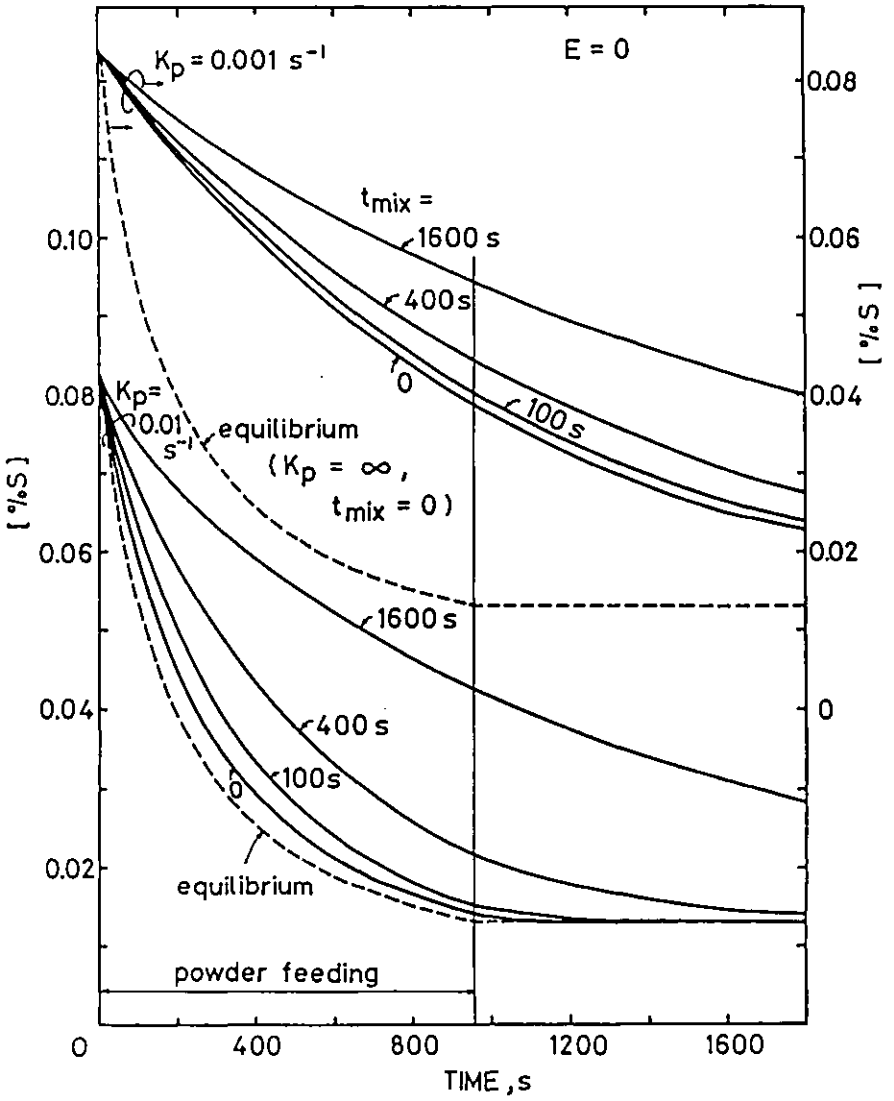

Fig.6.6. Effect of mixing time on the desulphurization curve in the case of permanent contact reaction only.

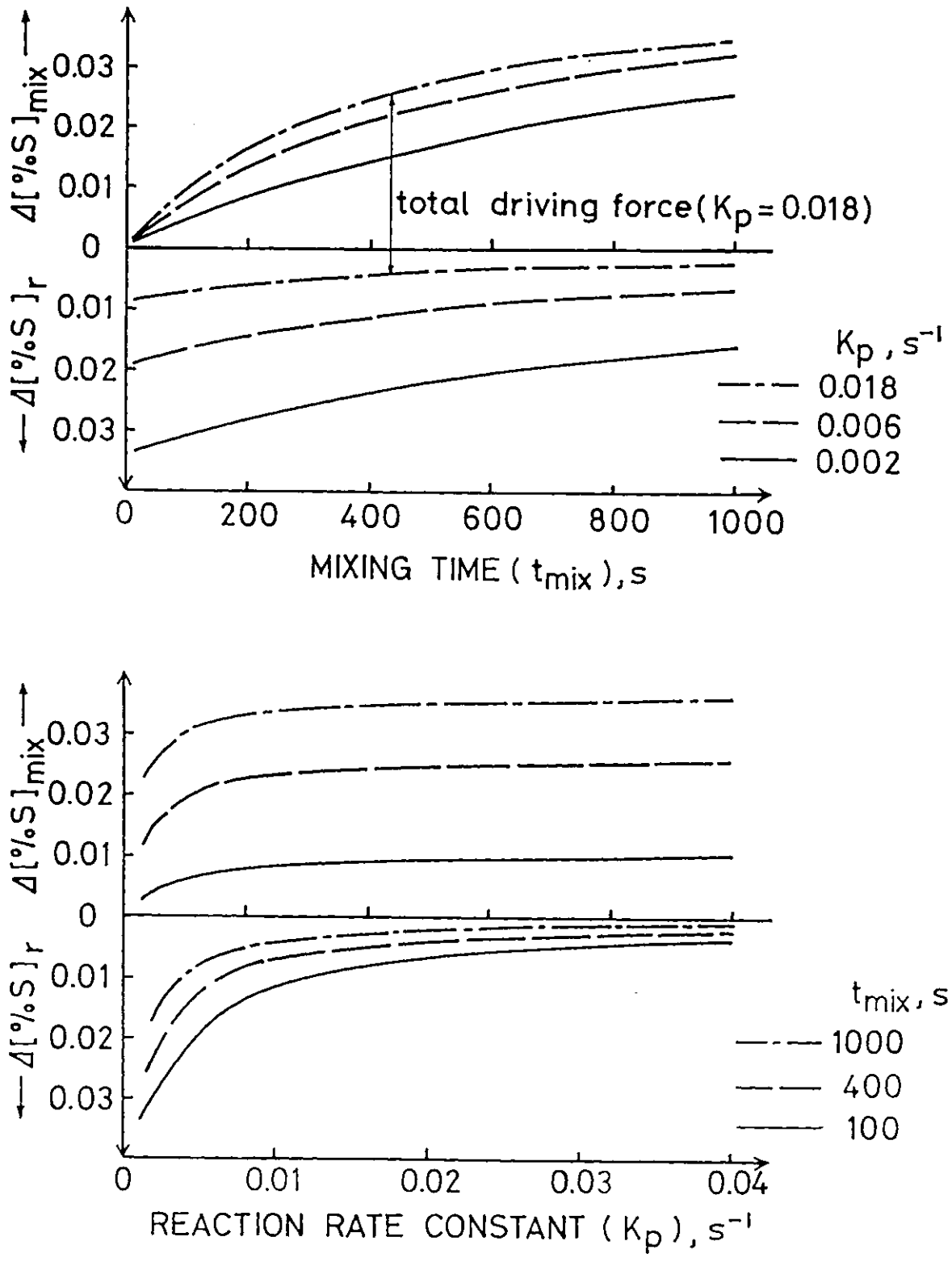

Fig.6.7. Effect of mixing time and reaction rate costant on the driving forces for mixing and interfacial reactions.

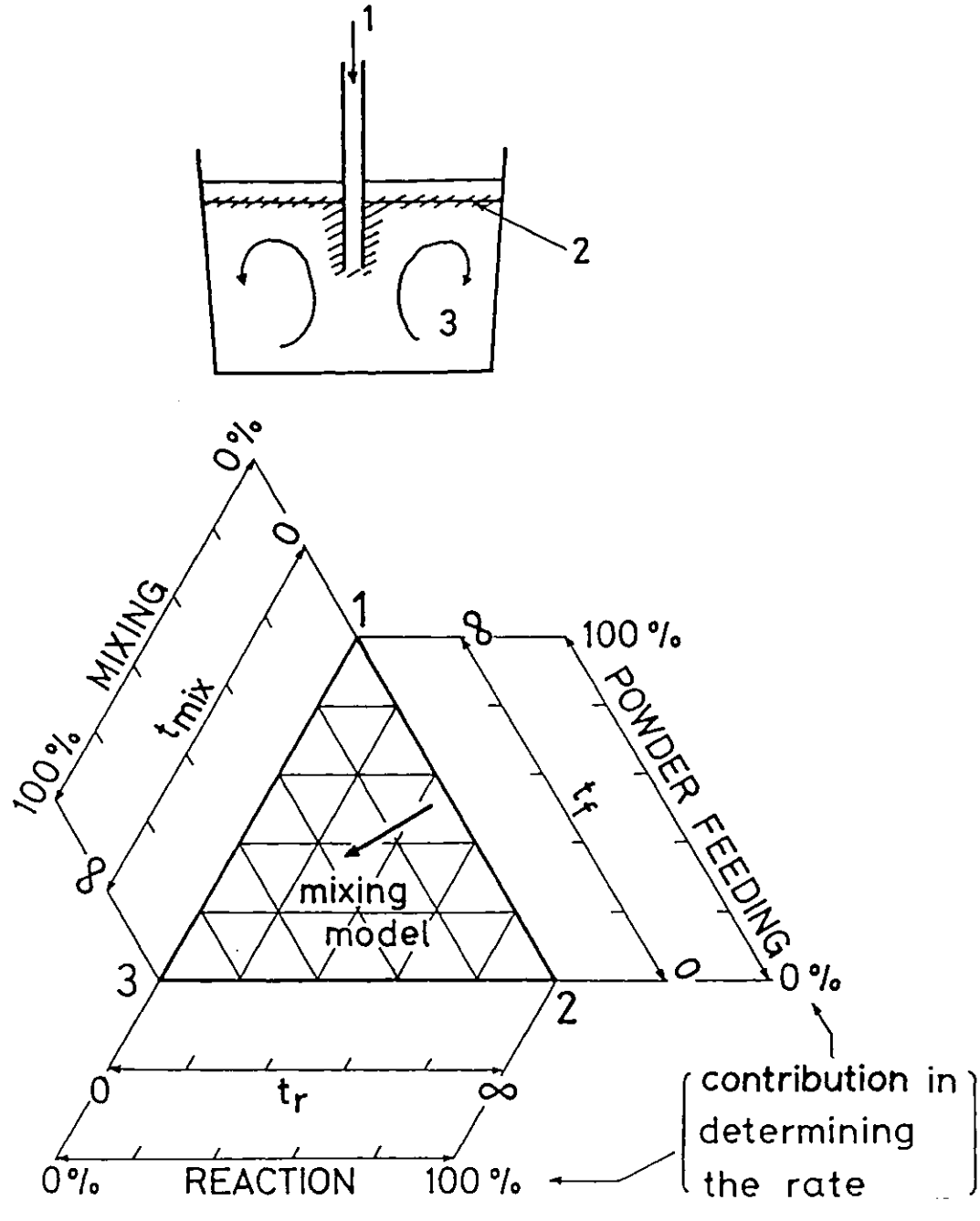

	rate determining process	factor
1	powder feeding	time to feed sufficient amount of powder $t_f = W_m/(P_{in}.L_{wt})$ sec
2	reaction or mass transfer in the vicinity of reaction interface	time for reaction $t_r = V/(A.k)$ sec
3	mixing of the bulk phase	time for mixing t_{mix} sec

Fig.6.8. Schematic diagram showing the rate determining processes during powder injection refining.

Chapter 7: SIMULTANEOUS DEPHOSPHORIZATION AND DESULPHURIZATION OF MOLTEN PIG IRON

Abstract

Laboratory scale experiments using $CaO-CaF_2-CaCl_2-Fe_2O_3$ powdered flux were carried out to clarify the effect of the silicon on the kinetics of simultaneous dephosphorization and desulphurization of molten pig iron. The dephosphorization occurs after the cessation of the vigorous desiliconization reaction with high or medium initial silicon (0.34 and 0.13 wt % respectively), while it proceeds immediately in the case of low initial Si (0.02 wt %). Stagnation of the desulphurization reaction was observed during the later half of powder feeding period.

These characteristics observed in the experiments can be interpreted using a kinetic model taking coupled reactions into account and assuming that the rates were determined by transport in the slag and metal phases. The effect of the powder feeding period was calculated using the kinetic model.

Chapter 7: SIMULTANEOUS DEPHOSPHORIZATION AND DESULPHURIZATION OF MOLTEN PIG IRON

7.1. Introduction

There has been a growing interest in study of simultaneous dephosphorization and desulphurization of molten pig iron in Japan[6]. The simultaneous dephosphorization and desulphurization treatment of pig iron for steelmaking is not only useful in production of ultra low P and S steel in conventional steelmaking processes, but also enables new steelmaking processes[59-62] in which so called "slagless" blowing in BOF is applied. A typical example of the new processes is shown in Figure 7.1. Despite the addition of a pretreatment stage to the conventional process, it is reported that the new process brings about higher iron yield and less industrial waste[60,65] thanks to "slagless" blowing in converters[63-65].

Generally sodium carbonate or CaO-based fluxes have been used as reagents for the simultaneous reactions, and the consensus obtained from earlier investigations is as follows.

a) Sodium carbonate alone has strong dephosphorizing and desulphurizing power[61,66].

b) CaO-based reagent requires both flux components such as CaF_2, $CaCl_2$ or NaF_2 and an oxidizer such as FeO, Fe_2O_3, or O_2 for effective simultaneous reactions[41,67].

c) Initial silicon concentration should be low (typically less than 0.1%~0.2%[61,68,69] for sufficient performance of dephosphorization.

d) In a large scale trial, bath agitation is necessary for efficient reaction. Agitation may be obtained by such means as powder injection

[62,70-72], gas stirring[65,73,74], mechanical stirring by an impeller[73,74].

e) In one large scale trial[60] a counter current reactor was used to obtain efficient reaction with powder dumping and oxygen surface blowing.

In the literature referred to earlier, references 59, 60, 61, 65 and 68 are of plant-scale trials on the simultaneous dephosphorization and desulphurization using Na_2CO_3, and reference 62 is a report from a production line putting the new process using Na_2CO_3 into practice, though the capacity of the facilities is small (2000 ton/day, commissioned in May 1982, Kasima Works of Sumitomo Metal Industry). References 69, 72 and 74 are of plant-scale trials using CaO-based fluxes. The new process using CaO-based flux has not yet been put into a proper production line.

Incidentally a desiliconization only process has been in use since October 1979 in the Muroran Works of NSC, where substantially all the hot metal is treated to reduce the Si content to about 0.15% and where the slag volume in the LD converter is close to a third of that in the conventional process (42 kg/ton steel)[75].

In these circumstances, large efforts are being made to establish the new steelmaking processes making use of simultaneous dephosphorization and desulphurization. However, fundamental research in this field has been insufficient. The importance of the initial silicon contents in hot metal is well recognized, but its effect on the kinetics has not been satisfactorily clarified. Ozawa et al[68] carried out simultaneous reaction experiments using submerged powder injection in a torpedo car. They found that in the case of hot metal containing

relatively high silicon (0.1%) the desiliconization occurs prior to the dephosphorization, and the dephosphorization proceeds after a fall of silicon level, while the desulphurization proceeds from the beginning. This was excellent work, but further investigations from a kinetic point of view are necessary for clarification of the results.

In the present work, small scale experiments using $CaO-CaF_2-CaCl_2-Fe_2O_3$ powdered flux were carried out to clarify the effect of the silicon on the kinetics of simultaneous dephosphorization and desulphurization. The experimental results were interpreted with a kinetic model[76,77] taking coupled reactions into account.

Na_2CO_3 is a very powerful reagent combining both strong dephosphorizing and desulphurizing capacities, but Na_2CO_3 slag is very corrosive to refractories. Its evaporation and decomposition at elevated temperature lead to high heat losses and losses of reagent, also the off-gases must be cleaned. CaO-based flux is expected to be more economical, if it can be made to exhibit sufficient desphorizing and desulphurizing performance. Therefore CaO-based flux was chosen in this work.

By reference to the work done by Nakamure et al[67], CaF_2 and $CaCl_2$ were chosen as additive components of the flux to achieve a high dephosphorization ratio (85%) and a moderate desulphurization ratio (50%), which enables "slagless" blowing in the converter (initial concentrations of 0.1% P and 0.03% S in blast-furnace iron to final 0.015% P and 0.015% S in steel).

7.2. Experimental

The experimental apparatus and procedure used are the same as in Chapter 4 except for the following points. Powdered flux (nominal composition of 30% CaO - 20% CaF_2 - 20% $CaCl_2$ - 30% Fe_2O_3) was prepared by mixing premelted CaO-CaF_2-$CaCl_2$ powder with Fe_2O_3 powder. Low silicon hot metal was made by carburizing Armco iron using a graphite crucible and a graphite stirring rod. Compositions of the metal were adjusted by addition of ferro-phosphorus, ferro-sulphur and ferro-silicon.

In the actual experiments approximately 3kg of hot metal was melted using an alumina crucible, and the experimental temperature was 1350°C. Powdered flux was blown onto the surface of melts (surface blowing) rather than submerged injection used in the previous work, because it was difficult to achieve stable submerged powder injection (see Chapted 4) with the present powder which contained fine Fe_2O_3 particles, and also because the elimination of the transitory reaction would facilitate the application of a kinetic model.

The nozzle diameter of the powder feeding lance was 2mm, and the flow rate of the carrier gas (argon) was about 6Nl/min. Argon gas injection was also simultaneously used to stir the metal bath throughout the experiments, and the gas flow rate and the nozzle diameter were respectively 3Nl/min and 1mm.

The amount of powder used was typically 180g (60g/kg-metal), and this corresponded to a CaO consumption rate of 18g-CaO/kg-metal, which was decided by reference to the work of Umezawa et al[73].

Metal samples were taken using silica suction tubes, and slag samples were taken in the end of the runs (2100 ~ 2400 sec from the start of powder feeding). Analyses of the samples were made by the Process Technology R & D Laboratories of NSC. Metal samples were analysed by an inductively coupled plasma quantorecorder (P and Si) or using high frequency combustion and infra-red absorption spectrophotometry (S and C). Slag analysis methods used are given in the bottom of Table 7.2.

7.3. Results of Experiments

A summary of the experimental runs is given in Table 7.1. Results of slag analyses are given in Table 7.2, where samples G, H and I are of the fresh powders from different batches. Table 7.3. gives slag compositions calculated from the data given in Table 7.2 by assuming stoichiometric compounds of CaO, CaF_2, $CaCl_2$, P_2O_5, CaS, SiO_2, Al_2O_3, FeO and Na_2O. The compositions of the powdered fluxes used are given in Table 7.3, where the Fe_2O_3 content (30%) is the value of the amount of Fe_2O_3 mixed with the premelted powder, and the other components are calculated from the results of the analyses. In Table 7.3 the calculated powder compositions show good agreement with the nominal values. The calculated $CaCl_2$ content shows slightly higher values than that of the nominal value. This is because 10% excess $CaCl_2$ was used when making up the powders for premelting, but the evaporation loss of $CaCl_2$ was smaller than expected. Also, CaC_2 content in the powder was estimated from C_2H_2 generation reaction with water, and it was confirmed that CaC_2 content was 0.1% or less.

Changes of P, S, Si and C concentrations in metal with time are

shown in Figures 7.2~7.7, where the actual powder feeding periods are indicated in the figures. The results of metal analyses are given in Appendix 3. In all the runs, significant slag foaming was observed. Nozzle clogging of the powder feeding lance occurred in some of the runs, as the nozzle tip was mostly covered with slag due to splashing or foaming of the slag.

In the standard Run A (Figure 7.2), P and S concentrations at the end of the powder feeding were respectively 0.006% and 0.011%. These results were quite good (more than 95% dephosphorization and almost 70% desulphurization), and are consistent with the performance expected from the literature[73]. The phosphorus concentration gave a minimum value soon after the end of the powder feeding, and the noticeable reversion of phosphorus followed thereafter. On the other hand, substantially no reversion of sulphur was observed. The desiliconization reaction proceeded rapidly in the early stage, giving a very low silicon level (less than analytical limit). Carbon content decreased constantly during the powder feeding.

The performance of Run B (Figure 7.3) was not so good as that of Run A probably because of the smaller amount of powder fed. In run B nozzle clogging occurred at the end of the powder feeding period, and therefore the actual powder quantity may have been slightly smaller than 145g.

Results of the medium Si Run C (Figure 7.4) showed interesting behaviour. Desiliconization quickly occurred in the early stage. Dephosphorization showed a delay up to 350 sec, while the rapid desiliconization reaction proceeded. The delay of phosphorus reaction in the early stage was in marked contrast to the low Si Runs A and B.

After the silicon level dropped below 0.02 wt %, phosphorus concentration decreased rapidly and gave a minimum value soon after the end of the powder feeding period, and the reversion followed. On the other hand desulphurization did not show any such delay in the early stage. These phenomena correspond well to the observations made by Ozawa et al[68] on the plant scale experiments using powder injection.

Further close observation of the desulphurization curve in the figure suggested the existence of a flat zone (stagnation of desulphurization) from 400 sec to 800 sec, though this was not very clear. This phenomena will be discussed later using the kinetic model. Decrease in carbon concentration in Run C was much smaller than in the standard cases (Runs A and B).

Figure 7.5 shows the results of high Si Run D. As is seen from the figure, dephosphorization barely occurred, showing a small fall of P in the later stage of the powder feeding, but thereafter most of the phosphorous in the slag reverted to the metal. In contrast the desulphurization reaction was not apparently affected by the high silicon level. Decrease in the carbon content was very small when compared with the low Si runs.

Figure 7.6. shows the results in the case of 30%CaO - 40% CaF_2-30% Fe_2O_3 powder (Run E). A very good dephosphorization performance was observed in this run, while desulphurization was not so good as in the case of $CaCl_2$-containing powders. This was probably due to the small solubility limit of FeO in the CaO-CaF_2-FeO system at the experimental temperature as estimated from the phase diagram at higher temperature[81].

A trial using Na_2CO_3-containing powder was carried out. The powder was a physical mixture of 10% of Na_2CO_3, 30% of Fe_2O_3 and 60% of premelted $CaO-CaF_2-CaCl_2$ powders. It was reported that small amount of Na_2CO_3 addition improved the performance of CaO-based flux for both dephosphorization and desulphurization[71,78]. However the present results (Figure 7.7) were not very good. Desulphurization was very satisfactory, but dephosphorization was rather bad, showing peculiar behaviour of P concentration. The reason for this is not known. The surface blowing method used might not be a suitable way of feeding the very reactive Na_2CO_3-containing powder. In fact very significant fume was evolved during the powder feeding period, and it was not possible to see inside the furnace. Submerged powder injection could be used in order to make use of the transitory phosphorus removal.

The vapour pressure of pure $CaCl_2$ at 1350°C (7.2 mm Hg) is expected to be 300 times as large as that of pure CaF_2 (0.023 mm Hg), where the vapour pressures are calculated by extrapolation from the data compiled by Kubaschewski[79]. However a comparison of $CaCl_2$ and CaF_2 contents in the fresh powder (Table 7.4) and slag samples (Table 7.3) suggested that no significant $CaCl_2$ loss occurred during a run.

Phosphorus and sulphur contents in the slags almost agreed with those predicted from the mass balances, if the uncertainty of the slag analyses and the late sampling times were taken into account (the slag was sampled after 2100~2400 sec). However the Si contents of the slags showed smaller values than those expected from mass balances. In Runs C and D, the analysed results of Si

contents in slags were 60~70% of those estimated from mass balances using the metal phase concentrations. Total iron concentrations in slags were very small, as most of the iron oxide was reduced during a run. In Run F the Na content was extremely small. Presumably most of the Na_2CO_3 was evaporated immediately, when the powder contacted with hot metal. This partly explains the bad performance in Run F.

Aluminium contents in slags were analysed to evaluate the amount of dissolution of the alumina crucible. The choice of flux scarcely affected it, but silica concentration did (Tables 7.2 or 7.3). A slag with large silica content gave smaller dissolution of alumina, though it was slightly risky to judge from the small number of experiments.

7.4. Application of a Kinetic Model

The transition curve of P and Si concentrations in the medium silicon run (Figure 7.4) strongly suggests that the two reaction affect each other, because it is difficult to explain the delay of the phosphorus reaction in the early stage from a straightforward consideration as an independent reaction. Therefore a kinetic model which takes coupled reactions into account has been applied to interpret the experimental results.

1) Kinetic Model

The available kinetic models in which the coupled reactions can be handled quantitatively are those of Lu[80], Kawai[76] and Robertson[77]. Lu applied irreversible thermodynamics to slag/metal reactions based on the electrochemical potentials[80].

However it is virtually impossible to determine all the phenomenological coefficients in his linear equations in such a complicated case as the present experiments. The present author also thinks the mass transfer kinetics in metal and slag phases is likely to determine the rate rather than the interfacial chemical reactions.

Both the models of Kawai[76] and Robertson[77] are based on the assumption that the kinetics are controlled by mass transfer in both metal and slag phases, assuming equilibrium at the slag/metal interface. In these models the coupling phenomena are taken into account through the interfacial reactions. Kawai and Mori[76] carried out calculations for some relatively simple cases involving simultaneous dephosphorization and desulphurization reactions. Robertson et al[77] carried out similar calculations, using a much more general model. They also introduced a "by-pass" reaction for oxygen transfer through CO bubbles produced during the reactions.

In the present work the kinetic model applied is essentially that of Robertson[77], but modification of the mass balance of slag has been made to cope with the continuous feeding of the powdered flux. In order to facilitate the calculations some simplifications have also been made. The present simplified model is fully explained in the next section.

CO gas evolution has been evaluated by assuming a phenomenological rate parameter for CO reaction instead of the "by-pass " reaction of oxygen transfer through the CO bubbles. The rate of CO evolution in the present calculation corresponds to the by-pass oxygen transfer in the original model[77] from point of view of oxygen evolution as CO.

2) Formulation

The reactions considered in this work (Figure 7.8) are as follows:

$$\underline{Si} + 2O = (SiO_2) \qquad K_{Si} = \frac{\gamma_{SiO_2} \cdot (SiO_2)}{f_{Si} \cdot \%\underline{Si} \cdot a_{0\%}^2} \tag{7.1}$$

$$\underline{P} + 2.5O = (PO_{2.5}) \qquad K_P = \frac{\gamma_{PO_{2.5}} \cdot (PO_{2.5})}{f_P \cdot \%\underline{P} \cdot a_{0\%}^{2.5}} \tag{7.2}$$

$$Fe + O = (FeO) \qquad K_{Fe} = \frac{\gamma_{FeO} \cdot (FeO)}{a_{Fe} \cdot a_{0\%}} \tag{7.3}$$

$$\underline{C} + O = CO \uparrow \qquad K_C = \frac{P_{CO}}{f_C \cdot \%\underline{C} \cdot a_{0\%}} \tag{7.4}$$

$$\underline{S} + (CaO) = (CaS) + O \qquad K_S = \frac{\gamma_{CaS} \cdot (CaS) \cdot a_{0\%}}{f_S \cdot \%\underline{S} \cdot \gamma_{CaO} \cdot (CaO)} \tag{7.5}$$

where $a_{0\%}$ is the Henrian activity of oxygen based on the weight % solution in iron. Concentrations in metal phase are in terms of weight %, while oxides and sulphide in slag phase are in terms of molecular fractions.

In the model[77] it is assumed that the chemical reactions at interface are rapid and equilibrated at any time, and that the reaction rates are determined by mass transfer kinetics in both metal and slag phases.

In the model calculations the iron oxide in the slag was treated as ferrous oxide rather than ferric oxide which was used in the experiments. This was done, because at elevated temperature ferric oxide is unstable, and because CO gas bubbles may reduce the ferric

oxide in the slag to ferrous oxide. This treatment of iron oxide brings on underestimation of the oxygen amount supplied by powder feeding. However this is rather realistic, if one considers the oxygen consumption due to CO_2 formation and oxidation of Mn and other impurities (Armco iron typically contains 0.3% of manganese).

For the sake of brevity the above equilibrium constants are modified to the effective equilibrium constants (E) expressed in weight % at the interface. These are

$$E_{Si} = \frac{(\%SiO_2)^*}{\%\underline{Si}^* . a_{0\%}^{*2}} = \frac{100\, C_t \cdot M_{SiO_2} \cdot f_{Si} \cdot K_{Si}}{\rho_s \cdot \gamma_{SiO_2}} \qquad (7.6)$$

$$E_P = \frac{(\%PO_{2.5})^*}{\%\underline{P}^* . a_{0\%}^{*2.5}} = \frac{100\, C_t \cdot M_{PO_{2.5}} \cdot f_P \cdot K_P}{\rho_s \cdot \gamma_{PO_{2.5}}} \qquad (7.7)$$

$$E_{Fe} = \frac{(\%FeO)}{a_{0\%}^*} = \frac{100\, C_t \cdot M_{FeO} \cdot a_{Fe} \cdot K_{Fe}}{\rho_s \cdot \gamma_{FeO}} \qquad (7.8)$$

$$E_C = \frac{P_{CO}^*}{\%\underline{C}^* . a_{0\%}^*} = f_C \cdot K_C \qquad (7.9)$$

$$E_S = \frac{(\%CaS)^* . a_{0\%}^*}{\%\underline{S}^* . (\%CaO)^*} = \frac{M_{CaS} \cdot f_S \cdot \gamma_{CaO} \cdot K_S}{M_{CaO} \cdot \gamma_{CaS}} \qquad (7.10)$$

where (%i) is weight % of i component in slag, and C_t is the total molecular concentration (total molecule/volume) in slag. Asterisks denote the interfacial values. Oxygen activity $a_{0\%}^*$ can be written as

$$a_{0\%}^* = f_0 \cdot \%\underline{O}^* \qquad (7.11)$$

The rate of each reaction can be written using the following flux density equations based on mass transfer kinetics. Fe concentration in metal and CaO concentration in slag are assumed to be effectively the same at the bulk and at the interface, $(\%Fe^b = \%Fe^*, (\%CaO)^b = (\%CaO)^*)$.

$$J_{Si} = F_{Si}(\%\underline{Si}^b - \%\underline{Si}^*) = F_{SiO_2}\,((\%SiO_2)^* - (\%SiO_2)^b) \tag{7.12}$$

$$J_P = F_P(\%\underline{P}^b - \%\underline{P}^*) = F_{PO_{2.5}}\,((\%PO_{2.5})^* - (\%PO_{2.5})^b) \tag{7.13}$$

$$J_S = F_S(\%\underline{S}^b - \%\underline{S}^*) = F_{CaS}\,((\%CaS)^* - (\%CaS)^b) \tag{7.14}$$

$$J_{Fe} = F_{FeO}\,((\%FeO)^* - (\%FeO)^b) \tag{7.15}$$

$$J_C = F_C(\%\underline{C}^b - \%\underline{C}^*) = G_{CO}\,(P^*_{CO}/P_1 - 1) \qquad (P_1 = 1\ \text{atm}) \tag{7.16}$$

$$J_O = F_O(\%\underline{O}^b - \%\underline{O}^*) \tag{7.17}$$

Where J_i is the molecular flux density of i across the interface (mol/cm^2s), and F_i is the modified mass transfer coefficient (mol/cm^2s for 1 wt. % driving force) of i, which is given by

$$F_i = k_i.\rho/(100\ M_i) \tag{7.18}$$

where k_i is the usual mass transfer coefficient defined by mole/volume concentrations, and ρ is the density of either metal or slag phases.

From the condition of electro-neutrality (or balance of oxygen) one can obtain the next relation for the simultaneous reactions.

$$2J_{Si} + 2.5J_P - J_S + J_{Fe} + J_C - J_O = 0 \tag{7.19}$$

The flux density equation of carbon (Equation 7.16) has been derived by the following assumption. It is assumed that effective CO gas evolution per unit reaction area is proportional to the CO supersaturation ratio at the interface $((P^*_{CO} - 1 \text{ atm})/1 \text{ atm})$. The proportionality constant, which is the phenomenological rate constant for CO gas evolution, is denoted by G_{CO}. G_{CO} has the units of mol/cm^2s for unit supersaturation ratio.

It should be noted that CO gas evolution considered here includes all the CO evolution not only at the nominal slag/metal interface but also at the crucible surface and in the bulk metal phase. The value of G_{CO} can be estimated by comparison of the simulation for decarburization or iron oxide consumption with the experimental results. Equation 7.16 gives supersaturation pressure of CO, which corresponds to the oxygen activity at the interface, according to the carbon reaction rate. In the simulation some cases (low silicon metal) give very high supersaturation pressure (as high as 50 atm at maximum). This high supersaturation is acceptable, because very high supersaturation pressure was experimentally measured for nucleation of CO gas bubbles[83] at low oxygen potentials. Once a gas bubble is nucleated at the slag/metal interface, the supersaturation pressure will drop in the vicinity, but the formation of the bubble will also break the slag/metal contact. Therefore the effective CO supersaturation for the slag/metal reactions remains high, even if CO gas generation occurs.

Using the equations described hitherto, one can calculate the interfacial concentrations from the bulk concentrations under given kinetic and equilibrium constants and some other necessary

data. Eliminating the interfacial concentrations using Equations 7.6~7.17 and substituting the flux densities to Equation 7.19, one can ultimately obtain an algebraic equation for one unknown quantity, for example $a^*_{O\%}$. The final equation can be solved numerically. In the present calculation the bisection method was used. Then one can calculate every interfacial value.

Using the interfacial values obtained, one can calculate the mass transfer of each component and the resultant concentration change during a small time step Δt.

The concentration change ($\Delta\%\underline{i}$) of component i in metal phase (except oxygen) is given by

$$V_m \cdot \Delta\%\underline{i} / \Delta t = A.k_i \, (\%\underline{i}^* - \%\underline{i}^b) \qquad (7.20)$$

where V_m is volume of the metal, and A is the reaction area. In the present work, oxygen concentration in bulk metal is assumed to be that determined by $\underline{C} + \underline{O} = CO$ (1 atm) reaction.

For the slag phase the mass change of each component (ΔW_i) is given by

$$100 \, \Delta W_i/\Delta t = A. \, k_i \cdot \rho_s((\%i)^* - (\%i)^b) + P_{in} \cdot (\%i)_{pow} \qquad (7.21)$$

where P_{in} and $(\%i)_{pow}$ are respectively powder injection rate and weight percents of i in the powder.

Thus, making use of Equations 7.20 and 7.21, one can obtain new bulk concentrations, and can move to the calculation of the next time step. In the present work, time steps used are 0.01s (in the early stage of powder feeding)~1s. The list of the

computer program DSP8 is given in Appendix A.2.

3) Calculation Data

Typical data for model calculations are given in Table 7.5. These values were used in the present simulations, unless specifically mentioned.

The mass transfer rate constants were estimated from the desulphurization experiments described in Chapter 5 (overall mass transfer rate constant measured was 0.03 cm/s) with consideration of the different temperature and slag composition.

Decarburization rate and the resultant iron oxide contents in the slag depends on the value of the phenomenological rate parameter for CO evolution (G_{CO}). This will be shown later. The G_{CO} value was determined so that the model simulation could reproduce the experimental decarburization curve and the final iron oxide contents in the slag for the low Si standard runs. The determined value is 0.3×10^{-6} mol/cm^{2}s.

Equilibrium constants were evaluated from thermodynamic data or from the slag and metal analysis results in the present experiments. The experimental results show a very low silicon level in the metal (less than the analytical limit 0.001%), so that the modified equilibrium constant E_{Si} must be very large, though it cannot be estimated from the experimental results. From thermodynamic data[84,85a] the equilibrium constant of silicon reaction (Equation 7.1) is given by $K_{Si} = 10^7$. Modifying it to the effective equilibrium constant (Equation 7.6) using $f_{Si} = 12$ and $\gamma_{SiO_2} = 0.1$, we derived $E_{Si} = 10^{11}$, where f_{Si} is estimated from the

interaction coefficients[85a,86], and the γ_{SiO_2} value was estimated, as the basicity of the present flux is very high. The E_{Si} value may be even larger than the deduced value, if formation of dicalcium silicate is taken into account.

The E_p value can be estimated as $10^9 \sim 10^{10}$ from the results of the final slag and metal analyses, where time difference between the slag and metal samplings was taken into account. The solubility limit of CaO in the present flux is thought to be small. The present experimental temperature was less than the eutectic temperature of the CaF_2-CaO binary system[81], and the CaO solubility limit in a $CaCl_2$ melt is only 14.4% at 1350°C (estimated by Inoue et al[87]). Therefore, solid CaO particles may have been suspended in the present slag. Even if this was not so, the CaO activity in the slag must have been very high (almost that of pure solid CaO). Winkler and Chipman[88] determined the equilibrium constant for the dephosphorization reaction ($2\underline{P} + 5\underline{O} + 4CaO = 4CaO.P_2O_5$). Assuming the CaO activity is almost unity, one can obtain $K_p = 10^{7.7}$ from their relation. Also, the equilibrium constant of solid tetra-calcium phosphate formation from solid CaO, $\underline{P}$ and $\underline{O}$[85b] gave a similar value for K_p. Furthermore, it is reported that phosphate capacity (defined by $(\text{wt\% P})/f_P.\%\underline{P}.a_{0\%}^{2.5}$) of CaO-$CaF_2$ slag at 1365°C is 10^9[89]. Therefore the effective modified equilibrium constant E_p was determined as 10^9.

Some other data[82,90a-92] for phosphorus equilibrium are available, but these are not applicable mainly because of the different slag compositions, especially their high silica contents.

The equilibrium constants for FeO reaction was estimated from

the thermodynamic data[84,85a], and K_{Fe} was derived as 29. Using $a_{Fe} = 0.7$[93] and $\gamma_{FeO} = 3$, the modified equilibrium constant is given by $E_{Fe} = 500$. the γ_{FeO} value was estimated in the following manner. The activity coefficient of FeO in 25 wt % CaO - 75 wt % CaF_2 slag at 1460°C is 2 according to the measurements made by Kay et al[94]. $CaCl_2$ also increases the FeO activity as well as CaF_2, and the measured value of γ_{FeO} in 30 mol % CaO - 70 mol % $CaCl_2$ slag at 1300°C is approximately 3[95]. The effect of CaF_2 and $CaCl_2$ is more significant at low temperature. From these data, $\gamma_{FeO} = 3$ was adopted.

E_C was derived from thermodynamic data[84,85a], where f_C used was 4[85a,86]. E_C was 2000.

For the sulphur reaction the E_S value can be calculated from the analysis results, and it is approximately 0.007. On the other hand, thermodynamic data[84,85a] gives the estimation of $E_S = 0.03$, where γ_{CaO} is assumed to be equal to γ_{CaS}, and f_S is 3. From the value of the sulphide capacity of CaO-CaF_2 slag[89], one can deduce the similar E_S value to that obtained from thermodynamic data. Ultimately $E_S = 0.015$ was chosen for the model simulation.

The activity coefficient of oxygen (f_O) was assumed to be one. The reported value of the interaction coefficient of C to the oxygen activity in molten high carbon iron (C is more than 4%) are scattered between -0.32 and +0.1[96], and the f_O value affects the oxygen flux in metal (Equation 7.17). However this oxygen flux in the metal is always very small when compared with the other reactions in which oxygen is supplied or consumed. For example, in the medium Si case the oxygen flux due to the FeO transfer is

25~500 times as large as that in the metal.

Consequently the f_O value does not affect the interfacial oxygen activity, and the only noticeable effect of f_O is on the oxygen concentrations at the interface and in the bulk metal.

7.5. Results of Model Simulation and Discussion

1) Results and Discussion

Using the data given in Table 7.5, model simulations of the standard low Si, medium Si and high Si runs have been carried out, and the results are shown in Figures 7.9~7.11. As is seen from the figures, the present model simulations successfully reproduce most of the characteristics of the experimental results.

The silicon and sulphur concentrations decrease from the beginning in all the cases, while the phosphorus concentration decreases immediately only in the case of low Si metal (Figure 7.9). In the medium Si case (Figure 7.10) the delay of dephosphorization in the early stage is seen, and in the high Si case (Figure 7.11) dephosphorization occurred only slightly in the very late stage of powder feeding, being followed by the reversion thereafter. On the other hand the sulphur content shows a further decrease after the end of powder feeding, corresponding to the reduction of FeO. These features agree with the experimental results very well, though the strict quantitative comparison gives some discrepancy in the magnitudes.

The delay of dephosphorization in the medium and high Si simulations occurs because the desiliconization reaction solely

consumes most of the oxygen supplied from the powder feeding and from the sulphur reactions, and keeps oxygen activity at the slag/metal interface low. The oxygen activity at the interface is shown in the top of the figure. It is seen that the oxygen activity is low during the vigorous desiliconization. After slow-down in the silicon reaction the oxygen activity increases, and the dephosphorization begins. The desiliconization rates during the delay of the phosphorus reaction in the medium and the high Si cases give almost the same constant value despite the large difference in their silicon levels. This suggests that the feeding of iron oxide determines the rate of the silicon reaction which consumes most of the oxygen during this stage.

In the medium Si case the delay of the dephosphorization in the simulation is shorter than that in the experiment. This is partly because the effect of the slag basicity is not taken into account in the model simulation. It is expected that the silica concentration at the interface should be high under significant desiliconization reaction, and that the high silica concentration should reduce the effective phosphorus distribution. Harashima et al[97] measured the distribution coefficient of phosphorus between $CaO-CaF_2-CaCl_2$ flux and hot metal, and found that the effect of the silica in the slag could be understood using the basicity B defined by (mol % CaO) / (2 (mol % SiO_2) + 3 (mol % P_2O_5)). This characteristic basicity is based on the release and capture of oxygen ions between the basic and acid components. From their experimental results, the present author obtained a relation of $E_p \propto B^{7.7}$ over the range B = 0.7~1.3. Using this relation at the interfacial equilibrium ($E_p = 10^6 \times B^{7.7}$), a model simulation

was carried out, and the result of the dephosphorization curve is given by a broken line in Figure 7.10. Except for the phosphorus concentration no significant change in other quantities was observed. As is seen from the figure, the simulation taking basicity into account gives better agreement with the experimental resutls , i.e. longer delay of dephosphorization in the early stage and smaller phosphorus reversion after the end of the powder feeding.

Reversion of phosphorus can be seen both in the experiments and in the simulations. However the model simulations give much larger reversion. As described above, the effect of the basicity reduces the reversion to some extent, but still not enough. The small reversion of phosphorus in the experiments may be due to some effect which is not taken into account in the model, such as inactivation of part of the slag due to splashing and solidifying, change of slag composition (alumina dissolution) or effect of manganese oxide.

In Figures 7.9 and 7.10 a flat zone of the desulphurization curve is seen in the period of from 400 sec to 750 sec. The corresponding flat zone is also observed in the experimental results (Figures 7.2 and 7.4). This flat zone is formed in response to the rise in the oxygen activity at the interface. For the small value of G_{CO} in Figure 7.12 the flat zone becomes a bump, corresponding to a large peak in the oxygen activity. This bump is also very noticeable in the case where the mass transfer rate constants are made high (Figure 7.13), because the sulphur concentration reflects the interfacial equilibrium more quickly.

The decrease in carbon concentration in the case of the simula-

tion of a high Si run is very small as is the case of the experiments. In the case of a medium Si simulation, decarburization occurs after some delay. This delay is more significant in the case with large mass transfer rate constants (Figure 7.13).

2) Effect of the Basic Data

The derivation of the various values used in the calculations was described earlier. However some of the values chosen are not necessarily correct because of the uncertainties in the thermodynamic data and/or the experimental results. Therefore calculations were carried out so as to study the effect of each quantity.

Figure 7.12 shows the effect of the phenomenological rate parameter for CO evolution G_{CO}. G_{CO} affects the decarburization and CO supersaturation level significantly, and consequently oxygen activity at the interface. The effect on the desulphurization has already been described. The dephosphorization shows a better performance for the smaller value of G_{CO}, and the time that gives the minimum %P delays because of the slowdown in FeO reduction. The slowdown in FeO reduction also leads to a slower rate for the phosphorus reversion.

Figure 7.13 shows the case where the mass transfer coefficients were increased by a factor of two, and other conditions kept the same as those for Figure 7.10. The rate of desulphurization is increased in the early stage corresponding to the increase in the rate constant. The flat zone of the dephosphorization and decarburization curves in the early stage become clearer in this case. The rate of desiliconization in the early stage is almost the same as in the case of Figure 7.10., because supply of oxygen dominates

the rate. It is seen from the figures that the selective progress of the reactions is more distinct in the case of the large rate constants for the slag/metal reactions. The priority in the oxidation reactions is desiliconization > dephosphorization > decarburization in this case.

The effects of the other parameters have been also simulated by changing each parameter by a factor of 3 and 1/3 against the standard value. Change of the equilibrium constant E_{Si} scarcely affects the results, because the silicon concentration at the interface is very low in any case thanks to the large E_{Si} value. The equilibrium constant E_P affects the dephosphorization curve, but the main characteristics do not change.

The E_{Fe} value affects only FeO content in slag, and has no effect on other quantities, because the oxygen activity at the interface remains almost the same. Desulphurization depends on the E_S value, but the other quantities are hardly affected. The characteristics of the sulphur reaction do not change either.

The equilibrium constant E_C for carbon reaction affects the dephosphorization, desulphurization and decarburization reactions through the effect on the interfacial oxygen activity. However changing E_C does not alter the qualitative behaviour. In any case the thermodynamic data for CO reaction is considered to be reliable. The effect of the activity coefficient for oxygen f_O is very small as mentioned earlier, because oxygen flux in the metal is negligible when compared with oxygen supply and consumption from the other reactions.

3) Simulation of Powder Dumping and Effect of Feeding Period

To illustrate the usefulness of the full understanding of the reactions achieved using the kinetic model it was decided to use the model to predict the effect of injection period on the simultaneous dephosphorization and desulphurization using CaO-based flux. The results should be useful in the design of further small scale or full scale tests on the process.

The case of powder dumping was simulated by setting the powder feeding period as 70 sec, thus taking the time required for powder melting into account. As long as the feeding period is enough small, the results do not change very much.

The results with three levels of Si are shown in Figure 7.14. As is seen from the figure, dephosphorization occurs from the beginning without regard to the initial silicon level. Decarburization also occurs from the beginning. These results are in great contrast to the case of powder feeding (Figures 7.9~7.11).

As is seen in Figure 7.14, the dephosphorization curve is not affected by the initial Si level up to 150 sec. This suggests that phosphorus transfer itself determines the dephosphorization rate up to 150 sec. In the case of powder dumping the silicon reaction cannot consume all the oxygen, unlike the early stage of the powder feeding (Figures 7.10 ~ 7.13), as a large amount of iron oxide is provided in the early stage. Even the combined silicon and phosphorus reactions cannot consume the iron oxide provided. Therefore, the interfacial oxygen activity increases, and the decarburization reaction proceeds at the same time.

The effect of the silicon level on the dephosphorization is smaller in the powder dumping (Figure 7.14) than in the powder feeding simulations (Figure 7.9 ~ 7.11). This can be explained as follows. In the case of powder feeding, phosphorus concentration is relatively close to the transient equilibrium at the interface. The silicon level influences the interfacial equilibrium very much through the interfacial oxygen activity. On the other hand the oxygen input from the powder is so large in the case of the early stage of the powder dumping simulation that the effect of the silicon reaction on the interfacial oxygen activity is small. Consequently Si level affects less in the case of powder dumping than in powder feeding.

Figure 7.15 shows the effect of the powder feeding period using a constant total amount of powder (180g) on the dephosphorization curve and the interfacial oxygen activity. In the case of the short injection period (less than 150 sec), the dephosphorization curve follows the same route up to 200 sec. During this period the phosphorus reaction (mass transfer kinetics of phosphorus) solely determines the rate of phosphorus removal. For the longer injection period than 300 sec, the rate of powder feeding becomes important as a rate determining process.

This fact can be explained on the ternary diagram of kinetics during powder injection (Figure 6.8) described in Chapter 6. The mixing time of the bulk phase is assumed to be negligible. For injection periods shorter than 150 sec the time to feed sufficient powder is so small that the reaction kinetics (mass transfer) solely determine the total rate (Vertex 2, reaction at interface determining the rate). With increase in the injection period, i.e. decrease in

the injection rate, the importance of the powder feeding rate increases, and the rate of the powder feeding affects the total reaction rate (between Vertices 1 and 2, reaction at interface and powder feeding determine the kinetics].

As is seen from Figure 7.15, the cases where the powder feeding period is between 700 and 1000 sec give the lowest value for the minimum phosphorus concentration. In the case of a shorter injection period, the interfacial oxygen activity is very high in the early stage, but sufficient phosphorus removal cannot be achieved during this short period due to the limitation of the mass transfer kinetics. On the other hand in the case of very long injection period, the bulk phosphorus concentration is almost equilibrated to the interfacial value, but the interfacial oxygen activity cannot be sufficiently high, because the iron oxide in the slag is reduced gradually by the carbon reaction during the long powder feeding period.

7.6. Concluding Remarks

Experiments were carried out using surface powder feeding to clarify the effect of silicon on the kinetics of the simultaneous dephosphorization and desulphurization reactions. In the medium or high Si runs (0.13 and 0.34 wt % respectively) the dephosphorization occurs after the cessation of the vigorous desiliconization reaction, while it proceeds from the beginning in the case of the low Si run (0.02 wt %). Stagnation of the desulphurization was observed during the later half of the powder feeding period.

These characteristics obtained in the experiments can be interpreted using a kinetic model [77] taking coupled reactions into account.

The effect of powder feeding period was examined theoretically using the kinetic model which allowed a proper consideration of the rate determining processes.

List of Symbols. Chapter 7

A reaction area (cm^2)

a activity

$a^*_{0\%}$ Henrian activity of oxygen at slag/metal interface based on weight % solution

B characteristic basicity[97]

C_t total molecular concentration in slag (mol/cm^3)

E modified equilibrium constant defined by Equations 7.6~7.10

F modified mass transfer rate constant defined by Equation 7.18 (mol/cm^2s)

f Henrian activity coefficient as standard of 1 wt %

G_{CO} phenomenological rate parameter for CO evolution (mol/cm^2s)

i component i

%i concentration of i in weight % in metal

(%i) concentration of i in weight % in slag

J molar flux density (mol/cm^2s)

K equilibrium constant

k mass transfer coefficient (cm/s)

M molecular weight (g/mol)

P pressure (atm)

P^*_{CO} supersaturation pressure of CO at interface (atm)

P_{in} powder feeding rate (g/s)

t time (s)

V_m volume of metal (cm^3)

W weight (g)

γ activity coefficient as standard of pure substance

ρ density (g/cm^3)

Subscripts

i component i

in injection or powder feeding

m metal

O% oxygen in weight % solution

pow powder

s slag

Superscripts

b bulk

* at interface

TABLE 7.1 - Summary of Experiments

Run	Metal quantity	Powder composition	Powder quantity	Silicon level	Note
A	3.02 kg	CaFCl	184g	low	standard
B	3.00 kg	CaFCl	145g	low	standard (Powder quantity is small)
C	2.99 kg	CaFCl	180g	medium	%Si = 0.13
D	3.00 kg	CaFCl	180g	high	%Si = 0.34
E	3.01 kg	CaF	180g	low	CaF_2 flux
F	3.02 kg	CaFClNa	182g	low	Na_2CO_3 containing powder

Powder composition (nominal)

CaFCl = 30% CaO - 20% CaF_2 - 20% $CaCl_2$ - 30% Fe_2O_3

CaF = 30% CaO - 40% CaF_2 - 30% Fe_2O_3

CaFClNa= 26% CaO - 17% CaF_2 - 17% $CaCl_2$ - 10% Na_2CO_3 - 30% Fe_2O_3

Temperature = 1350°C

Table 7.2 - Slag Analyses

Sample	Ca	F	Cl	P	S	Si	Al	t-Fe	Fe^{2+}	Fe^{3+}	Na
A	42.6	12.6	17.3	1.12	0.56	0.59	4.28	0.22			
B	42.3	13.6	17.1	1.67	0.63	0.35	4.71	0.31			
C	41.9	12.7	14.1	2.11	0.82	1.80	3.21	0.21			
D	43.3	12.0	13.8	0.19	0.57	3.79	1.98	0.14	0.08	0.06	
E	46.7	23.4	0.65	0.98	0.73	0.49	4.17	0.17			
F	43.7	14.0	11.3	1.10	0.79	0.24	4.73	0.23			0.08
G	53.0	12.1	18.5				0.09				
H	54.2	12.9	19.3				0.07				
I	58.4	27.0	0.33				0.13				

Concentrations are in weight %. Samples G, H and I are fresh powders. The analysis methods are as follows:

Ca, Na -------- Atomic absorption spectroscopy.
Cl -------- Spectrophotometry (mercuric cyanate method).
Fe -------- Potassium dichromate titration.
P -------- Spectrophotometry (molybdenum yellow complex, solvent extraction).
F -------- Selective ion electrode method.
S -------- Combustion, potassium iodate titration.

TABLE 7.3 - Calculated Slag Compositions

Sample	CaO	CaF_2	$CaCl_2$	P_2O_5	CaS	SiO_2	Al_2O_3	FeO	Na_2O
A	26.8	25.9	27.1	2.56	1.38	1.26	8.09	0.28	
B	25.0	27.9	26.8	3.82	1.47	0.75	8.90	0.40	
C	27.9	26.1	22.1	4.83	1.91	3.85	6.07	0.27	
D	31.5	24.7	21.6	0.44	1.33	8.11	3.74	0.18	
E	29.6	48.1	1.0	2.24	1.70	1.05	7.88	0.22	
F	30.8	28.8	17.7	2.52	1.84	0.51	8.94	0.30	0.12
G	41.7	24.8	29.0				0.17		
H	41.5	26.5	30.2				0.13		
I	41.6	55.5	0.52				0.25		

Concentrations are weight %.
Samples G, H and I are fresh powders without Fe_2O_3.

TABLE 7.4 - Calculated Composition of Fresh Powders

Samples	CaO	CaF_2	$CaCl_2$	Al_2O_3	Fe_2O_3	Nominal
G	29.2	17.4	20.3	0.1	30	CaFCl
H	29.1	18.6	21.1	0.1	30	CaFCl
I	29.1	38.9	0.4	0.2	30	CaF

Concentrations are in weight %.

CaFCl = 30% CaO - 20% CaF_2 - 20% $CaCl_2$ - 30% Fe_2O_3

CaF = 30% CaO - 40% CaF_2 - 30% Fe_2O_3

TABLE 7.5 - Data for Model Calculations

Metal weight	3000g
Total amount of powder	180g
Powder feeding period	700s
Powder composition	30%CaO - 30%FeO - 40%(Neutral)
Density metal	$\rho_m = 7 g/cm^3$
slag	$\rho_s = 3 g/cm^3$
Mass transfer rate constants.	
metal phase	$k_m = 0.04$ cm/s
slag phase	$k_s = 0.02$ cm/s
CO evolution	$G_{CO} = 0.3 \times 10^{-6}$ mol/cm^{2}s
Reaction area	$A = 50$ cm^2
Total molecular concentration in slag	$C_t = 0.035$ mol/cm^3
Initial concentrations	$\%\underline{C} = 4.5$
	$\%\underline{P} = 0.1$
	$\%\underline{S} = 0.04$
	$\%\underline{Si} = 0.02$ (low Si metal)
	0.13 (medium Si metal)
	0.34 (high Si metal)
Equilibrium constants	$E_{Si} = 10^{11}$
	$E_P = 10^9$
	$E_S = 0.015$
	$E_{Fe} = 500$
	$E_C = 2000$
Activity coefficient of O	$f_O = 1$

Temperature = 1350°C

	blastfurnace iron	after de-Si	after de-P,S	steel
%Si	0.5	0.1	trace	trace
%P	0.1	0.1	< 0.015	<0.015
%S	0.03	0.03	< 0.015	<0.015
%C	4.5	4.45	4.2	0.1
processes	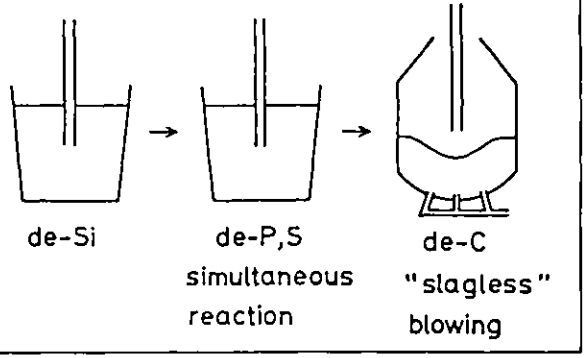			

Fig.7.1. An example of new steelmaking processes using simaltaneous de-P and de-S reactions and "slagless" blowing.

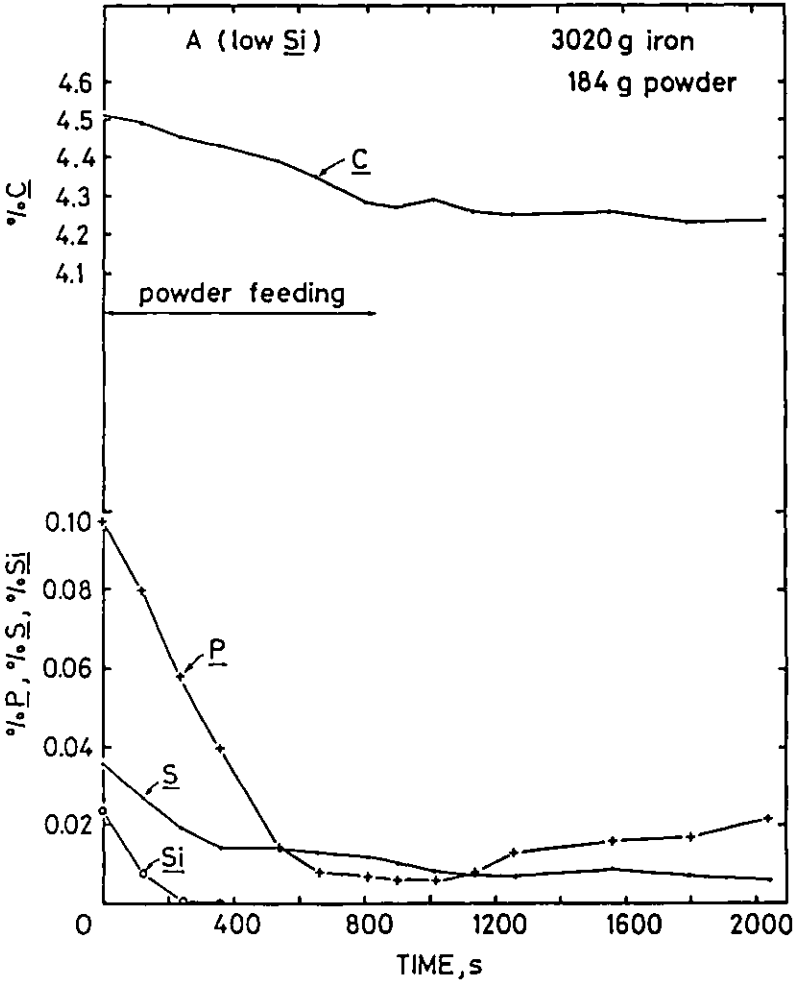

Fig.7.2. Experimental results of Run A.

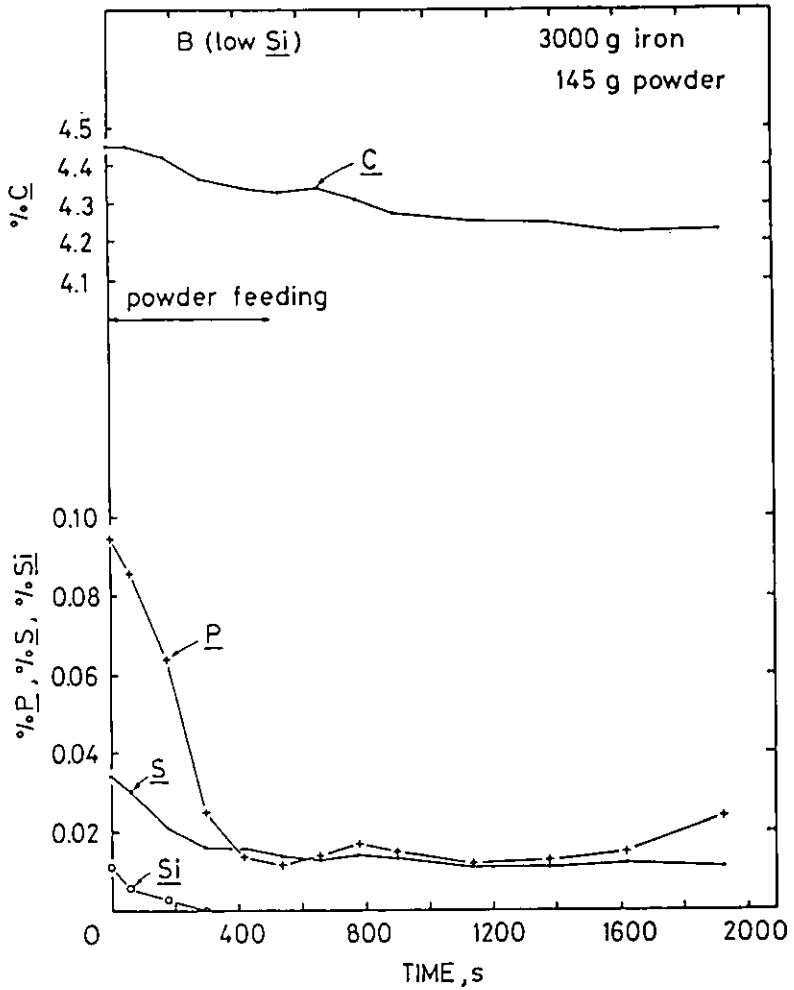

Fig.7.3. Experimental results of Run B.

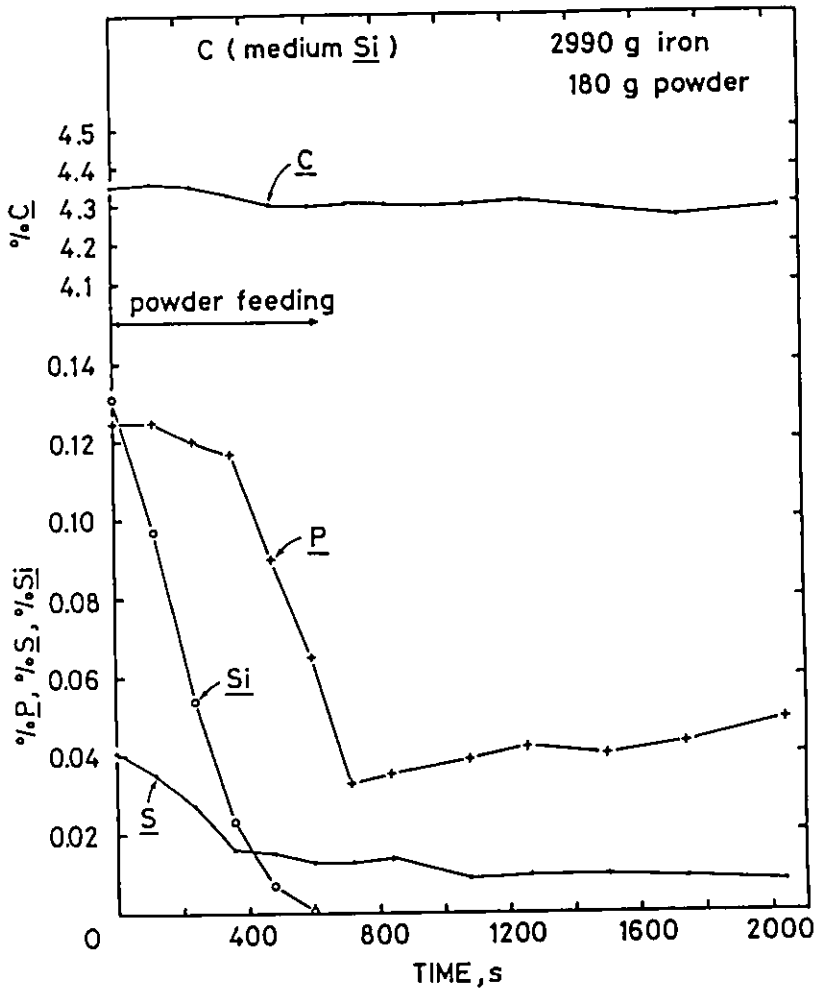

Fig.7.4. Experimental results of Run C.

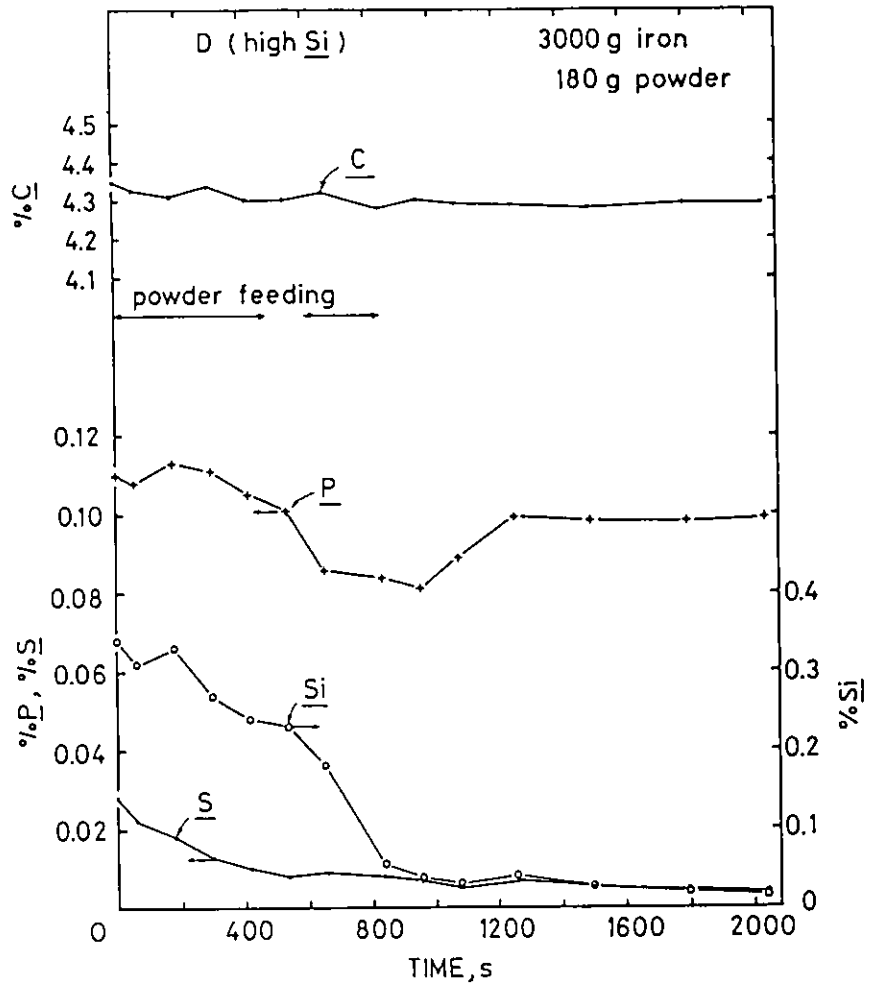

Fig.7.5. Experimental results of Run D.

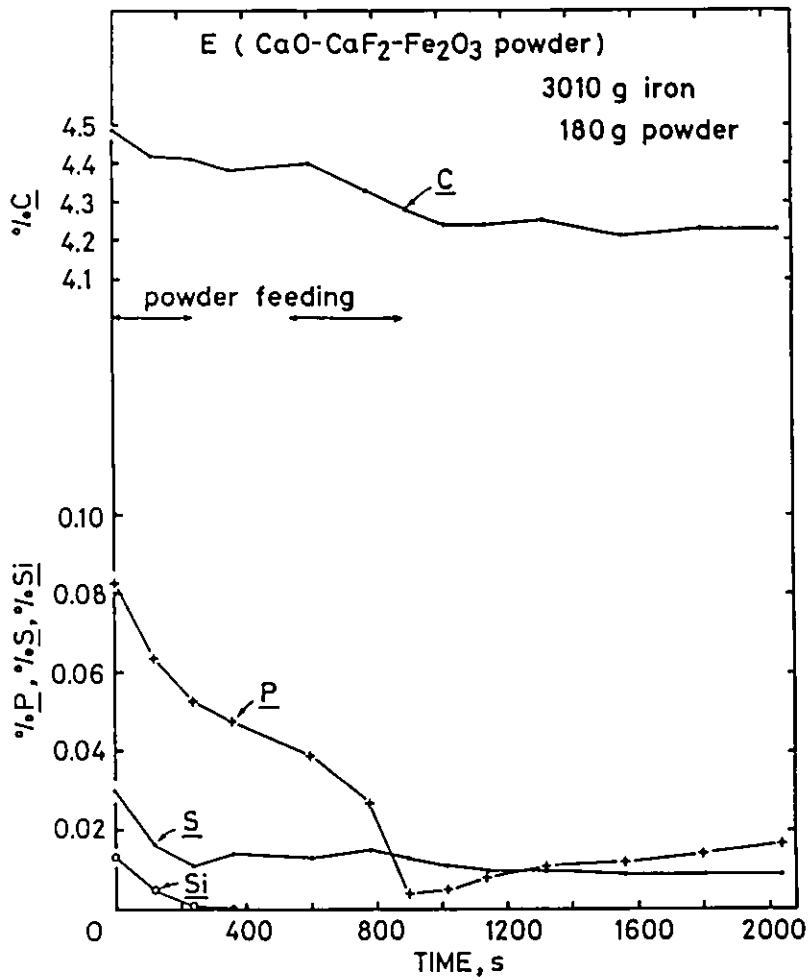

Fig.7.6. Experimental results of Run E.

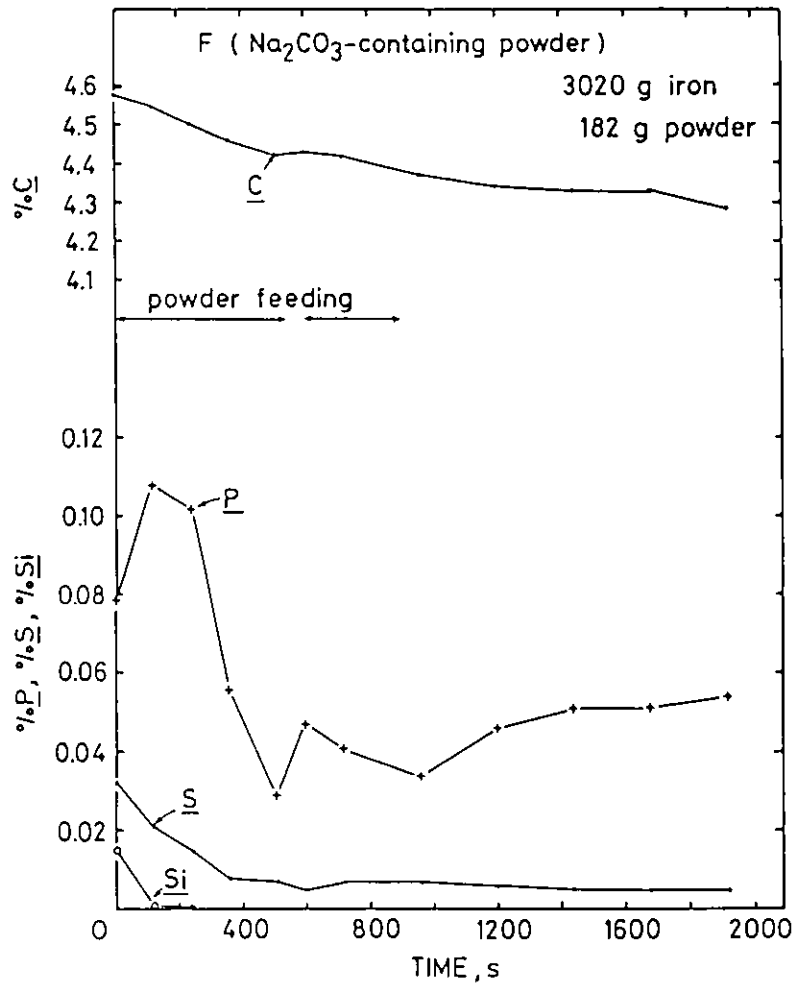

Fig.7.7. Experimental results of Run F.

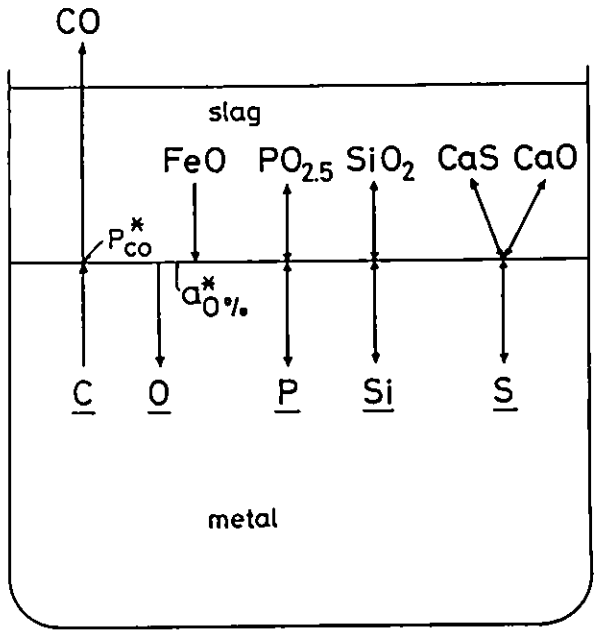

Fig.7.8. Reactions considered in the kinetic model.

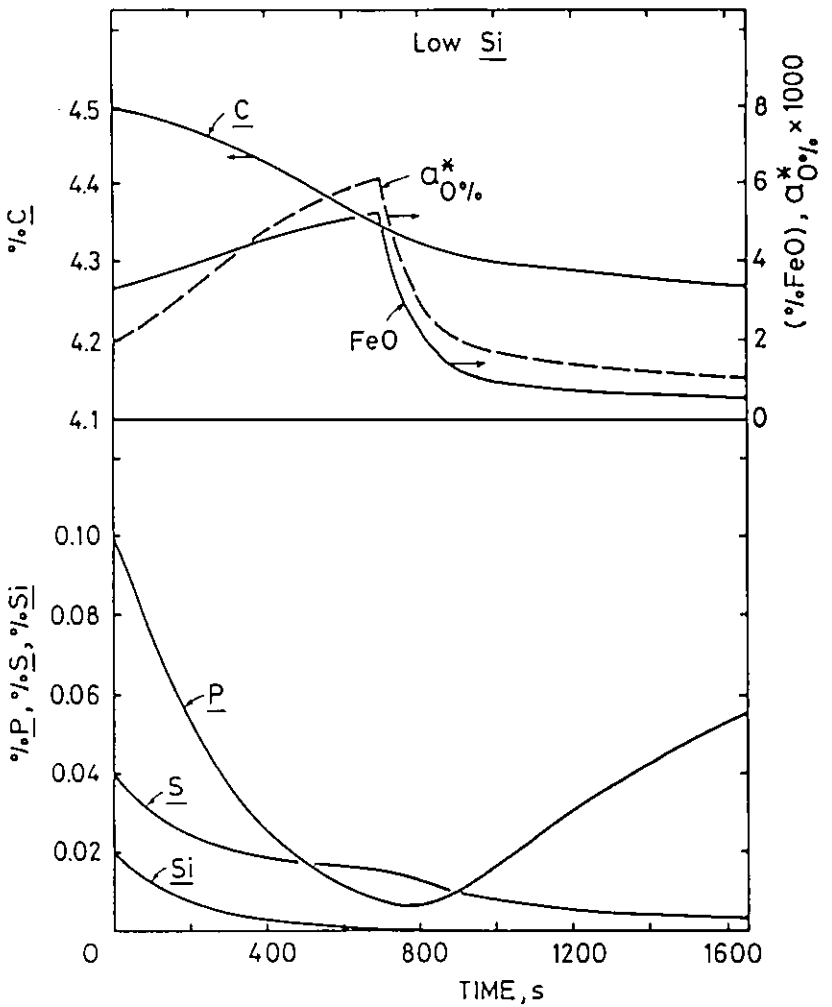

Fig.7.9. Simulation of low Si run.

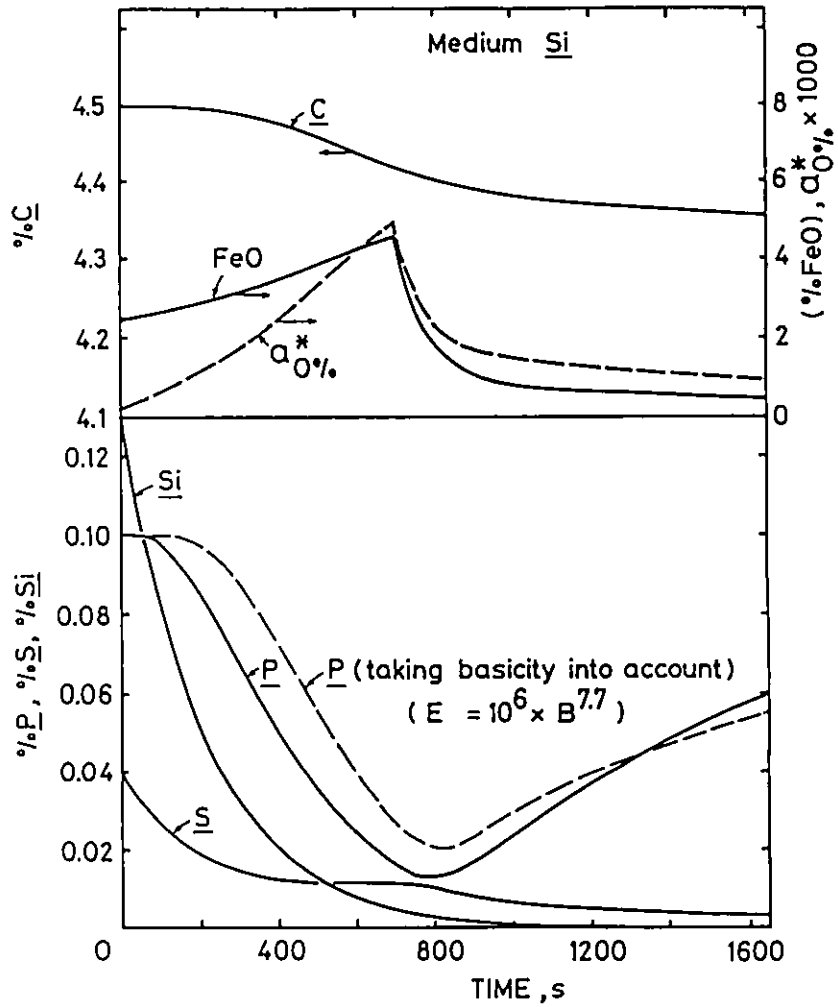

Fig.7.10. Simulation of medium Si run.

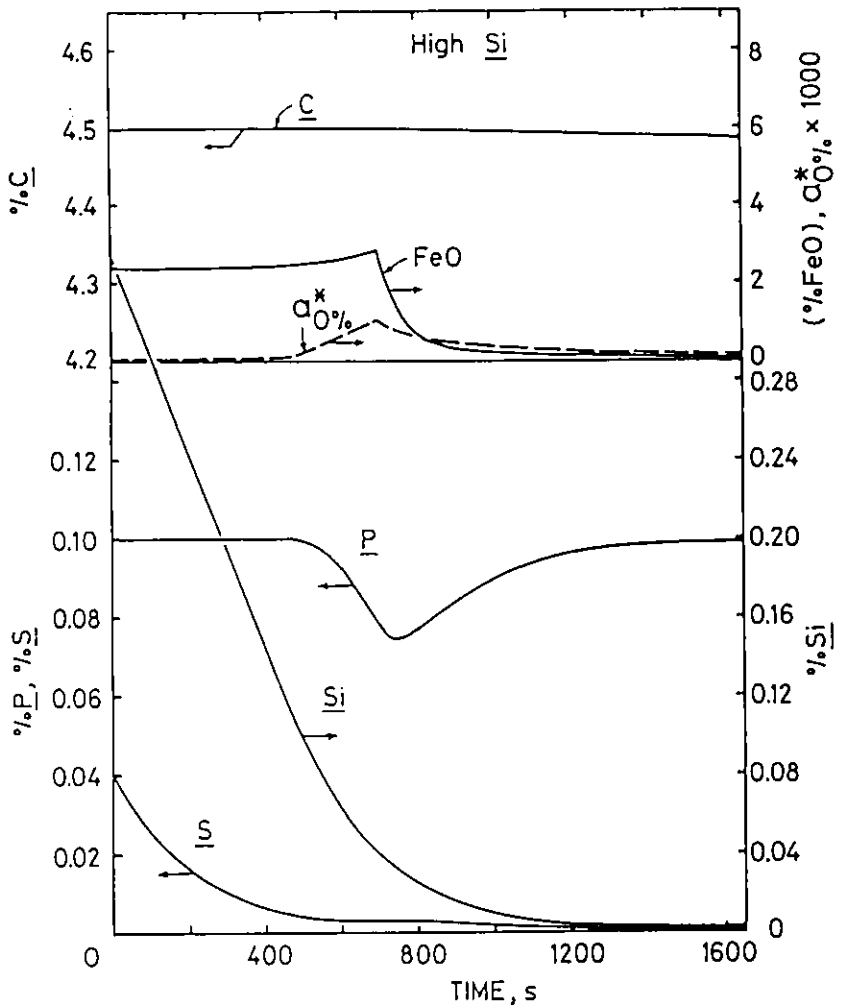

Fig.7.11. Simulation of high Si run.

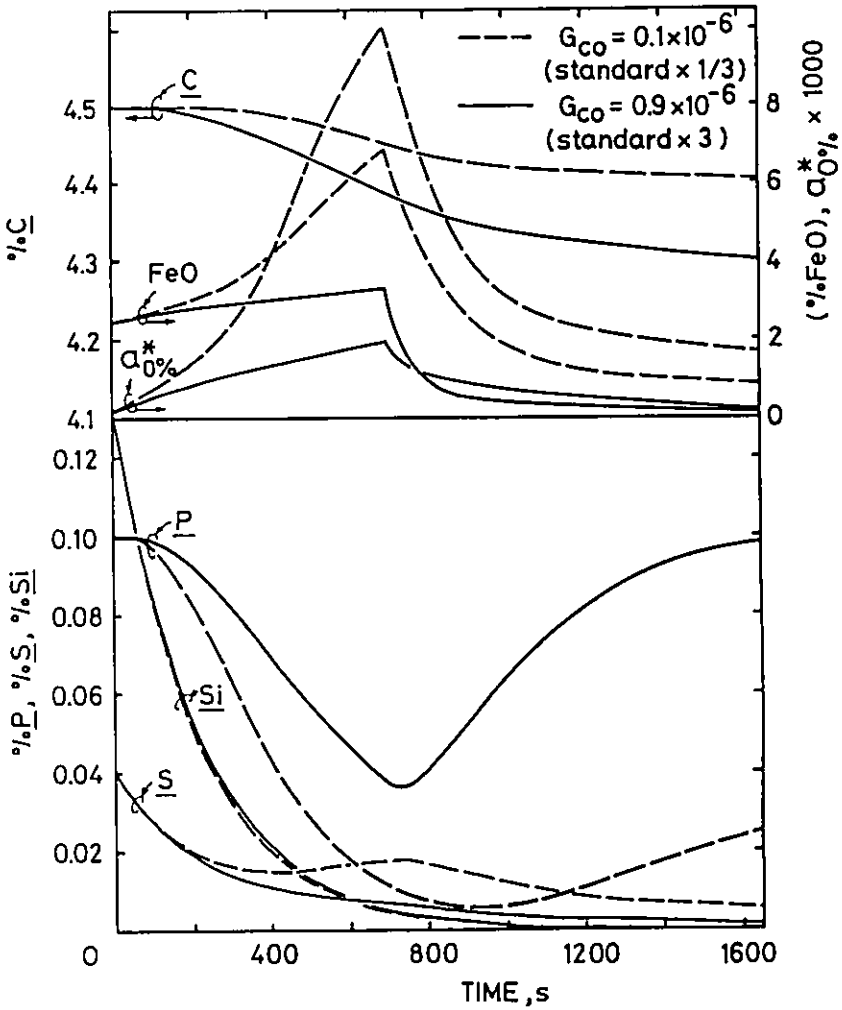

Fig.7.12. Effect of G_{CO}. Medium Si.

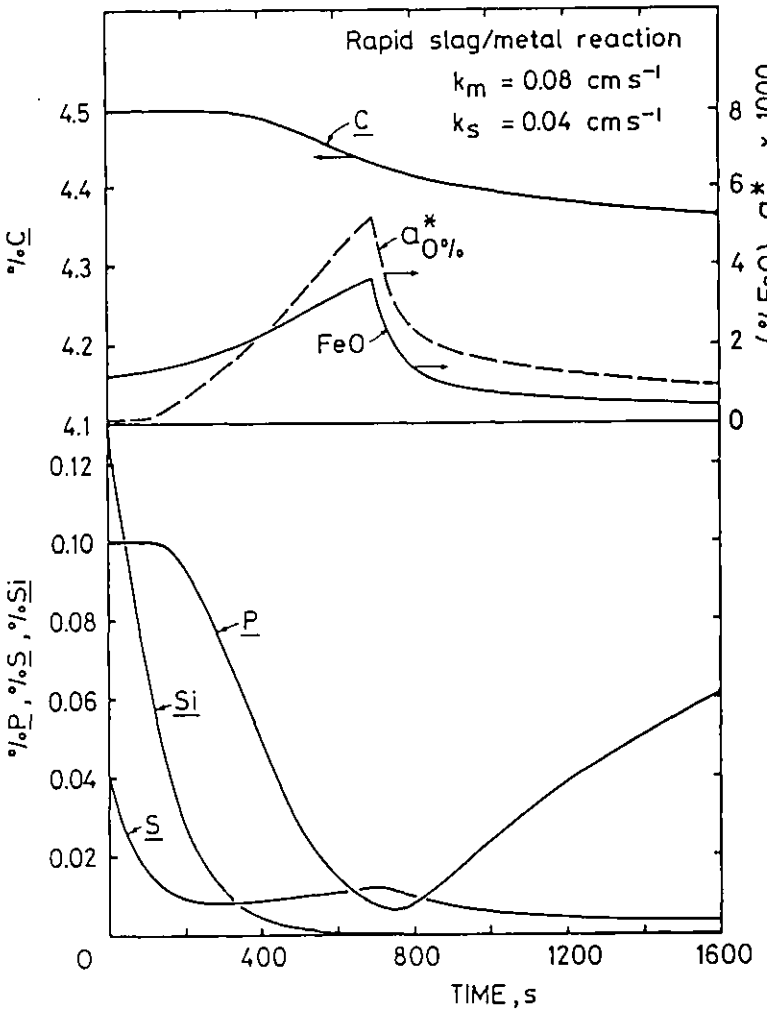

Fig.7.13. Simulation with large mass transfer rate constants. Medium Si.

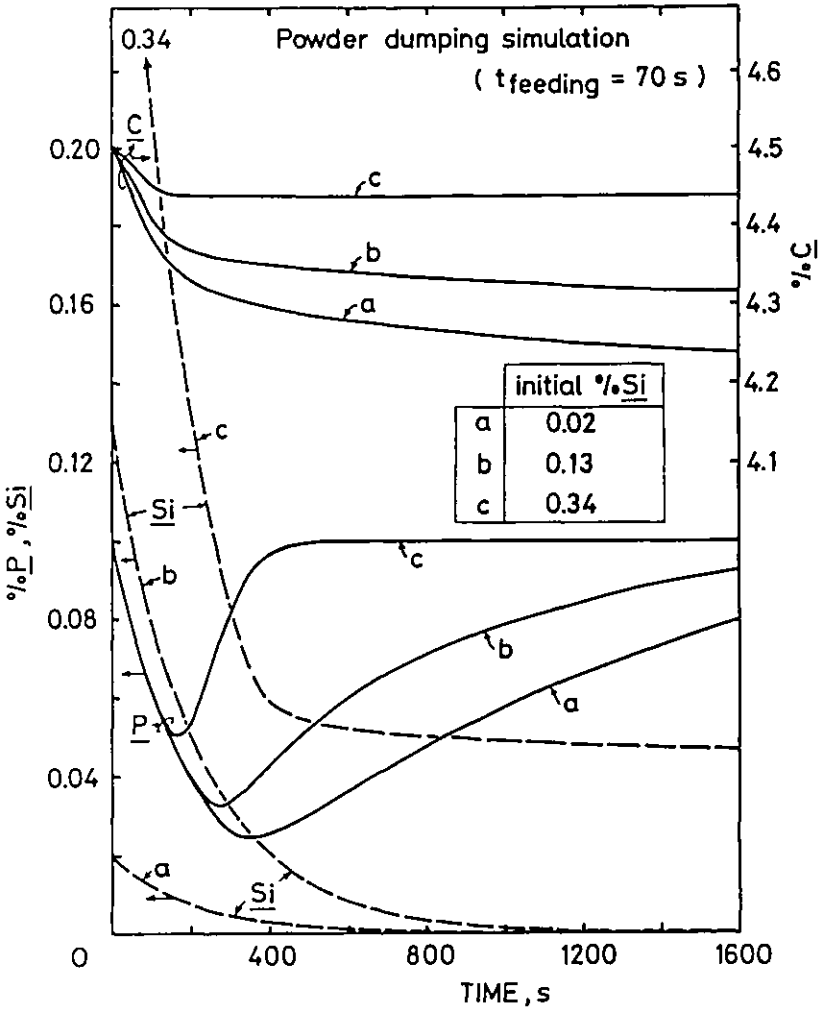

Fig.7.14. Simulation of powder dumping.

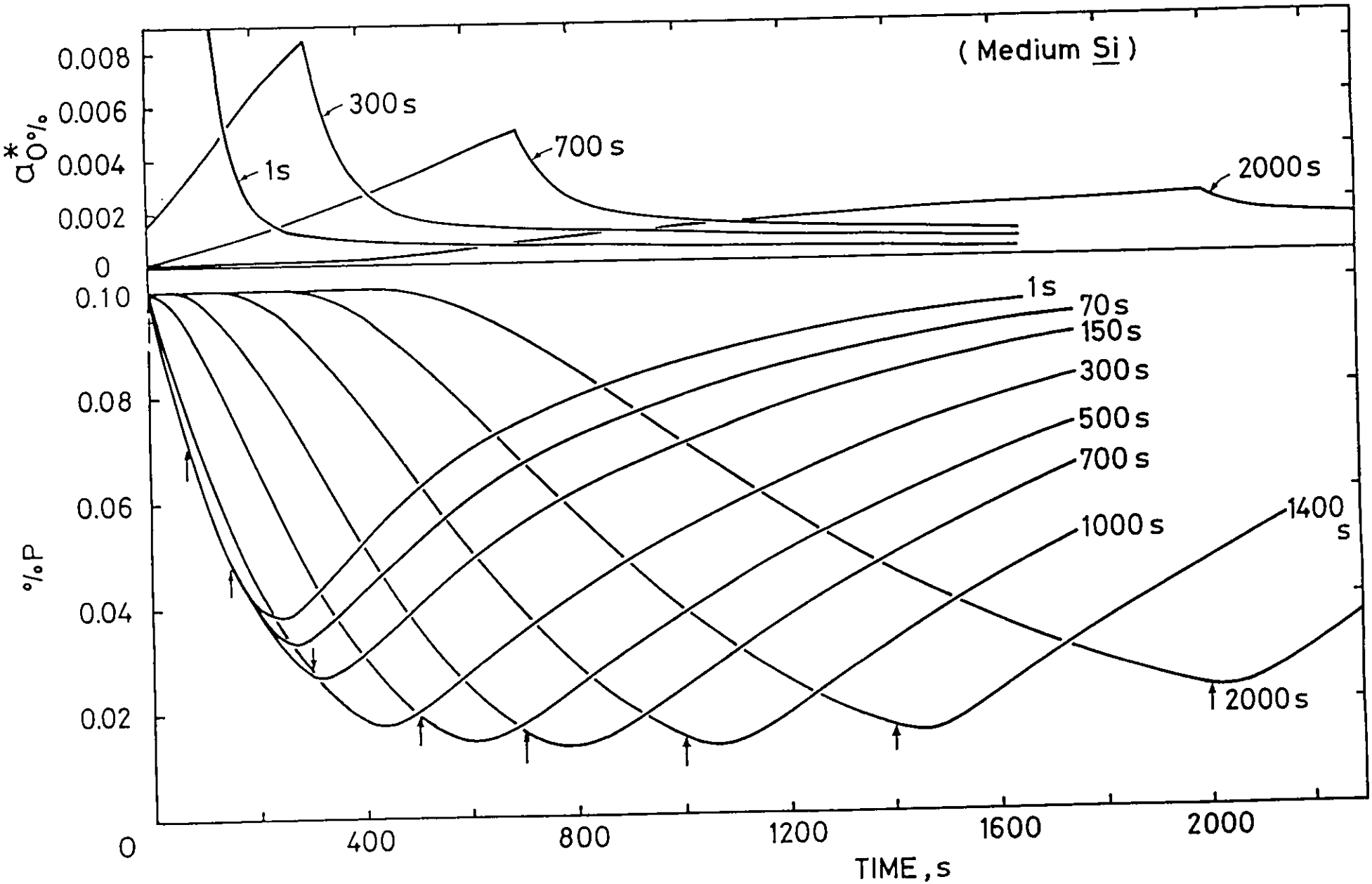

Fig.7.15. Effect of powder feeding period on the dephosphorization curve and the oxygen activity at interface. Vertical arrows indicate end of the powder injection period.

APPENDICES

Appendix A.1 : Derivation of the Finite Difference Equations

There are two ways to derive the finite difference equations i.e. (a) applying the finite difference approximations to the governing differential equations considered and (b) deriving the finite difference expressions directly from considerations of the heat or mass balance on a finite difference cell. In the present work the finite difference equations were derived by both methods, and the two results were shown to be the same. In this chapter, derivation of the equations is shown by both methods for the porous accretion model.

A.1.1. Heat Transfer Equations.

1) Inner mesh points in accretion.

First, the derivation from the differential equations is described. The governing equation is

$$\frac{\partial^2 T}{\partial Z^2} + \frac{\partial^2 T}{\partial r^2} + \frac{1}{r}\frac{\partial T}{\partial r} + \frac{\dot{q}}{k} = 0 \qquad (A.1.1)$$

where $$q = h_v (T_g - T)$$

Making use of the finite difference approximation, we obtain

$$\frac{T_n - 2T_o + T_s}{\Delta Z^2} + \frac{T_e - 2T_o + T_w}{\Delta r^2} + \frac{1}{r}\frac{T_e - T_w}{2\Delta r} + \frac{h_v (T_g - T_o)}{h} = 0$$

where the subscript ö denotes the value at the particular cell considered, and the subscripts n, s, e and w respectively indicate

the neighbouring cells in the north, south, east and west. The list of symbols in Chapter 3 applys to this appendix.

The explicit form with regard to T_o is

$$T_o = [(T_n + T_s)\,\Delta r/\Delta Z + (T_e + T_w)\,\Delta Z/\Delta r + (T_e - T_w) \cdot \Delta Z/2r + h_v.\Delta r.\Delta Z.\,T_g/k] \,/\, (2\Delta r/\Delta Z + 2\Delta Z/\Delta r + h_v\,.\,\Delta r.\,\Delta Z/k) \qquad (A.1.2)$$

Next, the direct derivation method from considerations of the heat balance is explained. The heat balance for a cell shown in Figure A.1.1. is given by

$$k.\,S_n\,(T_n - T_o)/\Delta Z + k.S_s\,(T_s - T_o)/\,\Delta Z + k.\,S_w\,(T_w - T_o)/\Delta r + k.S_e\,(T_e - T_o)/\Delta r + h_v.\,V\,(T_g - T_o) = 0$$

where S_n, S_s, S_e and S_w are the surface areas of the cell on the north, south, east and west sides, and V is the volume of the cells These are

$$S_s = S_n = r.\Delta r.\,\Delta\phi$$
$$S_e = (r + \Delta r/2)\Delta Z.\,\Delta\phi$$
$$S_w = (r - \Delta r/2)\Delta Z.\,\Delta\phi$$
$$V = r.\,\Delta r.\,\Delta Z.\,\Delta\phi$$

where ϕ is the angle ordinate. Substituting these, we get

$$(T_n + T_s)\Delta r/\Delta Z + (T_e + T_w)\Delta Z/\Delta r - 2\,(\Delta r/\Delta Z + \Delta Z/\Delta r)\,T_o + (T_e - T_w)\Delta Z/2r + h_v\,(T_g - T_o)\,\Delta r.\,\Delta Z/k = 0.$$

which is equivalent to Equation A.1.2.

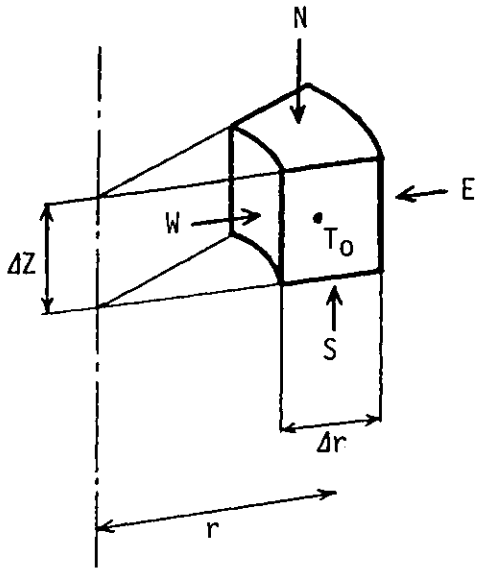

Figure A.1.1. A typical finite difference cell

2) Mesh points on axis of symmetry.

Derivation from the differential equation:

From the condition $\partial T/\partial r = 0$ at $r = 0$,

$$\frac{1}{r}\frac{\partial T}{\partial r} \doteq \frac{\partial^2 T}{\partial r^2}$$

Therefore, Equation A.1.1 becomes

$$\frac{\partial^2 T}{\partial Z^2} + 2\frac{\partial^2 T}{\partial r^2} + \frac{\dot{q}}{k} = 0$$

Using the finite difference approximazion, we get

$$\frac{T_n - 2T_o + T_s}{\Delta Z^2} + \frac{2(T_e - 2T_o + T_w)}{\Delta r^2} + \frac{h_v(T_g - T_o)}{k} = 0$$

As $T_e = T_w$, the explicit form is

$$T_o = [(T_n + T_s)\Delta r/\Delta Z + 4T_e.\Delta Z/\Delta r + h_v.T_g.\Delta r.\Delta Z/k] \\ /(2\Delta r/\Delta Z + 4\Delta Z/\Delta r + \Delta r.\Delta Z.h_v/k) \qquad (A.1.3)$$

Direct derivation from the heat balance:

The heat balance for the cell shown in Figure A.1.2 gives

$k.S_n\ (T_n - T_o)/\Delta Z +$
$k.S_s\ (T_s - T_o)/\Delta Z +$
$k.S_e\ (T_e - T_o)/\Delta r +$
$h_v.V\ (T_g - T_o) = 0$

where $S_n = S_s = \Delta r^2.\Delta\phi/8$

$S_e = \Delta r.\Delta Z.\ \Delta\phi/2$

$\Delta V = \Delta r^2.\Delta Z.\Delta\phi/8$

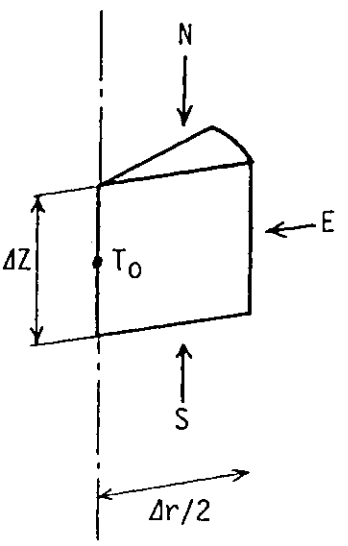

Figure A.1.2. A cell on the axis of symmetry.

Substituting these, we obtain

$$(T_n - T_o)\Delta r/\Delta Z + (T_s - T_o)\Delta r/\Delta Z + 4(T_e - T_o)\Delta Z/\Delta r$$
$$+ h_v\ (T_g - T_o)\Delta r.\Delta Z/k = 0$$

This is equivalent to Equation A.1.3.

3) Mesh point at nozzle tip (intersection between the symmetry axis and the accretion/refractory interface).

This finite difference cell is irregular, as the refractory-side of the cell is lacking. The south-side surface is assumed to be adiabatic. Making use of this condition ($T_s = T_n$) in Equation A.1.3 or considering the heat balance, we derived

$$T_o = [2T_n.\Delta r/\Delta Z + 4T_e.\Delta Z/\Delta r + h_v.T_g.\Delta r.\Delta Z/k] / (2\Delta r/\Delta Z + 4\Delta Z/\Delta r + h_v.\Delta r.\Delta Z/k)$$

4) Accretion/refractory interface.

Applying the same method as described above, we derive

$$T_o = [2k_m.T_n.\Delta r/\Delta Z_m + 2k_R.T_s.\Delta r/\Delta Z_R + ((1 - \Delta r/2r)T_w + (1 + \Delta r/2r)T_e)(k_m.\Delta Z_m + k_R.\Delta Z_R) /\Delta r + h_v.T_g.\Delta r.\Delta Z_m] / [2k_m.\Delta r/\Delta Z_m + 2k_R.\Delta r/\Delta Z_R + 2(k_m.\Delta Z_m + k_R.\Delta Z_R)/\Delta r + h_v.\Delta r.\Delta Z_m]$$

where the subscripts m and R respectively denoze the accretion (metal phase) and the refractory.

5) Mesh points in the bulk refractory.

Making the source term zero in the previous equation for the inner mesh points in the accretion, we derive

$$T_o = [(T_n + T_s)\Delta r/\Delta Z + (T_e + T_w)\Delta Z/\Delta r + (T_e - T_w)\Delta Z/2r] / (2\Delta r/\Delta Z + 2\Delta Z/\Delta r)$$

where ΔZ is the mesh interval in the refractory region.

A.1.2. Gas Flow Equations

It is assumed that the gas flow is expressed by a potential flow in the accretion. The governing equation for the flow potential is

$$\frac{\partial^2 P}{\partial Z^2} + \frac{1}{r}\frac{\partial P}{\partial r} + \frac{\partial^2 P}{\partial r^2} = 0$$

The same procedure as in the previous section gives, for the general mesh points,

$$P_o = [(P_n + P_s)\Delta r/\Delta Z + (P_e + P_w)\Delta Z/\Delta r + (P_e - P_w)\Delta Z/2r]$$
$$/(2\Delta r/\Delta Z + 2\Delta Z/\Delta r)$$

For the mesh points on the axis of symmetry, the explicit expression is

$$P_o = [(P_n + P_s)\Delta r/\Delta Z + 4P_e.\Delta Z/\Delta r]$$
$$/(2\Delta r/\Delta z + 4\Delta Z/\Delta r)$$

For the mesh point at the nozzle tip, where the gas injection rate is set, the final equation is given by

$$P_o = (P_n.\Delta r/\Delta Z + 2P_e.\Delta Z/\Delta r + f.\Delta r/\lambda)$$
$$/(\Delta r/\Delta Z + 2\Delta Z/\Delta r)$$

where $f = 4F_{total}/\pi\,\Delta r^2$

A.2: COMPUTER PROGRAMS

```
00100 PROGRAM REL6 (INPUT,OUTPUT,TAPE5=INPUT,TAPE6)
00110 REAL KS,KA,KD
00120 DIMENSION T(31,51),TG(51),REM(10),P(31,35),RN(30),R1(30),Z(51)
00130+,Z1(51)
00140 R(I)=EXP(.106*FLOAT(I)-.722)
00150 AX(I)=89.*EXP(1.444-.212*FLOAT(I))
00160 AZS=1.
00170 AZA=.4444
00180 TGO=30.
00190 TR=200.
00200 TM=1540.
00210 TSUP=10.
00220 TB=TM+TSUP
00230 TO=TM-TGO
00240C TN=(T-TGO)/TO
00250 TRN=(TR-TGO)/TO
00260 TBN=(TB-TGO)/TO
00270 RO=.6
00280C RN=R/RO
00290 RDN=3.5/.6
00300 KS=.07
00310 KA=.003
00320 KD=.7
00330 HS=.01
00340 HA=.003
00350C F=K/KS
00360 FA=KA/KS
00370 FS=1.
00380 FD=KD/KS
00390 FGS=HS*RO/KS
00400 FGA=HA*RO/KS
00410C GAS=HG/(DENSITY*CP*U)
00420 GASS=HS/(.000487*.124*10800.)
00430 GASA=HA/(.000487*.124*10800.)
00440C
00450C HG=2.*DZN*GAS
00460 HGS=2./.6*GASS
00470 HGA=2.*1.5/.6*GASA
00480C HK=H*DRN/K
00490 HKS=.1275/.6*FGS
00500 HKA=.1275/.6*FGA/FA
00510 HKI=.1275/.6*(FGS+1.5*FGA)/(1.+1.5*FA)
00520 TL=(TBN-1.)*FD+1.
00530C F=F/DZN
00540 FA=FA/1.5
00550 RDC=RDN*.6
00560 TG(51)=0.
00570 DO 10 I=2,30
00580 DO 20 J=1,35
00590 T(I,J)=TL-(TL-TRN)/204.*FLOAT(J-1)
00592 IF(J.LE.21) T(I,J)=TL
00594 IF(J.LE.29.AND.I.GE.24) T(I,J)=TL
00600 20 CONTINUE
00610 DO 30 J=36,51
00620 T(I,J)=TRN+(TL-TRN)/19.2*FLOAT(51-J)
00630 30 CONTINUE
00640 10 CONTINUE
00650 DO 40 J=1,25
00660 T(30,J)=TL
00670 40 CONTINUE
00680 READ(5,101)(REM(I),I=1,10)
00690 101 FORMAT(10A6)
00700 WRITE(6,102)(REM(I),I=1,10)
00710 102 FORMAT(//8H  ****  ,10A6)
00720 N=0
00730C
00740 200 HG=HGA
00750 DO 80 I=2,30
00760 DO 80 J=1,31
00770 P(I,J)=1.
00780 80 CONTINUE
00790 DO 50 K=2,51
00800 J=53-K
00810 IF(J.EQ.35) HG=HGS
00820 TS=T(2,J)
00830 IF(TS.GT.1.)TS=(TS-1.)/FD+1.
00840 TG(J-1)=TG(J)+HG*(TS-TG(J))
00850 50 CONTINUE
00860 N=N+1
00870 HK=HKS
00880 AZ=AZS
00890 T01=T(4,30)
00900 T02=T(17,30)
00910 T03=T(10,35)
00920 T04=T(7,40)
```

```
00930 DO 60 J=2,50
00940 IF(J.EQ.35) HK=HKI
00950 IF(J.EQ.36) HK=HKA
00960 T(1,J)=T(3,J)-HK*(T(2,J)-TG(J))
00970 IF(J.EQ.36) AZ=AZA
00980 DO 70 I=2,30
00990 IF(I.EQ.30.AND.J.LE.25) GOTO 70
01000 IF(I.EQ.30.AND.J.GE.26) T(31,J)=T(29,J)
01010 IF(J.EQ.35) GOTO 210
01020 TN=(AX(I)*(T(I-1,J)+T(I+1,J))+AZ*(T(I,J-1)+T(I,J+1)))/(AX(I)+
01030+AZ)/2.
01040 T(I,J)=1.08*TN-.08*T(I,J)
01050 GOTO 201
01060 210 TN=((FS/AZS+FA/AZA)*AX(I)*(T(I-1,J)+T(I+1,J))+2.*FS*
01070+T(I,J-1)+2.*FA*T(I,J+1))/(FS+(FS/AZS+FA/AZA)*AX(I)+FA)/2.
01080 T(I,J)=1.08*TN-.08*T(I,J)
01090 201 IF(T(I,J).GE.1..OR.J.GE.35) GOTO 70
01100 IF(T(I+1,J).LT.1..AND.T(I,J-1).LT.1.) GOTO 70
01110 KIM=INT(6.81+9.43*ALOG(R(I)+RDC))
01120 IF(KIM.GT.30) KIM=30
01130 DO 90 KI=I,KIM
01140 KJC=J-INT(SQRT(RDC*RDC-(R(KI)-R(I))**2))
01150 JEND=J
01160 IF(KI.EQ.I) JEND=35
01170 DO 100 KJ=KJC,JEND
01180 P(KI,KJ)=0.
01190 100 CONTINUE
01200 90 CONTINUE
01210 70 CONTINUE
01220 60 CONTINUE
01230 DO 110 I=2,30
01240 DO 110 J=1,31
01250 IF(P(I,J).EQ.1.) T(I,J)=TL
01260 110 CONTINUE
01270 IF(ABS(T(7,40)-TO4).GE..00007) GOTO 200
01280 IF(ABS(T(10,35)-TO3).GE..00007) GOTO 200
01290 IF(ABS(T(17,30)-TO2).GE..00007) GOTO 200
01300 IF(ABS(T(4,30)-TO1).GE..00007) GOTO 200
01310 DO 130 K=2,30
01320 RN(K)=EXP(.106*FLOAT(K)-.722)/.6
01330 R1(K)=RN(K)*RO
01340 130 CONTINUE
01350 DO 140 K=1,35
01360 Z(K)=(35.-FLOAT(K))/.6
01370 Z1(K)=Z(K)*RO
01380 140 CONTINUE
01390 DO 150 K=36,51
01400 Z(K)=(52.5-1.5*FLOAT(K))/.6
01410 Z1(K)=Z(K)*RO
01420 150 CONTINUE
01430 DO 160 I=2,30
01440 DO 160 J=1,35
01450 IF(T(I,J).GT.1.)T(I,J)=(T(I,J)-1.)/FO+1.
01460 160 CONTINUE
01470 WRITE(6,103)N
01480 103 FORMAT(//6X,5H  N =,I6,15X,1HR)
01490 WRITE(6,104)(RN(K),K=2,22)
01500 104 FORMAT(6X,14HZ       TGAS     ,21F5.2)
01510 WRITE(6,105)((Z(J),TG(J),(T(I,J),I=2,22)),J=1,51)
01520 105 FORMAT(6X,F5.1,3X,F5.3,1X,21F5.3)
01522 WRITE(6,108)(RN(K),K=23,30)
01526 WRITE(6,112)((Z(J),(T(I,J),I=23,30)),J=1,51)
01528 112 FORMAT(6X,F5.1,4X,8F5.3)
01530 DO 170 J=1,51
01540 TG(J)=TG(J)*TO+TGO
01550 DO 170 I=2,30
01560 T(I,J)=T(I,J)*TO+TGO
01570 170 CONTINUE
01580 WRITE(6,106)(R1(K),K=2,22)
01590 106 FORMAT(///6X,14HZ       TGAS     ,21F5.2)
01600 WRITE(6,107)((Z1(J),TG(J),(T(I,J),I=2,22)),J=1,51)
01610 107 FORMAT(6X,F5.1,3X,F5.0,1X,21F5.0)
01612 WRITE(6,108)(R1(K),K=23,30)
01614 108 FORMAT(//15X,8F5.2)
01616 WRITE(6,109)((Z1(J),(T(I,J),I=23,30)),J=1,51)
01618 109 FORMAT(6X,F5.1,4X,8F5.0)
01620 STOP
01630 END
```

```
00100 PROGRAM FDM18 (INPUT,OUTPUT,TAPE5=INPUT,TAPE6)
00110C ****  FDM18  ACCREATION FORMATION  ****
00120 REAL KS,KA
00130 DIMENSION A(44),B(44),C(44),D(44),REM(10),P(20,27)
00140 COMMON TO(17,44),TN(17,44),TG(44)
00150 RX(T,I,J,N)=22.25*EXP(1.868-.424*FLOAT(I))*ARP(T,J,N)
00160 FR(I)=EXP(.212*FLOAT(I)-.934)
00170C HG=2.*H/(RO*CP*R*U)
00180 HGA=2.*.003/(.000487*.124*.6*10800.)
00190 HGS=HGA*.010/.003
00200 KS=.07
00210 DS=KS/.2
00220 KA=.003
00230 DA=KA/1.5
00240C HK=H*DR/K
00250 HKS=.010*.2526/KS
00260 HKA=.003*.2526/KA
00270 HKI=(.2*.010+1.5*.003)*.2526/(KS*.2+KA*1.5)
00280 TS=10.
00290 TM=1540.
00300 PDS=3.5*.2/KS
00310 TL=TS*PDS+TM
00320 DO 10 I=2,17
00330 DO 20 J=1,27
00340 TN(I,J)=TL
00350 TO(I,J)=TL
00360 20 CONTINUE
00370 TN(I,28)=(TL+1000.)/2.
00380 TO(I,28)=TN(I,28)
00390 DO 30 J=29,44
00400 TN(I,J)=1000.-FLOAT(J-28)*800./16.
00410 TO(I,J)=TN(I,J)
00420 30 CONTINUE
00430 10 CONTINUE
00440 TG(44)=30.
00450 READ(5,101)(REM(I),I=1,10)
00460 101 FORMAT(10A6)
00470 WRITE(6,102)(REM(I),I=1,10)
00480 102 FORMAT(//8H  ****  ,10A6)
00490 CALL TYPE(0,PDS)
00500 DO 40 N=1,3640
00510 DZ=1.5
00520 HG=HGA
00530 DO 50 K=2,44
00540 J=46-K
00550 IF(J.EQ.28) HG=HGS
00560 IF(J.EQ.28) DZ=.2
00570 IF(J.EQ.23) DZ=1.
00580 TW=TN(2,J)
00590 IF(TW.GT.TM) TW=(TW-TM)/PDS+TM
00600 TG(J-1)=TG(J)+HG*(TW-TG(J))*DZ
00610 50 CONTINUE
00620C ****  Z=IMPLICIT  ******
00630 DO 55 I=2,16
00640 DO 55 J=2,20
00650 P(I,J)=1.
00660 55 CONTINUE
00670 CALL REPL
00680 HK=HKS
00690 DO 60 J=2,43
00700 IF(J.EQ.28) HK=HKI
00710 IF(J.EQ.29) HK=HKA
00720 TO(1,J)=TO(3,J)-HK*(TO(2,J)-TG(J))
00730 TO(17,J)=TO(15,J)
00740 60 CONTINUE
00750 DO 70 I=2,16
00760 DO 80 J=2,43
00770 IF(J.EQ.23) GOTO 201
00780 IF(J.EQ.28) GOTO 202
00790 A(J)=RZ(TO(I,J),J,N)
00800 B(J)=1.+2.*A(J)
00810 C(J)=A(J)
00820 D(J)=TO(I,J)+RX(TO(I,J),I,J,N)*(TO(I-1,J)-2.*TO(I,J)+TO(I+1,J))
00830 GOTO 80
00840 201 RZ1=RZ(TO(I,J),J,N)
00850 RZ2=RZ(TO(I,J),J+1,N)
00860 A(J)=.4
00870 B(J)=(1.+2.*RZ1)*.2/RZ1+(1.+2.*RZ2)/RZ2
00880 C(J)=2.
00890 D(J)=(.2/RZ1+1./RZ2)*(TO(I,J)+RX(TO(I,J),I,J,N)*
00900+(TO(I-1,J)-2.*TO(I,J)+TO(I+1,J)))
00910 GOTO 80
00920 202 RZS=RZ(TO(I,J),27,N)
00930 RZA=RZ(TO(I,J),29,N)
00940 RXS=RX(TO(I,J),I,27,N)
```

```
00950 RXA=RX(TO(I,J),I,29,N)
00960 A(J)=2.*DS
00970 B(J)=DS*(1.+2.*RZS)/RZS+DA*(1.+2.*RZA)/RZA
00980 C(J)=2.*DA
00990 D(J)=(DS/RZS+DA/RZA)*TO(I,J)+(DS*RXS/RZS+DA*RXA/RZA)*
01000+(TO(I-1,J)-2.*TO(I,J)+TO(I+1,J))
01010 80 CONTINUE
01020 D(2)=D(2)+A(2)*TO(I,1)
01030 C(43)=0.
01040 D(43)=D(43)+A(43)*TO(I,44)
01050C G/E
01060 DO 90 J=3,43
01070 B(J)=B(J)-A(J)*C(J-1)/B(J-1)
01080 D(J)=D(J)+A(J)*D(J-1)/B(J-1)
01090 90 CONTINUE
01100 DO 100 K=2,43
01110 J=45-K
01120 TN(I,J)=(D(J)+C(J)*TN(I,J+1))/B(J)
01130 100 CONTINUE
01140 70 CONTINUE
01150C ****  X=IMPLICIT  ****
01160 CALL REAL
01170 HK=HKS
01180 DO 110 J=2,43
01190 DO 120 I=2,16
01200 IF(J.EQ.23) GOTO 203
01210 IF(J.EQ.28) GOTO 204
01220 A(I)=RX(TO(I,J),I,J,N)
01230 B(I)=1.+2.*A(I)
01240 C(I)=A(I)
01250 D(I)=TO(I,J)+RZ(TO(I,J),J,N)*(TO(I,J-1)-2.*TO(I,J)+TO(I,J+1))
01260 GOTO 120
01270 203 RZ1=RZ(TO(I,J),J,N)
01280 RZ2=RZ(TO(I,J),J+1,N)
01290 RXS=RX(TO(I,J),I,J,N)
01300 A(I)=RXS*(.2/RZ1+1./RZ2)
01310 B(I)=(1.+2.*RXS)*(.2/RZ1+1./RZ2)
01320 C(I)=A(I)
01330 D(I)=.4*TO(I,J-1)+.2*(1./RZ1-2.)*TO(I,J)+(1./RZ2-2.)*TO(I,J)
01340++2.*TO(I,J+1)
01350 GOTO 120
01360 204 RZS=RZ(TO(I,J),27,N)
01370 RZA=RZ(TO(I,J),29,N)
01380 RXS=RX(TO(I,J),I,27,N)
01390 RXA=RX(TO(I,J),I,29,N)
01400 A(I)=DS*RXS/RZS+DA*RXA/RZA
01410 B(I)=DS*(1.+2.*RXS)/RZS+DA*(1.+2.*RXA)/RZA
01420 C(I)=A(I)
01430 D(I)=DS*(2.*TO(I,J-1)+TO(I,J)/RZS-2.*TO(I,J))+
01440+DA*(-2.*TO(I,J)+TO(I,J)/RZA+2.*TO(I,J+1))
01450 120 CONTINUE
01460 IF(J.EQ.28) HK=HKI
01470 IF(J.EQ.29) HK=HKA
01480 B(2)=B(2)+A(2)*HK
01490 C(2)=2.*C(2)
01500 D(2)=D(2)+A(2)*HK*TG(J)
01510 A(16)=2.*A(16)
01520 C(16)=0.
01530C G/E
01540 DO 130 I=3,16
01550 B(I)=B(I)-A(I)*C(I-1)/B(I-1)
01560 D(I)=D(I)+A(I)*D(I-1)/B(I-1)
01570 130 CONTINUE
01580 DO 140 K=2,16
01590 I=18-K
01600 TN(I,J)=(D(I)+C(I)*TN(I+1,J))/B(I)
01602 140 CONTINUE
01604 110 CONTINUE
01606 DO 180 J=2,27
01608 DO 190 I=2,16
01610 IF(TN(I,J).GE.TM) GOTO 190
01620 IF(TN(I+1,J).LT.TM.AND.TN(I,J-1).LT.TM) GOTO 190
01630 KIM=INT(4.41+4.72*ALOG(FR(I)+3.5))
01640 IF(KIM.GT.16) KIM=16
01650 DO 150 KI=I,KIM
01660 IF(J.GT.23) GOTO 205
01670 KJC=J-INT(SQRT(12.25-(FR(KI)-FR(I))**2))
01680 GOTO 206
01690 205 KJC=J-INT(SQRT(12.25-(FR(KI)-FR(I))**2)+.8*FLOAT(J-23))
01700 206 JEND=J
01710 IF(KI.EQ.I) JEND=20
01720 IF(JEND.GT.20) JEND=20
01730 DO 160 KJ=KJC,JEND
01740 P(KI,KJ)=0.
01750 160 CONTINUE
```

```
01760 150 CONTINUE
01770 190 CONTINUE
01780 180 CONTINUE
01790 DO 170 I=2,16
01800 DO 170 J=2,20
01810 IF(P(I,J).EQ.1.) TN(I,J)=TL
01820 170 CONTINUE
01830 IF(N.EQ.25.OR.N.EQ.30.OR.N.EQ.40) CALL TYPE(N,PDS)
01840 IF(N.EQ.60.OR.N.EQ.100.OR.N.EQ.190.OR.N.EQ.490)
01850+ CALL TYPE(N,PDS)
01860 IF(IFIX(FLOAT(N-40)/300.).EQ.(FLOAT(N-40)/300.).AND.N.GE.340)
01870+CALL TYPE(N,PDS)
01880 40 CONTINUE
01890 STOP
01900 END
02000C
02010 SUBROUTINE REPL
02020 COMMON TO(17,44),TN(17,44),TG(44)
02030 DO 11 J=2,43
02040 DO 11 I=2,16
02050 TO(I,J)=TN(I,J)
02060 11 CONTINUE
02070 RETURN
02080 END
02100C
02110 FUNCTION RZ(T,J,N)
02120 IF(J.LE.23) GOTO 301
02130 IF(J.LE.28) GOTO 302
02140 RZ=.4444*ARP(T,J,N)
02150 GOTO 303
02160 301 RZ=ARP(T,J,N)
02170 GOTO 303
02180 302 RZ=25.*ARP(T,J,N)
02190 303 RETURN
02200 END
02210C
02220 FUNCTION ARP(T,J,N)
02230 IF(J.GE.29) GOTO 305
02240 IF(T.GE.1530.) GOTO 306
02250 ARP=.0006
02260 GOTO 307
02270 306 IF(T.GE.1540.) GOTO 308
02280 ARP=.000015
02290 GOTO 307
02300 308 ARP=.0007*10.
02310 GOTO 307
02320 305 ARP=.00006
02330 307 IF(N.GT.25.AND.N.LE.60) ARP=5.*ARP
02340 IF(N.GT.60) ARP=10.*ARP
02350 RETURN
02360 END
02500C
02510 SUBROUTINE TYPE(N,PDS)
02520 DIMENSION R(16),Z(44),TY(17,44)
02530 COMMON TO(17,44),TN(17,44),TG(44)
02540 TI=.02*FLOAT(N)
02550 IF(N.GT.25) TI=.1*FLOAT(N)-2.
02560 IF(N.GT.60) TI=.2*FLOAT(N)-8.
02570 WRITE(6,103) TI
02580 103 FORMAT(///5X,6HTIME= ,F7.1,17X,1HR)
02590 DO 11 K=2,16
02600 R(K)=EXP(.212*FLOAT(K)-.934)
02610 11 CONTINUE
02620 DZ=1.
02630 Z(1)=23.
02640 DO 22 K=2,44
02650 IF(K.EQ.24) DZ=.2
02660 IF(K.EQ.29) DZ=1.5
02670 Z(K)=Z(K-1)-DZ
02680 22 CONTINUE
02690 DO 33 I=2,16
02700 DO 33 J=1,44
02705 TY(I,J)=TN(I,J)
02710 IF(TN(I,J).GT.1540.) TY(I,J)=(TN(I,J)-1540.)/PDS+1540.
02720 33 CONTINUE
02730 WRITE(6,104)(R(K),K=2,16)
02740 104 FORMAT(/6X,14H      TGAS      ,15F5.2)
02750 WRITE(6,105)((Z(J),TG(J),(TY(I,J),I=2,16)),J=1,44)
02760 105 FORMAT(6X,F5.1,3X,F5.0,1X,15F5.0)
02810 RETURN
02820 END
```

```
00100 PROGRAM POS7 (INPUT,OUTPUT,TAPE5=INPUT,TAPE6)
00110 REAL KS,KA
00120 DIMENSION REM(10),TO(22,30),T(22,30),TG(22,30),R(22),Z(30),
00130+P(22,30),Q(22,31)
00140 DR=1.
00150 DZ=1.
00160 RD=3.
00170 RRD=RD*RD
00180 DDR=DR*DR
00190 DZ2=2.
00200 CP=.124
00210 KS=.07
00220 KA=.003
00230 HSS=.1
00240 HA=.0012
00250 TG(1,1)=30.
00260 TR=200.
00270 TM=1540.
00280 TSUP=10.
00290 TB=TM+TSUP*RD*.2/KS
00300 WIN=3890.*.000487
00310 PG=1.
00320 VRP=DR*WIN/PG*4.
00330 READ(5,101)(REM(I),I=1,10)
00340 101 FORMAT(10A6)
00350 WRITE(6,102)(REM(I),I=1,10)
00360 102 FORMAT(//8H ****   ,10A6)
00370 DO 10 J=1,12
00380 TG(1,J)=TG(1,1)+(150.-TG(1,1))/12.*FLOAT(J-1)
00390 DO 10 I=1,17
00400 T(I,J)=TR+(1400.-TR)/11.*FLOAT(J-1)
00410 10 CONTINUE
00420 P(1,12)=5.
00430 DO 20 I=1,17
00440 R(I)=DR*FLOAT(I-1)
00450 DO 20 J=13,28
00460 Q(I,J)=1.
00470 TG(I,J)=400.+30.*FLOAT(J-13)
00480 TO(I,J)=TG(I,J)
00490 IF((J-12).GT.I)GOTO 11
00500 T(I,J)=1400.+(TB-1400.)/16.*FLOAT(I-1)
00510 IF(J.EQ.28)T(I,J)=TB
00520 IF(J.GE.16.AND.I.EQ.17)T(I,J)=TB
00530 P(I,J)=5.-5./16.*FLOAT(I-1)
00540 GOTO 20
00550 11 T(I,J)=1400.+(TB-1400.)/15.*FLOAT(J-13)
00560 P(I,J)=5.-5./15.*FLOAT(J-13)
00570 20 CONTINUE
00580 RZ=DR/DZ
00590 RZ2=DR/DZ2
00600 ZR=DZ/DR
00610 ZR2=DZ2/DR
00620 TS1=DR*DZ*HSS/KS
00630 TS2=1./(2.*(RZ+ZR)+TS1)
00640 TS3=1./(2.*RZ+4.*ZR+TS1)
00650 PS1=.5/(RZ+ZR)
00660 GS1=DR*DZ*HSS/2./CP
00670 PS2=1./(2.*RZ+4.*ZR)
00680 TI1=2.*KS*RZ
00690 TI2=2.*KA*RZ2
00700 TI3=KS*ZR+KA*ZR2
00710 TI4=HSS*DR*DZ
00720 TI5=1./(TI1+TI2+2.*TI3+TI4)
00730 TI6=HSS*DZ/2./CP/(WIN*4.)
00740 TR2=.5/(RZ2+ZR2)
00750 HK=2.*DR*HA/KA
00760 HG=2.*HA*DZ2/CP/WIN/DR
00770 N=0
00780C
00790 22 N=N+1
00800 T1=T(3,16)
00810 T2=T(5,10)
00820 T3=T(4,17)
00830 T4=T(3,20)
00840 T5=T(2,15)
00850C TEMP      ****************
00860 DO 30 J=2,12
00870 T(1,J)=T(3,J)+HK*(TG(1,J)-T(2,J))
00880 T(17,J)=T(15,J)
00890 DO 30 I=2,16
00900 T(I,J)=(RZ2*(T(I,J+1)+T(I,J-1))+ZR2*(T(I+1,J)+T(I-1,J))+
00910+.5*DZ2/R(I)*(T(I+1,J)-T(I-1,J)))*TR2
00920 30 CONTINUE
00930 T(1,13)=(2.*RZ*T(1,14)+4.*ZR*T(2,13)+TS1*TG(1,13))*TS3
00940 T(17,13)=T(15,13)
```

```
00950 DO 40 I=2,16
00960 T(I,13)=(TI1*T(I,14)+TI2*T(I,12)+TI3*((1.-.5*DR/R(I))*T(I-1,13)+
00970+(1.+.5*DR/R(I))*T(I+1,13))+TI4*TG(I,13))*TI5
00980 P(I,12)=P(I,14)
00990 40 CONTINUE
01000 DO 50 J=14,27
01010 IF(J.LE.17) T(17,J)=T(15,J)
01020 T(1,J)=(RZ*(T(1,J+1)+T(1,J-1))+4.*ZR*T(2,J)+TS1*TG(1,J))*TS3
01030 DO 50 I=2,16
01040 T(I,J)=(RZ*(T(I,J+1)+T(I,J-1))+ZR*(T(I+1,J)+T(I-1,J))+.5*DZ/R(I)
01050+*(T(I+1,J)-T(I-1,J))+TS1*TG(I,J))*TS2
01060 50 CONTINUE
01070 DO 140 I=1,16
01080 DO 150 J=13,27
01090 IF(T(I,J).GE.TM) GOTO 150
01100 IF(T(I+1,J).LT.TM.AND.T(I,J+1).LT.TM) GOTO 150
01110 KIM=I+3
01120 IF(KIM.GT.16) KIM=16
01130 DO 160 KI=I,KIM
01140 FIS=(KI-I)*(KI-I)
01150 KJC=J+INT(SQRT(RRD-DDR*FIS)/DZ)
01160 KJST=J
01170 IF(KI.EQ.I) KJST=13
01180 DO 160 KJ=KJST,KJC
01190 Q(KI,KJ)=0.
01200 160 CONTINUE
01210 150 CONTINUE
01220 140 CONTINUE
01230 DO 180 I=1,16
01240 DO 180 J=16,27
01250 IF(Q(I,J).EQ.1.) T(I,J)=TB
01260 Q(I,J)=1.
01270 180 CONTINUE
01280C GAS FLOW   **************
01290 DO 60 J=13,27
01300 P(1,J)=(RZ*(P(1,J+1)+P(1,J-1))+4.*ZR*P(2,J))*PS2
01310 IF(J.EQ.13) P(1,13)=(RZ*P(1,14)+2.*ZR*P(2,13)+VRP)*2.*PS2
01320 DO 60 I=2,16
01330 P(I,J)=(RZ*(P(I,J+1)+P(I,J-1))+ZR*(P(I+1,J)+P(I-1,J))+.5*DZ/
01340+R(I)*(P(I+1,J)-P(I-1,J)))*PS1
01350 60 CONTINUE
01360C GAS TEMP   **************
01370 DO 70 J=1,12
01380 TG(1,J+1)=TG(1,J)+HG*(T(2,J)-TG(1,J))
01390 70 CONTINUE
01400 TO(1,13)=TG(1,13)+TI6*(T(1,13)-TG(1,13))
01410 DO 80 J=14,27
01420 IF(T(1,J).GT.TM) GOTO 33
01430 CVS=.5*DZ*DZ*HSS/PG/(P(1,J-1)-P(1,J))/CP
01440 TO(1,J)=(TO(1,J-1)+CVS*(2.*T(1,J)-TO(1,J-1)))/(1.+CVS)
01450 TG(1,J)=.5*(TO(1,J-1)+TO(1,J))
01460 GOTO 80
01470 33 P(1,J)=0.
01480 TG(1,J)=T(1,J)
01490 80 CONTINUE
01500 DO 90 I=2,16
01510 IF(T(I,13).GT.TM) GOTO 66
01520 CVW=.5*DR*DR*HSS/PG/(P(I-1,13)-P(I,13))/CP
01530 TO(I,13)=(TO(I-1,13)+CVW*(2.*T(I,13)-TO(I-1,13)))/(1.+CVW)
01540 TG(I,13)=.5*(TO(I-1,13)+TO(I,13))
01550 GOTO 77
01560 66 P(I,13)=0.
01570 TG(I,13)=T(I,13)
01580 77 CONTINUE
01590 DO 100 J=14,27
01600 IF(T(I,J).GT.TM) GOTO 88
01610 FS=PG*R(I)*RZ*(P(I,J-1)-P(I,J))
01620 FW=PG*(R(I)-.5*DR)*ZR*(P(I-1,J)-P(I,J))
01630 FSW=1./(FS+FW)
01640 TIN=(TO(I,J-1)*FS+TO(I-1,J)*FW)*FSW
01650 TO(I,J)=(TIN+GS1*R(I)*(2.*T(I,J)-TIN)*FSW)/(1.+GS1*R(I)*FSW)
01660 TG(I,J)=.5*(TIN+TO(I,J))
01670 GOTO 100
01680 88 P(I,J)=0.
01690 TG(I,J)=T(I,J)
01700 100 CONTINUE
01710 90 CONTINUE
01720 IF(ABS(T1-T(3,16)).GE..01) GOTO 22
01730 IF(ABS(T2-T(5,10)).GE..01) GOTO 22
01740 IF(ABS(T3-T(4,17)).GE..01) GOTO 22
01750 IF(ABS(T4-T(3,20)).GE..01) GOTO 22
01760 IF(ABS(T5-T(2,15)).GE..01) GOTO 22
01770 DO 110 J=1,28
01780 Z(J)=-24.+2.*FLOAT(J-1)
01790 IF(J.GT.13) Z(J)=J-13
```

POS7 (ctd.)

```
01800 IF(J.LE.12)T(1,J)=99999.
01810 110 CONTINUE
01820 DO 120 J=13,28
01830 DO 130 I=1,16
01840 IF(T(I,J).EQ.TG(I,J)) TG(I,J)=-.001
01850 IF(T(I,J).GT.TM) T(I,J)=TM+(T(I,J)-TM)/RD/.2*KS
01860 130 CONTINUE
01870 120 CONTINUE
01880 WRITE(6,103) N
01890 103 FORMAT(//6X,5H  N =,I6,15X,1HR)
01900 WRITE(6,104)(R(I),I=1,16)
01910 104 FORMAT(3X,8HT(METAL)/6X,6H  Z   ,16F5.1)
01920 WRITE(6,105)((Z(J),(T(I,J),I=1,16)),J=1,28)
01930 105 FORMAT(6X,F6.1,2X,16F5.0)
01940 WRITE(6,106)(R(I),I=1,16)
01950 106 FORMAT(/3X,6HT(GAS)/6X,6H  Z   ,16F5.1)
01960 WRITE(6,105)((Z(J),(TG(I,J),I=1,16)),J=1,27)
01970 WRITE(6,107)(R(I),I=1,16)
01980 107 FORMAT(/3X,14HFLOW POTENTIAL/6X,6H  Z   ,16F5.1)
01990 WRITE(6,108)((Z(J),(P(I,J),I=1,16)),J=13,27)
02000 108 FORMAT(6X,F6.1,2X,16F5.3)
02010 STOP
02020 END
```

```
00100 PROGRAM POS9 (INPUT,OUTPUT,TAPE5=INPUT,TAPE6)
00110 REAL KS,KA
00120 DIMENSION REM(10),TO(22,30),T(22,30),TG(22,30),R(22),Z(30),
00130+P(22,30),Q(22,31),FE(30),FP(30)
00140 DR=1.
00150 DZ=1.
00152 RD=3.
00154 RRD=RD*RD
00156 DDR=DR*DR
00160 DZ2=2.
00170 CP=.124
00180 KS=.07
00190 KA=.003
00200 HSS=.1
00205 ALP=.8
00210 HA=.0012
00220 TG(1,1)=30.
00230 TR=200.
00240 TM=1540.
00250 TSUP=10.
00260 TB=TM+TSUP*RD*.2/KS
00270 WIN=3890.*.000487
00280 PG=1.
00290 VRP=DR*WIN/PG*4.
00300 READ(5,101)(REM(I),I=1,10)
00310 101 FORMAT(10A6)
00320 WRITE(6,102)(REM(I),I=1,10)
00330 102 FORMAT(//8H ****   ,10A6)
00340 DO 10 J=1,12
00350 TG(1,J)=TG(1,1)+(150.-TG(1,1))/12.*FLOAT(J-1)
00360 DO 10 I=1,17
00370 T(I,J)=TR+(1400.-TR)/11.*FLOAT(J-1)
00380 10 CONTINUE
00385 P(1,12)=5.
00390 DO 20 I=1,17
00400 R(I)=DR*FLOAT(I-1)
00410 DO 20 J=13,28
00412 Q(I,J)=1.
00420 TG(I,J)=400.+30.*FLOAT(J-13)
00430 TO(I,J)=TG(I,J)
00440 IF((J-12).GT.I)GOTO 11
00450 T(I,J)=1400.+(TB-1400.)/16.*FLOAT(I-1)
00452 IF(J.EQ.28)T(I,J)=TB
00454 IF(J.GE.16.AND.I.EQ.17)T(I,J)=TB
00460 P(I,J)=5.-5./16.*FLOAT(I-1)
00470 GOTO 20
00480 11 T(I,J)=1400.+(TB-1400.)/15.*FLOAT(J-13)
00490 P(I,J)=5.-5./15.*FLOAT(J-13)
00500 20 CONTINUE
00501 FP(12)=VRP
00502 FE(12)=WIN*4.
00503 DO 220 J=13,28
00504 FE(J)=FE(J-1)*ALP
00505 FP(J)=FE(J-1)*(1.-ALP)*DR/PG
00506 220 CONTINUE
00510 RZ=DR/DZ
00520 RZ2=DR/DZ2
00530 ZR=DZ/DR
00540 ZR2=DZ2/DR
00550 TS1=DR*DZ*HSS/KS
00560 TS2=1./(2.*(RZ+ZR)+TS1)
00570 TS3=1./(2.*RZ+4.*ZR+TS1)
00580 PS1=.5/(RZ+ZR)
00590 GS1=DR*DZ*HSS/2./CP
00600 PS2=1./(2.*RZ+4.*ZR)
00610 TI1=2.*KS*RZ
00620 TI2=2.*KA*RZ2
00630 TI3=KS*ZR+KA*ZR2
00640 TI4=HSS*DR*DZ
00650 TI5=1./(TI1+TI2+2.*TI3+TI4)
00660 TI6=HSS*DZ/2./CP/(WIN*4.)
00670 TR2=.5/(RZ2+ZR2)
00680 HK=2.*DR*HA/KA
00690 HG=2.*HA*DZ2/CP/WIN/DR
00700 N=0
00710C
00720 22 N=N+1
00730 T1=T(3,16)
00740 T2=T(5,10)
00750 T3=T(4,17)
00760 T4=T(3,20)
00770 T5=T(2,15)
00780C TEMP      ****************
00790 DO 30 J=2,12
00800 T(1,J)=T(3,J)+HK*(TG(1,J)-T(2,J))
```

```
00810 T(17,J)=T(15,J)
00820 DO 30 I=2,16
00830 T(I,J)=(RZ2*(T(I,J+1)+T(I,J-1))+ZR2*(T(I+1,J)+T(I-1,J))+
00840+.5*DZ2/R(I)*(T(I+1,J)-T(I-1,J)))*TR2
00850 30 CONTINUE
00860 T(1,13)=(2.*RZ*T(1,14)+4.*ZR*T(2,13)+TS1*TG(1,13))*TS3
00870 T(17,13)=T(15,13)
00880 DO 40 I=2,16
00890 T(I,13)=(TI1*T(I,14)+TI2*T(I,12)+TI3*((1.-.5*DR/R(I))*T(I-1,13)+
00900+(1.+.5*DR/R(I))*T(I+1,13))+TI4*TG(I,13))*TI5
00910 P(I,12)=P(I,14)
00920 40 CONTINUE
00930 DO 50 J=14,27
00940 IF(J.LE.17) T(17,J)=T(15,J)
00950 T(1,J)=(RZ*(T(1,J+1)+T(1,J-1))+4.*ZR*T(2,J)+TS1*TG(1,J))*TS3
00960 DO 50 I=2,16
00970 T(I,J)=(RZ*(T(I,J+1)+T(I,J-1))+ZR*(T(I+1,J)+T(I-1,J))+.5*DZ/R(I)
00980+*(T(I+1,J)-T(I-1,J))+TS1*TG(I,J))*TS2
00982 50 CONTINUE
00993 DO 140 I=1,16
00994 DO 150 J=13,27
00995 IF(T(I,J).GE.TM) GOTO 150
00996 IF(T(I+1,J).LT.TM.AND.T(I,J+1).LT.TM) GOTO 150
00997 KIM=I+3
00998 IF(KIM.GT.16) KIM=16
00999 DO 160 KI=I,KIM
01000 FIS=(KI-I)*(KI-I)
01001 KJC=J+INT(SQRT(RRD-DDR*FIS)/DZ)
01002 KJST=J
01003 IF(KI.EQ.I) KJST=13
01004 DO 160 KJ=KJST,KJC
01005 Q(KI,KJ)=0.
01006 160 CONTINUE
01007 150 CONTINUE
01008 140 CONTINUE
01009 DO 180 I=1,16
01010 DO 180 J=16,27
01011 IF(Q(I,J).EQ.1.) T(I,J)=TB
01012 Q(I,J)=1.
01013 180 CONTINUE
01017C GAS FLOW   **************
01018 DO 60 J=13,27
01020 P(1,J)=(RZ*(P(1,J+1)+P(1,J-1))+4.*ZR*P(2,J)+FP(J))*PS2
01030 IF(J.EQ.13) P(1,13)=(RZ*P(1,14)+2.*ZR*P(2,13)+FP(13))*2.*PS2
01040 DO 60 I=2,16
01050 P(I,J)=(RZ*(P(I,J+1)+P(I,J-1))+ZR*(P(I+1,J)+P(I-1,J))+.5*DZ/
01060+R(I)*(P(I+1,J)-P(I-1,J)))*PS1
01070 60 CONTINUE
01080C GAS TEMP   **************
01090 DO 70 J=1,12
01100 TG(1,J+1)=TG(1,J)+HG*(T(2,J)-TG(1,J))
01110 70 CONTINUE
01120 TO(1,13)=TG(1,13)+TI6*(T(1,13)-TG(1,13))
01130 DO 80 J=14,27
01140 IF(T(1,J).GT.TM) GOTO 33
01150 CVS=.5*DZ*HSS/CP/((P(1,J-1)-P(1,J))*PG/DZ+FE(J-1))
01160 TO(1,J)=(TO(1,J-1)+CVS*(2.*T(1,J)-TO(1,J-1)))/(1.+CVS)
01170 TG(1,J)=.5*(TO(1,J-1)+TO(1,J))
01180 GOTO 80
01190 33 P(1,J)=0.
01192 TG(1,J)=T(1,J)
01200 80 CONTINUE
01210 DO 90 I=2,16
01220 IF(T(I,13).GT.TM) GOTO 66
01230 CVW=.5*DR*DR*HSS/PG/(P(I-1,13)-P(I,13))/CP
01240 TO(I,13)=(TO(I-1,13)+CVW*(2.*T(I,13)-TO(I-1,13)))/(1.+CVW)
01250 TG(I,13)=.5*(TO(I-1,13)+TO(I,13))
01260 GOTO 77
01270 66 P(I,13)=0.
01272 TG(I,13)=T(I,13)
01280 77 CONTINUE
01290 DO 100 J=14,27
01300 IF(T(I,J).GT.TM) GOTO 88
01310 FS=PG*R(I)*RZ*(P(I,J-1)-P(I,J))
01320 FW=PG*(R(I)-.5*DR)*ZR*(P(I-1,J)-P(I,J))
01330 FSW=1./(FS+FW)
01340 TIN=(TO(I,J-1)*FS+TO(I-1,J)*FW)*FSW
01350 TO(I,J)=(TIN+GS1*R(I)*(2.*T(I,J)-TIN)*FSW)/(1.+GS1*R(I)*FSW)
01360 TG(I,J)=.5*(TIN+TO(I,J))
01370 GOTO 100
01380 88 P(I,J)=0.
01382 TG(I,J)=T(I,J)
01383 100 CONTINUE
01384 90 CONTINUE
01410 IF(ABS(T1-T(3,16)).GE..01) GOTO 22
```

```
01420 IF(ABS(T2-T(5,10)).GE..01) GOTO 22
01430 IF(ABS(T3-T(4,17)).GE..01) GOTO 22
01440 IF(ABS(T4-T(3,20)).GE..01) GOTO 22
01450 IF(ABS(T5-T(2,15)).GE..01) GOTO 22
01460 DO 110 J=1,28
01470 Z(J)=-24.+2.*FLOAT(J-1)
01480 IF(J.GT.13) Z(J)=J-13
01482 IF(J.LE.12)T(1,J)=99999.
01490 110 CONTINUE
01500 DO 120 J=13,28
01510 DO 130 I=1,16
01520 IF(T(I,J).EQ.TG(I,J)) TG(I,J)=-.001
01530 IF(T(I,J).GT.TM) T(I,J)=TM+(T(I,J)-TM)/RD/.2*KS
01540 130 CONTINUE
01550 120 CONTINUE
01560 WRITE(6,103) N
01570 103 FORMAT(//6X,5H  N =,I6,15X,1HR)
01580 WRITE(6,104)(R(I),I=1,16)
01590 104 FORMAT(3X,8HT(METAL)/6X,6H  Z   ,16F5.1)
01600 WRITE(6,105)((Z(J),(T(I,J),I=1,16)),J=1,28)
01610 105 FORMAT(6X,F6.1,2X,16F5.0)
01620 WRITE(6,106)(R(I),I=1,16)
01630 106 FORMAT(/3X,6HT(GAS)/6X,6H  Z   ,16F5.1)
01640 WRITE(6,105)((Z(J),(TG(I,J),I=1,16)),J=1,27)
01650 WRITE(6,107)(R(I),I=1,16)
01660 107 FORMAT(/3X,14HFLOW POTENTIAL/6X,6H  Z   ,16F5.1)
01670 WRITE(6,108)((Z(J),(P(I,J),I=1,16)),J=13,27)
01680 108 FORMAT(6X,F6.1,2X,16F5.3)
01690 DO 190 I=1,16
01700 DO 190 J=13,27
01710 T(I,J)=(P(I,J)-P(I,J+1))*PG/DZ
01720 TO(I,J)=(P(I,J)-P(I+1,J))*PG/DR
01730 190 CONTINUE
01740 WRITE(6,109)(R(I),I=1,16)
01750 109 FORMAT(/3X,25HR-DIR. GAS FLOW (G/CM2 S) /6X,6H  Z   ,16F5.1)
01760 WRITE(6,111)((Z(J),(TO(I,J),I=1,16)),J=13,27)
01770 111 FORMAT(6X,F6.1,2X,16F5.3)
01780 WRITE(6,112)(R(I),I=1,16)
01790 112 FORMAT(/3X,25HZ-DIR. GAS FLOW (G/CM2 S)/6X,6H  Z   ,16F5.1)
01800 WRITE(6,111)((Z(J),(T(I,J),I=1,16)),J=13,27)
01802 WRITE(6,113)
01804 113 FORMAT(/3X,19HPIPE-FLOW (G/CM2 S) )
01806 WRITE(6,114)((Z(J),FE(J)),J=13,27)
01808 114 FORMAT(6X,F6.1,2X,F6.3)
01810 STOP
01820 END
```

```
00100 PROGRAM SUL44 (INPUT,OUTPUT,TAPE5=INPUT,TAPE6)
00110 REAL KP,K2,MM,MP,IE(31),KPI(31)
00120 COMMON TI,MM,MP,SI,SLG,FP(10)
00130 DATA SAT,ALP,SE,DT/3.3,.1,.013,.5/
00140 SI=.084
00150 MM=3540.
00160 MP=104.
00170 TI=960.
00180 A=MP/TI
00190 JMAX=1800./DT
00200 FS=MM*(SI-SE)/MP/SE
00210 DO 20 K=1,22
00220 KPI(K)=.003+.0005*FLOAT(K-1)
00230 IE(K)=.02*FLOAT(K-1)
00240 20 CONTINUE
00250 DO 40 K=1,2
00260 AKP=KPI(K)
00270 DO 40 JE=7,10
00280 E=IE(JE)
00290 K2=FS*E*A/MM
00300 WRITE(6,101) AKP,E,SI,SE,MM,MP,TI,FS,SAT,ALP
00310 101 FORMAT(///6X,9H   KP    ,8H   E    ,9H   SI    ,9H   SE    ,
00320+9H  METAL  ,9H POWDER  ,9H T-INJ   ,9H S-SDIST  ,9H S-SATU  ,
00330+9H K-SAT/K ,/2X,4F9.4,4F9.1,2F9.2,
00340+///5X,9H   TIME  ,9H S-METAL ,9H S-SLAG  ,9H POWDER  ,
00350+9H    SEQ   ,9H    FRP   ,9H    FRT   )
00360 S=SI
00370 DO 10 J=1,JMAX
00380 T=DT*FLOAT(J)
00390 P=A*AMIN1(T,TI)
00400 SLG=MM/P*(SI-S)
00410 KP=AKP
00420 IF(SLG.GT.SAT)KP=ALP*AKP
00430 IF(FS*S*E.GT.SAT)GOTO 11
00440 IF(T.EQ.TI)K2=0
00450 A1=1.+.5*DT*((1.+MM/FS/P)*KP+K2)
00460 A2=2.-A1
00470 A3=KP*DT*MM*SI/FS
00480 S=(A2*S+A3/P)/A1
00490 RT=K2*S
00500 GOTO 22
00510 11 A4=((1.-E)/(1.-SAT/FS/S))**ALP
00520 SET=FS*S+(SAT-FS*S)*A4
00530 RT=A*SET/MM
00540 IF(T.GE.TI) RT=0
00550 A5=1.+.5*KP*(1.+MM/FS/P)*DT
00560 A6=2.-A5
00570 A7=DT*KP*MM/FS/P*SI
00580 S=(A6*S+A7-DT*RT)/A5
00590 22 CONTINUE
00600 RP=KP*(S-SLG/FS)
00610 FRP=RP/(RT+RP)
00620 N=J-10*INT(.1*FLOAT(J))+1
00630 FP(N)=FRP
00640 IF(MOD(J,60).EQ.0.AND.T.LT.(TI+600.))CALL TYPE(T,S,P,FS)
00650 IF(MOD(J,120).EQ.0.AND.T.GE.(TI+600.))CALL TYPE(T,S,P,FS)
00660 10 CONTINUE
00670 40 CONTINUE
00680 STOP
00690 END
00700C
00710 SUBROUTINE TYPE(T,S,P,FS)
00720 COMMON TI,FMM,FMP,SI,SSLG,FP(10)
00730 DIMENSION GR(51)
00740 SEQ=FMM*SI/(FMM+FS*P)
00750 FRP=0
00760 DO 60 N=1,10
00770 FRP=FRP+FP(N)
00780 60 CONTINUE
00790 FRP=.1*FRP
00800 IF(T.GE.TI) FRP=1.
00810 FRT=1.-FRP
00820 DO 50 I=1,51
00830 GR(I)=1H
00840 IF(MOD(I,10).EQ.1)GR(I)=1HI
00850 50 CONTINUE
00860 IG=INT(50.*S/SI+.5)
00870 GR(IG)=1H*
00880 ISTA=1H*
00890 IF(T.GT.TI) ISTA=1H
00900 WRITE(6,103)ISTA,T,S,SSLG,P,SEQ,FRP,FRT,GR
00910 103 FORMAT(3X,A1,F8.0,F9.4,F9.3,F9.1,F9.4,2F9.3,4X,51A1)
00920 RETURN
00930 END
```

```
00100 PROGRAM SUL55 (INPUT,OUTPUT,TAPE5=INPUT,TAPE6)
00110 REAL IE(31),KPI(31)
00120 COMMON TI,X,FP(10),B
00130 DATA XSAT,ALP,DT/1.,.1,.01/
00140 TI=6.
00150 TMAX=14.
00160 JMAX=TMAX/DT
00170 DO 20 K=1,20
00180 KPI(K)=.2*FLOAT(K-1)
00190 IE(K)=.04*FLOAT(K-1)
00200 20 CONTINUE
00210 DO 40 K=3,4
00220 AKP=KPI(K)
00230 DO 40 JE=1,20
00240 E=IE(JE)
00250 B=-ALOG(1-E)
00260 WRITE(6,101) AKP,E,B,TI,XSAT,ALP
00270 101 FORMAT(///6X,9H   A     ,8H   E    ,9H   B     ,9H   TI    ,
00280+9H  XSAT   ,9H K-SAT/K ,/2X,3F9.4,3F9.2)
00290 WRITE(6,102)
00300 102 FORMAT(//5X,9H   TIME  ,9H S-METAL ,9H S-SLAG  ,
00310+9H    SEQ   ,9H   FRP   ,9H   FRT   )
00320 Y=1.
00330 DO 10 J=1,JMAX
00340 T=DT*FLOAT(J)
00350 TP=AMIN1(T,TI)
00360 X=(1.-Y)/TP
00370 A=AKP
00380 IF(X.GT.XSAT)A=ALP*AKP
00390 IF(Y*E.GT.XSAT)GOTO 11
00400 IF(T.EQ.TI)E=0
00410 A1=1.+.5*DT*((1.+1./TP)*A+E)
00420 A2=2.-A1
00430 A3=A*DT/TP
00440 Y=(A2*Y+A3)/A1
00450 RT=E*Y
00460 GOTO 22
00470 11 A4=((1.-E)/(1.-XSAT/Y))**ALP
00480 XPE=Y+(XSAT-Y)*A4
00490 RT=XPE
00500 IF(T.GE.TI) RT=0
00510 A5=1.+.5*A*(1.+1./TP)*DT
00520 A6=2.-A5
00530 A7=DT*A/TP
00540 Y=(A6*Y+A7-DT*RT)/A5
00550 22 CONTINUE
00560 RP=A*(Y-X)
00570 FRP=RP/(RT+RP)
00580 N=J-10*INT(.1*FLOAT(J))+1
00590 FP(N)=FRP
00600 IF(MOD(J,50).EQ.0.AND.T.LT.(TI+4.)) CALL TYPE(T,Y)
00610 IF(MOD(J,100).EQ.0.AND.T.GE.(TI+4.))CALL TYPE(T,Y)
00620 10 CONTINUE
00630 40 CONTINUE
00640 STOP
00650 END
00660C
00670 SUBROUTINE TYPE(T,Y)
00680 COMMON TI,X,FP(10),B
00690 DIMENSION GR(51)
00700 SEQ=1./(1.+AMIN1(T,TI))
00710 FRP=0
00720 DO 60 N=1,10
00730 FRP=FRP+FP(N)
00740 60 CONTINUE
00750 FRP=.1*FRP
00760 IF(T.GE.TI) FRP=1.
00770 FRT=1.-FRP
00780 DO 50 I=1,51
00790 GR(I)=1H
00800 IF(MOD(I,10).EQ.1) GR(I)=1HI
00810 50 CONTINUE
00820 IG=INT(50.*X+1.5)
00830 GR(IG)=1H+
00840 IG=INT(50.*Y+1.5)
00850 GR(IG)=1H*
00860 ISTA=1H*
00870 IF(T.GT.TI) ISTA=1H
00880 WRITE(6,103)ISTA,T,Y,X,SEQ,FRP,FRT,GR
00890 103 FORMAT(3X,A1,F8.1,F9.3,F9.3,F9.4,2F9.3,4X,51A1)
00900 RETURN
00910 END
```

```
00100 PROGRAM SUL6 (INPUT,OUTPUT,TAPE5=INPUT,TAPE6)
00110 REAL KP,MM,MP
00120 DIMENSION A(99),B(99),C(99),D(99),S(99),TM(21)
00130 COMMON TI,MM,MP,SI,SLG,FP(10),SR
00140 SAT=3.3
00150 ALP=.1
00160 SI=.084
00170 SE=.013
00180 MM=3540.
00190 MP=104.
00200 TI=960.
00210 ND=20
00220 FS=MM*(SI-SE)/MP/SE
00230 DO 30 I=1,7
00240 TM(I)=100.*(2.**(I-2))
00250 30 CONTINUE
00260 AKP=.003
00270 DO 40 JE=1,7
00280 DM=.467/TM(JE)
00290 E=.14
00300 AP=MP/TI
00310 NF=ND+1
00320 FH=1./FLOAT(ND)
00330 RR=DM*.5/FH/FH
00340 DT=.05
00350 T=0
00360 DO 20 I=1,NF+1
00370 S(I)=SI
00380 20 CONTINUE
00390 WRITE(6,101) AKP,E,SI,SE,MM,MP,TI,FS,SAT,ALP,ND,TM(JE)
00400 101 FORMAT(///6X,9H   KP    ,8H   E    ,9H   SI    ,9H   SE    ,
00410+9H  METAL  ,9H POWDER  ,9H T-INJ   ,9H S-SDIST  ,9H S-SATU  ,
00420+9H K-SAT/K ,9H N-DIVID ,9H  T-MIX  ,/2X,4F9.4,4F9.1,2F9.2,I9,F9.1)
00430 WRITE(6,102)
00440 102 FORMAT(//2X,9H   TIME  ,9H S-METAL ,9H S-SLAG  ,9H POWDER  ,
00450+9H    SEQ   ,9H   FRP   ,9H   FRT   ,9H S-REACT )
00460 SR=SI
00470 SB=SI
00480 DO 10 J=1,8000
00490 IF(J.EQ.401) DT=.2
00500 IF(T.GE.TI+240.) DT=.4
00510 T=DT+T
00520 P=MP/TI*AMIN1(T,TI)
00530 SLG=MM/P*(SI-SB)
00540 KP=AKP
00550 IF(SLG.GT.SAT)KP=ALP*AKP
00560 IF(T.GT.TI) AP=0
00570 R=DT*RR
00580 DO 50 N=2,NF-1
00590 A(N)=R
00600 B(N)=1.+2.*R
00610 C(N)=R
00620 D(N)=R*(S(N-1)-2.*S(N)+S(N+1))+S(N)
00630 50 CONTINUE
00640 A(1)=0.
00650 B(1)=1.+2.*R
00660 C(1)=2.*R
00670 D(1)=2.*R*(S(2)-S(1))+S(1)
00690 A1=2.*FH/DM*(KP+AP*FS*E/MM)
00700 A2=2.*FH/DM*KP*SLG/FS
00710 IF(FS*E*SR.LE.SAT) GOTO 11
00720 SETS=FS*SR+(SAT-FS*SR)*((1.-E)/(1.-SAT/FS/SR))**ALP
00730 RT=AP*SETS/MM
00740 A1=2.*FH/DM*KP
00750 A2=2.*FH/DM*(KP*SLG/FS-RT)
00760 11 A(NF)=2.*R
00770 B(NF)=1.+2.*R+A1*R
00780 C(NF)=0.
00790 D(NF)=2.*R*(S(NF-1)-S(NF)-.5*A1*S(NF)+A2)+S(NF)
00800 DO 60 NG=2,NF
00810 B(NG)=B(NG)-A(NG)*C(NG-1)/B(NG-1)
00820 D(NG)=D(NG)+A(NG)*D(NG-1)/B(NG-1)
00830 60 CONTINUE
00840 DO 70 NG=1,NF
00850 JG=NF+1-NG
00860 S(JG)=(D(JG)+C(JG)*S(JG+1))/B(JG)
00870 70 CONTINUE
00880 SB=0
00890 DO 80 NB=2,NF-1
00900 SB=SB+S(NB)
00910 80 CONTINUE
00920 SR=S(NF)
00930 SB=(SB+.5*(S(1)+SR))*FH
00940 IF(FS*E*SR.LE.SAT) RT=AP*FS*E*SR/MM
00950 RP=KP*(SR-SLG/FS)
```

SUL6 (ctd.)

```
00960 FRP=RP/(RT+RP)
00970 NRP=J-10*INT(.1*FLOAT(J))+1
00980 FP(NRP)=FRP
00990 IF(MOD(J,250).EQ.50.AND.J.GT.400)CALL TYPE(T,SB,P,FS)
01000 IF(MOD(J,500).NE.50) GOTO 10
01010 IF(T.GE.TI+840.) GOTO 40
01020 WRITE(6,104)(S(I),I=1,NF)
01030 104 FORMAT(2X,21F6.4)
01040 10 CONTINUE
01050 40 CONTINUE
01060 STOP
01070 END
01080C
01090 SUBROUTINE TYPE(T,S,P,FS)
01100 COMMON TI,FMM,FMP,SI,SSLG,FP(10),SR
01110 DIMENSION GR(51)
01120 SEQ=FMM*SI/(FMM+FS*P)
01130 FRP=0
01140 DO 60 N=1,10
01150 FRP=FRP+FP(N)
01160 60 CONTINUE
01170 FRP=.1*FRP
01180 IF(T.GE.TI) FRP=1.
01190 FRT=1.-FRP
01200 DO 50 I=1,51
01210 GR(I)=1H
01220 IF(I.EQ.1.OR.I.EQ.11.OR.I.EQ.21.OR.I.EQ.31.OR.I.EQ.41.OR.
01230+I.EQ.51) GR(I)=1HI
01240 50 CONTINUE
01250 IG=INT(50.*S/SI+1.5)
01260 GR(IG)=1H*
01270 ISTA=1H*
01280 IF(T.GT.TI) ISTA=1H
01290 WRITE(6,103)ISTA,T,S,SSLG,P,SEQ,FRP,FRT,SR,GR
01300 103 FORMAT(A1,F8.0,F9.4,F9.3,F9.1,F9.4,2F9.3,F9.4,4X,51A1)
01310 RETURN
01320 END
```

```
00100 PROGRAM DSP8 (INPUT,OUTPUT,TAPE5=INPUT,TAPE6)
00110 COMMON FP,GPO,EP,PB,POB,CASB,CAO,FOB,CB,GPCO,OB,
00120+FSI,FS,EC,FO,GSIO,GCAS,GFO,ESI,ES,EF,EC,AFO,SIB,SIOB,SB
00130 DATA QST,QP,QS,QC,QO/5*.04/,RSIO,RPO,RCAS,RFO,AOR/5*.02/
00140+,WM,PPCAO,PPFO,TWP,TIN,ARE/3000.,30.,30.,180.,700.,50./
00150 PCAO=PPCAO/100.
00160 PFO=PPFO/100.
00170 PIR=TWP/TIN
00180 WRITE(6,111)WM,TWP,TIN,PPCAO,PPFO,ARE,PIR
00190 111 FORMAT(/"DSP8 = P-02.5 GPCO"/"   METAL-W  POWDER   TIN "
00200+,"   CAO-C    FEO-C   AREA    PI-R"/5F8.0,F8.2,F8.4)
00210 AW=ARE/WM*7.
00220 AS=ARE*3./100.
00230 DATA WPO,WSIO,WCAS,WFO,WCAO,WCF,TM/3*.02,2*0.,.05,0./
00240 SIB=.13
00250 PB=.1
00260 SB=.04
00270 CB=4.5
00280 WST=100./(WPO+WSIO+WCAS+WFO+WCAO+WCF)
00290 SIOB=WSIO*WST
00300 POB=WPO*WST
00310 CASB=WCAS*WST
00320 FOB=WFO*WST
00330 GPCO=.3E-6
00340 CAO=PPCAO
00350 ESI=.1E12
00360 EP=.1E10
00370 ES=.015
00380 EF=500.
00390 EC=2000.
00400 AFO=1.
00410 FSI=.01*QSI*7./28.09
00420 FP=.01*QP*7./30.97
00430 FS=.01*QS*7./32.06
00440 FC=.01*QC*7./12.
00450 FO=.01*QO*7/16.
00460 GSIO=.01*RSIO*3./60.09
00470 GPO=.01*RPO*3./141.94*2.
00480 GCAS=.01*RCAS*3./72.14
00490 GFO=.01*RFO*3./71.85
00500 CALL GRAF(SB,PB,SIB,CB,TM)
00510 WRITE(6,105)QSI,QP,QS,QO,QC,RSIO,RPO,RCAS,RFO
00520 105 FORMAT(/" RATE-C     KSI          KP          KS          KO          "
00530+,"KC        KSIO2      KP2O5       KCAS       KFEO"/"TRUE  ",9F10.4)
00540 WRITE(6,107)FSI,FP,FS,FO,FC,GSIO,GPO,GCAS,GFO
00550 107 FORMAT("MODIFY ",9F10.8)
00560 WRITE(6,108)ESI,EP,ES,EF,EC,AFO,GPCO
00570 WRITE(6,112)SIB,PB,SB,CB
00580 112 FORMAT("INITIAL",4E10.3)
00590 108 FORMAT(/" EQU.-C      ESI          EP          ES         EFE          "
00600+,"EC         AFO       GPCO-N  "/7X,7E10.3/)
00610 WRITE(6,102)
00620 DT=.05/11.
00630 DO 30 I=1,2411
00640 IF(I.EQ.12) DT=.05
00650 IF(I.EQ.211) DT=.2
00660 IF(I.EQ.911) DT=1.
00670 TM=TM+DT
00680 IF(TM.GE.TIN) PIR=0.
00690 WCAO=WCAO+PIR*PCAO*DT
00700 WCF=WCF+PIR*(1.-PCAO-PFO)*DT
00710 AOB=1/CB/EC
00720 OB=AOB/AFO
00730 AR1=AOR*.001
00740 AR2=AOR*20.
00750 IF(I.LT.4) AR1=.000000001
00760 IF(I.LT.4) AR2=.1
00770 F1=FNP(AR1)
00780 F2=FNP(AR2)
00790 IF(F1*F2.GT.0.) GOTO 88
00800 SGN1=F1/ABS(F1)
00810 81 ARM=(AR1+AR2)*.5
00820 IF(FNP(ARM)*SGN1)85,86,87
00830 87 AR1=ARM
00840 GOTO 84
00850 85 AR2=ARM
00860 84 IF(ABS(AR1-AR2).GT..00000001) GOTO 81
00870 86 AOR=ARM
00880 GOTO 99
00890 88 WRITE(6,113)I,ARM
00900 113 FORMAT(/"F1*F2.GT.0.  *******   I =",I6,"     ARM =",E12.4)
00910 STOP
00920 99 PR=(FP*PB+GPO*POB)/(EP*GPO*(AOR**2.5)+FP)
00930 OR=AOR/AFO
00940 SIR=(FSI*SIB+GSIO*SIOB)/(GSIO*ESI*AOR*AOR+FSI)
```

```
00950 SR=(FS*SB+GCAS*CASB)/(GCAS*ES*CAO/AOR+FS)
00960 FOR=EF*AOR
00970 CR=(FC*CB+GPCO)/(GPCO*EC*AOR+FC)
00980 PCOR=EC*CR*AOR
00990 SIOR=ESI*SIP*AOR*AOR
01000 POR=EP*PR*(AOR**2.5)
01010 CASR=ES*SR*CAO/AOR
01020 SB=SB+AW*QS*(SR-SB)*DT
01030 PB=PB+AW*QP*(PR-PB)*DT
01040 CB=CB+AW*QC*AMIN1((CR-CB),0.)*DT
01050 SIB=SIB+AW*QSI*(SIR-SIB)*DT
01060 WFO=WFO+AS*RFO*(FOR-FOB)*DT+PIR*PFO*DT
01070 WPO=WPO+AS*RPO*(POR-POB)*DT
01080 WSIO=WSIO+AS*RSIO*(SIOR-SIOB)*DT
01090 WCAS=WCAS+AS*RCAS*(CASR-CASB)*DT
01100 TWS=WPO+WFO+WSIO+WCAO+WCAS+WCF
01110 TWW=100./TWS
01120 POB=WPO*TWW
01130 FOB=WFO*TWW
01140 SIOB=WSIO*TWW
01150 CASB=WCAS*TWW
01160 CAO=WCAO*TWW
01170 IF(I.GE.900.AND.MOD(I,25).EQ.10) CALL GRAF(SB,PB,SIB,CB,TM)
01180 IF(I.GE.285.AND.I.LT.786.AND.MOD(I,125).EQ.35) CALL GRAF(SB,PB,
01190+SIB,CB,TM)
01200 IF(I.GE.900.AND.MOD(I,50).EQ.10) GOTO 91
01210 IF(I.EQ.410.OR.I.EQ.660) GOTO 91
01220 GOTO 30
01230 102 FORMAT("TIME",7X,"SI        P         S         O         C
01240+,"SIO2      P205      CAS       CAOR      FEO       AOR     SLAG-W  "
01250+," PCOR")
01260 91 WRITE(6,103)TM,SIB,PB,SB,OB,CB,SIOB,POB,CASB,CAO,FOB,AOR,TWS,PCOR
01270 103 FORMAT(F6.0,1X,11E10.3,2F8.2)
01280 IF(I.LT.950.OR.MOD(I,200).NE.160) GOTO 30
01290 WRITE(6,104)SIR,PR,SR,OR,CR,SIOR,POR,CASR,CAO,FOR,AOR
01300 104 FORMAT("INT.FC ",11E10.3)
01310 WRITE(6,102)
01320 30 CONTINUE
01330 CALL GRAF(0.,0.,0.,0.,-99.)
01340 STOP
01350 END
01360C
01370 FUNCTION FNP(AO)
01380 COMMON FP,GPO,EP,PB,POB,CASB,CAO,FOB,CB,GPCO,OB,
01390+FSI,FS,FC,FO,GSIO,GCAS,GFO,ESI,ES,EF,EC,AFO,SIB,SIOB,SB
01400 A1=4.*FSI*(SIB-(FSI*SIB+GSIO*SIOB)/(GSIO*ESI*AO*AO+FSI))
01410 A2=5.*FP*(PB-(FP*PB+GPO*POB)/(EP*GPO*(AO**2.5)+FP))
01420 A3=-2.*FS*(SB-(FS*SB+GCAS*CASB)/(GCAS*ES*CAO/AO+FS))
01430 A4=2.*GFO*(EF*AO-FOB)
01440 A5=2.*FC*(CB-(FC*CB+GPCO)/(GPCO*EC*AO+FC))
01450 FNP=-2.*FO*(OB-AO/AFO)+A1+A2+A3+A4+A5
01460 RETURN
01470 END
01480C
01490 SUBROUTINE GRAF(SB,PB,SIB,CB,TM)
01500 DIMENSION S(122),P(122),SI(122),C(122),T(122),GR(128)
01510 DATA N/0/
01520 IF(TM.EQ.-99.) GOTO 99
01530 N=N+1
01540 S(N)=SB
01550 P(N)=PB
01560 SI(N)=SIB
01570 C(N)=CB
01580 T(N)=TM
01590 RETURN
01600 99 WRITE(6,301)
01610 301 FORMAT(//10X,"PB , SB , SIB , CB/20."/"TIME   0",8X,
01620+".02",7X,".04",7X,".06",7X,".08",7X,".10",7X,".12",7X,".14",7X,
01630+".16",7X,".18",7X,".20",7X,".22",7X,".24")
01640 DO 10 K=1,N
01650 DO 20 I=1,128
01660 GR(I)=1H
01670 IF(MOD(I,10).EQ.1) GR(I)=1HI
01680 IF(I.EQ.INT(25.*C(K)+1.5)) GR(I)=1HC
01690 IF(I.EQ.INT(500.*S(K)+1.5)) GR(I)=1HS
01700 IF(I.EQ.INT(500.*SI(K)+1.5)) GR(I)=1HQ
01710 IF(I.EQ.INT(500.*P(K)+1.5)) GR(I)=1HP
01720 20 CONTINUE
01730 WRITE(6,302) T(K),GR
01740 302 FORMAT(F5.0,2X,128A1)
01750 10 CONTINUE
01760 RETURN
01770 END
```

A.3. RESULTS OF ANALYSIS

Table A.3.1. Metal Analyses

Sample	Time (min)	S	P	Si	C
A1	0	0.036	0.098	0.024	4.51
A2	2	0.027	0.080	0.008	4.49
A3	4	0.019	0.058	< 0.001	4.45
A4	6	0.014	0.040		4.43
A5	9	0.014	0.014		4.39
A6	11	0.013	0.008		4.35
A7	13.5	0.012	0.007		4.28
A8	15	0.010	0.006		4.27
A9	17	0.008	0.006		4.29
A10	19	0.007	0.008		4.26
A11	21	0.007	0.013		4.25
A12	26	0.009	0.016		4.26
A13	30	0.007	0.017		4.23
A14	34	0.006	0.022		4.24
B1	0	0.034	0.095	0.011	4.45
B2	1	0.030	0.086	0.006	4.45
B3	3	0.021	0.064	0.003	4.42
B4	5	0.016	0.025	< 0.001	4.36
B5	7	0.016	0.014		4.34
B6	9	0.014	0.012		4.33
B7	11	0.013	0.014		4.34
B8	13	0.014	0.017		4.31
B9	15	0.013	0.015		4.27
B10	19	0.011	0.012		4.25
B11	23	0.011	0.013		4.25
B12	27	0.012	0.015		4.22
B13	32	0.011	0.024		4.23
C1	0	0.041	0.125	0.131	4.35
C2	2	0.035	0.125	0.097	4.36
C3	4	0.027	0.120	0.054	4.35
C4	6	0.016	0.117	0.023	4.33
C5	8	0.015	0.090	0.007	4.30
C6	10	0.013	0.065	< 0.001	4.30
C7	12	0.013	0.033		4.31
C8	14	0.014	0.035		4.30
C9	18	0.009	0.039		4.30
C10	21	0.010	0.042		4.31
C11	25	0.010	0.040		4.29
C12	29	0.009	0.043		4.27
C13	35	0.008	0.049		4.29

Table A.3.1. Metal Analyses (Continued)

Sample	Time (min)	S	P	Si	C
D1	0	0.028	0.110	0.34	4.35
D2	1	0.022	0.108	0.31	4.33
D3	3	0.018	0.113	0.33	4.31
D4	5	0.013	0.111	0.27	4.34
D5	7	0.010	0.105	0.24	4.30
D6	9	0.008	0.101	0.23	4.30
D7	11	0.009	0.086	0.18	4.32
D8	14	0.008	0.084	0.051	4.28
D9	16	0.007	0.081	0.036	4.30
D10	18	0.005	0.089	0.031	4.29
D11	21	0.007	0.099	0.042	4.29
D12	25	0.005	0.098	0.027	4.28
D13	30	0.005	0.098	0.021	4.29
E1	0	0.030	0.083	0.013	4.49
E2	2	0.016	0.064	0.005	4.42
E3	4	0.011	0.053	0.001	4.41
E4	6	0.014	0.048	< 0.001	4.38
E5	10	0.013	0.039		4.40
E6	13	0.015	0.027		4.33
E7	15	0.013	0.004		4.28
E8	17	0.011	0.005		4.24
E9	19	0.010	0.008		4.24
E10	22	0.010	0.011		4.25
E11	26	0.009	0.012		4.21
E12	30	0.009	0.014		4.23
E13	34	0.009	0.017		4.23
F1	0	0.032	0.079	0.015	4.58
F2	2	0.021	0.108	0.001	4.55
F3	4	0.015	0.102	< 0.001	4.50
F4	6	0.008	0.056		4.46
F5	8.5	0.007	0.029		4.42
F6	10	0.005	0.047		4.43
F7	12	0.007	0.041		4.42
F8	16	0.007	0.034		4.37
F9	20	0.006	0.046		4.34
F10	24	0.005	0.051		4.33
F11	28	0.005	0.051		4.33
F12	32	0.005	0.054		4.28

Concentrations are weight %.

The analysis methods are as follows:

P,Si ---------- Inductively coupled plasma quantorecorder.

S,C ---------- High frequency combustion, infra-red spectrophometry.

ACKNOWLEDGEMENTS

The author wishes to express his most sincere gratitude to his supervisor, Dr. D.G.C. Robertson for his expert guidance, discussion and contribution throughout the course of this work. He also wishes to thank Professors P. Grieveson and J.H.E. Jeffes and Dr. B. Deo for many useful discussions and encouragement.

This work was carried out as part of a larger project on liquid metal refining supported by the SERC. This financial support is gratefully acknowledged. The experimental work was performed in collaboration with Dr. B. Deo. Thanks are also due to Messrs. A. Neve, A. Willis, T. Scott and N. Eastham for making various items of equipment.

The author wishes to thank Foseco International Limited for help with sulphur analyses in the desulphurization experiments (Chapter 5). He also wishes to express his gratitude to Process Research and Development Laboratories, especially Messrs. Y. Itoh and J. Tanaka, of NSC for a large number of metal and slag analyses in the simultaneous dephosphorization and desulphurization experiments (Chapter 7).

Finally, special thanks are extended to Professor T. Fuwa, Dr. K. Segawa and Nippon Steel Corporation for arranging this period of study at Imperial College.

REFERENCES

1. SCANINJECT: International Conference on Injection Metallurgy, Lulea, Sweden, June 1977.

2. SCANINJECT:II: International Conference on Injection Metallurgy, Lulea, Sweden, June 1980.

3. Meeting on Gas Injection into Liquid Metals, University of Newcastle upon Tyne, England, April 1979.

4. Meeting on Injection Phenomena in Extraction and Refining, University of Newcastle upon Tyne, England, April 1982.

5. 65th Steelmaking Conference Proceedings, ISS of AIME, Pittsburgh, USA, March 1982, 85-130 and 189-226.

6. T. Fuwa, Iron & Steelmaker , 1981, 8, June, 18. ibid, 1981, 8, July, 25.

7. J.C.C. Leach, A. Rodgers and G. Sheehan, Ironmaking & Steelmaking, 1978, 5, 107.

8. H. Nakamura, and T. Emi et al., Tetsu-to-Hagane, 1981, 67, S873.

9. R. Uchimura, and K. Nakanishi et al., ibid, 1981, 67, S265.

10. K. Okohira, Private communication, Yawata Works, Nippons Steel Corp., 1982.

11a. W.A. Krivsky and R. Schuhmann, Trans. AIME, 1959, 215, 82.

11b. R. Guther and P. Opel, Neue Hutte, 1978, 23, 254.

12. G. Denier, J.C. Grosjean and H. Zanetta, Ironmaking & Steelmaking, 1980, 7, 123.

13. S. Ohguchi and D.G.C. Robertson, Proceeding of Injection Phenomena in Extraction and Refining, Newcastle upon Tyne, 1982, J 1-37.

14. G. Boxall, A.K. Sabharwal , T. Robertson and R.J. Hawkins, ibid, 1982, B1-18.

15a. G.D. Smith, Numerical Solution of Partial Differential Equations. Oxford University Press, First Edition, 1965, 149. ibid, Second Edition, 1978, 300.

15b. ibid, First Edition, 1965, 42.
ibid, Second Edition, 1978, 38.

15c. ibid, First Edition, 1965, 147.
ibid, Second Edition, 1978, 229.

15d. ibid, First Edition, 1965, 17.
ibid, Second Edition, 1978, 18.

16. R.E. Bolz and G.L. Tuve,
Handbook of Tables for Applied Engineering Science,
CRC Press, Cleveland, Ohio.

17. S. Yamada et al.,
Tetsu-to-Hagane, 1981, 67, S266.

18. S. Ohguchi and D.G.C. Robertson,
"Formation of Porous Accretion around a Tuyere during
Gas Injection", to be published in Ironmaking & Steelmaking
1983, 10, No.1.

19. R.B. Bird, W.E. Steward and E.N. Lightfoot,
Transport Phenomena, John Wiley and Sons Inc., New York,
London, 1960, 411.

20. J. Szekely, Y.K. Chuang and J.W. Hlinka,
Met. Trans. 1972, 3, 2825.

21. A.H. Castillejos,
M.Sc. Thesis, Imperial College, London 1979.

22. S. Hara, K. Ogino and I. Kurata,
Tetsu-to-Hagane, 1980, 66, S727.

23. T.A. Engh, H. Sandberg et al.,
Scand. J. Metallurgy, 1972, 1, 103.

24. A. Wikander,
SCANINJECT: Int. Conf. on Injection Metallurgy, Lulea,
Sweden, June 1977, 3:1.

25. S.K. Saxena,
ibid, D8:1.

26. R.F. Jones, P. Gale et al.,
JISI, 1966, 204, 505.

27. H. Schenck, E. Steinmetz and M.G. Frohberg,
Arch. Eisenhuttenw., 1963, 34, 659.

28. H. Schenck,
Stahl u. Eisen, 1964, 84, 311.

29. T. Lehner,
SCANINJECT: Int. Conf. on Injection Metallurgy, Lulea, Sweden, June 1977, 11:1.

30. M. Turunen,
Jernkont. Ann., 1975, 159, 7.

31. P. Ritakallio,
SCANINJECT: Int. Conf. on Injection Metallurgy, Lulea, Sweden, June 1977, 13:1.

32. K. Brotzmann and D. Papamentellos,
Iron & Steelmaker , May 1978, 5, 23.

33. S. Tanaka et al.,
Tetsu-to-Hagane, 1980, 66, S262.

34. K. Wada, S. Ogibayashi et al.,
SCANINJECT II: Int. Conf. on Injection Metallurgy, Lulea, Sweden, June 1980, 21:1.

35a. H. Tanabe, M. Hirano et al.,
Tetsu-to-Hagane, 1980, 66, S258.

35b. T. Usui, K. Yamada et al.,
Ibid, 1980, 66, S259.

35c. Fukuyama works, N.K.K.,
75th Symposium of Steelmaking Committee, Japan Soc. for Promotion of Science, March 1980.

36. N. El-Kaddah and J. Szekely,
Ironmaking & Steelmaking, 1981, 8, 269.

37. L. Chang and K.M. Goldman,
Trans. AIME, 1948, 176, 309.

38. K.M. Goldman, G. Derge and W.O. Philbrook,
Trans. Metall. Soc. AIME, 1954, 200, 534.

39. S. Ramachandran, T.B. King and N.J. Grant,
J. Metals, 1956, 8, 1549.

40. R.G. Ward and K.A. Salmon,
JISI, 1960, 196, 393.

41. T. Takenouchi and K. Suzuki,
Tetsu-to-Hagane, 1978, 64, 1133.,Trans. ISIJ, 1979, 19, 758.

42. E. Takeuchi, M. Kishimoto et al.,
Tetsu-to-Hagane, 1978, 64, 1704.

43. F.D. Richardson,
Physical Chemistry of Melts in Metallurgy Vol. 2., 1974, Academic Press, London, New York, p.300.

44. A.A. Deryabin, S.I. Popel and L.N. Subarov,
Izv. Akad. Nauk. SSSR, Metally., 1968, No. 5., 51.

45. H. Ooi, T. Nozaki and Y. Yoshii,
Tetsu-to-Hagane, 1972, 58, 830.

46. H. Gruner, F. Bardenheuer et al.,
Stahl. u. Eisen , 1976, 96, 960.

47. H. Bester and K.W. Lange,
Arch. Eisenhuttenw., 1972, 43, 207.

48. D.S. Conochie and D.G.C. Robertson,
Trans. Inst. Min. Met., 1980, 89, C54.

49. D.G.C. Robertson and E.B. Staples,
Process Engineering of Pyrometallurgy, IMM., London 1974, 51.

50. T. Usui, K. Yamada et al.,
SCANINJECT II: Int. Conf. on Injection Metallurgy, Lulea,
Sweden, June 1980, 12:1.

51. S. Watanabe et al.,
Tetsu-to-Hagane, 1968, 54, S448.

52. Y. Kato, T. Nozaki et al.,
Tetsu-to-Hagane, 1979, 65, No.8., A137.

53. K. Nakanishi, K. Saito et al.,
65th Steelmaking Conference Proceedings, ISS-AIME,
Pittsburgh, USA, March 1982, 101.

54. K. Okohira, S. Murakami et al.,
Tetsu-to-Hagane, 1982, 68, No.2., A37.

55. K. Nakanishi, T. Fujii and J. Szekely,
Ironmaking and Steelmaking, 1975, 2, 193.

56. S. Asai, T. Okamoto et al.,
Tetsu-to-Hagane, 1982, 68, 426.

57. O. Haida, T. Emi et al.,
SCANINJECT II: Int. Conf. on Injection Metallurgy, Lulea,
Sweden, June 1980, 20:1.

58. N.J. Cavaghan, D. Ford and A. Woodhead,
Ironmaking and Steelmaking, 1981, 8, 66.

59. K. Marukawa, Y. Shirota, S. Anezaki and H. Hirahara,
Tetsu-to-Hagane, 1980, 66, No.8., A145.

60. S. Yamamoto, H. Ishikawa, T. Matsuo and H. Kajioka,
ibid, A149.

61. K. Marukawa, Y. Shirota, S. Anezaki and H. Hirahara, Tetsu-to-Hagane, 1981, 67, 323.

62. A. Takahashi, K. Marukawa et al., Tetsu-to-Hagane, 1982, 68, S1027.

S. Anezaki, K. Marukawa et al., ibid, S1028.

63. I. Kokubo, M. Ogata et al., Tetsu-to-Hagane, 1979, 65, S213.

64. M. Kimura, M. Kitamura, S. Itoh and H. Matsui, Tetsu-to-Hagane, 1981, 67, S880.

65. K. Yamada, Y. Miyashita et al., Tetsu-to-Hagane, 1980, 66, No.8., A141.

66. T. Moriya and M. Fujii, Trans. ISIJ, 1981, 21, 732.

67. Y. Nakamura, K. Harashima and Y. Fukuda, Tetsu-to-Hagane, 1981, 67 , 2138.

68. M. Ozawa, S. Okano et al., Tetsu-to-Hagane, 1981, 67, S939.

69. M. Sumida, H. Nakajima et al., Tetsu-to-Hagane, 1981, 67, S936.

70. J. Katsuta, K. Narita et al., Tetsu-to-Hagane, 1981, 67, S184.

71. H. Matsumoto, K. Narita et al., Tetsu-to-Hagane, 1981, 67, S185.

72. T. Nozaki, K. Nakanishi et al., Tetsu-to-Hagane, 1982, 68, 1737.

73. K. Umezawa, S. Nisugi and Y. Arima, Tetsu-to-Hagane, 1980, 66, S729.

74. S. Tonomura, M. Yamahiro et al., Tetsu-to-Hagane, 1981, 67, S181.

75. Y. Itoh, S. Satoh and Y. Kawaguchi, Tetsu-to-Hagane, 1981, 67, 2675.

76. Y. Kawai and K. Mori, Tetsu-to-Hagane, 1982, 68, No.2., A21.

77. D.G.C. Robertson, B. Deo and S. Ohguchi, Submitted to Ironmaking and Steelmaking.

78. A. Hikosaka, K. Narita, T. Makino and H. Matsumoto, Tetsu- to-Hagane, 1980, 66, S728.

79. O. Kubaschewski and C.B. Alcock , Metallurgical Thermochemistry, 5th Edition, Pergamon Press, 360.

80. W -K. Lu, Trans. ISIJ, 1971, 11, 32.

81. K.C. Mills and B.J. Keene, Int. Metals Reviews, 1981, 26, 21.

82. H. Suito and R. Inoue, Tetsu-to-Hagane, 1982, 68, 1541.

83. N. El-Kaddah and D.G.C. Robertson, J. Colloid and Interface Science, 1977, 60, 349.

84. I. Barin et al., Thermochemical Properties of Inorganic Substances, Springer, (1973).

85a. Japan Iron and Steel Inst., Tekko-Binran, 3rd Edition, Maruzen, Vol. 1., Chapter 1.1.

85b. ibid, Page 151.

86. G.K. Sigworth et al., Metal Science J., 1974, 8, 298.

87. H. Inoue, Y. Shigeno, M. Tokuda and M. Ohtani, Tetsu-to-Hagane, 1983, 69, 210.

88. T.B. Winkler and J. Chipman, Trans. AIME, 1946, 167, 111.

89. H. Suito and R. Inoue, Tetsu-to-Hagane, 1983, 69, No.2., A25.

90a. E.T. Turkdogan and J. Pearson, JISI, 1953, 173, 217.

90b. ibid, 1953, 175, 393.

90c. ibid, 1954, 176, 59.

91. G.J.W. Kor, Met. Trans., 1977, 8B, 107.

92. G.W. Healy, JISI, 1970, 208, 664.

93. H. Ohtani, Thermodynamics of Ferrous Metallurgy, Nikkan Kogyo Shinbun, 1971, 224.

94. D.A.R. Kay, A. Mitchell and M. Ram,
JISI,1970, 208, 141.

95. T. Arato, M. Tokuda and M. Ohtani,
Tetsu-to-Hagane, 1980, 66, S900.

96. S. Matoba and S. Ban-ya,
Tetsu-to-Hagane, 1980, 66, 1406.

97. K. Harashima, Y. Fukuda, H. Kajioka and Y. Nakamura,
Tetsu-to-Hagane, 1982, 68, S961.